Università degli Studi di Ferrara

DOTTORATO DI RICERCA IN
SCIENZE DELL'INGEGNERIA

CICLO XXII

COORDINATORE *Prof. Ing. Stefano Trillo*

MODELLING OF PILED RAFT FOUNDATIONS IN SAND

Settore Scientifico Disciplinare ICAR/07

Dottorando
Dott. Daniela Giretti

Tutore
Prof. Ing. Vincenzo Fioravante

Tutore
Prof. Ing. Michele Jamiolkowski

Anni 2007/2009

ACKNOWLEDGEMENTS

I would like to express my sincere gratitude to my supervisor, Professor Vincenzo Fioravante, for having given me the opportunity of undertaking the doctoral studies and for his extremely experienced guidance. He has always guided me in the right direction during my research and supported me whenever I was discouraged. His passion and enthusiasm have proved contagious.

I also wish to gratefully acknowledge my advisor Professor Michele Jamiolkowski for his kind and precious technical guidance through this project.

I would like to thank the Istituto Sperimentale Modelli Geotecnici (ISMGEO) of Seriate (Bergamo, Italy) for fully supporting the experimental part of this research and all of the ISMGEO staff for their competent and highly professional contribution during the experimental work. Special thanks are due to Sergio Airoldi for his tireless dedication and assistance during the centrifuge tests.

Thanks are extended to Maurizio Fontana of Studio Geotecnico Italiano (SGI) for his invaluable guidance and assistance in the numerical analyses performed in this project.

Finally, I wish to acknowledge Marguerite Jones who kindly checked my halting English during the writing of the thesis.

ABSTRACT

A piled raft is a composite foundation in which the piles are used as settlement reducers and they share, with the raft, the load from the superstructure. The applied load is transferred from the raft to the shallow soil and to the pile heads, and from the piles it is diffused through the shaft and the base to deeper soil. The pile–raft and pile–pile interactions represent the distinctive aspect of the piled raft foundations since they modify the load–bearing behaviour of each foundation component, compared to an analogous isolated element, thus determining the overall foundation behaviour.

The main aim of this thesis is to highlight the effects of the raft–soil–pile interactions on the resistance and stiffness of axially loaded piled raft foundations in sand.

A series of centrifuge tests on models of rigid circular piled rafts in loose saturated sand has been performed to this end, employing both non displacement and displacement piles. The raft settlement and the load transmitted to the pile heads and bases were monitored during the tests, which also included unpiled raft and isolated pile tests.

The test results have been analysed in terms of bearing capacity and stiffness; the former according to a load efficiency method, the latter by comparing the values obtained from centrifuge tests with those evaluated through a simplified analytical method.

In order to clarify the effect of the pressure transmitted by the raft to the soil on the behaviour of a single capped pile, some of the centrifuge tests were simulated via finite element numerical analyses, using an elasto–plastic strain hardening constitutive model for the sand. The geometry and the dimensions of the numerical models corresponded to those of the physical ones and the simulations were carried out applying an accelerated gravitational field to the mesh.

The influence of a granular layer, interposed between the raft and the pile heads, on the load transfer mechanism has also been analysed, through an additional series of centrifuge tests which was performed on square rigid raft models on displacement piles in dry dense sand.

Index

List of figures

Chapter 2

Chapter 3

Chapter 4

Chapter 5

Chapter 6

Chapter 7

List of tables

Chapter 3

Chapter 4

Chapter 6

Chapter 7

List of symbols

Roman (Uppercase)

A_p	the cross–sectional area of a pile
A_g	pile group area
A_{pg}	the total cross–sectional area of the piles in the group
B	square raft side
B_e	loading area side of the square raft
C_G	material constant for the evaluation of the small strain shear modulus [Fioravante (2000), Saccenti (2006)]
C_0, C1, C2	correlation factor for the evaluation of the cone resistance [Jamiolkowski et al. (2003)]
D	internal diameter of the model container
D_p	pile diameter
D_R	relative density
D_{50}	mean diameter of the soil grains
E_{eq}	Young's modulus of the equivalent pier
E_p	Young's modulus of the piles
E_r	Young's modulus of the raft
E_s	Young's modulus of the subsoil
E_{s0}	small strain Young's modulus of the subsoil
F_D	correction factor for the embedment of the equivalent raft
G_S	specific density
G	elastic shear modulus [Li and Dafalias (2000) constitutive model]
G_0	small strain shear modulus of the subsoil
G^*_0	material constant for the evaluation of the elastic modulus [Li and Dafalias (2000) constitutive model]

H_i	thickness of the i^{th} soil layer
I_ε	vertical strain factor
J_r	moment of inertia of the raft
K	elastic bulk modulus
K_p	plastic hardening modulus [Li and Dafalias (2000) constitutive model]
L	length
L_p	pile length
L_{AB}, L_{AC}, L_{CB}	distance between measurement sections A–B, A–C, C–B
M	critical stress ratio
N	geometrical scaling factor
Q	load
Q_A, Q_C, Q_B	load measured at the pile head, mid–pile and pile base
Q_p	load transmitted to the pile heads
Q_{py}	pile yielding load
Q_r	load transmitted by the raft to the subsoil
Q_S	pile shaft resistance
$Q_{S,AB}$	shaft resistance acting between load cells A and B
$Q_{S,AC}$	shaft resistance acting between load cells A and C
$Q_{S,CB}$	shaft resistance acting between load cells C and B
Q_t	total load applied to the raft
Q_{Su}	pile shaft ultimate capacity
R	radial distance from the raft axis
R_t, R_n	absolute and normalised pile skin roughness
U_C	soil uniformity coefficient
V_S	shear wave velocity
W_{AB}, W_{AC}	pile dead weight between load cells A–B and A–C

Roman (Lowercase)

a	centrifuge acceleration
b	ratio of the circular cap diameter to pile diameter
c	load cell calibration constant
d	small increment

d	material constant for the evaluation of the small strain shear modulus [Fioravante (2000)]
d_c	piezocone diameter
d_{eq}	diameter of the equivalent pier
d_r	circular raft diameter
d_0	dilatancy parameter [Li and Dafalias (2000) constitutive model]
e	void ratio
e	group efficiency exponent [Flemming et. al (1992)]
e_Γ	material constant for the Li and Wang (1998) critical state envelope
g	gravitational acceleration
h	interposed layer thickness
h, h_1, h_2	hardening parameter [Li and Dafalias (2000) constitutive model]
k_p	pile stiffness
k_{pr}	piled raft stiffness
k_r	raft stiffness
k_{rs}	raft–soil stiffness ratio
l_0	pile segment length
m	dilatancy parameter [Li and Dafalias (2000) constitutive model]
n	number of piles
n	hardening parameter [Li and Dafalias (2000) constitutive model]
nv, nh	material constant for the evaluation of the small strain shear modulus [Fioravante (2000)]
n_s	number of soil layer
p’	mean effective stress
p'_a	atmospheric pressure
q	deviator stress
q_A, q_C, q_B	unit load measured at the pile head, mid–pile and pile base
q_c	cone point resistance
q_r	pressure transmitted by the raft to the subsoil
q_t	pressure applied to the raft
r_m	radius of influence of a pile
r_r	circular raft radius

s	pile spacing
s_c	the distance of the miniaturise piezocone from the container side wall
t_r	thickness of the raft
w	settlement
w_e	the elastic compression of the piles above the level of the equivalent raft
w_p	pile settlement
w_{pr}	piled raft settlement
w_r	raft settlement
w_s	subsoil surface settlement
w_{ur}	settlement of the unpiled raft
z	depth from the subsoil surface

Greek (Uppercase)

Δ	finite increment
Σ	summation

Greek (Lowercase)

α	pile–pile interaction factor
α_{pr}, α_{rp}	pile–raft, raft–pile interaction factor
β	pile group stiffness coefficient
γ_d	dry density
δ’	soil–pile interface friction angle
ε_a	axial strain
ε_q	distortional strain
ε_v	volumetric strain
ζ	piled raft settlement efficiency
η	stress ratio
λ	material constant for the Li and Wang (1998) critical state envelope
μ	pile group efficiency factor [Flemming et. al (1992)]
ν_r	raft Poisson’s ratio

ν_s	subsoil Poissons' ratio
ξ	material constant for the Li and Wang (1998) critical state envelope
ξ_1, ξ_2, ξ_{2S}, ξ_{2B}, ξ_3, ξ_4, ξ_5	load efficiencies
ρ	soil density
ρ_s	soil inhomogeneity factor
σ'_v	vertical effective stress
σ'_h	horizontal effective stress
τ_S	shear stress
$\tau_{S,AB}$, $\tau_{S,AC}$, $\tau_{S,CB}$	mean shear stress acting between load cells A–B, A–C, C–B
φ'_{cv}	shearing resistance angle at critical state
ψ	state parameter
ω_1	pile flexibility

Chapter 1

Introduction

1.1 Background

Piles can be included in a foundation for two main design reasons: in order to provide adequate bearing capacity or to reduce settlements to an acceptable level.

The everyday design of piled footings is based on the assumption that the total weight of the superstructure is supported by the piles, even when the second design criterion is more critical. A different approach, involving the use of piles as *settlement reducers*, has been postulated by Burland et al. (1977), Padfield and Sharrock (1983), Hansbo and Jedenby (1983), Hansbo (1984), Cooke (1986). The basic concept of this approach is that the foundation comprises only the number of piles that are necessary to reduce settlements to a tolerable amount and the loads from the structure are transmitted, via a raft, in part to the piles and in part to the foundation soil (load shared between the raft and piles). This approach allows the piled footing design to be optimized and the number of piles to be significantly reduced.

Foundations on *settlement reducing piles*, herein also referred to as *piled rafts*, have to rely on the ductile behaviour of piles, since the

serviceability settlements are often sufficient to fully mobilise the pile bearing capacity [Burland et al. (1977), Burland (1995)]. Friction piles are adequate for use as settlement reducers, as the shaft capacity is mobilised at small settlements and, for most soils, it remains almost constant, even for relatively large settlements.

Settlement reducing piles can be used for two reasons: to decrease the total settlement, in the case of rigid foundations and to reduce both the total and the differential settlements, when dealing with flexible rafts [Randolph and Clancy (1994), Horikoshi and Randolph (1998), Russo and Viggiani (1998), Viggiani (2001), Poulos (2001), Randolph (2003), Mandolini (2003), Randolph et al. (2004)]. In the latter case, the design is focused on the distribution of the piles in the plane and on the spacing which minimises the raft deflections.

However, a relatively small number of piles could raise the problem of high bending moments and cracking in the raft and a concentration of axial stresses in the pile heads. Constraint reactions between the pile heads and the raft can be reduced by disconnecting the piles from the raft through the use of an interposed fill layer [Wong et al. (2000), Burghignoli et al. (2007), Jamiolkowski et al. (2009)].

1.2 Objectives

The resistance and stiffness of a piled raft and the load sharing mechanism between the raft and the piles are governed by the complex soil–structure interactions which take place between the load–bearing components of the foundation: the piles, the raft and the soil.

The present work is aimed at (i) highlighting the effects of the raft–soil–pile interactions on the load–settlement behaviour and stiffness of the piled rafts, (ii) understanding the load transfer mechanisms which take

place within a piled raft and (iii) exploring the load sharing mechanisms between the raft and the piles. The behaviour of piled raft foundations in sand subject to vertical axial loading has been investigated.

A series of centrifuge tests on models of rigid circular piled rafts in loose saturated sand were performed to this end, employing both non displacement and displacement piles, in order to compare the influence of the installation method on the efficiency of the piles as settlement reducers. The testing programme included the models of isolated single pile, unpiled raft and piled rafts on 1, 3, 7 and 13 piles; the piles were in direct contact with the raft.

Finite element numerical analyses were also performed, using an elasto–plastic strain hardening constitutive model, in order to reproduce some of the centrifuge tests that were carried out and to highlight the effect of the pressure transmitted by the raft to the soil on the behaviour of a single pile beneath the raft. The geometry and the dimensions of the numerical models corresponded to those of physical ones and the simulations were carried out applying an accelerated gravitational field to the mesh.

Finally, the influence of a granular layer, interposed between the raft and the pile heads, on the load transfer mechanisms and on the overall load–settlement behaviour of piled rafts was analysed, through a second series of centrifuge tests which was performed on models of square rigid raft on 1, 4 and 9 displacement piles in dry dense sand.

1.3 Thesis structure

The present thesis consists of the following seven chapters.

- A *literature review* on piled raft foundation analysis and design techniques is presented in Chapter 2. Analytical and experimental

methods are presented, as well as field observations of real structures on settlement reducing piles.

- In Chapter 3 the *characteristics of the centrifuge tests* performed on models of *rigid circular piled rafts in loose saturated sand*, with both non displacement and displacement piles, are illustrated. The test soil, the geometry of the models and the testing procedures are described in detail. The most important features concerning centrifuge modelling are also outlined.

- The *experimental results* of the centrifuge tests (as described in Chapter 3) are presented and discussed in Chapter 4. The influences of the soil–pile, pile–raft and pile–pile interactions on the piled raft stiffness and resistance are the primary concerns. First, the load–settlement behaviour of an isolated single pile is analysed. The influence of the raft pressure on the soil surface on the behaviour of a single capped pile is then pointed out. The effects of the interaction between the piles in a piled raft are then highlighted. Finally, the overall load–settlement behaviour of the piled raft models and the efficiency of piles as settlement reducers are analysed. Results are presented for both non displacement and displacement piles.

- The centrifuge test results (as presented in Chapter 4) are analysed in terms of *bearing capacity and stiffness* in Chapter 5. The piled raft bearing capacity is examined according to a load efficiency method. The piled raft stiffness is analysed by comparing the values obtained from centrifuge tests with those evaluated through a simplified analytical method.

- In Chapter 6, the results of the *finite element numerical simulations* are presented and compared with the centrifuge test results, previously shown in Chapter 4.
- Some of the results of a *second series of centrifuge tests*, which were performed on models of *square rigid piled rafts in dense sand*, with displacement piles, both in contact with the raft and disconnected from the raft through a granular bed, are analysed in Chapter 7. The details of the experimental set–up and of the test procedure are also given.
- A *summary* of the main results obtained from the present work is presented in Chapter 8.

Chapter 2

Literature review

2.1 Introduction

A review of analytical and experimental methods concerning the analysis and design techniques of piled raft foundations is presented as well as recent field observations of real structures on settlement reducing piles.

2.2 Experimental works

1g model tests

Akinmusuru (1980) performed laboratory tests on an unpiled raft, free–standing pile groups and piled rafts in dry sand and showed that the capacity of the piled foundations exceeds the sum of the bearing capacity of the pile group and the cap, due to the increase in the pile bearing capacity caused by the pile–raft interaction (contact pressure of the raft on the soil).

Cooke (1986) reported an extensive series of small scale model tests on unpiled rafts, free–standing pile groups and piled rafts of various sizes, in stiff clay. He noted that the piled raft stiffness was as a maximum 30% greater than that of the free–standing pile groups, while the pile raft bearing capacity was much greater than that of the free–standing pile

groups. He pointed out the importance of pile length on the piled raft behaviour and observed that piles should be long in relation to the raft size. He also observed that, in the case of a rigid raft, the distribution of the load between the piles of piled raft foundations depends on the number of piles and their spacing. For the most common spacings, the external piles can be expected to carry at least twice the load carried by the interior piles.

Phung (1993) performed large scale field tests on shallow footings, isolated piles, free–standing pile groups and piled rafts in loose to dense sand and used several load efficiency coefficients, which varied according to the settlement level considered, to compare the capacities of the elements of the piled footings with those of the single pile, the pile group and the unpiled raft. He found that that piled raft behaviour is mainly governed by the raft–pile interaction, which causes an increase in the pile shaft capacity due to the contact pressure of the raft on the soil. He noted that the centre pile of the piled rafts always takes the largest load portion.

Lee and Chung (2005) executed small scale model tests on free–standing pile groups and piled footings in dense sand and analysed the influence of the pile cap on the behaviour of vertically loaded pile groups. From the test results it was found that the effect of the cap in contact with the underlying soil results in an increase in the skin friction, mainly after the pile yielding load has been reached, with dependency on the pile spacing. They also observed that a much lower load is carried by the raft in piled rafts than by the raft alone, at least at the initial loading stage.

Centrifuge model tests

Horikoshi (1995) and *Horikoshi and Randolph (1996)* presented the results of centrifuge tests on models of a flexible circular raft on small

centred pile groups and a fully piled foundation in clay. They found that even a small pile group can significantly reduce the differential settlement of a raft in spite of the relatively low loads being transferred to the pile group. Loading tests conducted on isolated single piles and single capped piles showed that a small cap in contact with the soil could significantly increase the pile bearing capacity, because of the transfer of the load to the soil through the cap.

Conte el al. (2003) extended the experimental work of Horikoshi (1995) and Horikoshi and Randolph (1996) and carried out centrifuge tests on models of stiff square pile groups and piled rafts in clay. They found that the contribution of the pile capacity to the overall capacity of piled rafts decreases where the raft protrudes beyond the pile group and that central settlement reducing piles beneath the raft can be loaded close to their full capacity without compromising the foundation stability.

Fioravante and Jamiolkowski (2005) performed centrifuge tests on models of a rigid circular piled raft in overconsolidated clay and found that the load distribution within a pile group under a rigid raft, in the working load range, is not uniform and is consistent with the prediction of a linear–elastic analysis. They also observed that the load transfer mechanism within a group of settlement reducing piles is different from that observed for an isolated pile and the difference can mainly be ascribed to the effect of the load that is transferred by the raft to the soil and to the additional confinement between the neighbouring piles.

2.3 Analytical works

Several methods of analysing piled rafts have been developed, and some of these have been summarized by Poulos et al. (1997), Poulos (2001a and b). Three classes of analysis method have been identified:

- simplified calculation methods, which involve a number of simplifications in relation to the modelling of the soil profile and the loading conditions on the raft;
- approximate computer–based methods, such as the "strip–on–springs" approach, in which the raft is represented by a series of strip footings, and the piles are represented by springs of appropriate stiffness, or the "plate–on–springs" approach, in which the raft is represented by a plate and the piles as springs;
- more rigorous computer–based methods, such as boundary element methods, in which both the raft and the piles within the system are discretised with boundary elements, and use is made of the elastic theory; methods combining boundary elements for the piles and finite element analysis for the raft; simplified finite element analyses, which usually involve the representation of the foundation system as a plane strain problem or an axisymmetric problem; three–dimensional finite element analyses.

2.3.1 Simplified analysis methods

Equivalent raft method

The foundation is considered as a whole and the piled raft settlement is estimated considering an equivalent raft situated two–thirds of the way down the part of the piles which penetrate the main foundation stratum, or at the level of the pile bases for end bearing piles [Tomlinson (1986), Bowles (1988)]. The average settlement at the ground level is calculated as:

$$w_{avg} = w_r + w_e \qquad [L] \qquad (2.1)$$

where:

w_r = raft settlement [L];

w_e = elastic compression of the piles above the level of the equivalent raft, which are treated as free–stand columns [L].

A load–spread of 1 in 4 is generally assumed in order to evaluate the equivalent raft area. A convenient method of calculating w_r is based on the integration of the vertical strains below the equivalent raft, allowing for variations in the soil modulus and correcting the raft embedment below the ground surface, as follows [Poulos (1993)]:

$$w_r = F_D q_t \sum_{l=1}^{n_s} \left(\frac{I_\varepsilon}{E_s} \right)_i H_i \qquad [L] \qquad (2.2)$$

where:

q_t = average pressure applied to the raft [FL^{-2}];

I_ε = influence factor from which the vertical strain may be calculated [-];

H_i = thickness of the i^{th} layer [L];

E_s = Young's modulus of the i^{th} layer [FL^{-2}];

F_D = correction factor according to Fox (1948) [-];

n_s = number of soil layers [-].

For consistency, the embedment depth should be taken as that below the top of the main bearing stratum, rather than that from the ground surface. Poulos (1993) presented the results of a parametric study that compared the equivalent raft method with more rigorous analysis and found that, for groups containing more than 16 piles, the equivalent raft method can be a useful approach for settlement prediction, while it significantly overpredicts the settlement for a relatively small number of piles.

Equivalent pier method

The region of the soil in which the piles are embedded is considered as a continuum and the pile group is replaced by an equivalent pier [Poulos

and Davis (1980)]. For a pile group of area A_g, the diameter of the equivalent pier is taken as:

$$d_{eq} = \sqrt{\frac{4}{\pi} A_g} = 1.13\sqrt{A_g} \qquad [L] \qquad (2.3)$$

and Young's modulus of the pier as:

$$E_{eq} = E_s + (E_p - E_s)\frac{A_{pg}}{A_g} \qquad [FL^{-2}] \qquad (2.4)$$

where:

E_p = Young's modulus of the piles [FL^{-2}];

E_s = average Young's modulus of the soil penetrated by the piles [FL^{-2}];

A_{pg} = total cross–sectional area of the piles in the group [L^2].

Poulos (1993) presented the results of a parametric study which compared the equivalent pier method with more rigorous analysis and found that the equivalent pier method tends to underpredict the settlement as the number of piles in the group increases while, for groups containing a relative small number of piles, it can be used with some confidence.

Poulos–Davis–Randolph (PDR) method

The ultimate load capacity of the piled raft foundation is taken as the lower of the following two values:

- the sum of the ultimate capacities of the raft plus all the piles;
- the ultimate capacity of a block containing the piles and the raft, plus that of the portion of the raft outside the periphery of the piles.

The approach outlined by Randolph (1994) can be adopted in order to estimate the load–settlement behaviour. The stiffness of the piled raft foundation is estimated as follows:

$$k_{pr} = \frac{k_p + k_r\left(1 - 2\alpha_{rp}\right)}{1 - \alpha_{rp}^2\left(k_r / k_p\right)} \qquad [FL^{-1}] \qquad (2.5)$$

where:

k_{pr} = stiffness of the piled raft [FL^{-1}];

k_p = stiffness of the pile group [FL^{-1}];

k_r = stiffness of the raft alone [FL^{-1}];

α_{rp} = raft–pile interaction factor [-].

The proportion of the total applied load carried by the raft is:

$$\frac{Q_r}{Q_t} = \frac{k_r\left(1 - \alpha_{rp}\right)}{k_p + k_r\left(1 - 2\alpha_{rp}\right)} \qquad [-] \qquad (2.6)$$

where:

Q_r = load transmitted by the raft to the soil [F];

Q_t = total load applied to the raft [F].

Eqs. 2.5 and 2.6 are used to develop a tri–linear load–settlement curve, as shown in Figure 2.1(a). The stiffness of the piled raft is computed from Eq. (2.5) for the number of piles being considered. This stiffness will remain operative until the pile capacity is fully mobilised (point A).

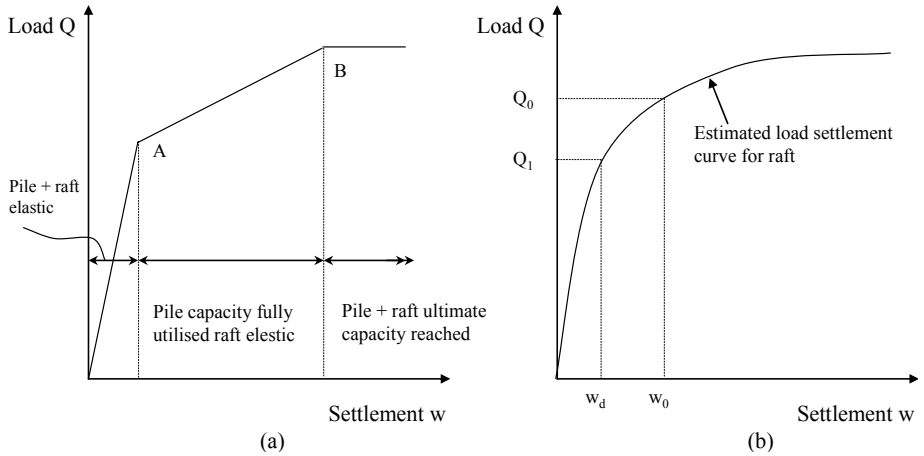

Figure 2.1. (a) PDR method and (b) Burland's simplified design concept.

Beyond Point A, the stiffness of the foundation system is that of the raft alone (k_r), and this holds until the ultimate load capacity of the piled raft foundation system is reached (Point B). At this stage, the load–settlement relationship becomes horizontal.

Poulos (2001b) compared the piled raft load–settlement behaviour, computed with the PDR method, with that obtained from more rigorous methods and found good agreement.

Burland's approach

Burland (1995) developed the following simplified design process for piles that are chosen to act as settlement reducers and to develop their full geotechnical capacity at the working load:

- estimate the total long–term load–settlement relationship for the raft without piles (see Figure 2.1(b)). The design load Q_0 gives a total settlement w_0;
- assess an acceptable design settlement w_d, which should include a margin of safety: Q_1 is the load carried by the raft corresponding to w_d;
- the load excess $Q_0 - Q_1$ is assumed to be carried by settlement-reducing piles. The shaft resistance of these piles will be fully mobilized and therefore no factor of safety is applied.

However, Burland suggested that a "mobilisation factor" of about 0.9 can be applied for a "conservative estimate" of the ultimate shaft capacity, Q_{Su}. If the piles are located below columns that carry a load in excess of Q_{Su}, the piled raft may be analysed as a raft on which reduced column loads act. The reduced load at such columns is $Q_r = Q - 0.9Q_{Su}$ and the bending moments in the raft can therefore be obtained by analysing the piled raft as a raft subjected to the reduced loads Q_r. Burland did not explicitly give out a process to estimate the settlement of piled rafts;

Poulos (2001b) suggested adopting the approximate Randolph (1994) approach, in which: $w_{pr} = w_r \cdot k_r / k_{pr}$, where w_{pr} = settlement of the piled raft, w_r = settlement of the raft without piles subjected to the total applied load. Eq. 2.5 can be used to estimate k_{pr}.

2.3.2 Approximate computer methods

Strip–on–springs approach

An example of the strip–on–springs method has been presented by Poulos (1991). A section of the raft is represented by a strip and the supporting piles by springs. An approximate allowance is made for all the interaction components between the foundation elements; the effects of the parts of the raft outside the strip section being analysed are taken into account by computing the free–field soil settlements due to these parts. These settlements are then incorporated in the analysis, and the strip section is analysed to obtain the settlements and moments due to the applied load on that strip section and the soil settlements due to the sections outside the raft. The soil non–linearity is taken into account in an approximate manner by limiting the strip–soil contact pressures so that it does not exceed the bearing capacity (in compression) or the raft uplift capacity in tension. The pile loads are similarly limited so that the compressive and uplift capacities of the piles are not exceeded. However, the ultimate pile load capacities must be pre–determined, and are usually assumed to be the same as those of isolated piles. In reality, as shown by Cooke (1986), Phung (1993), Lee and Chung (2005), Horikoshi and Randolph (1996), Katzenbach et al. (1998), Katzenbach et al. (2000), Fioravante and Jamiolkowski. (2005), the load transmitted to the soil by the raft can have a beneficial effect on the pile behaviour in the piled raft system. Good agreement between the strip–on–springs method and other

calculation methods (simplified and more rigorous) has been found by Poulos (2001b).

Plate–on–springs approach

In this type of analysis, the raft is represented by an elastic plate, the soil is represented by an elastic continuum and the piles are modelled as interacting springs [Clancy and Randolph (1993), Poulos (1994)]. Poulos (1994) employed a finite difference method for the plate. Allowance is made for the various interactions via approximate elastic solutions. Allowance is also made for layering of the soil profile, the effects of the piles reaching their ultimate capacity (both in compression and tension), the development of bearing capacity failure below the raft, and the presence of free–field soil settlements acting on the foundation system. A later version of this analysis method has replaced the finite difference analysis for the raft with a finite element analysis, and has employed a modified approach to consider the development of the ultimate load capacity in the piles. Russo (1998) and Russo and Viggiani (1998) described a similar approach to the previous methods, in which the various interactions are obtained from the elastic theory and non–linear behaviour of the piles is considered via the assumption of a hyperbolic load–settlement curve for single piles. The pile–pile interactions are only applied to the elastic component of pile settlement, while the non–linear component of settlement of the pile is assumed to arise only from loading on that particular pile.

2.3.3 More rigorous computer methods

Mixed technique

El-Mossallamy and Franke (1998) and Franke et al. (2000) presented a method that combines boundary element and finite element analysis. The

raft is modelled by FEM as a plate–in–bending, acted on by the superstructure loads and supported by non–linear elastic springs at each node of the mesh. These springs in part represent the piles and in part the soil. The contact pressure between the raft and the soil and between the piles and the soil are modelled by BEM, i.e. the boundary element mesh contains only elements at the raft–soil and pile–soil interfaces [a similar solution to that proposed by Butterfield and Banerjee (1971)]. The finite stiffness of the raft and the piles, as well as the non–linear pile response, are taken into account.

The model was successfully applied for the back–calculation of the behaviour of the Messeturm and Westendstrasse buidings in Frankfurt. In particular the Authors found that on one hand the effect of the pile–raft interaction decreases the modulus of pile reaction but, on the other, it increases the ultimate pile load. These effects depend on the load level, on the raft and group dimensions and on the pile location in the pile group. Moreover, the pile skin friction is mobilised from the pile tip upwards, in contrast to what happens for an isolated pile, since the soil just beneath the raft is forced to settle by the same amount as the raft and the pile tops. The degree of shaft friction mobilisation along the piles depends on the pile location.

Two–dimensional numerical analyses

The foundation is assumed to be a two–dimensional (plane strain) problem, or an axially symmetric three–dimensional problem. In both cases, significant approximations need to be made, especially with respect to the piles, which must be smeared to a wall or to an annulus and given an equivalent stiffness equal to the total stiffness of the piles being represented. Problems are also encountered in representing concentrated loadings in such an analysis, since these must also be smeared.

Poulos (2001b) compared the results of a plane–strain analyses with those obtained from the PDR approach, from the approximate computer methods previously mentioned and from a complete three–dimensional analysis and found that two–dimensional analysis can seriously over-predict settlements because of the implicit assumption of plane strain in the analysis. He suggested that plane strain analyses of piled rafts must be approached with extreme caution because the results may be misleading if the raft is essentially square or rectangular.

Three–dimensional numerical analyses

A complete three–dimensional analysis of a piled raft foundation system can be carried out by finite element analysis. Katzenbach and Reul (1997) and Katzenbach et al. (1998) described a structural model which allows the different load–settlement behaviour of rafts and piles and the raft–soil, raft–pile and pile–pile interactions to be analysed. In the numerical simulation presented, the continuum and the piles are represented by three–dimensional isoparametric finite elements while the raft is modelled with shell elements. Infinite elements, which respond like an elastic half–space, are used at the borders. The piles are simulated as linear elastic and the raft is considered rigid. The soil is modelled as an elasto–plastic material. Shearing at the pile shaft is considered by shearing of the finite elements that represented the soil.

The structural model has successfully been applied for the design of tall buildings [Katzenbach et al. (1997)]. The author showed that the piles within the piled raft foundation develop more than twice the shaft resistance of a single isolated pile or a pile within a normal pile group, with the centre piles showing the largest values. This is because of the increased normal stresses generated between the soil and the pile shaft by the loading on the raft.

However, the main problem related to FE analyses is the time involved in obtaining a solution. Such analyses are more suitable for obtaining benchmark solutions against which to compare simpler analysis methods, rather than as routine design tools. Katzenbach et al. (1998) developed an interaction diagram which relates the relative settlement (ratio of the settlement of the piled raft to the raft alone) to the number of piles and their length–to–diameter ratio, L/d. This diagram clearly shows that, for a given number of piles, the relative settlement is reduced as L/d increases. It also shows that there is generally very little benefit to be obtained in using more than about 20 piles.

2.2 Field data and case studies

Most case histories of piled raft foundations deal with piled rafts in clayey soils. In the last few years, the application of piled rafts has been extended to sandy soils.

Katzenbach et al. (2000) and Reul (2003) reported on the performance of several piled raft foundations recently realised in Germany, both in soft clay (Frankfurt clay) and in loose sand (Berlin sand). In almost every case, the piled rafts were built using large diameter cast in situ bored piles. All were controlled by geotechnical monitoring. The results of the monitoring on the first piled raft projects (in which the piles carried about 80% of the structural load) allowed the piled raft design to be optimised. In the most recent projects, 1/1 and 1.5/1 load sharing values between the raft and piles have been obtained. A great influence of the position of the pile beneath the raft on the pile load–settlement behaviour has been observed for the piled raft in the Frankfurt clay, where the load increases from the centre to the external piles. The variation in the load with the pile position is due to the block deformation of the pile group, which

causes small differential settlements between the piles at the centre of the raft and the surrounding soil. Hence, the pile shaft loads of the centre piles are smaller than the pile shaft loads of the edge and corner piles. The Authors also observed that piled rafts effectively reduce maximum and differential settlements and, in urban environments, these positive effects also help guarantee the stability and serviceability of existing buildings. In comparison to conventional pile foundations, the application of piled rafts can lead to economic reductions of up to 60% in the total number and length of the piles needed for the foundations.

O'Neill (2005) summarised 24 case histories of piled raft foundations. The subsoil conditions which were analysed ranged from soft clay to stiff soil overlying rock; the pile types were bored, auger and driven. O'Neill observed that in most cases the piles were bored and placed on a more–or–less uniform grid under the tower part of the structure, at 4 to 5 pile diameters on the centres, mainly in order to reduce raft stresses and differential settlements under sustained loads. Under these conditions, and if the soil is overconsolidated, a 1/1 load sharing between the raft and piles can be gained if the piles are allowed to be loaded to about 80% of their ultimate load. When the soil is slightly overconsolidated and the piles are loaded in excess of 80% of their ultimate capacity, the raft tends to carry a higher proportion of the loads. Instead, when the piles are loaded to about 50% of their ultimate capacity, the piles carry more than one–half of the sustained working loads. This is the condition that was observed for most of the case histories reported.

Chapter 3

Experimental set–up

3.1 on centrifuge modelling

The mechanical behaviour of a natural soil depends on its "state parameters": its nature (e.g. mineralogical composition), its physical properties (such as water content or relative density), its chemical properties (such as digenesis, cementation), its effective stress state and its stress history. A physical model can artificially reproduce the mechanical behaviour of a soil only if the model correctly replicates the prototype state.

Due to the intrinsic difficulties involved in reproducing all the relevant aspects of a soil state, some approximation are generally accepted in physical modelling; the skill is to spot the appropriate level of simplification, to recognise the most important features with respect to the engineering problems that have to be considered. Maintaining consistency in the stress field of the physical model is certainly one of the key factors to accurate modelling.

Multi-g physical modelling is based on the principle that, if a model, in which each linear dimension is reduced by a factor N, is subjected to a centrifuge acceleration of $a = Ng$ (where g is the gravity field), the self-

weight of any material used for the model is N times larger than in a 1g gravity field. Therefore, a 1/N model at the centrifuge acceleration of $a = Ng$ achieves the equivalent vertical stress of the full scale prototype, assuming that a material with the same mass density is used in the model. If the stress–strain characteristic of the model material is the same as in the prototype, for example if the same soil is used in the model, similarity of strains is also achieved.

If the scaling factor for a generic quantity is defined as: $x^* = x_{prot}/x_{mod}$ (where x_{prot} = the value of the quantity x at the prototype scale and x_{mod} = the value of the quantity x at the model scale), in a soil model prepared from the prototype material (i.e. identical material rheology in the model as in the prototype and density scaling factor $\rho^* = \rho_{prot}/\rho_{mod} = 1$), geometrically scaled down N times with respect to the prototype (geometrical scaling factor $L^* = L_{prot}/L_{mod} = N$) and subject to a gravitational field N times higher than the prototype (gravity scaling factor $g^* = g_{prot}/g_{mod} = 1/N$), the centrifuge acceleration reproduces the same stresses and strains as in the prototype so that the model exhibits identical mechanical behaviour as the prototype soil [Schofield (1980)]. The observations from the model can be related to the prototype using the similarity relationships reported in Table 3.1, which are valid within continuum mechanics.

Much effort is still being devoted to understanding the reproducibility, at a small scale, of interface problems, such as pile shaft friction mobilisation, which are a matter of discontinuity mechanics rather than continuum mechanics. The displacement required to mobilise the ultimate shaft friction of model piles is often comparable with that required for full scale piles (from about 1 to 10 mm), which would

suggest that the relative–displacement scaling factor is very close to unity, i.e. $w_{prot} \approx w_{mod}$ [Fioravante et al. (2008a)].

Table 3.1. Similarity relationships.

Quantity	Prototype	Model
Acceleration	1	N
Length	1	1/N
Area	1	$1/N^2$
Volume	1	$1/N^3$
Velocity (projectile)	1	1
Velocity (undrained conditions)	1	N
Mass	1	$1/N^3$
Force	1	$1/N^2$
Energy	1	$1/N^3$
Stress	1	1
Strain	1	1
Mass Density	1	1
Energy density	1	1
Time (Dynamic)	1	1/N
Time (Diffusion)	1	$1/N^2$
Time (Creep)	1	1
Frequency	1	N

In centrifuge modelling, the following points should be taken into account:

- The centrifuge acceleration applied to the model is radius dependent; thus the vertical stress distribution of the model is parabolic and it diverges slightly from the linear distribution of the overburden stresses in the prototype.
- The soil surface and the free water surface of the model are not flat.
- The existence of rigid side walls and a rigid base may affect the behaviour of the model; care is necessary when designing the boundary conditions in the model.
- In centrifuge models, the same type of soil is generally used as in the prototype, in order to ensure the same stress–strain response. Thus the

proportion of the particle size to the structure size is not scaled. The particle size effects are generally negligible for clay, while they have to be carefully controlled for sand and silt.

3.2 The ISMGEO geotechnical centrifuge

The model tests were performed using the ISMGEO (Istituto Sperimentale Modelli Geotecnici, Seriate – BG – Italy) geotechnical centrifuge, herein simply called IGC, which is a beam centrifuge made up of a symmetrical rotating arm with a diameter of 6 m, a height of 2 m and a width of 1 m, which gives it a nominal radius of 2 m. The arm holds two swinging platforms, one used to carry the model container and the other the counterweight; during the test, the platforms lock horizontally to the arm to prevent transmitting the working loads to the basket suspensions. An outer fairing covers the arm and they concurrently rotate to reduce air resistance and perturbation during flight. The centrifuge has the potential of reaching an acceleration of 600g at a payload of 400 kg. The maximum dimensions of the model are: length = 1 m, height = 0.8 m, with = 0.5 m; further details can be found in Baldi et al. (1988). Figure 3.1 shows a scheme of the IGC. The unusual shape of the arm offers the following advantages:

- small distortion of the centrifugal field in the model, since its main dimension is parallel to the rotation axis;
- low deflection of the support plane of the swinging basket;
- easy location of instruments close to the rotation axis because of the absence of a central shaft across the arm.

The IGC houses a shaking table, which is capable of reproducing a single degree of freedom prototype strong motion events at a model scale. The

axis of motion of the shaker is parallel to the centrifuge rotational axis, thus problems related to Corioli's acceleration are avoided. The shaker is not integrated into the swinging platform, but is directly connected to the rigid arm: the model container is moved into contact with the table in flight and released before dynamic excitation of the model starts; the shaker forces are entirely transferred from the slip table to the model container by mechanical coupling.

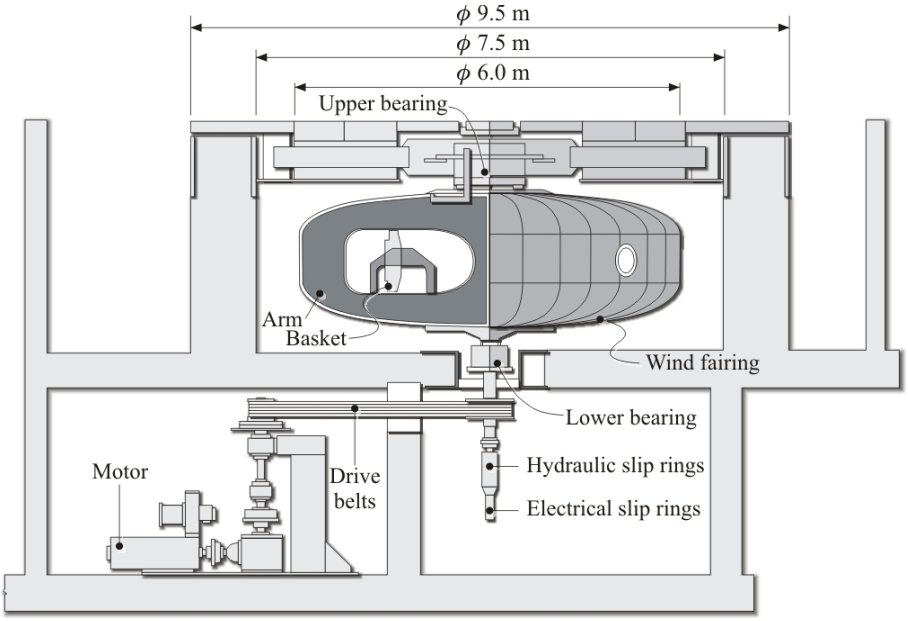

Figure 3.1. The ISMGEO Geotechnical Centrifuge.

3.3 Test soil

Experiments have been performed using saturated FF sand (FFS), a very fine and uniform silica powder derived by grinding and sieving pit rocks. It mainly consists of sub angular particles and it is made of 98.2% quartz, 1.3% feldspar and 0.5% mica. Figure 3.2 reports the grain size distribution of FFS, whose physical properties are summarised in Table 3.2.

The mechanical behaviour of FFS was characterised through a large series of triaxial tests; wide ranges of initial mean stress, p'_0, and void ratio, e_0, were experienced, p'_0 and e_0 ranging from 15 to 800 kPa and from 0.88 to 1.09, respectively. The local strain and the shear wave propagation velocity were measured using bender elements (BE) during some tests.

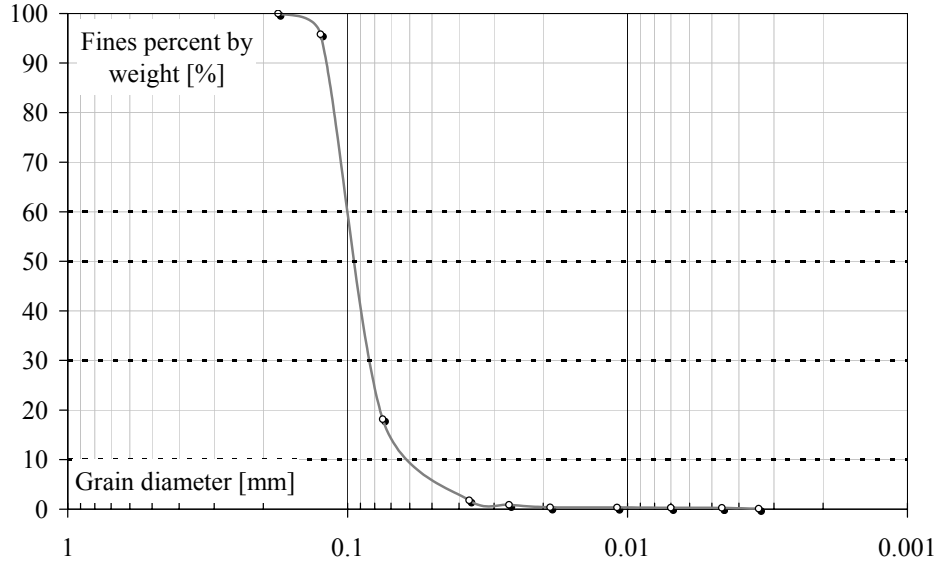

Figure 3.2. Grain size distribution of the FF sand.

Table 3.2. Physical properties of the FF sand.

$\gamma_{d,min}$ [kN/m^3]	$\gamma_{d,max}$ [kN/m^3]	e_{max} [-]	e_{min} [-]	G_S [-]	D_{50} [mm]	U_C [-]
11.58	14.78	1.211	0.732	2.61	0.093	1.88

$\gamma_{d,max}$ and $\gamma_{d,min}$ = maximum and minimum dry density
e_{max} and e_{min} = maximum and minimum void ratio
G_S = specific density
D_{50} = mean particle size
U_C = uniformity coefficient

Table 3.3 reports, for all the tests, the values of the void ratio, e, the relative density, D_R, the confining pressure, p', the deviator stresses, q, and the stress ratio, η, measured at the beginning of the tests and at the critical state condition.

The experimental results of the undrained and drained tests performed on specimens characterised by initial D_{R0} and p_0' values comparable with those of the centrifuge soil models (i.e. $D_{R0} \approx 25\% \div 35\%$ and $p'_0 < 250$ kPa, see next sections) are shown in Figures 3.3o t 3.7. The *q-p'* effective stress paths are reported in Figures 3.3 and 3.5, for the undrained and drained tests, respectively; the stress-strain responses are represented in the q/p'-ε_a space in Figures 3.4 and 3.6 (where ε_a = axial deformation of the specimens); the *e-p'* paths are shown in Figure. 3.7. The critical state conditions are highlighted in Figures 3.3, 3.5 and 3.7.

Table 3.3. Triaxial tests on the FF sand.

Test*	Initial condition					Critical state			
	e_0 [-]	D_{R0} [%]	p'_0 [kPa]	q_0 [kPa]	η_0 [-]	e_{cv} [-]	p'_{cv} [kPa]	q_{cv} [kPa]	η_{cv} [-]
CIU148	0.889	67.2	593	0	0	0.889	1304	1860	1.426
CIU 119	1.022	39.5	800	0	0	1.022	404	565.3	1.399
CIU1_07	1.069	29.5	25	0	0	1.069	391	525.4	1.341
CIU2_07	1.065	30.5	50	0	0	1.065	421.3	560.2	1.33
CIU3_07	1.032	37.3	100	0	0	1.032	487	652	1.339
CIU4_07	1.047	34.1	200	0	0	1.047	528	713	1.350
CIU5_07	1.064	30.6	15	0	0	1.064	481.7	631.8	1.312
CIU6_07	1.017	40.4	25	0	0	1.017	655.7	857.6	1.308
CIU23_07	1.053	33	100	0	0	1.053	573	799	1.393
CIU_1_100	1.005	43	100	0	0	1.005	435.3	591.2	1.358
CID1_07	1.076	28.2	25	0	0	1.145	45.1	60.4	1.338
CID2_07	1.064	30.7	50	0	0	1.109	97.9	143.6	1.467
CID101	1.073	28.8	50	0	0	1.085	91.7	123.7	1.349
CID102	1.088	25.6	100	0	0	1.074	178.6	237.3	1.329
CID103	1.054	32.8	250	0	0	1.008	455.4	609.7	1.339
CID104	1.062	31	400	0	0				
CID104B	1.056	32.3	400	0	0	0.970	718.2	951.9	1.325
CID107**	1.092	24.8	100	0	0	1.088	182.1	241.2	1.325
CK0D112	1.029	38.1	290	170	0.58	1.005	422.4	561	1.328
CID121	0.999	44.2	250	0	0	0.986	479.7	691.6	1.442
CID132	0.890	66.9	100	0	0	0.966	194.0	275.4	1.420
CID134	0.878	69.6	400	0	0				
CID137**	0.941	56.3	100	0	0	0.999	187.3	260.6	1.391
CK0D140	0.931	58.5	73	39	0.53	1.016	115.2	163.2	1.416
CID138	0.947	55.1	100	0	0	1.004	189.0	268.4	1.420
CK0D142	0.894	66.1	275	195	0.7				

* CIU = isotropic compression, undrained shear
CID = isotropic compression, drained shear
CK0D = one-dimensional compression, drained shear
** Overconsolidation ratio OCR = 2

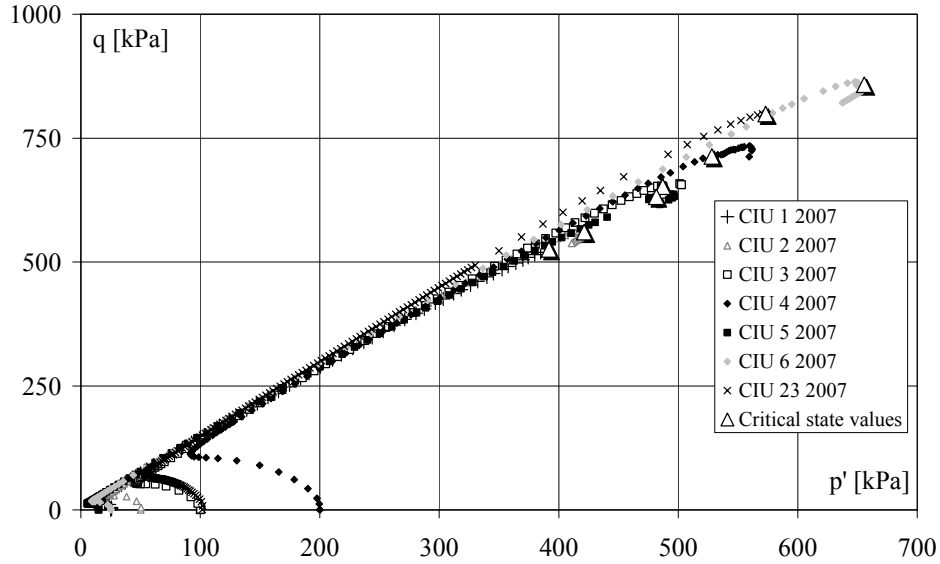

Figure 3.3. Undrained tests: effective stress paths.

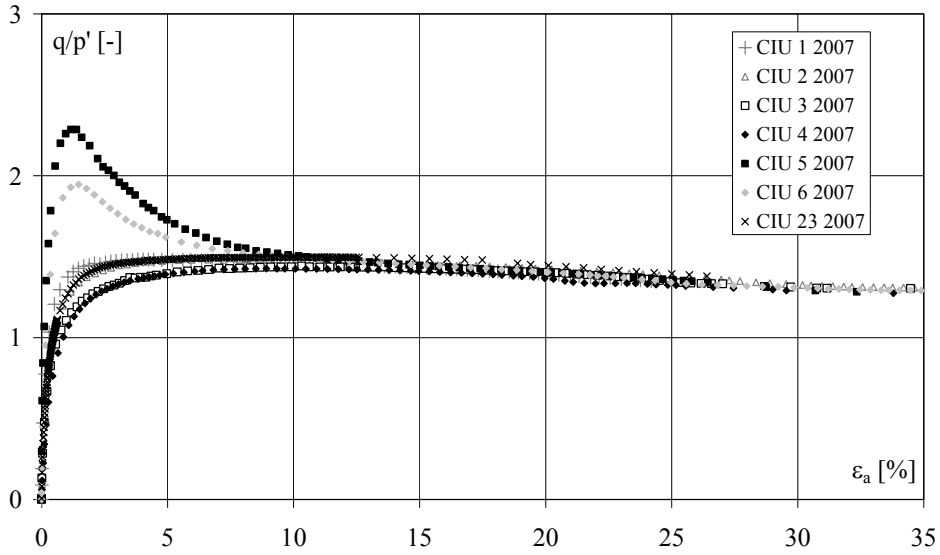

Figure 3.4. Undrained tests: stress–strain response.

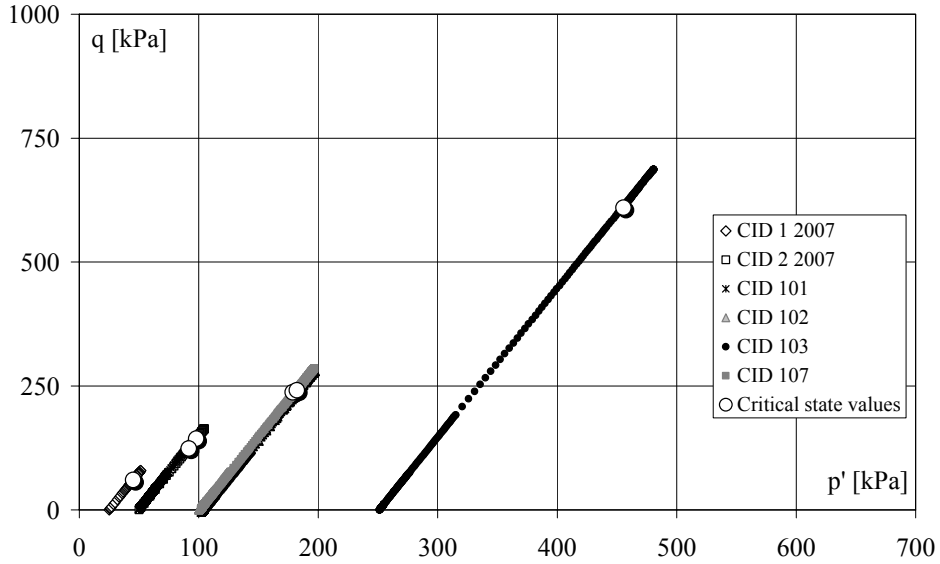

Figure 3.5. Drained tests: effective stress paths.

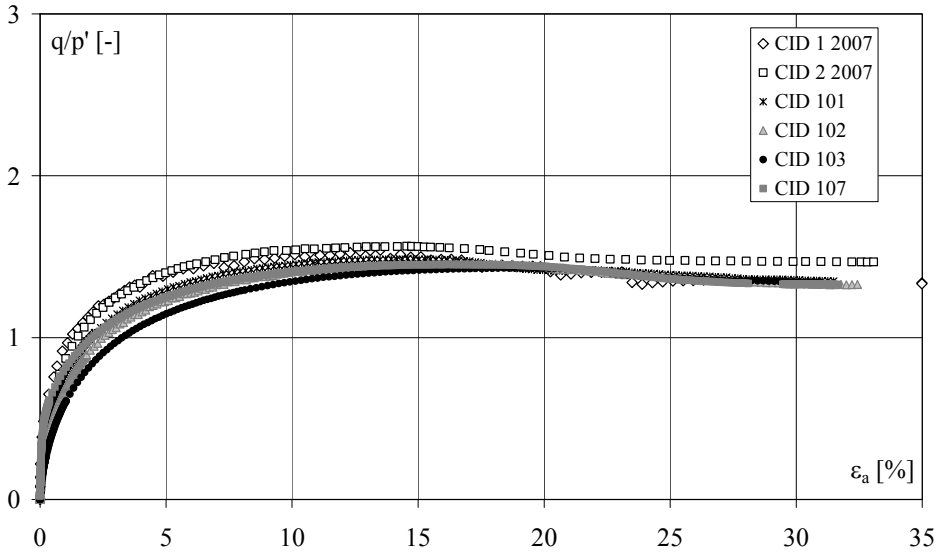

Figure 3.6. Drained tests: stress–strain response.

As shown in Figures 3.3 and 3.4, the specimens subjected to an undrained shear passed through a so–called 'phase transformation state' [(Ishihara et al. (1975)] and then approached the critical state, while those subjected to drained tests (Figs. 3.5, 3.6 and 3.7) experienced a stress peak followed by stress softening and failure at the critical state.

The FFS at low density and low confining pressure behaves like "dense" sand and exerts dilative behaviour.

The stress ratios at critical state η_{cv} resulted to be almost the same for all the triaxial tests, as can be seen in Table 3.3, thus the value of the critical stress ratio M was assumed equal to 1.35; this gives a shearing resistance angle at critical state $\varphi'_{cv} \approx 33°$.

In order to define the position of the critical state line (CSL) in the *e-p'* space, fitting was carried out of all the critical state conditions reported in Figure 3.7, using the approach proposed by Li and Wang (1998), which defines the equation of the CSL as:

$$e_{cv} = e_{\Gamma} - \lambda\left(\frac{p'}{p_a}\right)^{\xi} \qquad [-] \qquad (3.1)$$

where:

e_{Γ}, λ, ξ = material constant that determines the position of the critical state line in the *e-p'* space [-];

p_a = 101 kPa = atmospheric pressure for stress normalisation [FL^{-2}].

The critical state parameters of the FFS, calibrated on the basis of the triaxial test results, are summarised in Table 3.4; the computed CSL is represented in Figure 3.7.

Table 3.4. Critical state parameters for the FFS.

M	e_{Γ}	λ	ξ
[-]	[-]	[-]	[-]
1.35	1.15	0.026	0.901

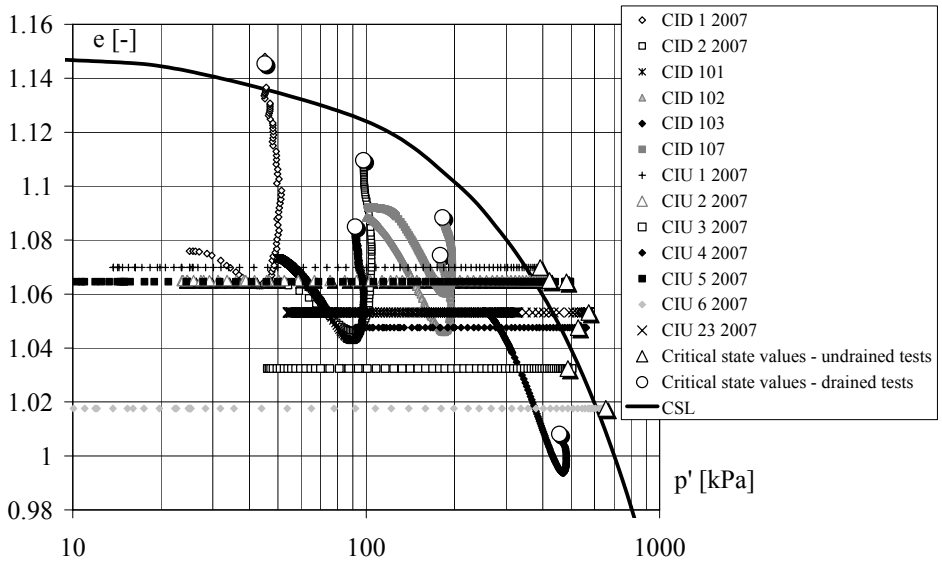

Figure 3.7. Undrained and drained tests: e-p' paths.

With reference to the triaxial tests with BE, Table 3.5 lists the values of the mean pressure, *p'*, of the vertical and horizontal stresses, σ'_v and σ'_h, and of the void index, *e*, at which the shear wave velocity V_S was measured; the values of the small strain shear modulus, G_0, are also reported. From the measured values, G_0 has been expressed as a function of the current effective stresses and void ratio, according to the relation proposed by Fioravante (2000):

$$G_0 = C_G e^{2d} \left(\frac{\sigma'_v}{p_a} \right)^{2nv} \left(\frac{\sigma'_h}{p_a} \right)^{2nh} \qquad [FL^{-2}] \qquad (3.2)$$

where:

d, nv, nh = non–dimensional function exponents, determined experimentally by Fioravante (2000) for Ticino sand, and equal to –0.4, 0.136, 0.084, respectively [-];

C_G = 60 MPa = dimensional material constant determined by fitting the experimental data for FFS [FL^{-2}].

The measured and computed G_0 values are plotted in Figure 3.8 as a function of the mean stress p'. As expected, G_0 increases as the confining pressure increases.

Table 3.5. Bender Element test results.

Test	p' [kPa]	σ'_v [kPa]	σ'_h [kPa]	OCR [-]	e [-]	V_S [m/s]	G_0 [MPa]
CID101	49.7	50.2	49.5	1	1.073	134.6	32.3
CID102	100.1	100.3	100.0	1	1.088	166.9	49.4
CID103	251.2	251.2	251.2	1	1.054	217.0	84.0
CID107	101.7	103.2	100.9	2	1.092	174.6	53.9
CK0D112	290.8	403.7	234.3	1	1.029	238.7	102.2
CID121	249.7	250.2	249.5	1	0.999	234.5	99.2
CID134	399.7	399.9	399.6	1	0.878	273.6	139.0
CID137	100.2	100.3	100.1	2	0.941	189.5	65.7
CK0D140	73.3	99.0	60.4	1	0.931	157.7	45.6

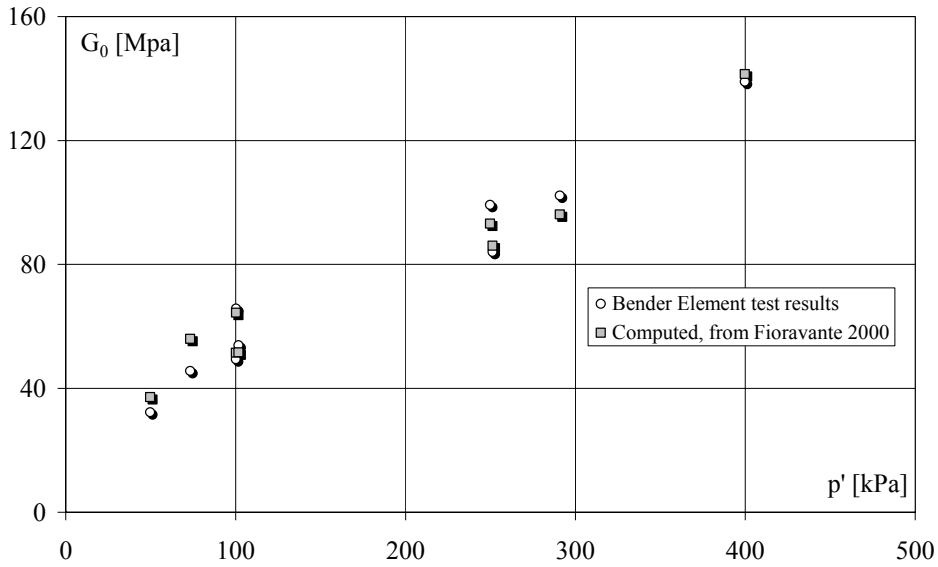

Figure 3.8. Measured and computed small strain shear modulus.

The degradation curves of the secant Young's modulus, $E_{s,sec} = q/\varepsilon_a$, have been derived from the triaxial tests in which the local strains have been measured, as shown in Figure 3.9, where the values of $E_{s,sec}$, normalised over the small strain value E_{s0}, are plotted as a function of the axial strain

ε_a. An elastic threshold can be individuated at $\varepsilon_a \approx 0.002\% \div 0.005\%$. The stress–strain response of the FFS becomes highly non–linear at higher strains than the elastic threshold; the rate of the decay of the secant shear stiffness does not seem to be influenced by the stress history.

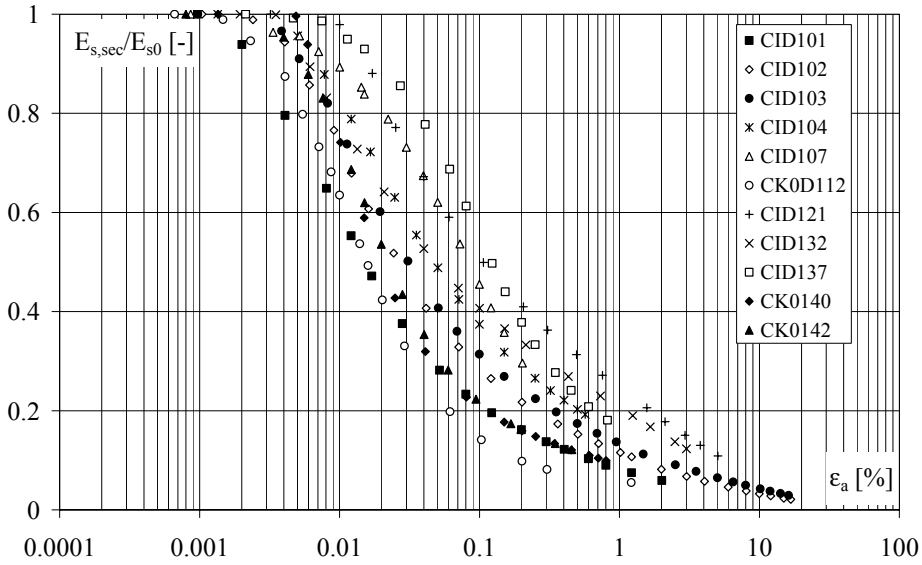

Figure 3.9. Normalised secant Young's modulus degradation curves.

3.4 Model raft and model piles

The adopted geometrical scaling factor of the models was $N = 100$; all the piled raft models were tested under an acceleration field of $a = 100g$, which was reached in correspondence to the soil surface.

The model raft was a 88 mm diameter (d_r) and 15 mm thick (t_r) steel disc, characterized by a modulus of elasticity $E_r = 2.1 * 10^5$ MPa and a moment of inertia, evaluated with respect to the barycentric axis, of $J_r = 294.37$ m^4 at the prototype scale.

The raft–soil stiffness ratio, k_{rs}, defined hereafter, resulted to be high enough ($k_{rs} = 95$) to consider the raft rigid [Horikoshi and Randolph

(1997)]. As a consequence, the settlement of the raft was considered uniform in the test interpretation.

$$k_{rs} = \frac{E_r}{E_{s0}} \frac{1-\nu^2_s}{1-\nu^2_r} \left(\frac{t_r}{d_r / 2} \right)^3 \quad [-] \qquad (3.3)$$

where:

E_{s0} = 87 MPa = small strain Young's modulus of the subsoil evaluated via the elastic theory from Eq. 3.2, at depth $z = d_r/2$, as suggested by Mayne and Poulos (1999)] [FL^{-2}];
ν_s = 0.24 = Poisson's ratio of the soil [-];
ν_r = 0.3 = Poisson's ratio of the raft [-].

The model piles employed in the centrifuge tests were close–ended and free headed and they had an external diameter D_p of 8 mm and a length L_p of 160 mm (slenderness ratio of 20).
The value of D_p was chosen as large as possible to allow a group of 13 model piles, with adequate spacing, to be loaded by a sufficiently small raft to minimise the geometrical constraints of the container, as shown in Figure 3.10, where the main geometrical characteristics of the models and the boundary conditions are reported. The ratio between the diameter of the container (400 mm) and the diameter of the raft (d_r = 88 mm) was equal to 4.5 and, during the tests, the distance of the pile tips from the container bottom was always greater than $30D_p$.
The ratio of the model pile diameter normalised with respect to the mean particle size dimension was D_p/D_{50} = 86 and this was considered high enough to minimise the effects of grain size on the interface behaviour [Garnier and Konig (1998), Foray et al. (1998), Fioravante (2002), Garnier (2002)].

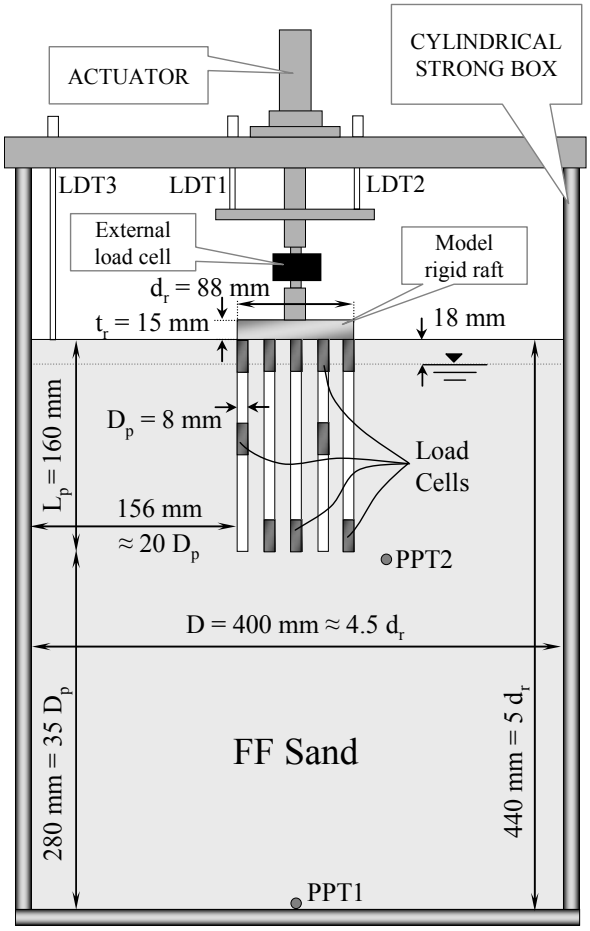

Figure 3.10. Boundary conditions and model test set-up.

The piles were made from an aluminium alloy hollow pipe which had an external skin roughness $R_t \approx 120 \div 300$ μm, which was obtained through mechanical turning and measured peak to peak by a micrometrical profilometer. The minimum value of the relative roughness was $R_n = R_t/D_{50} \approx 1.3$. A relative roughness $R_n > 0.1$ ensures that shear failure occurs in the soil surrounding the pile and produces an interface friction angle, δ', equal to the shearing resistance angle at the critical state, φ'_{cv}, so that the ultimate value of the shear resistance does not depend on the

pile roughness [Yoshimi and Kishida (1981), Kishida and Uesugi (1987), Jardine et al. (1993), Foray et al. (1995), Garnier and Konig (1998)].

Some of the model piles were instrumented with load cells, as shown in Figure 3.10. The fairly small diameter allowed a maximum of two load cells per pile to be incorporated, and these measured the loads at two positions along the shaft.

The instrumented model piles were assembled in two configurations: the upper load cell was placed at the pile head (hereafter referred to as position A) while the lower load cell was placed at the pile base (position B) or alternatively at mid–pile length (position C). The measurement sections of load cells A, C and B were at depths of $0.22L_p$, $0.61L_p$ and $0.99L_p$ from the pile top, respectively. Figure 3.11 reports a scheme of the instrumented model piles.

The adopted instrumentation allowed the axial loads transmitted to each instrumented pile to be measured and the load transmitted through the shaft to be estimated.

The miniaturised load cells, made of stainless steel, had a 4 mm x 4 mm square cross-section. Two active strain gauges were coated with an acrylic moisture barrier onto each of the four flat surfaces. One was used to measure the pile–longitudinal strains, the other the pile–transversal strains (the flat surfaces caused negligible pre–straining of the gauges). The 8 strain gauges were connected within a complex Wheatstone bridge which permitted bending and temperature effects to be cancelled in the readings and gave a very accurate measurement of the axial load.

The instrumented cross-section was covered by a coaxial protective stainless steel jacket which prevented the strain gauges from being compressed by radial stresses.

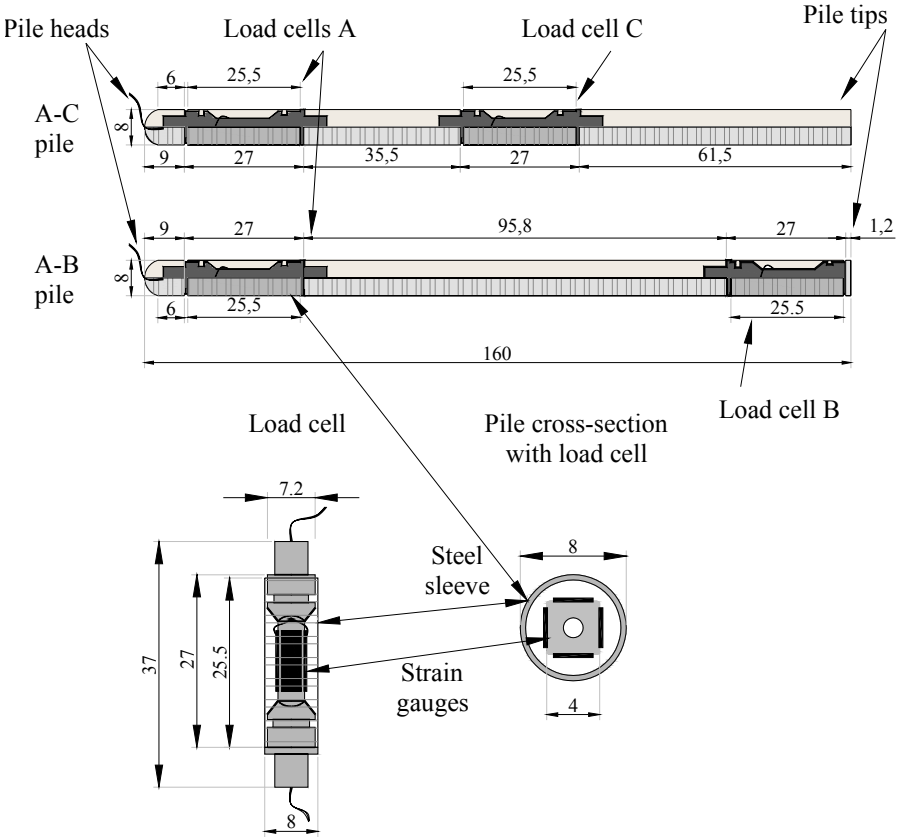

Figure 3.11. Scheme of the instrumented model piles (all dimensions in mm).

The sleeve, which had an external diameter of 8 mm and the same external skin roughness as the aluminium pipe, was sealed with O–rings as a second moisture barrier.

Very thin wires, connecting the load cell to the data acquisition system, were guided through the centre cavity of the model piles. A picture of a load cell and of the instrumented model piles is reported in Figure 3.12.

Each load cell was calibrated and the calibration load cycle was repeated three times to verify the repeatability and the absence of significant hysteresis in the measurements. The drift of the offset at zero loads was carefully detected and minimised. The output signals from the load cells were amplified by a factor of 100. The calibration curves of two load

cells are shown in Figure 3.13, where the electrical output signals of the cells are plotted vs. the applied axial load.

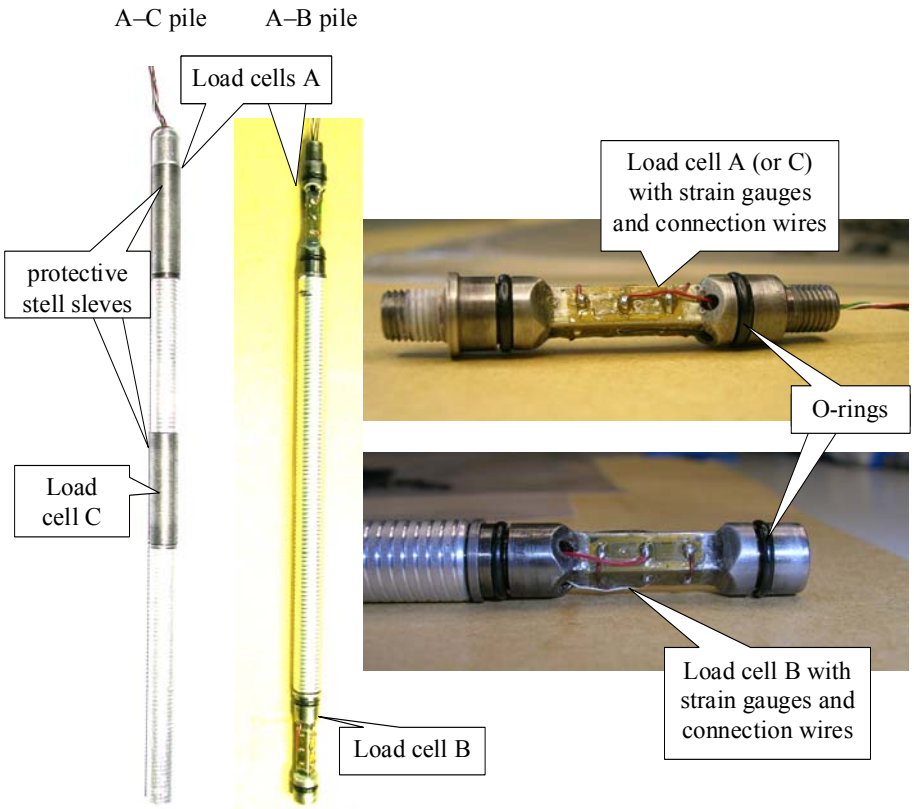

Figure 3.12. Model piles and miniaturised load cells.

The equivalent axial stiffness of the instrumented model piles was measured through a series of load controlled axial load test with a Shenk-TREBBLE testing machine; during the tests, the shortening Δl_0 of a pile segment of initial length $l_0 \approx 0.94 L_p$ was measured with two LDTs for different applied axial load values. As shown in Figure 3.14, where the applied axial load Q is plotted vs. the measured axial strain ε_a the pile axial stiffness was obtained through a linear regression of the measured data and it resulted that:

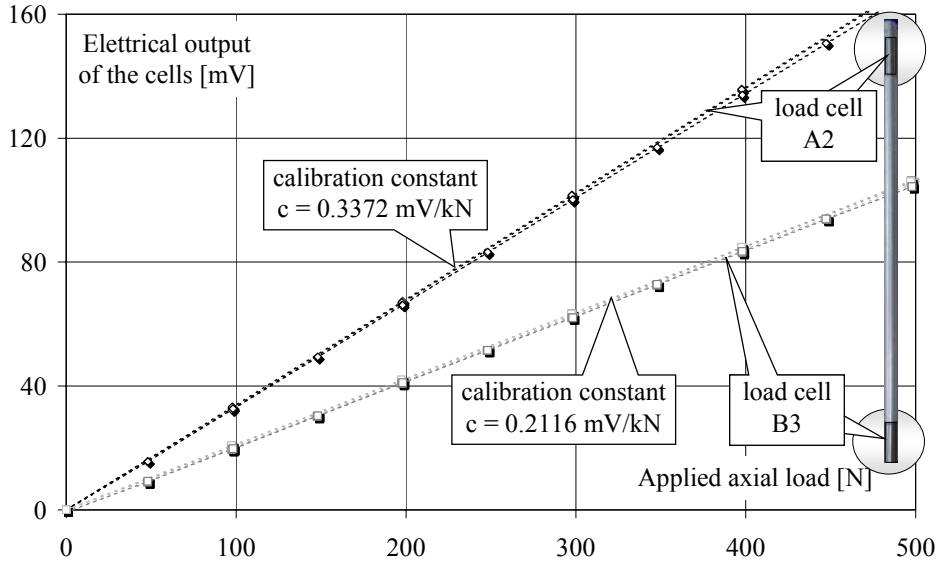

Figure 3.13. Load cell calibration curves.

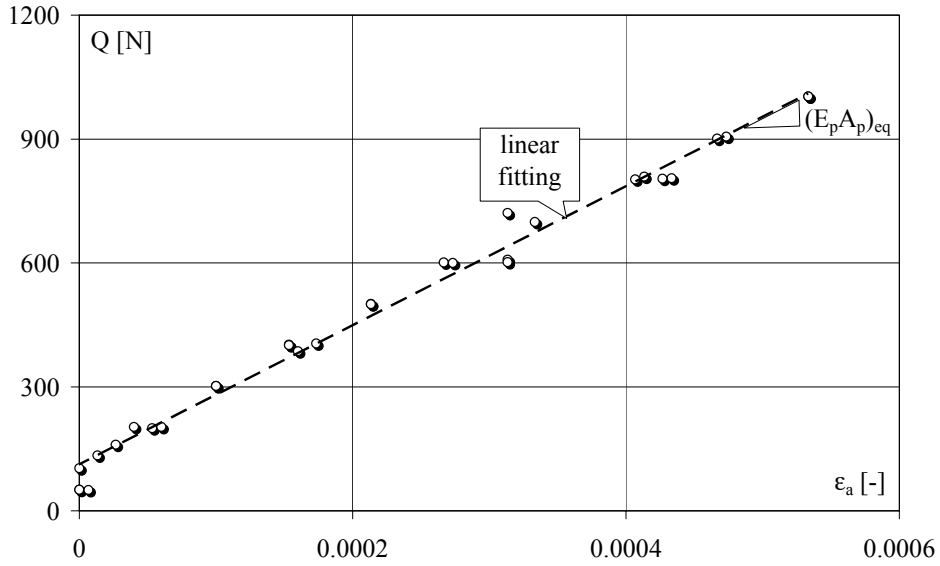

Figure 3.14. Axial load–axial strain response of an instrumented model pile.

$(E_pA_p)_{eq} = \Delta Q/\varepsilon_a = 1615$ kN (model scale) [F] (3.4)

where:

$E_p = 74000$ MPa = Young's modulus of the pile [FL^{-2}];

A_p = the cross–sectional area of the pile [L^2];

ΔQ = applied load increment [F];

$\varepsilon_a = \Delta l_0/l_0$ = axial strain of the pile [-].

Due to their high axial stiffness, the piles were considered rigid in the test interpretation and their settlements were assumed constant with depth.

3.5 Test programme and test procedures

The test programme consisted of twenty loading tests conducted on the eight model schemes shown in Figure 3.15 and listed below. Al the foundations were subject to vertical axial loading. Figure 3.16 reports the load cell configuration in the tests. The dimensions of the foundations are reported in the model and the prototype scale in Table 3.6.

- model scheme R: unpiled raft (test No. 1)
- model scheme IP: isolated single pile (tests No. 2, 3, 4, 5, 10 and 11)
- model scheme PR1: 1-pile raft (tests No. 6 and 12)
- model scheme PR3(A): 3-pile raft, spacing $s = 8.66D_p$ (tests No. 7, 8, 13 and 14)
- model scheme PR7(A): 7-pile raft, spacing $s = 5D_p$ (tests No. 9, 15 and 16)
- model scheme PR13: 13-pile raft, radial spacing $s = 2.5D_p$ (tests No. 17 and 18)
- model scheme PR3(a): 3-pile raft, spacing $s = 4.33D_p$ (test No. 19)
- model scheme PR7(a): 7-pile raft, spacing $s = 2.5D_p$ (test No. 20)

Table 3.6. Foundation dimensions (model and prototype scale).

Dimensions		Model (mm)	Prototype (m)
Raft diameter d_r		88	8.8
Pile diameter D_p		8	0.8
Pile length L_p		160	16.0
Pile spacing s	PR3(A)	69.3	6.93
	PR7(A)	40	4
	PR13	20*	2*
	PR3(a)	34.65	3.46
	PR7(a)	20	2

* radial distance

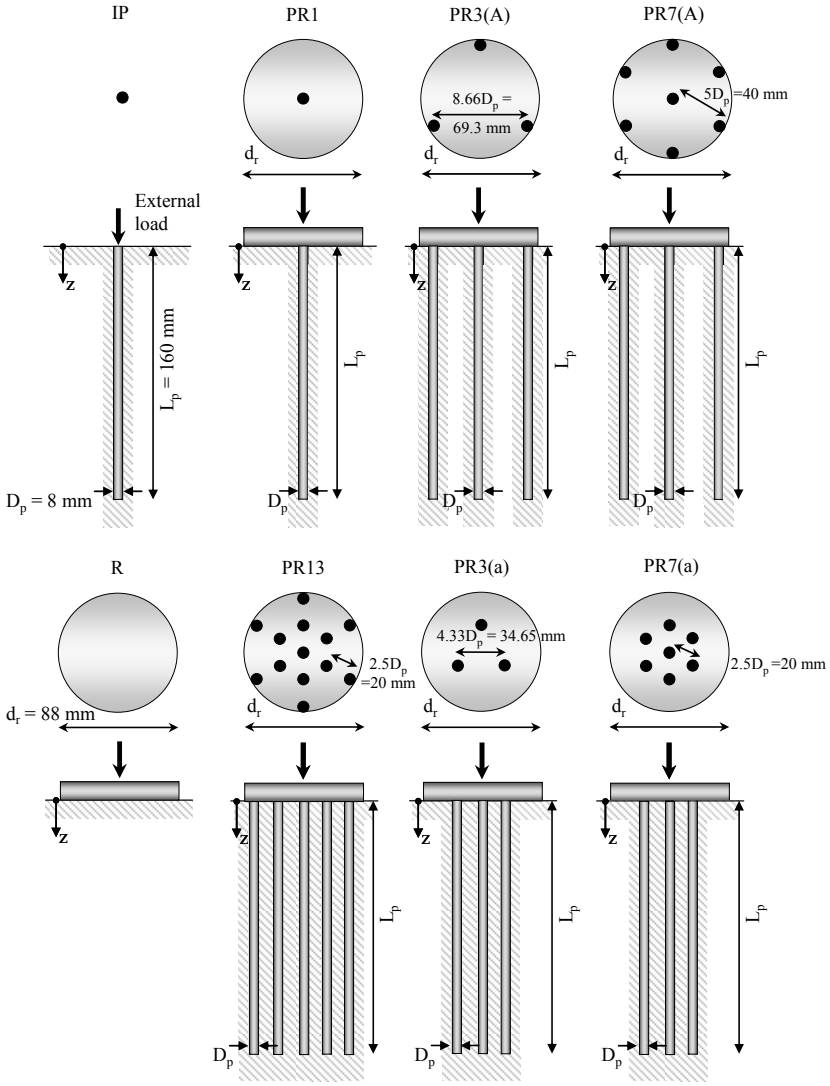

Figure 3.15. Model schemes.

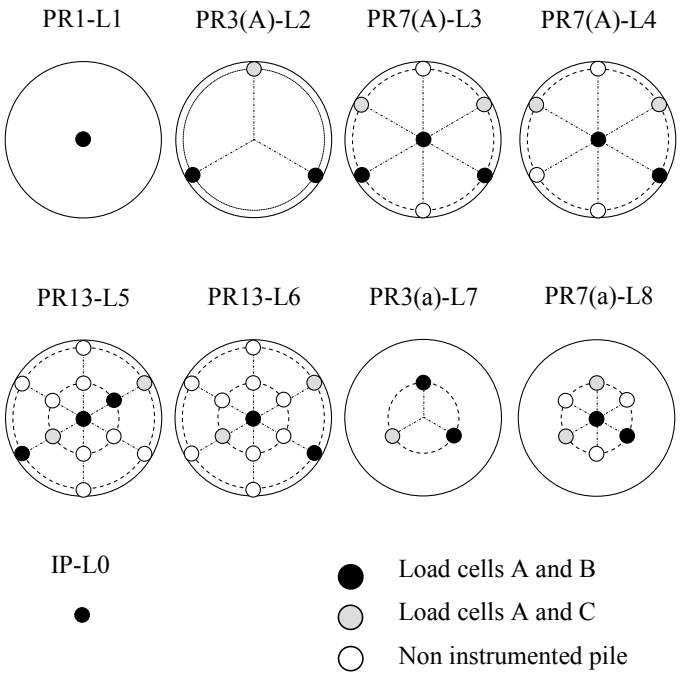

Figure 3.16. Test load cell configurations.

The following test procedure was adopted.

Non displacement pile rafts

(a) At 1*g*: each soil model was reconstituted to a very low relative density ($D_R \approx 15\% \div 20\%$) by pluviating, in air, the dry sand into a cylindrical container at a very small and constant height of fall. The cylindrical container had an internal diameter of 400 mm, a height of 840 mm and rigid walls to avoid lateral displacements of the soil. During the pluvial deposition, two miniaturised pore pressure transducers were inserted into the soil mass (PPTs 1 and 2 in Figure 3.10), the first placed on the container bottom, the second near the pile tips. At the end of the deposition, the soil surface was located at a level of 440 mm above the container bottom. After deposition, the sand was saturated through an upward tap water flow with a small hydraulic gradient to avoid soil disturbance. The water level was kept

constant at a depth of 18 mm from the soil surface during the following centrifuge spinning (1.8 m at the prototype scale), as monitored by the PPTs.

(b) At 1*g*: the model piles were completely embedded into the soil specimen in pre-bored holes. A very rigid frame, which held two linear displacement transducers to monitor the raft displacement (LDTs 1 and 2 in Fig. 3.10), an external load cell to measure the applied load, the raft plate and a hydraulic actuator, was mounted onto the container top. In the isolated pile load tests, the raft plate was replaced by a 8 mm diameter piston. The container was then loaded onto the centrifuge and accelerated to 75*g*.

(c) At 75*g*: as the model was subjected to the acceleration field in the centrifuge, the soil surface settled and the model consolidated, as monitored by the PPTs and by a further LDT fixed to the container wall which measured at a distance of 150 mm from the centre of the container (LDT3 in Fig. 3.10). Even though the weight of the model piles was close to that of the substituted soil, differential settlements occurred between the piles and the surrounding soil during the in–flight consolidation and the soil surface settled 1–1.5 mm more than the piles. This is illustrated in Figure 3.17, which compares the profile of the soil consolidation settlement predicted by a numerical simulation, as a function of the model depth, z, with the pile settlement profile. Thus, at the end of the consolidation, the piles were pushed down slightly by the raft plate (or by the piston for the isolated pile) in order to align them with the soil surface; then the raft plate was lifted and the piles were unloaded, the centrifuge speed was increased to the target value of 100*g* and a second consolidation occurred. This “atypical” procedure was adopted to minimise the

unavoidable problem of the different alignments of the pile heads with respect to the soil surface. The piles installed in this manner simulated ideally bored prototype piles.

(d) At 100*g*: the raft plate (or the piston for the isolated pile) was slowly lowered until contact with the soil surface and the pile heads was achieved, then the loading test was performed until a relative pile displacement $w/D_p \approx 100\%$ was reached, where w is the measured settlement.

Displacement pile rafts

(a) At 1*g*: as for the non displacement pile raft models, each soil model was reconstituted to a very low relative density ($D_R \approx 15\% \div 20\%$) by pluviating, in air, the dry sand into a cylindrical container at a very small and constant height of fall. The cylindrical container had an internal diameter of 400 mm, a height of 840 mm and rigid walls to avoid lateral displacements of the soil. During the pluvial deposition, two miniaturised pore pressure transducers were inserted into the soil mass (PPTs 1 and 2 in Figure 3.10), the first placed on the container bottom, the second near the pile tips. At the end of the deposition, the soil surface was located at a level of 440 mm above the container bottom. After deposition, the sand was saturated through an upward tap water flow with a small hydraulic gradient to avoid soil disturbance. The water level was kept constant at a depth of 18 mm from the soil surface during the following centrifuge spinning (1.8 m at the prototype scale), as monitored by the PPTs.

(b) At 1*g*: the piles were inserted into pre–bored holes for a length of 130 mm (embedded length = $0.8L_p$). The rigid frame, with LDTs 1 and 2, the external load cell, the raft plate and the hydraulic actuator, was mounted onto the container top (as for the bored piles, in the

isolated pile load tests the raft was replaced by a 8 mm diameter piston), the container was loaded onto the centrifuge and accelerated to 100*g*.

(c) At 100*g*: the soil model was allowed to consolidate. The raft plate (or the piston for the isolated pile) was then slowly lowered until contact with the pile heads was achieved and the model piles were jacked for 30–32 mm into the soil model at 100*g*; the raft was then lifted up and the jacking load was removed. Drained penetration conditions were ensured by a low penetration rate and confirmed by the constant pore pressure values measured by PPT2. This pile installation procedure was assumed adequate to fully mobilise the end bearing capacity, since the piles penetrated $3.75D_p$ at least, but it produced a lower densification of the soil around the pile than a 100*g* full pile length penetration would; however, it was necessary to jack the groups of free headed piles simultaneously.

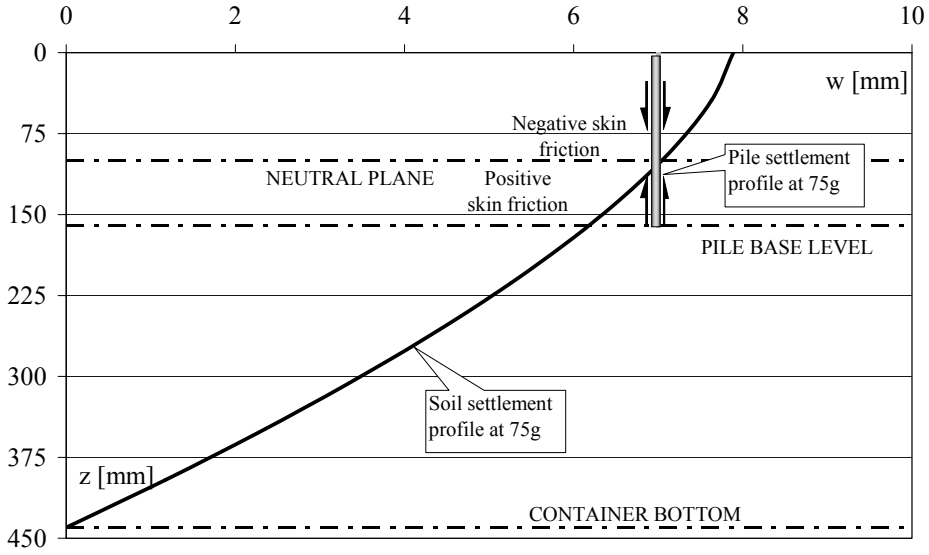

Figure 3.17. Schematic of the soil and pile displacement profiles after in–flight consolidation at 75g. Model scale.

(d) At 100*g*: the raft plate (or the piston for the isolated pile) was slowly lowered until contact with the soil surface and the pile heads was achieved, then the loading test was performed until a relative pile displacement $w/D_p \approx 100\%$ was reached, where w is the measured settlement.

In both the non displacement and displacement pile raft load tests, the jacking and the loading phases were executed at a constant loading rate of 50 N/min. The compression load, applied by the servo–controlled hydraulic actuator, was measured by the external load cell. The external and internal forces as well as the raft and sand settlements were continuously recorded (acquisition frequency equal to 0.1 Hz). The pore pressure measured by PPT2 showed constant values during the tests, i.e. the loading conditions were drained. The foundation settlement, w, was obtained by averaging the measurement values of LDTs 1 and 2, which were placed in diametrically opposite positions from the actuator, as shown in Figure 3.10.

The installation procedure (jacking and jacking load removal for the displacement pile; in–flight alignment, alignment load removal and acceleration to 100*g* for the non displacement piles) produced residual stresses (negative skin friction in the upper shaft balanced by positive lower shaft friction and base resistance) which have been accounted for in the interpretation of the loading test results [Fioravante et al. (2006)].

The data presented in the following chapters refer to the average density attained at the end of the 100g in–flight consolidation, which was about $D_R \approx 34\%$ in all tests, as reported in Table 3.7, where the main characteristics of the tests are summarised.

The actual settlement pattern of the sand during the in–flight consolidation is non–linear with depth, as shown in Figure 3.17, thus the

relative density increases with depth and is slightly lower at the soil surface and slightly higher at the container bottom, with respect to the average value. The maximum scatter from the average value has been estimated to be about ±5%.

The soil densification around the pile shaft produced by the in–flight jacking has not been quantified.

Table 3.7. Main characteristics of the performed tests.

Test No.	Test name	Scheme	No. of piles n	Type of piles	Load cell layout	D_R (%)
1	URLT0	R	-	-		31
2	D-PLT1	IP	1	Displacement	L0	39
3	D-PLT2	IP	1	Displacement	L0	33
4	D-PLT3	IP	1	Displacement	L0	36
5	D-PLT4	IP	1	Displacement	L0	34
6	D-PRLT1	PR1	1	Displacement	L1	34
7	D-PRLT2	PR3(A)	3	Displacement	L2	31
8	D-PRLT3	PR3(A)	3	Displacement	L2	32
9	D-PRLT4	PR7(A)	7	Displacement	L3	35
10	ND-PLT5	IP	1	Non displacement	L0	35
11	ND-PLT6	IP	1	Non displacement	L0	35
12	ND-PRLT5	PR1	1	Non displacement	L1	35
13	ND-PRLT6	PR3(A)	3	Non displacement	L2	35
14	ND-PRLT7	PR3(A)	3	Non displacement	L2	35
15	ND-PRLT8	PR7(A)	7	Non displacement	L3	37
16	ND-PRLT9	PR7(A)	7	Non displacement	L4	35
17	ND-PRLT10	PR13	13	Non displacement	L5	41
18	ND-PRLT11	PR13	13	Non displacement	L6	35
19	ND-PRLT12	PR3(a)	3	Non displacement	L7	31
20	ND-PRLT13	PR7(a)	7	Non displacement	L8	30

3.6 In–flight cone penetration tests

In order to check the soil model uniformity and the repeatability of the deposition procedure, two in–flight static cone penetration tests were performed on dummy models, using the ISMGEO miniaturised electrical piezocone. The cone has a diameter d_c = 11.3 mm, an apex angle of 60° and a sleeve friction of 11 mm in diameter and 37 mm in length. One load cell measures the cone resistance and another one measures the cone

resistance plus the shaft friction, up to forces of 9.8 kN. A Druck PDCR42 pressure transducer (35 bar capacity) has been installed on the tip for interstitial pressure measurements.

Figure 3.18 shows a CPT model test scheme. The boundary conditions and particle size ratio for the tests were: D/d_c = 35, where D is the internal diameter of the container; s_c/d_c = 17, where s_c is the CPT distance from the side wall; d_c/D_{50} = 121.5. These values, according to Bolton et al. (1999) are large enough to minimise any scale effects on the results.

During the tests, a penetration rate of 2 mm/s ensured drained conditions, as shown by the pore pressure measurement.

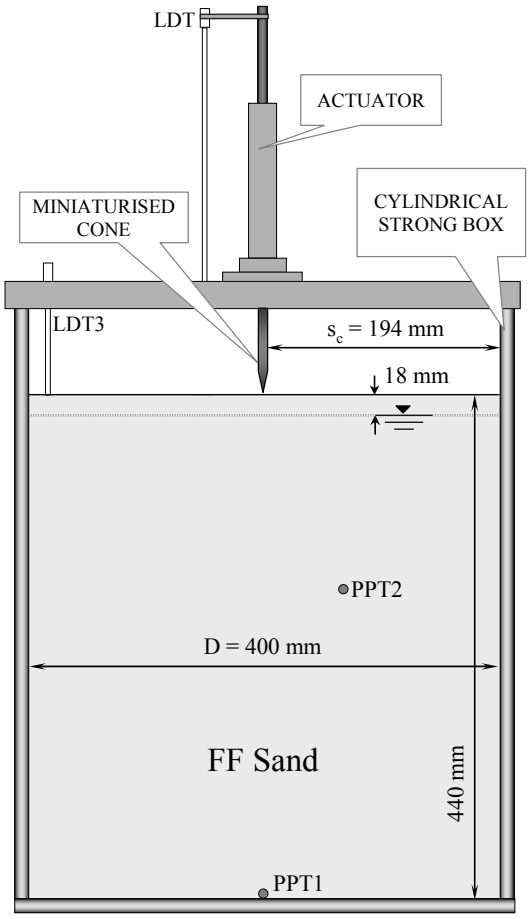

Figure 3.18. Cone penetration test set–up.

The obtained cone resistance q_c profiles are shown in the prototype scale in Figure 3.19 as a function of the depth z. A good uniformity and repeatability of the test samples can be observed. The measured q_c profiles are compared in the Figure with the q_c values computed using the empirical correlation, which was established on the basis of CPTs performed in a large calibration chamber on four silica sands, as proposed by Jamiolkowski et al. (2003):

$$\frac{q_c}{p_a} = C_0 \left(\frac{p'_0}{p_a} \right)^{C1} \exp(D_R C_2) \qquad [-] \qquad (3.5)$$

where:

p'_0 = mean effective stress at cone depth [FL^{-2}];

p_a = 101 kPa = atmospheric pressure [FL^{-2}];

C_0, C1, C2 = non–dimensional correlation factors [-], equal to 18, 0.46 and 2.96 respectively. The correlation has been adapted to centrifuge results, modifying the C_0 coefficient. A good agreement between the computed and measured values can be observed.

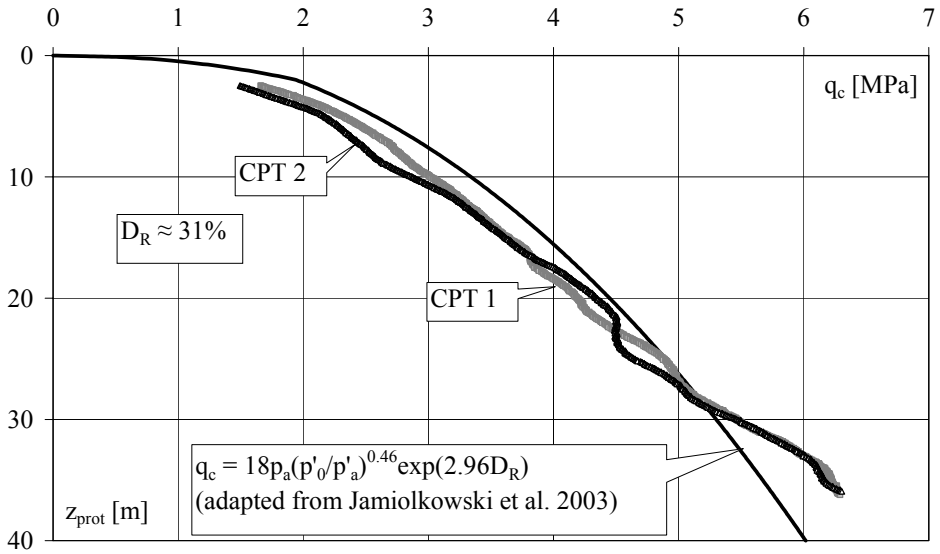

Figure 3.19. Measured and computed q_c profiles. Prototype scale.

Chapter 4

Test results

4.1 Introduction

A piled raft is a composite foundation that consists of three load–bearing components: a raft, piles and the subsoil. Its behaviour is determined by complex soil–structure interactions between the elements of the foundation and the subsoil, which can be represented by a functional scheme, as reported Figure 4.1.

The soil–pile (S–P) interaction is mainly governed by the pile installation procedure that is adopted, these procedures range from non displacement to displacement methods.

The soil–raft (S–R) interaction depends above all on the relative stiffness of the raft–soil.

The pile–raft (P–R) and pile–pile (P–P) interactions depend on the number of piles, on their spacing and on the piled raft geometry (raft dimensions, pile length and diameter). The P–R and P–P interactions modify the load–bearing behaviour of each foundation component, compared to an analogous isolated element.

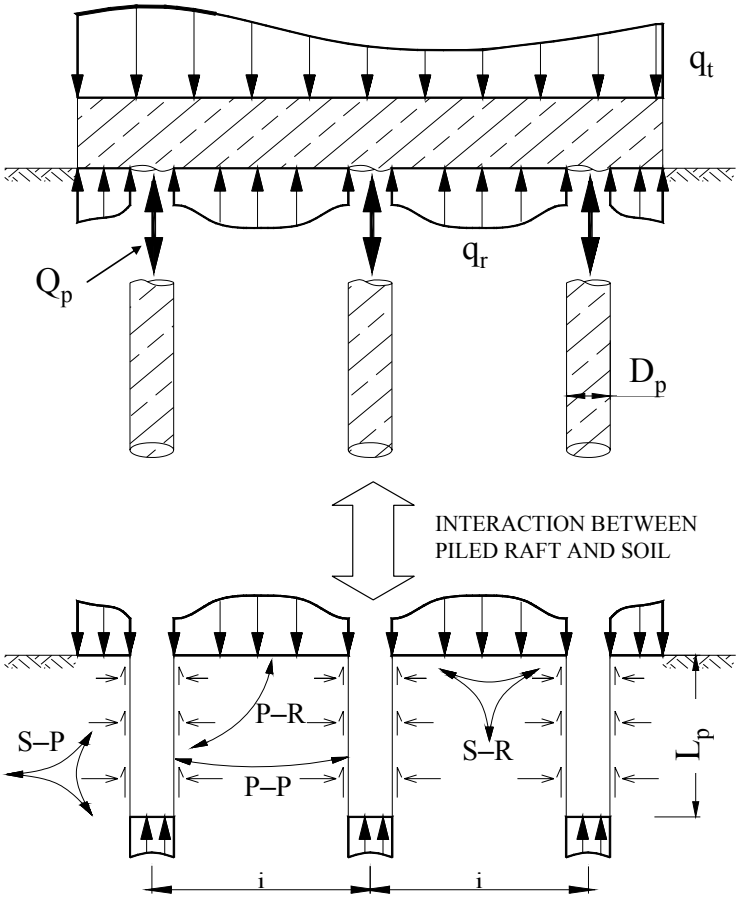

q_t = applied stress Q_p = load transmitted to piles q_r = pressure transmitted to soil

(S–P) Soil–pile interaction (S–R) Soil–raft interaction

(P–R) Pile–raft interaction (P–P) Pile–pile interaction

Figure 4.1. Soil–structure interaction effects for a piled raft foundation, adapted from Katzenbach et al. (1998) and Katzenbach et al. (2000).

Pile–raft interaction (P–R in Figure 4.1)

The shear stress distribution along a pile depends on the relative movements between the pile and the soil. As pointed out by Butterfield and Banerjee (1971), Cooke et al. (1980), Randolph (1983), Burland (1995) the raft in a piled raft exerts a "shielding effect" on the pile skin

friction mobilisation and causes a different load–transfer mechanism from the piles to the soil, with respect to an isolated pile.

The soil under the raft is forced to settle by the same amount as the piles and no skin friction can develop at the pile heads. Thus, the skin friction mobilisation (S–P in Fig. 4.1) starts at the pile tips and moves upwards; the degree of shaft friction mobilisation is maximum at the pile bases and reduces to zero at the pile tops.

As a consequence, the rate at which shaft friction mobilisation takes place with increasing settlement is slower for a pile that is part of a piled raft than for a single free standing pile. In addition, the overlapping of the individual displacement fields of the cap and the piles can produce a softer pile response [Randolph (1983), Randolph (1994)].

On the other hand, the raft–soil contact pressure (S–R in Fig. 4.1) causes an increase in the soil stress level around the piles, like a corresponding overburden pressure, therefore the ultimate shear resistance of a pile in a piled raft increases compared to an isolated pile [Phung (1993), El-Mossallamy and Franke (1998), Franke *et al*. (2000), Katzenbach *et al*. (2000), Poulos (2001)].

As a consequence of the raft–pile interactions, the ultimate skin friction and the pile displacement required to mobilise it are greater in the case of a pile that is part of a piled raft than in the case of an isolated pile.

The presence of piles also influences the behaviour of the raft in comparison to an equivalent shallow foundation. The load shed from the piles (S–P in Fig. 4.1) causes displacements in the soil mass, particularly at the soil surface beneath the raft, which lead to a decrease in the contact pressure beneath the raft next to the pile shaft. Thus, the load carried by the raft for a given displacement is modified by the load transmitted by the piles to the soil [Randolph (1983), Katzenbach *et al*. (2000)].

Pile–pile interaction (P–P in Figure 4.1)

In comparison to an isolated single pile, two main interaction effects take place in a group of piles, as it has been pointed out by several authors, including Poulos (1968), Randolph and Wroth (1979), Poulos and Davis (1980), Cooke et al. (1980), O'Neill (1983), Mylonakis and Gazetas (1998): (i) on one hand the decrease in the pile reaction modulus (i.e. the load–settlement ratio) and on the other (ii) the increase in the pile bearing capacity. These effects depend on the load level, on the raft and group dimensions and on the location of the pile within the group.

The increase in settlement of an individual pile in a group is due to the superimposition of the deformation fields of the neighbouring piles in the group (i.e. group effect). The increase in the ultimate capacity of an individual pile in a group standing in a soil with internal friction is due to the increase in the intergranular stresses due to confinement by the neighbouring piles.

These effects are enhanced in a piled raft due to the previously described raft–soil contact pressure effect (S–R in Fig. 4.1).

In this chapter, the influence of the S–P, P–R and P–P interactions on the piled raft stiffness and resistance is discussed, on the basis of an analysis of the centrifuge test results. The chapter is formed as follows:

- isolated single pile: comparison between the load–settlement behaviour of non displacement (ND) and displacement (D) piles;
- single pile beneath the raft: comparison between the load–settlement behaviour of non displacement (ND) and displacement (D) piles;
- groups of non displacement (ND) piles beneath the raft: comparison between the load–settlement behaviour of piles in a piled footing with that of a single pile under the raft;

- groups of displacement (D) piles beneath the raft: comparison between the load–settlement behaviour of piles in a piled footing with that of a single pile under the raft;
- piled rafts: comparison between the overall load–settlement behaviour of non displacement (ND) and displacement (D) pile rafts.

In this chapter, the data are presented in dimensionless form, except where otherwise noted. The load settlement–curves in the Figures are plotted vs. the measured settlement w, normalised both to the pile diameter, w/D_p, and to the raft diameter, w/d_r. In the Figures where the foundation stiffness is represented, the stiffness values are reported for relative settlements w/D_p >1% or w/d_r > 0.1%; smaller measured displacement values have not been considered reliable enough.
The experimental results were very consistent and therefore not all the test results are shown.

Forces and stresses on piles from centrifuge tests

In the test interpretation, all the forces have been assumed to act parallel to the vertical axis of the piles. With reference to Figure 4.2, the load acting on the pile head, Q_A (i.e. pile total capacity), has a downward positive sign, while the shaft resistance, Q_S, and the loads acting at mid–pile, Q_C, and on the pile base, Q_B (i.e. base capacity), have an upward positive sign.
The loads acting on the pile head, Q_A, at mid–pile, Q_C, and at pile base, Q_B, were directly measured during the tests by means of load cells named A, C and B, respectively (see Figure 4.2).
The shaft resistance acting between load cells A–B, $Q_{S,AB}$ and between load cells A–C, $Q_{S,AC}$ have been computed from the cell readings by means of the equilibrium equation:

$$Q_{S,AB}(w) = Q_A(w) + W_{AB} - Q_B(w) \qquad [F] \qquad (4.1)$$

$$Q_{S,AC}(w) = Q_A(w) + W_{AC} - Q_C(w) \qquad [F] \qquad (4.2)$$

where:

W_{AB} = the dead weight of the pile between positions A and B [F];

W_{AC} = the dead weight of the pile between positions A and C [F];

w = measured settlement [L].

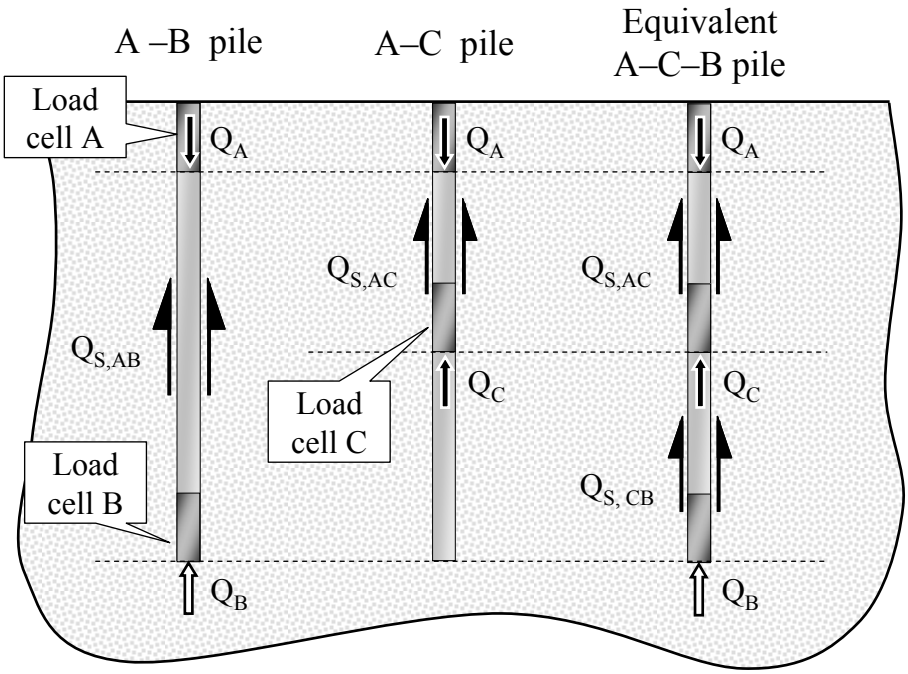

Figure 4.2. Forces on piles subjected to a compressive axial load.

Due to the axial–symmetry of the load and geometry, it has been assumed that the piles placed at the same radial distance from the raft centre have experienced the same load distribution with depth; therefore, the measurements obtained from model piles alternatively instrumented A–B and A–C have been merged to compose an equivalent A–C–B pile, at that radius, see Figures 4.2 and 4.3. The shaft resistance acting between load cells C–B, $Q_{S,CB}$ has been derived as follows:

$$Q_{S,BC}(w) = Q_{S,AB}(w) - Q_{S,AC}(w) \qquad [F] \qquad (4.3)$$

The unit loads acting on the pile head, q_A, at mid–pile, q_C, and at pile base, q_B, and the shear stresses acting between positions A–B, $\tau_{S,AB}$, A–C, $\tau_{S,AC}$, and C–B, $\tau_{S,CB}$ have been computed as follows:

$$q_X(w) = \frac{Q_X(w)}{\frac{\pi D_p^2}{4}} \qquad X = A, C, B \qquad [FL^{-2}] \qquad (4.4)$$

$$\tau_{S,AB}(w) = \frac{Q_{S,AB}(w)}{L_{AB}\pi D_p} \qquad [FL^{-2}] \qquad (4.5)$$

$$\tau_{S,AC}(w) = \frac{Q_{S,AC}(w)}{L_{AC}\pi D_p} \qquad [FL^{-2}] \qquad (4.6)$$

$$\tau_{S,CB}(w) = \frac{Q_{S,CB}(w)}{L_{CB}\pi D_p} \qquad [FL^{-2}] \qquad (4.7)$$

where:

D_p = pile diameter [L];

L_{AB}, L_{AC}, L_{CB} = the distance between the measurements sections of load cells A–B, A–C, and C–B, respectively [L].

It should be noted that residual stresses, caused by the installation procedure, acted on the piles, in all the tests, for both non displacement and displacement piles, before the loading tests (zero external load and $w = 0$). For the displacement piles, the removal of the jacking load at the end of the 100*g* in–flight jacking caused the elastic extension of the pile and the consequent mobilisation of negative skin friction on the upper shaft. As for the non displacement piles, the 100*g* in–flight consolidation caused a small downwards shallow soil–pile relative settlement and the mobilisation of negative skin friction on the upper shaft. The negative skin friction and the pile self weight for both the displacement and the

non displacement piles were balanced by positive lower shaft and base resistances.

The residual stresses acting on the piles have been taken into account in the test interpretation [Fioravante et al. (2006)].

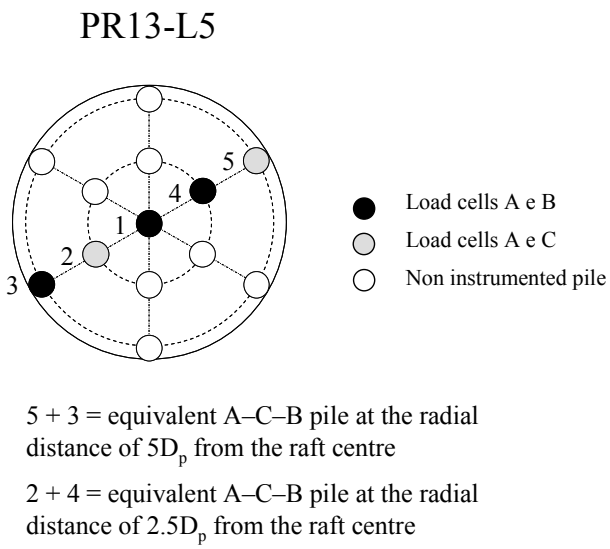

Figure 4.3. Equivalent edge and inner piles in the PR13 model (test ND-PRLT10).

4.2 Isolated pile

Six tests were carried out on isolated non displacement (ND) and displacement (D) model piles (IP model scheme, see Figures 3.15 and 3.16, and Table 3.7). The scatter of the results of analogous loading tests was very limited, which confirmed the repeatability of the model preparation method.

The results of two tests (ND-PLT6 and D-PLT3 tests, Table 3.7) are compared in Figures 4.4 and 4.5, where the unit loads acting on the pile head and base, q_A and q_B, and the shaft friction acting between the load cells A and B, $\tau_{S,A\mathrm{B}}$, are represented as a function of the measured settlement normalised to the pile diameter, w/D_p. The main test results are summarised in Table 4.1.

Table 4.1. Main results of the IP models

	Isolated single piles			
	ND IP pile		D IP pile	
SHAFT FRICTION	$\tau_{S,AB}$ [kPa]	w/D_p [%]	$\tau_{S,AB}$ [kPa]	w/D_p [%]
at peak	35.5	8	40	8
at large w/D_p	32	100	27	100
BASE RESISTANCE	q_B [MPa]	w/D_p [%]	q_B [MPa]	w/D_p [%]
at large w/D_p	3.5	100	4.1	100
TOTAL CAPACITY	q_A [MPa]	w/D_p [%]	q_A [MPa]	w/D_p [%]
at peak	-	-	5.8	9
at large w/D_p	5.3	100	5.5	100

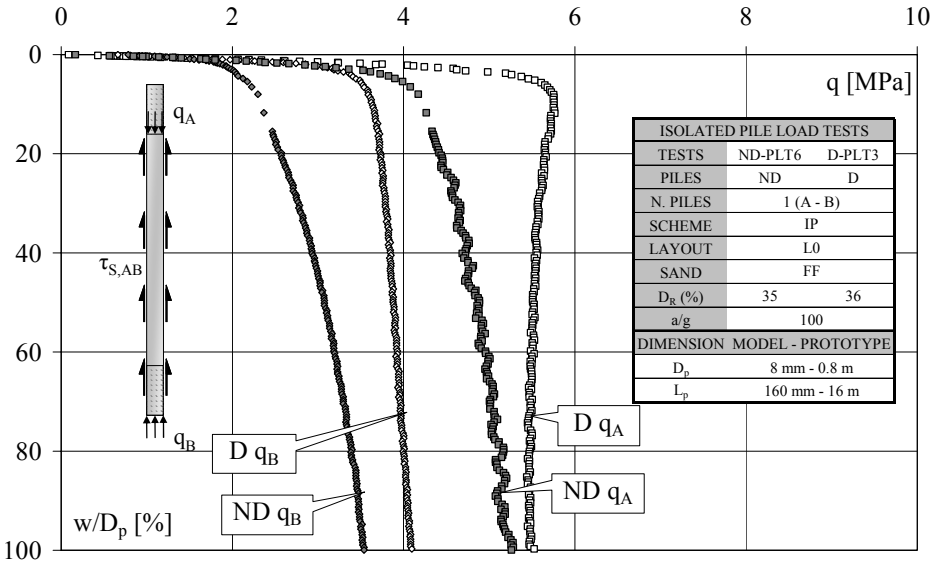

Figure 4.4. Unit loads acting on the pile head q_A and base q_B vs. the pile settlement normalised to the pile diameter w/D_p for the ND and D isolated piles.

As for the D pile, the unit load acting on the pile head, q_A increases to a peak value which is reached at $w/D_p \approx 9\%$, then it reduces towards a steady post peak value; the ND pile shows a progressive q_A mobilisation with settlements and it reaches almost the same values as the D pile at $w/D_p = 100\%$ (Figure 4.4). As expected, the base load of the D pile is

almost fully mobilised at w/D_p = 10%, while a larger value of w/D_p than 100% is required to completely mobilise the q_B of the ND pile (Figure 4.4). As far as the shaft friction is concerned (Figure 4.5), $\tau_{S,AB}$ for both the D and the ND piles increases to a peak value which is reached at $w/D_p \approx 8\%$, (the peak value attained by the D pile is slightly larger than that achieved by the ND pile) and then it decreases as w/D_p increases, toward a steady value; a reduction of 32% and 10% can be observed for the displacement and the non displacement pile, respectively.

The occurrence of sand dilatancy in the interface zone could have caused the $\tau_{S,AB}$ peaks and the following stress softening observed for both the displacement and the non displacement piles [Wernick (1978), Boulon and Foray (1986), Boulon (1988) and (1989)]. The dilatancy effects are more pronounced in the displacement pile, probably due to the effect of the sand densification around the shaft which was produced by the 100g in–flight jacking.

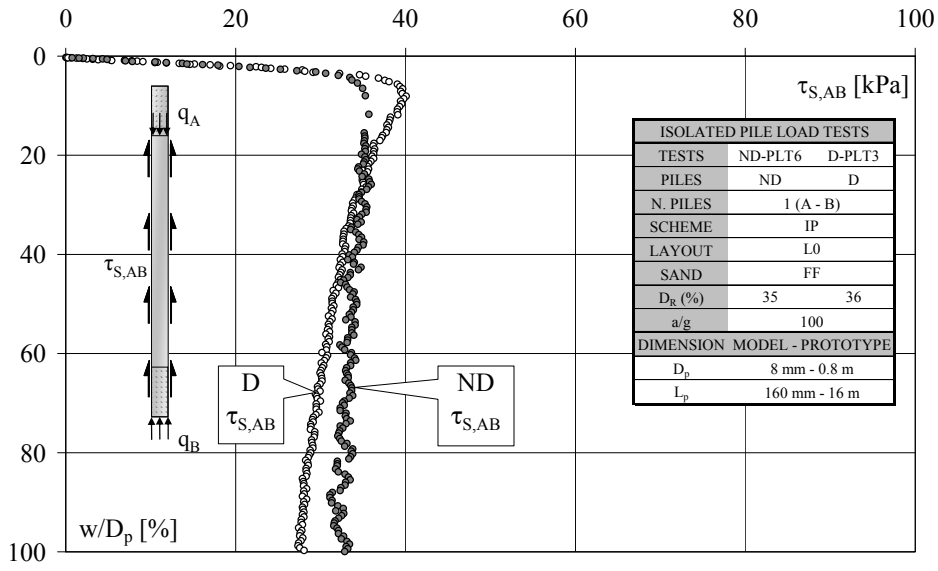

Figure 4.5. Shear stress acting between load cells A and B $\tau_{S,AB}$ vs. the pile settlement normalised to the pile diameter w/D_p for the ND and D isolated piles.

The mobilisation curves of the ND and D isolated piles stiffness, $k_{p,IP}$ (i.e. load–settlement ratio) are plotted at the prototype scale in Figure 4.6 vs. the pile relative settlement, w/D_p. The curves are similar to those of the decay of the soil stiffness and they are characterised by a significant decay which occurs in the w/D_p range from 1% to 10%. The D isolated single pile results ≈ 20% stiffer than the ND pile at w/D_p <10%.

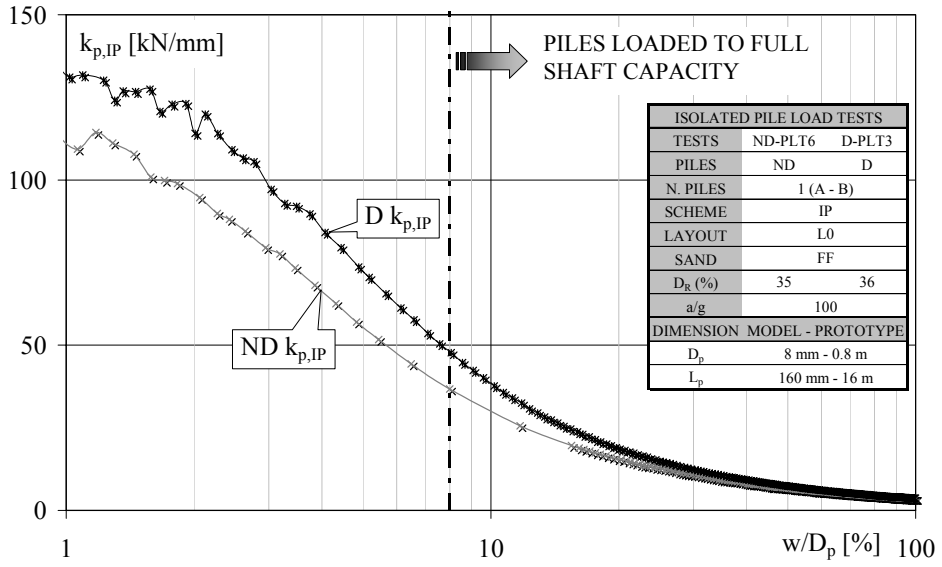

Figure 4.6. Isolated pile stiffness k_p vs. the pile settlement normalised to the pile diameter w/D_p for the ND and D isolated piles. Prototype scale.

4.3 Single pile beneath the raft

The load–settlement curves of the single pile beneath the raft derived from the ND and D 1-pile raft tests (tests ND-PRLT5 e D-PRLT1, PR1 model scheme, see Figures 3.15 and 3.16 and Table 3.7) are reported in Figures 4.7 to 4.10, as a function of the settlement normalised to the pile diameter, w/D_p (left–hand side) and to the raft diameter, w/d_r (right–hand side). The unit loads acting on the pile head and base, q_A and q_B, are shown in Figures 4.7 and 4.9, for the ND and the D piles, respectively;

the shear stress acting between load cells A and B, $\tau_{S,AB}$ is plotted in Figures 4.8 and 4.10 for the ND and the D piles, respectively. For comparison purposes, the Figures report the results of the ND and D IP tests.

The relevant results of the PR1 tests are summarised and compared with those of the isolated pile tests in Table 4.2; their qualitative analysis highlights the great influence of the pile–raft interaction on the pile capacity mobilisation. The interpretation of the presented data can be summarised as follows:

- the base capacity, q_B mobilised by the ND and D PR1 piles, is comparable with that of the analogous isolated pile (Figures 4.7 and 4.9);
- the ND and the D PR1 piles experience similar values of the shear stress, $\tau_{S,AB}$ (Figures 4.8 and 4.10);

Table 4.2. Main results of the IP and PR1 models

	ND piles				D piles			
	IP pile		PR1 pile		IP pile		PR1 pile	
SHAFT FRICTION	$\tau_{S,AB}$ [kPa]	w/D_p [%]	$\tau_{S,AB}$ [kPa]	w/D_p [%]	$\tau_{S,AB}$ [kPa]	w/D_p [%]	$\tau_{S,AB}$ [kPa]	w/D_p [%]
at peak	35.5	8	63	8.6	40	8	52	10
after peak	-	-	53	20	-	-	50	15.5
at large w/D_p	32	100	77	100	27	100	76	100
BASE RESISTANCE	q_B [MPa]	w/D_p [%]	q_B [MPa]	w/D_p [%]	q_B [MPa]	w/D_p [%]	q_B [MPa]	w/D_p [%]
at large w/D_p	3.5	100	3.5	100	4.1	100	4.2	100
TOTAL CAPACITY	q_A [MPa]	w/D_p [%]	q_A [MPa]	w/D_p [%]	q_A [MPa]	w/D_p [%]	q_A [MPa]	w/D_p [%]
at peak	-	-	5.8	9.5	5.8	9	7.1	10
after peak	-	-	5.5	20	-	-	6.9	20
at large w/D_p	5.3	100	8	100	5.5	100	8.5	100

- both the ND and the D PR1 piles mobilise shear stress peak values. The settlements required to mobilise the peaks are $w/D_p \approx 8.6\%$ and 10%, respectively. These w/D_p values are comparable with those required to mobilise the peaks of the analogous isolated piles;
- after the peak has been attained, the $\tau_{S,AB}$ curves of both the ND and the D PR1 piles exhibit a tendency to decrease slightly, to a settlement value that ranges from 1.5 to 2.0 times the w/D_p values at the peak, followed, at larger w/D_p, by a steady trend to increase. At w/D_p = 100%, the ND and the D piles reach $\tau_{S,AB}$ values that are 22% and 46% higher than those at the peak, respectively;
- the values of $\tau_{S,AB}$ at the peak settlement and at larger settlements than the peak, of both the ND and the D PR1 piles, are substantially larger than those observed for the corresponding isolated piles;
- due to the higher shaft resistances, the pile capacity q_A, for both the ND and D PR1 piles, is significantly higher than that of the analogous isolated pile, over the whole settlement range experienced (Figures 4.7 and 4.9). The PR1 q_A curves are characterised by a peak value, due to the mobilisation of the $\tau_{S,AB}$ peak, after which the pile capacity increases further (stress hardening) at an almost steady rate. Neither the ND nor the D PR1 piles mobilise their ultimate capacity at the maximum settlement reached.

The different shaft friction mobilisation mechanisms observed for the isolated pile and for the single pile beneath the raft can be ascribed to the effect of the pressure transmitted directly by the raft to the underlying soil, q_r (see Figure 4.1). This load induces an increase in the vertical stress in the soil $\Delta\sigma'_v$ which, in turn, causes an increase in the radial

stress acting on the pile shaft, $\Delta\sigma'_r$, which generates an increase in shaft resistance, especially in the upper pile portion ("$\Delta\sigma'_r$ effect").

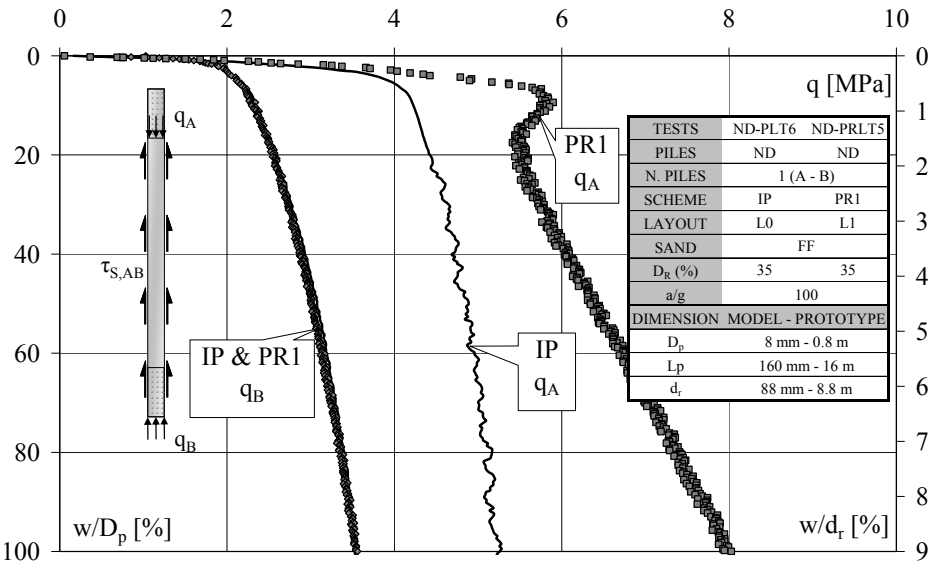

Figure 4.7. Unit loads acting on the pile head q_A and base q_B vs. the settlement normalised to the pile diameter w/D_p (left–hand side) and to the raft diameter w/d_r (right–hand side) for the isolated and single capped ND piles.

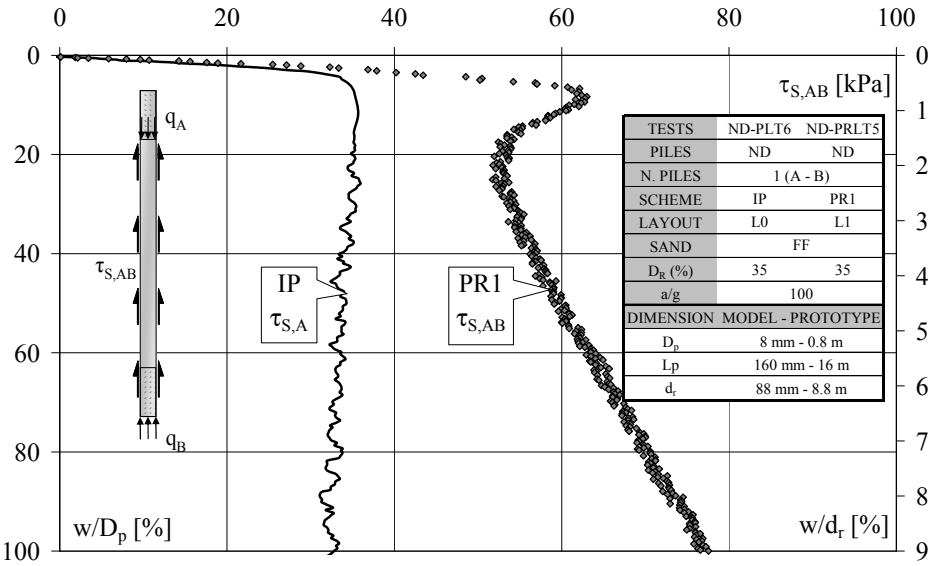

Figure 4.8. Shear stress acting between load cells A and B $\tau_{S,AB}$ vs. the settlement normalised to the pile diameter w/D_p (left–hand side) and to the raft diameter w/d_r (right–hand side) for the isolated and single capped ND piles.

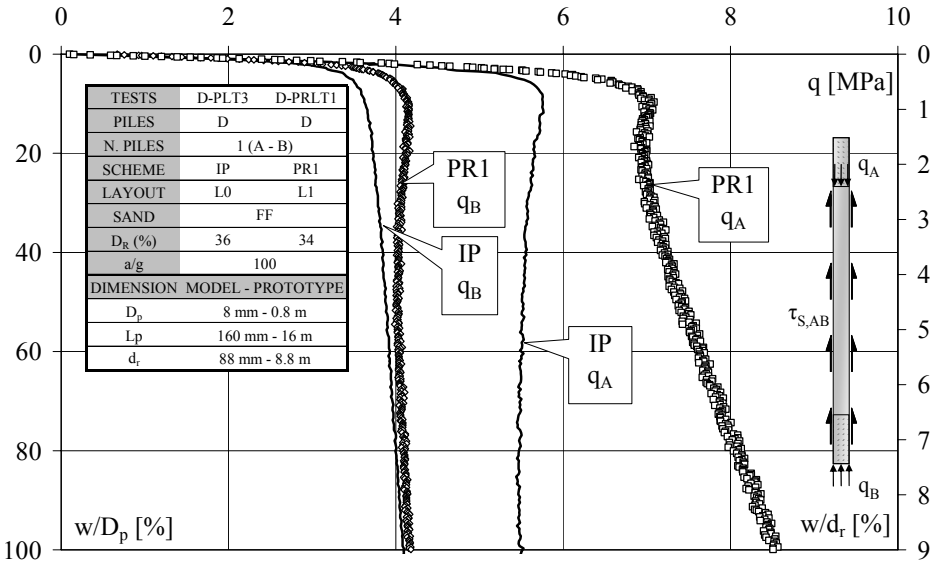

Figure 4.9. Unit loads acting on the pile head q_A and base q_B vs. the settlement normalised to the pile diameter w/D_p (left–hand side) and to the raft diameter w/d_r (right–hand side) for the isolated and single capped D piles.

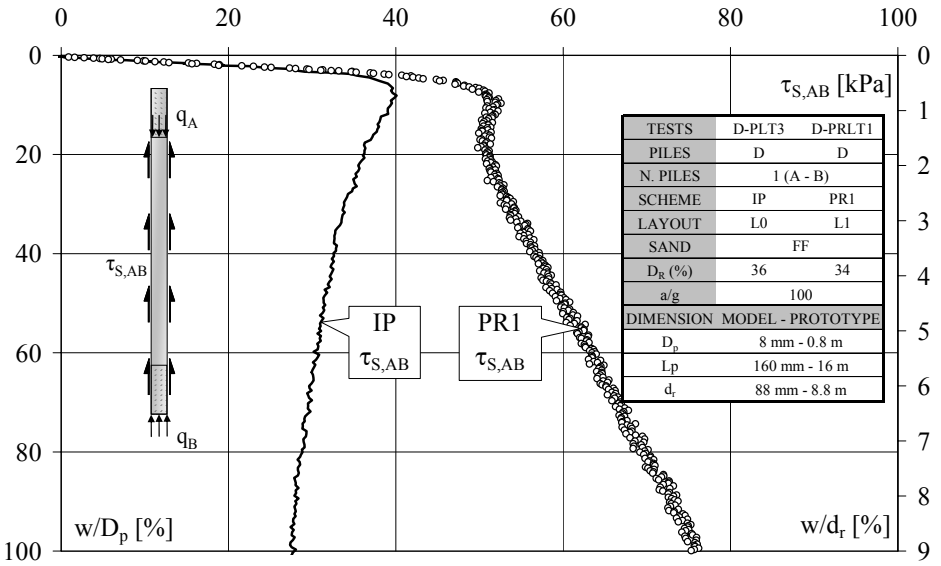

Figure 4.10. Shear stress acting between load cells A and B $\tau_{S,AB}$ vs. the settlement normalised to the pile diameter w/D_p (left–hand side) and to the raft diameter w/d_r (right–hand side) for the isolated and single capped D piles.

The "$\Delta\sigma'_r$ effect" becomes relevant when the pile is approaching its ultimate shear stress and it has resulted to be slightly more pronounced in the ND pile than in the D pile.

The "$\Delta\sigma'_r$ effect" seems to have a negligible influence on the base resistance mobilisation, at least in the settlement range that has been investigated.

At lower settlements than the peak values, neither a softer pile response, caused by the overlapping of the individual displacement fields of the cap and the pile [Randolph (1983), Randolph (1994)] nor a minor shear stress mobilisation due to the "shielding effect" [Burland (1995), Franke et. al (2000), Katzenbach (2000)] have been observed, as they were probably compensated for by the "$\Delta\sigma_r$ effect". Instead, the single piles beneath the raft result to be slightly stiffer than the isolated piles, as shown in Figure 4.11, where the stiffness of the both the ND and D PR1 piles, $k_{p,PR1}$, is plotted vs. w/D_p (data at the prototype scale). The stiffness mobilisation curves of the ND and D IP pile are also reported in the Figure.

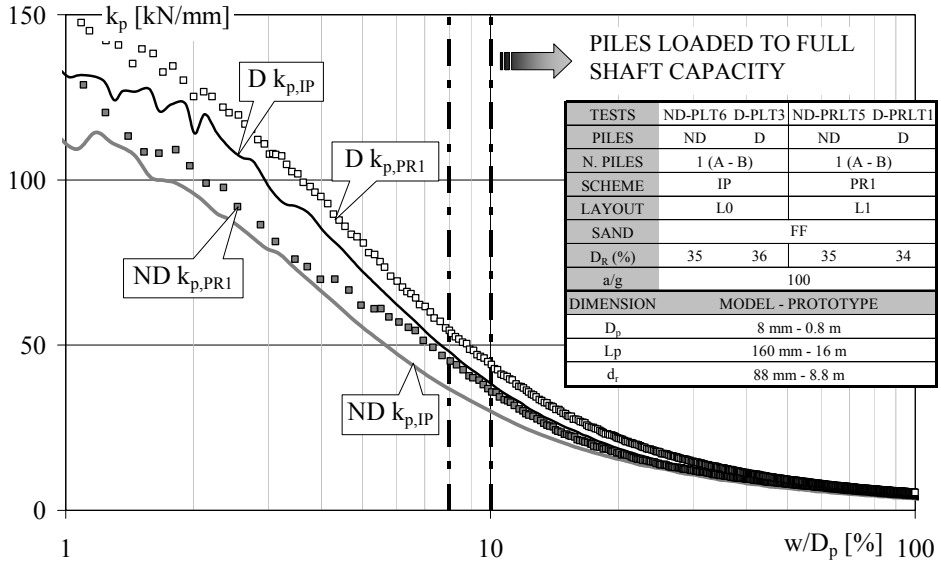

TESTS	ND-PLT6	D-PLT3	ND-PRLT5	D-PRLT1
PILES	ND	D	ND	D
N. PILES	1 (A - B)		1 (A - B)	
SCHEME	IP		PR1	
LAYOUT	L0		L1	
SAND	FF			
D_R (%)	35	36	35	34
a/g	100			
DIMENSION	MODEL - PROTOTYPE			
D_p	8 mm - 0.8 m			
Lp	160 mm - 16 m			
d_r	88 mm - 8.8 m			

Figure 4.11. Pile stiffness k_p vs. the settlement normalised to the pile diameter w/D_p for the ND and D isolated and single capped piles. Prototype scale.

4.4. Groups of piles beneath the raft

4.4.1 Non displacement pile groups

Groups of 3 ND piles: PR3(A) and PR3(a) models

The pile load–settlement curves obtained from two load tests on 3-pile raft models, with the ND piles placed alternatively at spacing $s = 8.66D_p$ and $s = 4.33D_p$ (tests ND-PRLT7 and ND-PRLT12, model schemes PR3(A) and PR3(a), see Figures 3.15 and 3.16 and Table 3.7) are plotted in Figures 4.12 and 4.13 vs. the settlement normalised to the pile diameter, w/D_p (left–hand side) and to the raft diameter, w/d_r (right–hand side). The Figures report the loads acting on the pile head and the base, q_A and q_B, and the shear stress acting between load cells A and B, $\tau_{S,AB}$, of the equivalent pile of the groups. The data relative to the single ND pile beneath the raft are also reported, for comparison purposes. The main results of the tests are summarised in Table 4.3.

The equivalent ND PR3(A) pile has almost the same load–settlement behaviour as the ND single pile beneath the raft; the q_A, q_B and $\tau_{S,AB}$ curves of the PR3(a) equivalent pile are similar to those of the ND PR1 pile, with slightly lower values of the unit base load and almost the same shaft friction values. The increase in the pile shaft capacity, due to the pressure exerted by the raft on the underlying soil ("$\Delta\sigma'_r$ effect"), is the same as in PR1, for the whole range of settlements experienced. At small w/D_p, both piles are softer than the single pile beneath the raft, as shown in Figure 4.14, where the stiffness mobilisation curves of the ND equivalent PR3(A) and PR3(a) piles are compared with that of the ND PR1 pile (data at the prototype scale), and this is probably due to pile–pile interactions that were even experienced at the large spacing $s = 8.66D_p$.

Table 4.3. Main results of the PR3(A) and PR3(a) models – ND piles.

	ND pile rafts					
	PR1 pile		PR3(A) eq. pile		PR3(a) eq. pile	
SHAFT FRICTION	$\tau_{S,AB}$ [kPa]	w/D_p [%]	$\tau_{S,AB}$ [kPa]	w/D_p [%]	$\tau_{S,AB}$ [kPa]	w/D_p [%]
at peak	63	8.6	61	9.7	59	9.5
post peak	53	20	54	25	54	25
at large w/D_p	77	100	77	100	71	100
BASE RESISTANCE	q_B [MPa]	w/D_p [%]	q_B [MPa]	w/D_p [%]	q_B [MPa]	w/D_p [%]
at large w/D_p	3.5	100	3.5	100	3.1	100
TOTAL CAPACITY	q_A [MPa]	w/D_p [%]	q_A [MPa]	w/D_p [%]	q_A [MPa]	w/D_p [%]
at peak	5.8	9.5	5.6	10.6	5.2	10.7
post peak	5.5	20	5.5	20	5	20
at large w/D_p	8	100	7.9	100	7.2	100

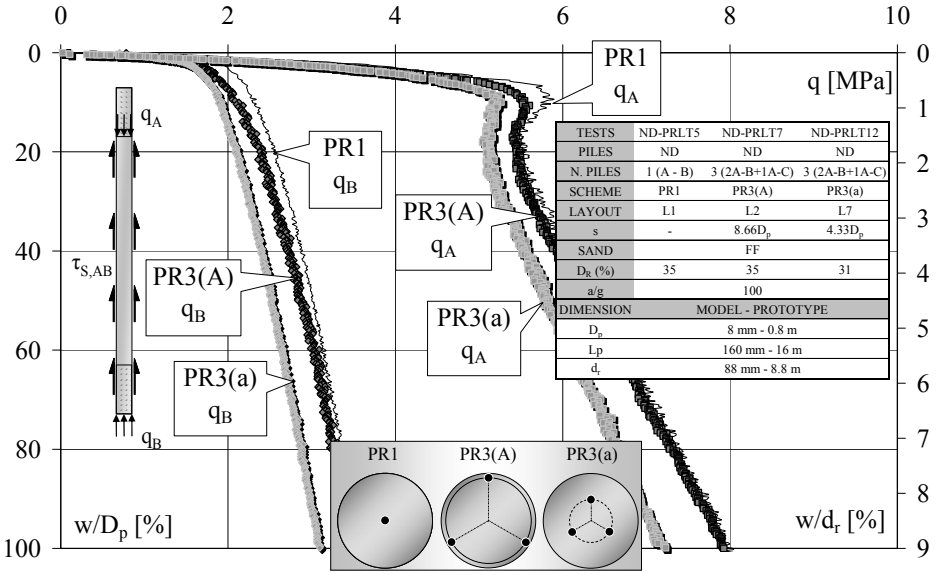

Figure 4.12. Unit loads acting on the pile head q_A and base q_B vs. the settlement normalised to the pile diameter w/D_p (left–hand side) and to the raft diameter w/d_r (right–hand side) for the ND equivalent piles of the PR3(A) and PR3(a) models and the ND PR1 pile.

In Figure 4.15, the shear stress acting on the equivalent pile of the PR3(A) model is divided into two components, the upper and the lower shaft friction transfer curves, $\tau_{S,AC}$ and $\tau_{S,CB}$; unfortunately, the load cell C

readings stopped at $w/D_p \approx 42\%$. The Figure shows that $\tau_{S,AC}$ reaches a peak value at $w/D_p = 9.7\%$ and then, as the settlement increases, after an initial stress softening, it is subject to a further increment that can be attributed to the radial stress increment induced around the upper pile shaft by the raft in direct contact with the soil. $\tau_{S,CB}$ reaches a limit value at $w/D_p = 8\%$, beyond which it seems to remain essentially constant; this suggests that in the ND PR3(A) model, the effects of the contact pressure transmitted by the raft to the soil do not influence the lower part of the shaft, at least up to the level of displacement analysed. As expected, $\tau_{S,AC}$ is lower than $\tau_{S,CB}$, in the settlement range analysed and, at smaller settlements than the peak value, it is mobilised at a lower rate.

Load cell C did not work during the tests on the PR3(a) model, thus it was not possible to derive the local shaft friction transfer curve of the equivalent pile.

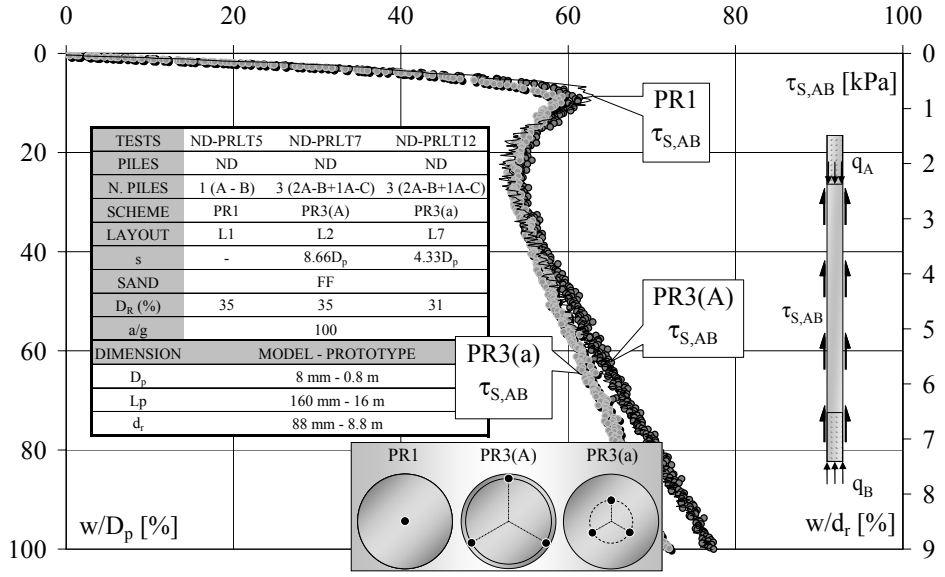

Figure 4.13. Shear stress acting between load cells A and B $\tau_{S,AB}$ vs. the settlement normalised to the pile diameter w/D_p (left–hand side) and to the raft diameter w/d_r (right–hand side) for the ND equivalent piles of the PR3(A) and PR3(a) models and the ND PR1 pile.

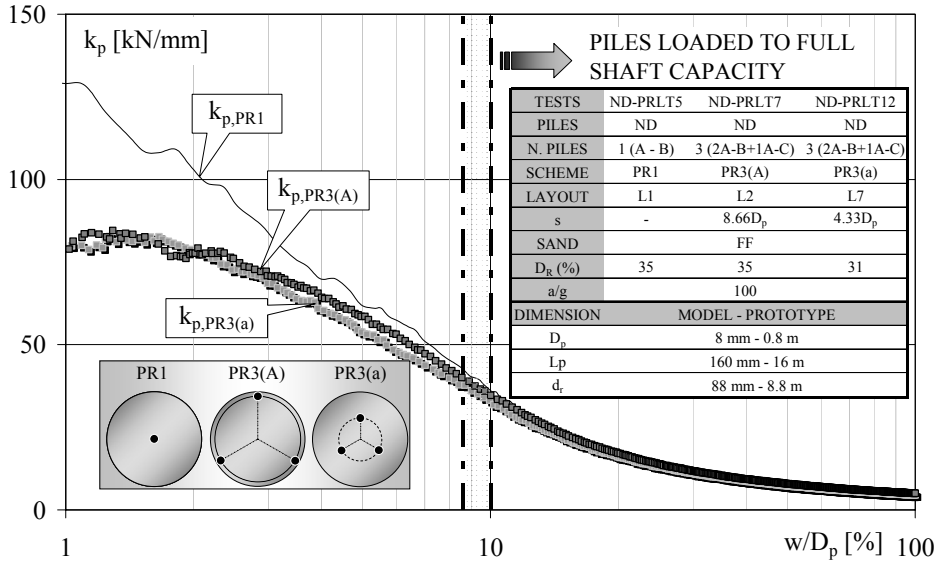

Figure 4.14. Pile stiffness k_p vs. the settlement normalised to the pile diameter w/D_p for the ND equivalent piles of the PR3(A) and PR3(a) models and the ND PR1 pile. Prototype scale.

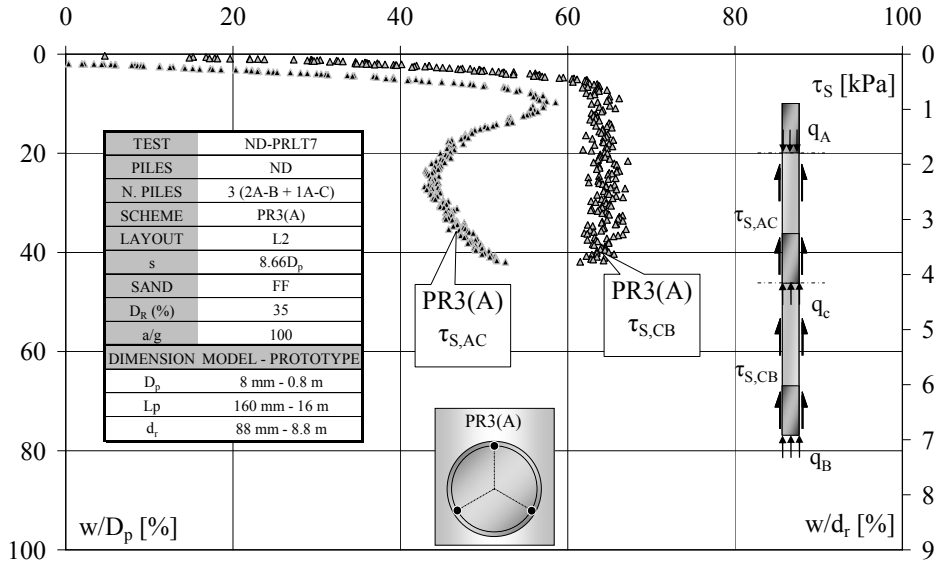

Figure 4.15. Shear stress acting between load cells A–C $\tau_{S,AC}$ and C–B $\tau_{S,CB}$ vs. the settlement normalised to the pile diameter w/D_p (left–hand side) and to the raft diameter w/d_r (right–hand side) for the ND equivalent piles of the PR3(A) model.

Group of 7 ND piles: PR7(A) model

The load–settlement curves of the centre and the equivalent edge piles of the ND PR7(A) model (ND-PRLT9 test, pile spacing $s = 5D_p$, see Figures 3.15 and 3.16 and Table 3.7) are represented in Figures 4.16 (q_A and q_B) and 4.17 ($\tau_{S,AB}$), vs. relative settlements w/D_p, (on the left–hand side) and w/d_r, (on the right–hand side). The results of the ND single pile beneath the raft are also reported in the Figures. The main test results are summarised in Table 4.4.

The shaft friction mobilisation curves of both the centre and the edge piles have a similar shape to that of the ND PR1 pile but they are characterised by a lower mobilisation gradient at small settlement (before the $\tau_{S,AB}$ peak values are reached), indicating that the interactions between the piles in the PR7(A) group start to produce significant effects on the pile stiffness. The centre and edge pile $\tau_{S,AB}$ peak values are comparable with the peak value of the ND single pile under the raft and they are reached at relative settlements which are approximately 1.6÷1.8 times the w/D_p value required to mobilise the PR1 $\tau_{S,AB}$ peak.

After the peaks have been attained, the edge pile $\tau_{S,AB}$ curve is almost coincident with that of the ND PR1 pile, while the centre pile shear stress increases with a greater rate than the $\tau_{S,AB}$ mobilisation gradient of the ND PR1 pile, reaching a 50% greater value than the peak value at w/D_p = 100%. This would seem to suggest that the "$\Delta\sigma'_r$ effect", observed for the single pile beneath the raft, is enhanced by the confining effect exercised by the peripheral piles for the centre ND PR7(A) pile, at settlement w/D_p > 15%.

As shown in Figure 4.7, the pressure transmitted by the raft to the soil seems to exert negligible effects on the ND PR1 pile q_B mobilisation, thus the increase in q_B of the PR7(A) centre and edge piles, with respect

to the PR1 pile, shown in Figure 4.16, could be due to the non homogeneity of the local soil or to interaction effects between the pile tips, especially for the centre pile.

Table 4.4. Main results of the PR7(A) model – ND piles.

	ND pile rafts					
	PR1 pile		PR7(A) eq. edge pile		PR7(A) centre pile	
SHAFT FRICTION	$\tau_{S,AB}$ [kPa]	w/D_p [%]	$\tau_{S,AB}$ [kPa]	w/D_p [%]	$\tau_{S,AB}$ [kPa]	w/D_p [%]
at peak	63	8.6	58.5	14	65.5	15.5
post peak	53	20	55	26	63.5	26
at large w/D_p	77	100	81	100	99	100
BASE RESISTANCE	q_B [MPa]	w/D_p [%]	q_B [MPa]	w/D_p [%]	q_B [MPa]	w/D_p [%]
at large w/D_p	3.5	100	4.2	100	4.6	100
TOTAL CAPACITY	q_A [MPa]	w/D_p [%]	q_A [MPa]	w/D_p [%]	q_A [MPa]	w/D_p [%]
at peak	5.8	9.5	5.9	14.5	6.5	16.5
post peak	5.5	20	5.9	20	6.5	20
at large w/D_p	8	100	8.8	100	10.4	100

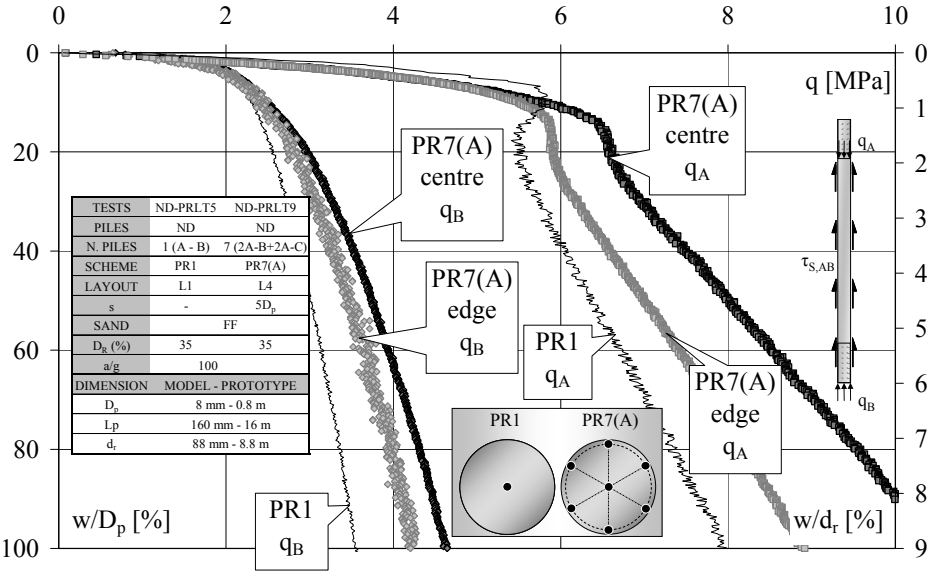

Figure 4.16. Unit loads acting on the pile head q_A and base q_B vs. the settlement normalised to the pile diameter w/D_p (left–hand side) and to the raft diameter w/d_r (right–hand side) for the centre and eq. edge ND piles of the PR7(A) model and the ND PR1 pile.

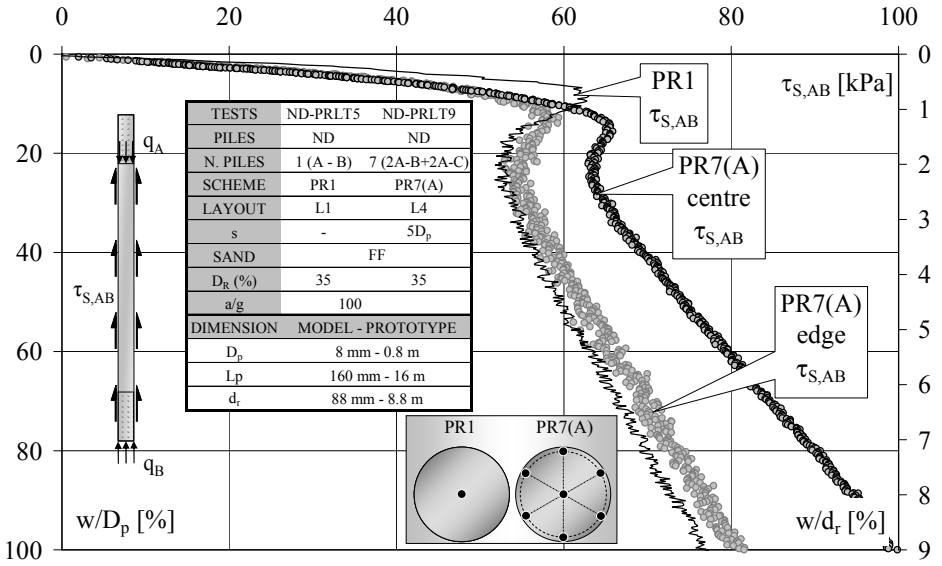

Figure 4.17. Shear stress acting between load cells A–B $\tau_{S,AB}$ vs. the settlement normalised to the pile diameter w/D_p (left–hand side) and to the raft diameter w/d_r (right–hand side) for the centre and eq. edge ND piles of the PR7(A) model and the ND PR1 pile.

The PR7(A) q_A curves show that, before reaching a threshold value at small settlements (w/D_p = 15%÷16%), both the edge and the centre PR7(A) piles are softer than the ND PR1 pile (due to the softer shaft response). This is also highlighted in Figure 4.18, where the k_p mobilisation curve of the average pile of the group is compared with that of the ND PR1 pile (data at the prototype scale).

At larger settlements than the threshold value, the edge pile experiences slightly higher q_A values than the PR1 pile, but at the same mobilisation rate. The centre pile, once the q_A threshold value has been reached, has a stiffer response than the single pile beneath the raft and it experiences significantly higher bearing capacity values.

In Figure 4.19, the shear stress acting on the equivalent edge pile of the ND PR7(A) model is divided into the two components, $\tau_{S,AC}$ and $\tau_{S,CB}$. The upper shaft friction transfer reaches a peak value at w/D_p = 13.6%

and then, as the settlement increases, after an initial stress softening, it further increases, due to the "$\Delta\sigma'_r$ effect", reaching a higher value than $\tau_{S,CB}$ at $w/D_p \approx 70\%$

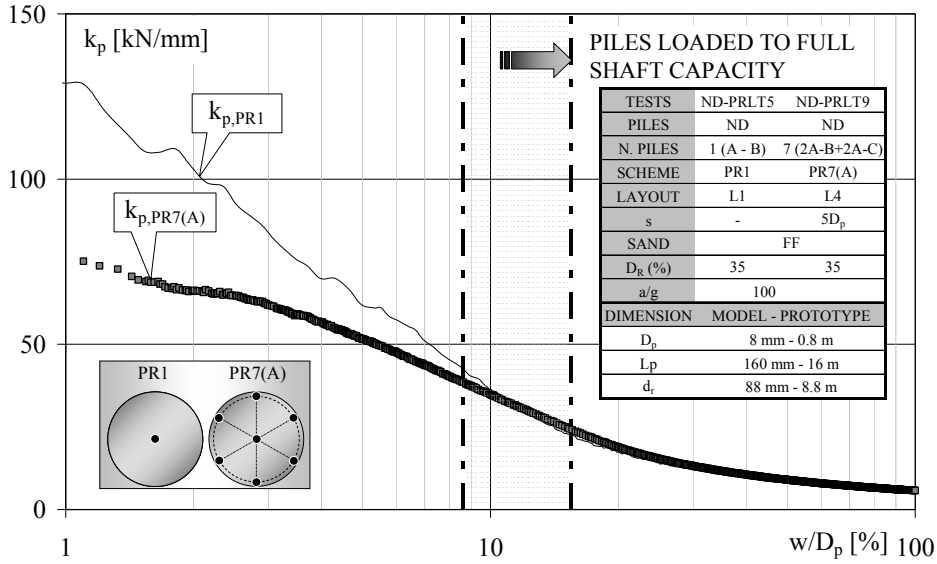

Figure 4.18. Pile stiffness k_p vs. the settlement normalised to the pile diameter w/D_p for the ND average pile of the PR7(A) model and the ND PR1 pile. Prototype scale.

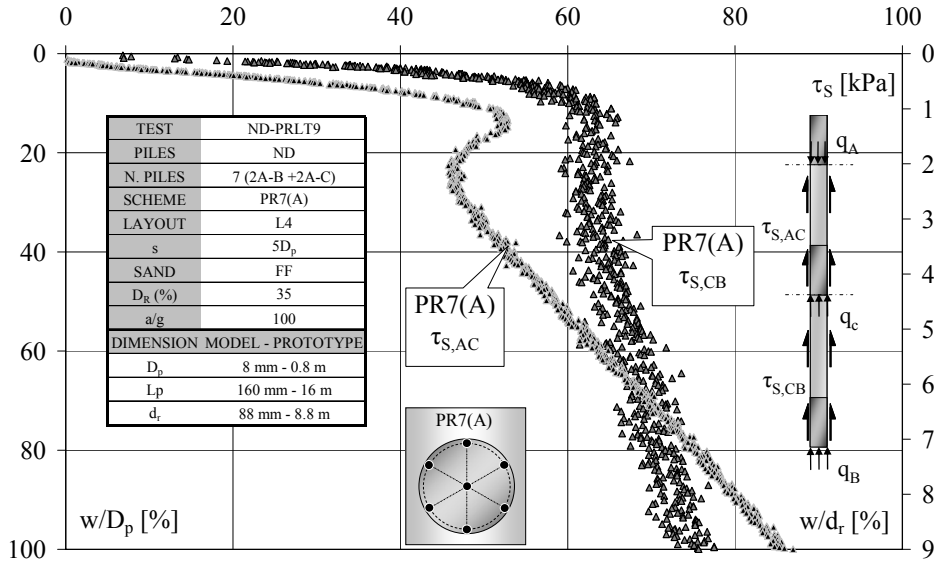

Figure 4.19. Shear stress acting between load cells A–C $\tau_{S,AC}$ and C–B $\tau_{S,CB}$ vs. the settlement normalised to the pile diameter w/D_p (left–hand side) and to the raft diameter w/d_r (right–hand side) for the ND eq. edge piles of the PR7(A) model.

As for the lower shaft friction transfer curve, $\tau_{S,CB}$ reaches a limit value at w/D_p = 12%, then it increases slightly at w/D_p > 40%, suggesting that the effects of the contact pressure transmitted by the raft to the soil beyond this settlement level also begin to influence the lower part of the shaft. $\tau_{S,CB}$ is mobilised at small settlements with a higher rate than $\tau_{S,AC}$.

Group of 7 ND piles: PR7(a) model

The load–settlement curves of the centre and the equivalent edge ND piles of the PR7(a) model (ND-PRLT13 test, pile spacing $s = 2.5D_p$, see Figures 3.15 and 3.16 and Table 3.7) are plotted in Figures 4.20 and 4.21, where the unit loads acting on the pile head and tip, and the shear stresses acting between load cells A and B are plotted, respectively. The results of the ND single pile beneath the raft are also reported in the Figure. The relevant test results are summarised in Table 4.5.

Table 4.5. Main results of the PR7(a) model – ND piles.

	ND pile rafts					
	PR1 pile		PR7(a) eq. edge pile		PR7(a) centre pile	
SHAFT FRICTION	$\tau_{S,AB}$ [kPa]	w/D_p [%]	$\tau_{S,AB}$ [kPa]	w/D_p [%]	$\tau_{S,AB}$ [kPa]	w/D_p [%]
at peak	63	8.6	60	20	73	35
post peak	53	20	-	-	-	-
at large w/D_p	77	100	80	100	90	100
BASE RESISTANCE	q_B [MPa]	w/D_p [%]	q_B [MPa]	w/D_p [%]	q_B [MPa]	w/D_p [%]
at large w/D_p	3.5	100	3.4	100	5.2	100
TOTAL CAPACITY	q_A [MPa]	w/D_p [%]	q_A [MPa]	w/D_p [%]	q_A [MPa]	w/D_p [%]
at peak	5.8	9.5	-	-	-	-
post peak	5.5	20	-	-	-	-
at large w/D_p	8	100	8	100	10.4	100

The $\tau_{S,AB}$ curves of the PR7(a) piles are characterised by a progressive mobilisation of the shear resistance, with a considerable lower gradient than the single pile beneath the raft, and a shear stress peak, followed by

stress softening, is no longer evident. The edge pile reaches a $\tau_{S,AB}$ yielding value at w/D_p = 20%, which is comparable with the $\tau_{S,AB}$ peak value of the ND single pile under the raft; its shear stress curve approaches that of the PR1 pile at larger settlements. The centre pile experiences a considerably higher $\tau_{S,AB}$ yielding value than the ND PR1 pile peak stress, at w/D_p = 35%; its shear stress further increases at larger settlements. As for the ND piles of the PR7(A) model, these results suggest that the interactions between the piles in the PR7(a) group cause a significant decrease in the shaft friction mobilisation rate; on the other hand, the confinement effects exerted by the neighbouring piles enhance the "$\Delta\sigma'_r$ effect" that has already been observed for the single pile beneath the raft and produce an increase in the limit capacity of the shaft for the centre pile.

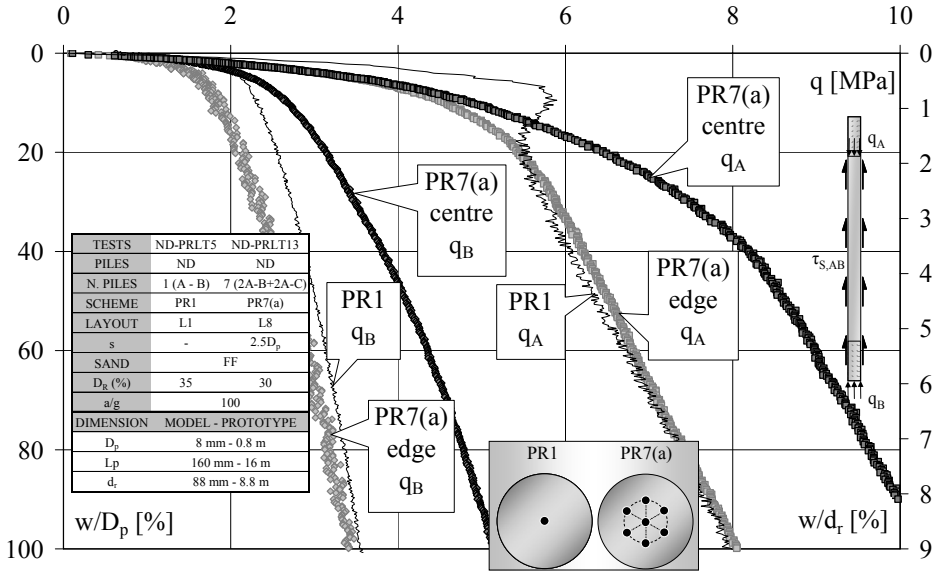

Figure 4.20. Unit loads acting on the pile head q_A and base q_B vs. the settlement normalised to the pile diameter w/D_p (left–hand side) and to the raft diameter w/d_r (left–hand side) for the ND centre and eq. edge piles of the PR7(a) model and the ND PR1 pile.

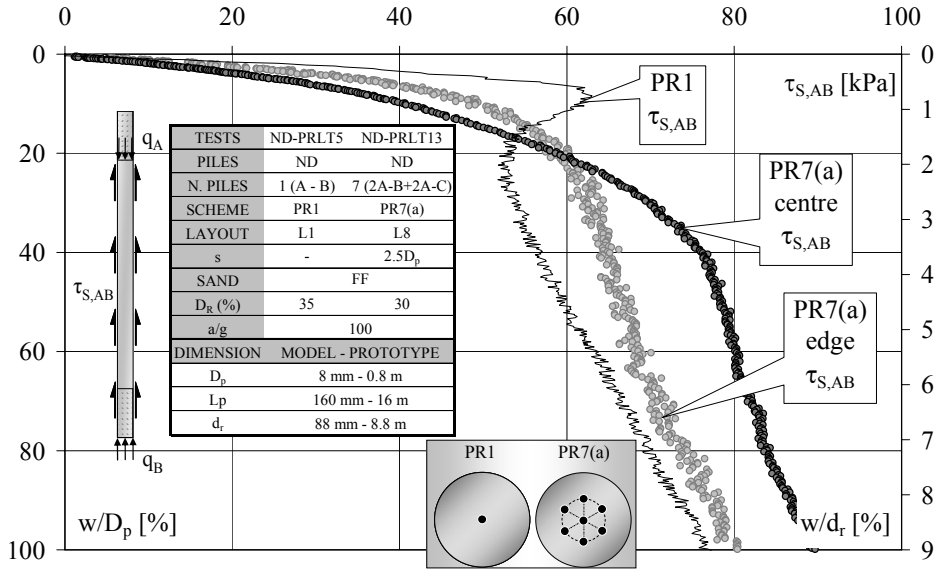

Figure 4.21. Shear stress acting between load cells A and B $\tau_{S,AB}$ vs. the settlement normalised to the pile diameter w/D_p (left–hand side) and to the raft diameter w/d_r (left–hand side) for the ND centre and eq. edge piles of the PR7(a) model and the ND PR1 pile.

As far as the base capacity is concerned, the edge pile has a very similar q_B mobilisation curve to that of the PR1 pile (Figure 4.20), whereas the centre pile experiences notably higher q_B values, as observed for the PR7(A) centre pile. These results support the hypothesis of interaction effects between the peripheral pile tips on the centre pile base.

The following comments can be made on the total capacity of the PR7(a) piles:

- q_A is mobilised progressively for both the edge and centre piles and neither a peak nor failure values are reached;
- at small settlements, the pile tangent stiffness is noticeably lower than that of the ND PR1 pile (negative group effects), which is also shown in Figure 4.22, where the k_p mobilisation curve of the average pile of the group is compared with that of the ND PR1 pile (data at the prototype scale);

- at w/D_p > 15%, the load carried by the centre pile, q_A is considerably greater than that of the ND PR1 pile (positive group effects);
- the total capacity of the centre pile is higher than that of the edge pile over the whole range of settlements experienced.

In Figure 4.23, the shear stress acting on the equivalent edge pile of the PR7(a) model is divided into the two components, $\tau_{S,AC}$ and $\tau_{S,CB}$. Both $\tau_{S,AC}$ and $\tau_{S,CB}$ reach a threshold value at $w/D_p \approx 20\%$ and then, as the settlement increases, they further increase, due to the effect of the contact pressure transmitted by the raft to the soil. At lower settlements than 20%, $\tau_{S,CB}$ is mobilised at a higher rate than $\tau_{S,AC}$.

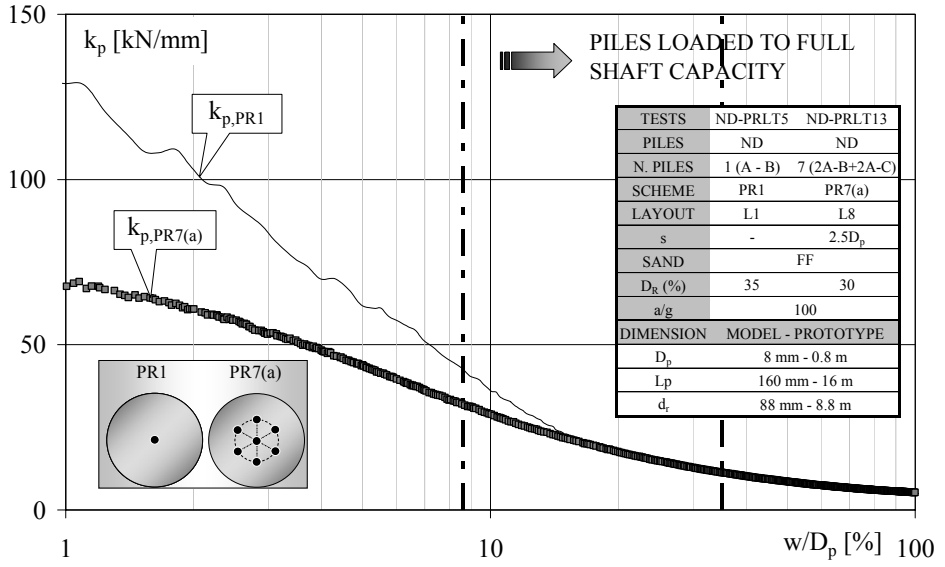

Figure 4.22. Pile stiffness k_p vs. the settlement normalised to the pile diameter w/D_p for the average ND PR7(a) pile and the ND PR1 pile. Prototype scale.

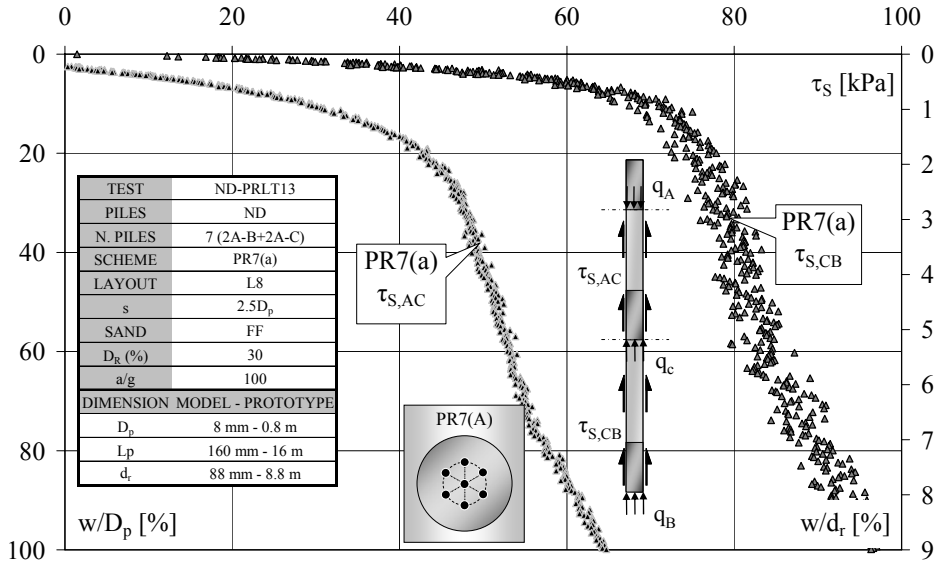

Figure 4.23. Shear stress acting between load cells A–C $\tau_{S,AC}$ and C–B $\tau_{S,CB}$ vs. the settlement normalised to the pile diameter w/D_p (left–hand side) and to the raft diameter w/d_r (left–hand side) for the ND PR7(a) eq. edge pile.

Group of 13 ND piles: PR13 model

Figures 4.24 and 4.25 present the 13-pile raft test results (ND-PRLT10 test, PR13 model scheme, see Figure 3.15 and 3.16 and Table 3.7) vs. the relative settlements w/D_p (on the left–hand side) and w/d_r (on the right–hand side). The Figures compare the load–settlement behaviour of the centre, the inner ($2.5D_p$ from the raft centre) and the edge ($5D_p$ from the raft centre) piles with that of the ND single pile beneath the raft. The main test results are summarised in Table 4.6. Figure 4.26 compares the k_p mobilisation curve of the average pile of the group with that of the ND PR1 pile, at the prototype scale. The local shaft friction transfer curves of the edge and inner equivalent piles are reported in Figures 4.27 and 4.28. The presented results confirm that the confinement effect exerted by the neighbouring piles causes an increase in the pile shear stress limit value and a decrease in the shaft friction mobilisation rate at small settlements.

In fact, the $\tau_{S,AB}$ yielding value increases moving from the outer to the centre pile and the gradient of the $\tau_{S,AB}$ curves at smaller w/D_p than the yielding value decreases from the outer to the centre pile.

The base resistance q_B also increases from the outer to the centre pile, and this highlights the interaction and confinement effects exerted by the peripheral pile tips on the inner and centre pile bases.

Table 4.6. Main results of the PR13 model – ND piles.

	ND 13-pile rafts					
	eq. edge pile		eq. inner pile		centre pile	
SHAFT FRICTIO	$\tau_{S,AB}$ [kPa]	w/D_p [%]	$\tau_{S,AB}$ [kPa]	w/D_p [%]	$\tau_{S,AB}$ [kPa]	w/D_p [%]
at peak	70	20	80	40	90	48
at large w/D_p	93	100	96	100	86	100
BASE RESISTANCE	q_B [MPa]	w/D_p [%]	q_B [MPa]	w/D_p [%]	q_B [MPa]	w/D_p [%]
at large w/D_p	4.7	100	5.9	100	10.1	100
TOTAL CAPACITY	q_A [MPa]	w/D_p [%]	q_A [MPa]	w/D_p [%]	q_A [MPa]	w/D_p [%]
at large w/D_p	10.1	100	11.6	100	15.2	100

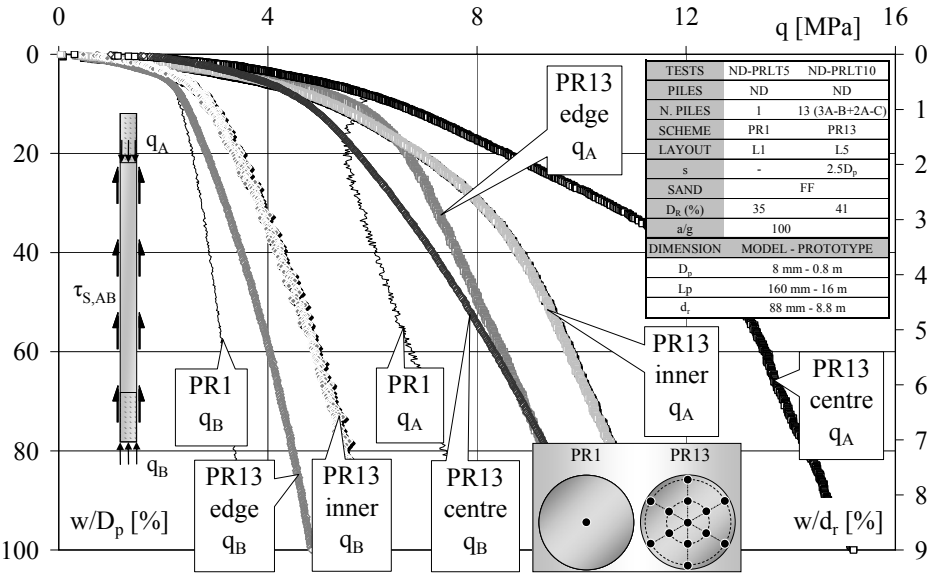

Figure 4.24. Unit loads acting on the pile head q_A and base q_B vs. the settlement normalised to the pile diameter w/D_p (left–hand side) and to the raft diameter w/d_r (right–hand side) for the centre, eq. inner and eq. edge ND piles of the PR13 model.

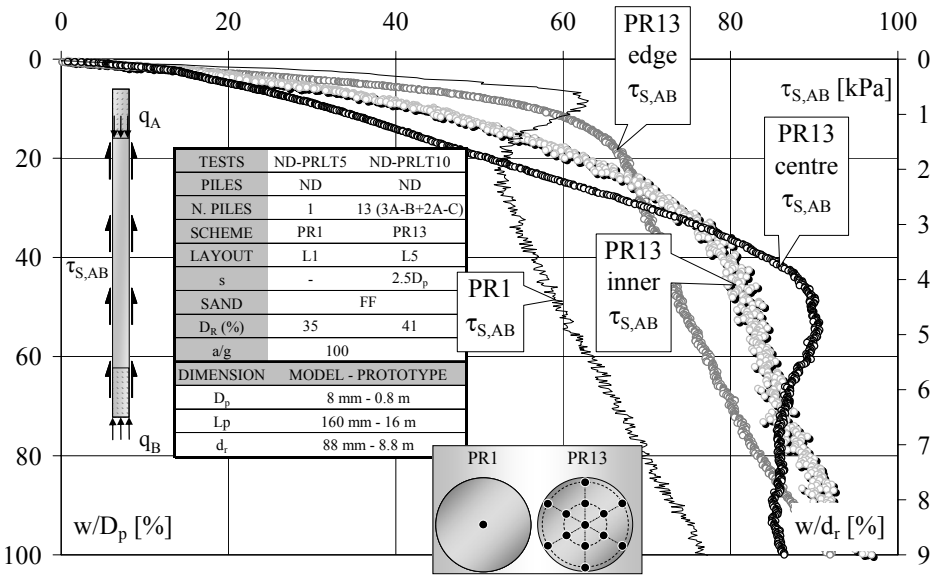

Figure 4.25. Shear stress acting between load cells A and B $\tau_{S,AB}$ vs. the settlement normalised to the pile diameter w/D_p (left–hand side) and to the raft diameter w/d_r (right–hand side) for the centre, eq. inner and eq. edge ND piles of the PR13 model.

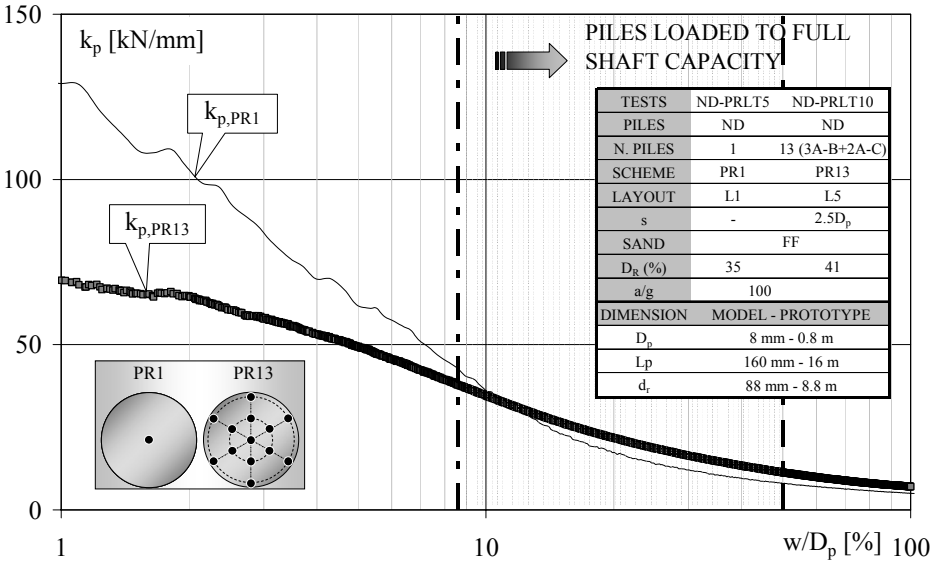

Figure 4.26. Pile stiffness k_p vs. the settlement normalised to the pile diameter w/D_p for the ND PR13 average pile and the ND PR1 pile. Prototype scale.

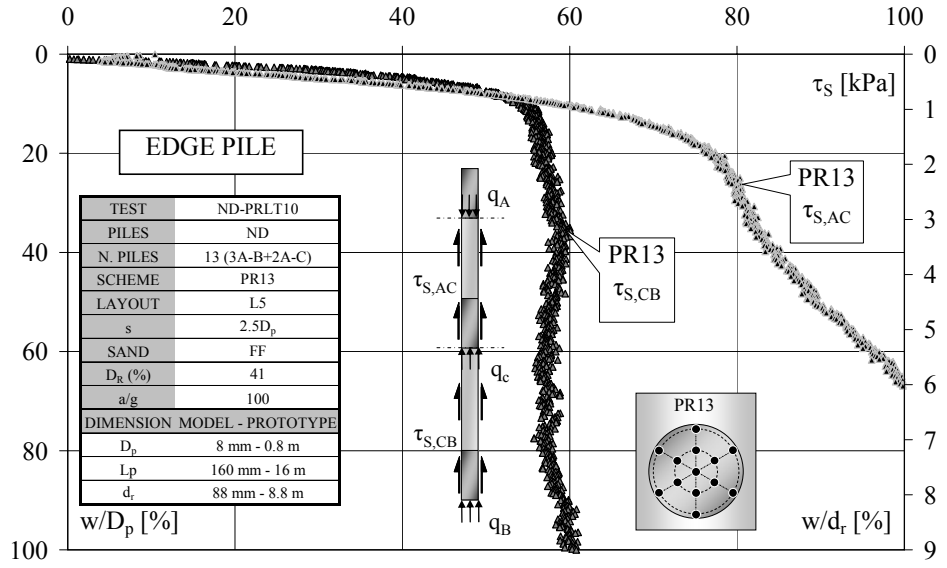

Figure 4.27. Shear stress acting between load cells A–C $\tau_{S,AC}$ and C–B $\tau_{S,CB}$ vs. the settlement normalised to the pile diameter w/D_p (left–hand side) and to the raft diameter w/d_r (right–hand side) for the ND eq. edge pile of the PR13 model.

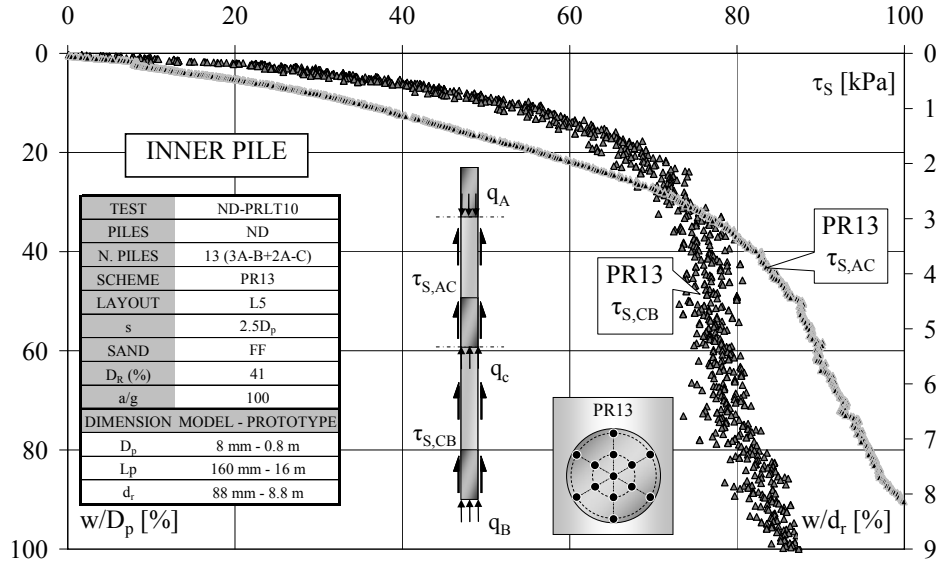

Figure 4.28. Shear stress acting between load cells A–C $\tau_{S,AC}$ and C–B $\tau_{S,CB}$ vs. the settlement normalised to the pile diameter w/D_p (left–hand side) and to the raft diameter w/d_r (right–hand side) for the ND eq. inner pile of the PR13 model.

4.4.2 Displacement pile groups

Group of 3 D piles: PR3(A)model

The pile load–settlement curves obtained from a 3-pile raft load test with the displacement piles placed at the spacing s = 8.66D_p (test D-PRLT3, model scheme PR3(A), see Figures 3.15 and 3.16 and Table 3.7) are plotted in Figures 4.29 and 4.30 vs. the settlement normalised to the pile diameter, w/D_p (on the left–hand side) and to the raft diameter, w/d_r (on the left–hand side). The Figures report the loads acting on the pile head and base, q_A and q_B, and the shear stress acting between load cells A and B, $\tau_{S,AB}$ of the equivalent pile in the group.

They also report the results of the single D pile under the raft (PR1). The main test results are summarised in Table 4.7.

The equivalent D PR3(A) pile mobilises slightly lower values of q_B and slightly higher values of $\tau_{S,AB}$, compared with the D PR1 pile, but with the same mobilisation mechanisms.

Table 4.7. Main results of the PR3(A) model – D piles.

	D pile rafts			
	PR1 pile		PR3(A) eq. pile	
SHAFT FRICTION	$\tau_{S,AB}$ [kPa]	w/D_p [%]	$\tau_{S,AB}$ [kPa]	w/D_p [%]
at peak	52	10	57	9.8
post peak	50	15.5	55.5	16.7
at large w/D_p	76	100	80	100
BASE RESISTANCE	q_B [MPa]	w/D_p [%]	q_B [MPa]	w/D_p [%]
at large w/D_p	4.2	100	3.7	100
TOTAL CAPACITY	q_A [MPa]	w/D_p [%]	q_A [MPa]	w/D_p [%]
at peak	7.1	10	6.8	10
post peak	6.9	20	6.7	17.5
at large w/D_p	8.5	100	8.3	100

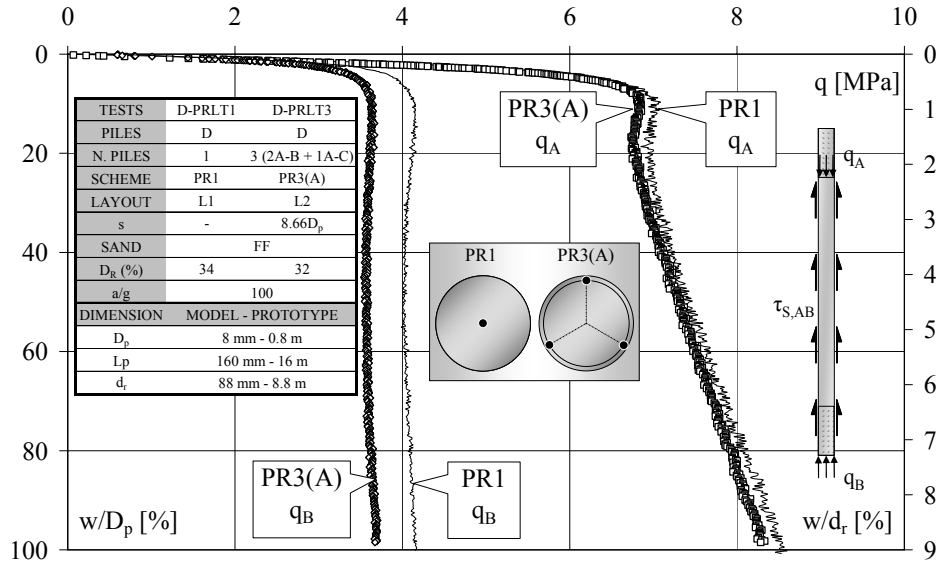

Figure 4.29. Unit loads acting on the pile head q_A and base q_B vs. the settlement normalised to the pile diameter w/D_p (left–hand side) and to the raft diameter w/d_r (right–hand side) for the D eq. pile of the PR3(A) model.

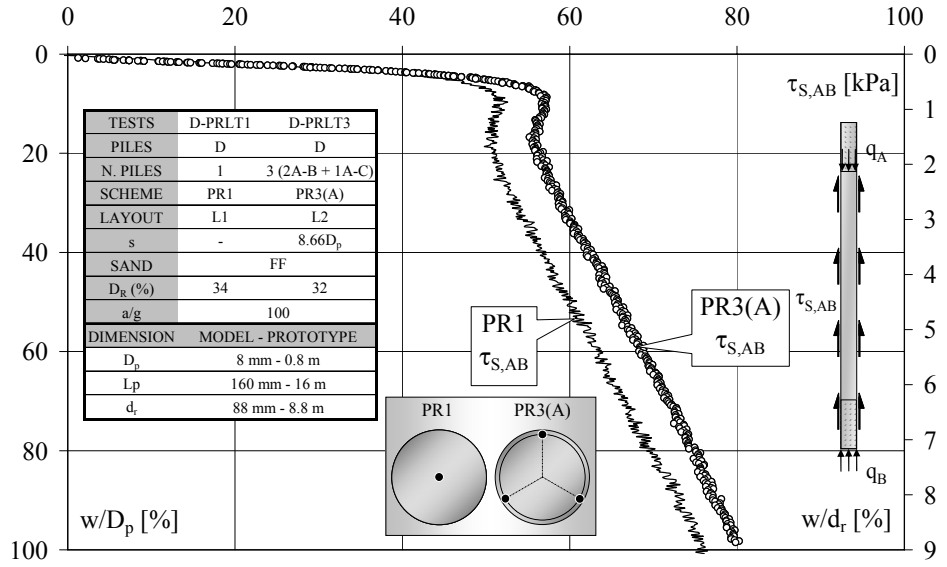

Figure 4.30. Shear stress acting between load cells A and B $\tau_{S,AB}$ vs. the settlement normalised to the pile diameter w/D_p (left–hand side) and to the raft diameter w/d_r (right–hand side) for the D eq. pile of the PR3(A) model.

The increase in the pile shaft capacity, due to the pressure exerted by the raft on the underlying soil ("$\Delta\sigma'_r$ effect"), is the same as in PR1, over the whole settlement range experienced.

The overall load–settlement behaviour of the piles in the PR3(A) group (q_A curve) is the same as that of the single pile beneath the raft.

The k_p mobilisation curve of the equivalent D PR3(A) pile, plotted at the prototype scale in Figure 4.31 vs. w/D_p, after an initial non–linearity, is identical to that of the D PR1 pile at $w/D_p > 3\%$, indicating that the possible interaction effects between the 3 displacement piles are negligible at spacing $s = 8.66D_p$.

In Figure 4.32, the shear stress acting on the equivalent pile of the group is divided into two components, the upper and the lower shaft friction transfer curves, $\tau_{S,AC}$ and $\tau_{S,CB}$. $\tau_{S,AC}$ reaches a peak value at $w/D_p = 8.5\%$ and then, as the settlement increases, after an initial stress softening, it receives a further increment due to the "$\Delta\sigma'_r$ effect".

$\tau_{S,CB}$ reaches a yielding value at $w/D_p = 10\%$, beyond which it steadily increases, due to the contact pressure of the raft on the soil. Unlike what was observed for the ND PR3(A) piles, the "$\Delta\sigma'_r$ effect" is extended to the lower segment of the pile, suggesting a stiffer response of the soil, probably due to the soil densification produced by the pile jacking.

The upper shaft friction $\tau_{S,AC}$ is lower than $\tau_{S,CB}$ over the whole settlement range experienced and it is mobilised with a lower rate.

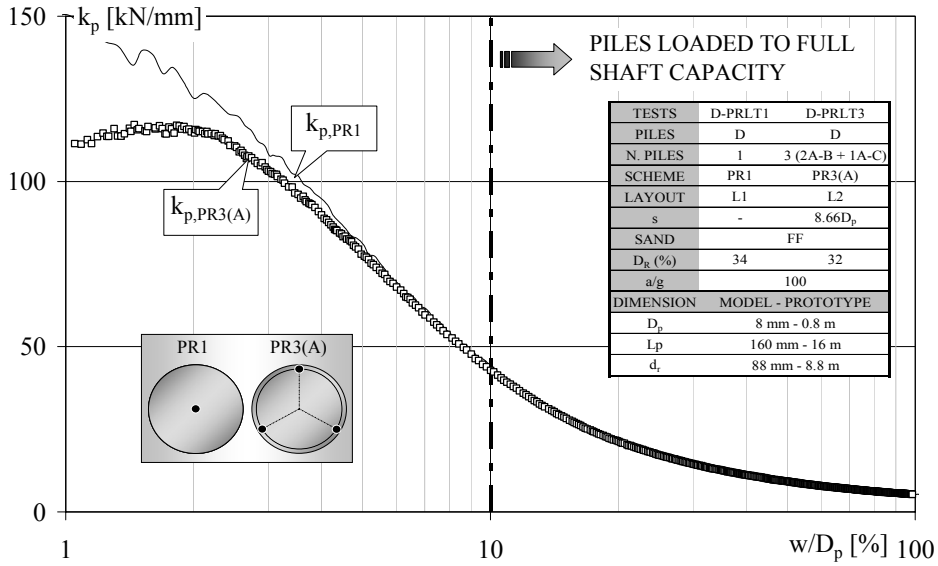

Figure 4.31. Pile stiffness k_p vs. the settlement normalised to the pile diameter w/D_p for the D eq. pile of the PR3(A) model and the D PR1 pile. Prototype scale.

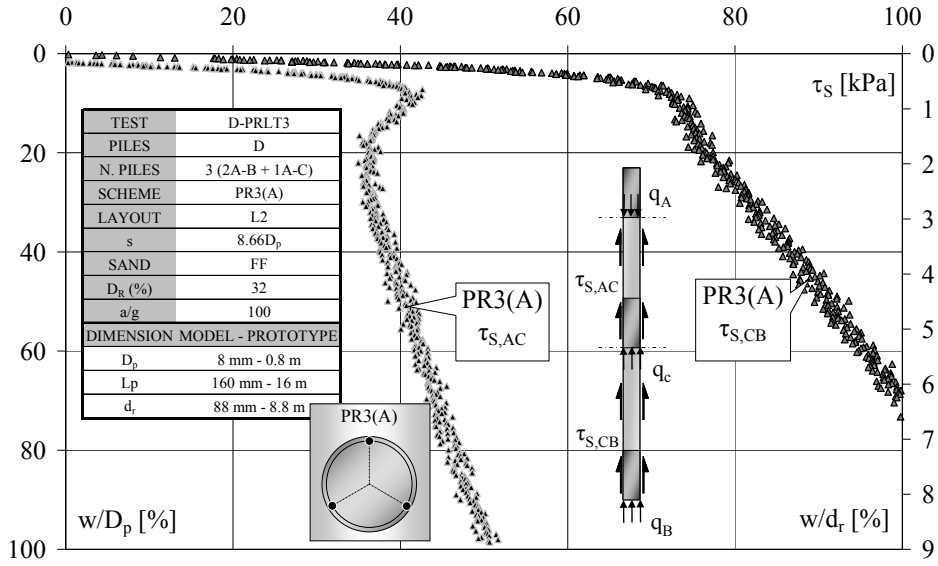

Figure 4.32. Shear stress acting between load cells A–C $\tau_{S,AC}$ and C–B $\tau_{S,CB}$ vs. the settlement normalised to the pile diameter w/D_p (left–hand side) and to the raft diameter w/d_r (right–hand side) for the D eq. pile of the PR3(A) model.

Group of 7 D piles: PR7(A) model

The load–settlement curves of the centre and the equivalent edge piles of the PR7(A) model (D-PRLT4 test, pile spacing s = $5D_p$, see Figures 3.15 and 3.16 and Table 3.7) are represented in Figures 4.33 (q_A and q_B) and 4.34 ($\tau_{S,AB}$), with respect to the relative settlements, w/D_p and w/d_r. The results of the D single pile beneath the raft test are also reported in the Figures. The relevant test results are summarised in Table 4.8.

The shear stress and the base load of both the edge and centre piles result to be considerably greater than those of the single displacement pile beneath the raft, over almost the whole settlement range investigated. With respect to the PR1 pile base capacity, the q_B values of the edge and the centre piles are about 20% and 50% higher, respectively. The observed increase in q_B can be attributed to the superimposition of the compaction zones under the pile tips and to the increase in the radial stress around the pile bases produced by the pile jacking. This effect is more pronounced for the centre pile, as it is more confined.

Table 4.8. Main results of the PR7(A) model – D piles.

	D pile rafts					
	PR1 pile		PR7(A) eq. edge pile		PR7(A) centre pile	
SHAFT FRICTION	$\tau_{S,AB}$ [kPa]	w/D_p [%]	$\tau_{S,AB}$ [kPa]	w/D_p [%]	$\tau_{S,AB}$ [kPa]	w/D_p [%]
at peak	52	10	73.5	11.5	75.5	13.5
post peak	50	15.5	68.7	24.2	70	26
at large w/D_p	76	100	102	100	104	100
BASE RESISTANCE	q_B [MPa]	w/D_p [%]	q_B [MPa]	w/D_p [%]	q_B [MPa]	w/D_p [%]
at large w/D_p	4.2	100	5.1	100	6.6	100
TOTAL CAPACITY	q_A [MPa]	w/D_p [%]	q_A [MPa]	w/D_p [%]	q_A [MPa]	w/D_p [%]
at peak	7.1	10	9.2	13.5	10.8	15
post peak	6.9	20	9	24	10.5	26.4
at large w/D_p	8.5	100	11.1	100	12.7	100

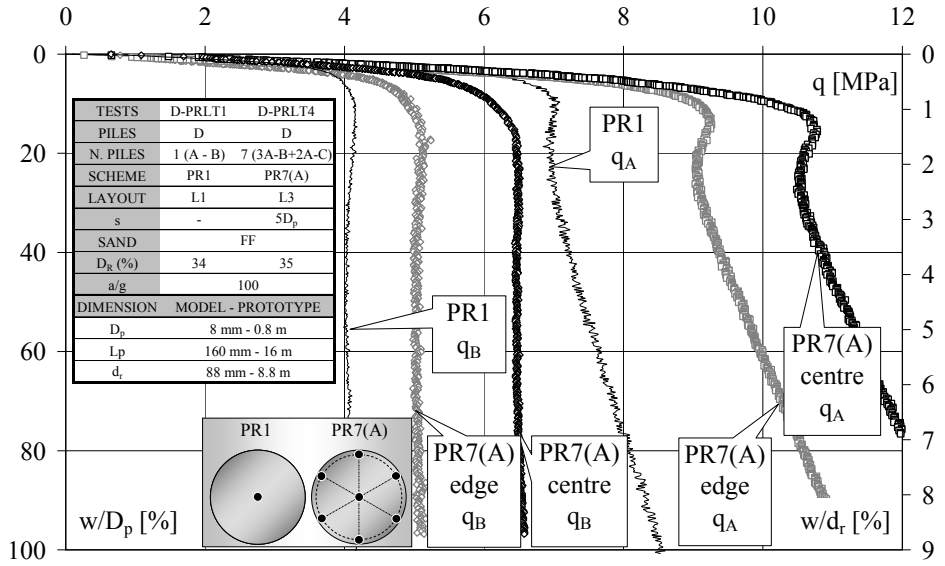

Figure 4.33. Unit loads acting on the pile head q_A and base q_B vs. the settlement normalised to the pile diameter w/D_p (left–hand side) and to the raft diameter w/d_r (right–hand side) for the D centre and eq. edge piles of the PR7(A) model and the D PR1 pile.

As far as the shaft friction is concerned, the edge and the centre piles show similar values of $\tau_{S,AB}$ and they both have similar shaped mobilisation curves as that of the displacement PR1 pile. The peak values are considerably higher (about 45%) than that of the D PR1 pile and they are reached at a slightly higher rate. The very high values of the shear stress mobilised by all the PR7(A) piles, with respect to the PR1 pile, confirm that the "$\Delta\sigma'_r$ effect" is increased due to the confining effect exercised by the neighbouring piles, and this leads to an enhanced shaft capacity. They also suggest that a further shaft capacity improvement is produced by the soil densification and the increase in radial stresses induced in the soil mass by the jacking of the pile group. This further improvement involves all the piles of the PR7(A) group and it likely occurs to compensate for, or even exceed, the interaction effects between the piles on the shaft capacity mobilisation rate. This is confirmed by the

k_p mobilisation curve of the average pile of the group which is plotted vs. w/D_p in Figure 4.35, where the k_p curve of the D PR1 pile is also reported (data at the prototype scale): from w/D_p >2%, the stiffness values of the average pile of the PR7(A) group is higher than that of the single pile beneath the raft.

The local shaft friction transfer curves of the equivalent edge pile, reported in Figure 4.36, show that $\tau_{S,AC}$ is characterised by a peak value that is reached at w/D_p = 12.4% and then, after an initial stress softening, it further increases as the settlement increases due to the "$\Delta\sigma'_r$ effect". As for the lower shaft friction transfer curve, $\tau_{S,CB}$ is mobilised with a higher rate than $\tau_{S,AC}$ and it reaches a limit value at w/D_p = 10.6%, then it increases, as it is influenced like $\tau_{S,AC}$ by the effect of the contact pressure of the raft on the soil.

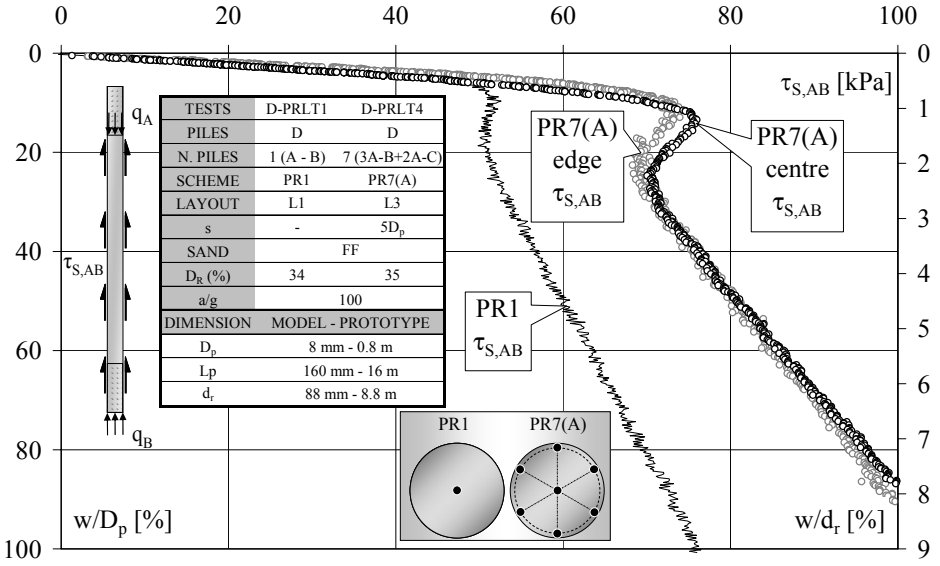

Figure 4.34. Shear stress acting between load cells A–B $\tau_{S,AB}$ vs. the settlement normalised to the pile diameter w/D_p (left–hand side) and to the raft diameter w/d_r (right–hand side) for the D centre and eq. edge piles of the PR7(A) model and the D PR1 pile.

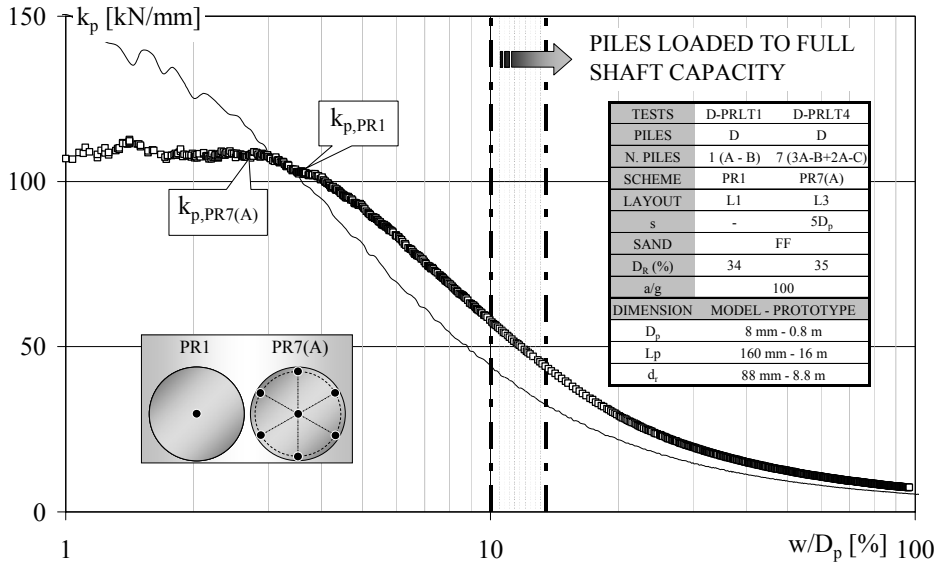

TESTS	D-PRLT1	D-PRLT4
PILES	D	D
N. PILES	1 (A - B)	7 (3A-B+2A-C)
SCHEME	PR1	PR7(A)
LAYOUT	L1	L3
s	-	$5D_p$
SAND	FF	
D_R (%)	34	35
a/g	100	
DIMENSION	MODEL - PROTOTYPE	
D_p	8 mm - 0.8 m	
Lp	160 mm - 16 m	
d_r	88 mm - 8.8 m	

Figure 4.35. Pile stiffness k_p vs. the settlement normalised to the pile diameter w/D_p for the D PR7(A) average pile and the D PR1 pile. Prototype scale.

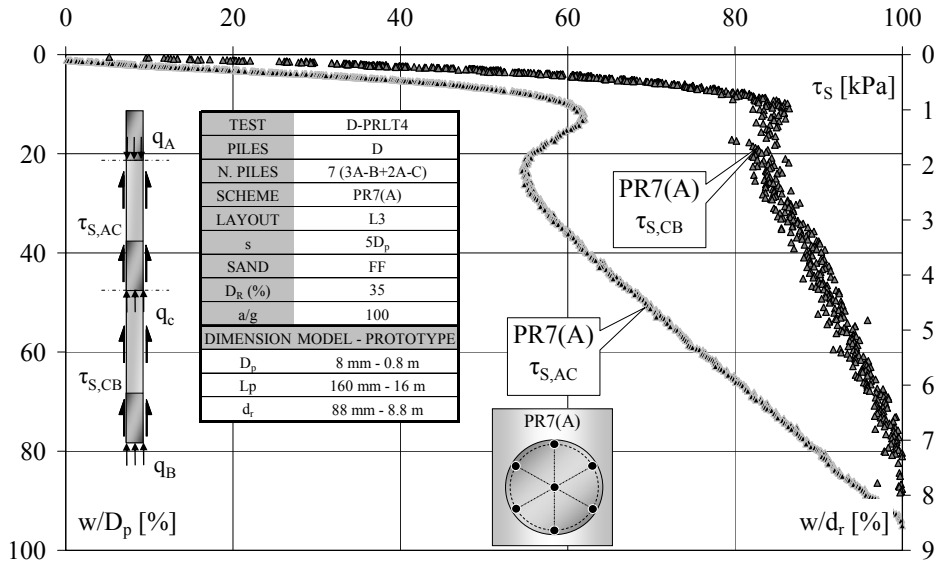

TEST	D-PRLT4
PILES	D
N. PILES	7 (3A-B+2A-C)
SCHEME	PR7(A)
LAYOUT	L3
s	$5D_p$
SAND	FF
D_R (%)	35
a/g	100
DIMENSION	MODEL - PROTOTYPE
D_p	8 mm - 0.8 m
Lp	160 mm - 16 m
d_r	88 mm - 8.8 m

Figure 4.36. Shear stress acting between load cells A–C $\tau_{S,AC}$ and C–B $\tau_{S,CB}$ vs. the settlement normalised to the pile diameter w/D_p (left–hand side) and to the raft diameter w/d_r (right–hand side) for the D edge eq. piles of the PR7(A) model.

4.5 Load sharing and efficiency of piled rafts

In this section, the overall load–settlement behaviour of the piled rafts is reported and analysed. The results of the centrifuge tests on the non displacement pile rafts (tests ND-PRLT5, 7, 9, 10, 12, 13) are presented in the Figures 4.37, 4.38. 4.39 and 4.40, which report, with respect to the measured settlement normalised to the raft diameter, w/d_r, the total unit load carried by the raft, q_t, the total axial load transmitted by the raft to the pile heads, Q_p (in the model scale), the pressure transmitted by the raft to the soil, q_r and the piled raft stiffness k_{pr} (load/settlement ratio) curves, respectively. The analogous results obtained from the tests on the displacement pile rafts (tests D-PRLT1, 3, 4) are shown in Figures 4.41, 4.42, 4.43 and 4.44. The piled raft stiffness is represented at the prototype scale. Figures 4.37, 4.39, 4.41 and 4.43 also report the results of the unpiled raft load test, R (test URLT0) for which $q_t = q_r$.

The q_t, Q_p and q_r values have been evaluated as follows:

$$q_t(w) = Q_t(w) / (\pi d_r^2/4) \qquad [FL^{-2}] \qquad (4.8)$$

$$Q_p(w) = \sum_{i=1}^{n} Q_{Ai}(w) \qquad n = 1, 3, 7, 13 \quad [F] \qquad (4.9)$$

$$q_r(w) = \frac{Q_r(w)}{\frac{\pi d_r^2}{4} - n \cdot \frac{\pi D_p^2}{4}} \qquad n = 1, 3, 7, 13 \quad [FL^{-2}] \qquad (4.10)$$

where:

Q_t = measured load applied to the raft [F];

n = number of piles [-];

Q_{Ai} = axial load measured at the head of the i^{th} pile [F];

$Q_r = Q_t - Q_p$ = load transmitted by the raft to the soil [F].

In the interpretation of the tests performed on model schemes PR7(A), PR7(a) and PR13, the axis symmetry of the geometry and of the loading

conditions allowed us to account for the non instrumented piles, which have been considered to be as loaded as the instrumented piles placed at the same radial distance from the raft centre.

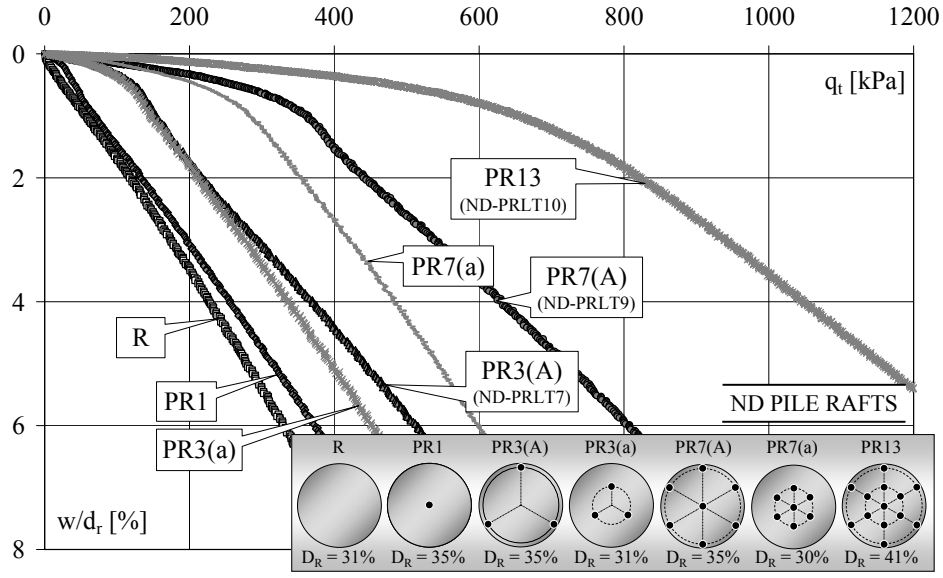

Figure 4.37 Total applied stress q_t vs. the raft relative settlement w/d_r for the ND pile rafts.

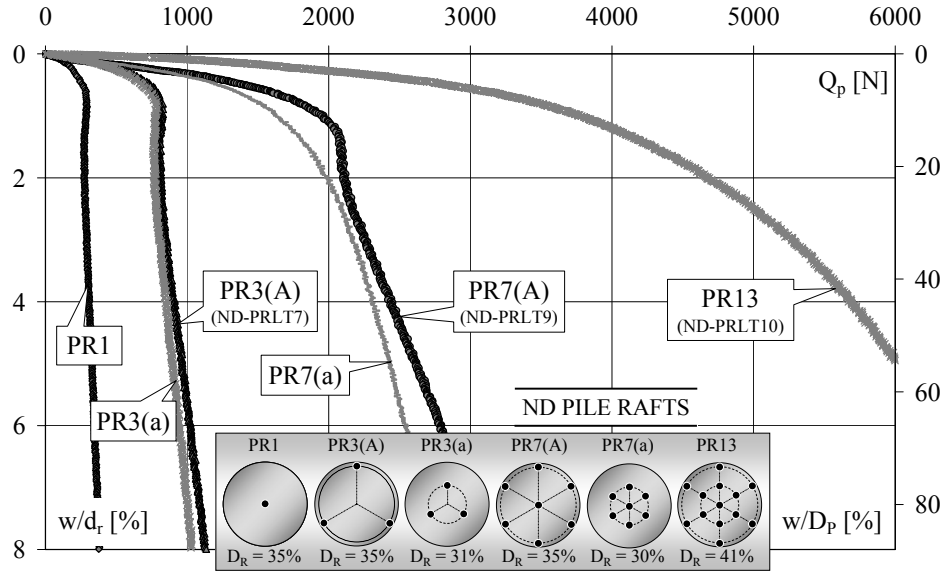

Figure 4.38. Load transmitted to the piles Q_p vs. the raft relative settlement w/d_r for the ND pile rafts. Model scale.

The load sharing mechanisms between the soil and piles, expressed by the ratios Q_p/Q_t and Q_r/Q_t, have been computed on the basis of the results reported in Figures 4.37 to 4.39 and 4.41 to 4.43; they are shown in Figure 4.45, for the ND pile rafts and in Figure 4.46 for the D pile rafts, respectively.

The piled raft settlement efficiency has been evaluated as follows:

$$\zeta = (w_{ur} - w_{pr}) / w_{ur} \qquad [-] \qquad (4.11)$$

where:

w_{ur} = settlement of the unpiled raft at a given applied pressure, q_t [L];

w_{pr} = settlement of the piled rafts at the same q_t [L].

The ζ curves, which have been derived from the results reported in Figures 4.37 and 4.41, are shown in Figures 4.47 (ND pile rafts) and 4.48 (D pile rafts) as a function of the number of piles and for values of q_t ranging from 25 to 530 kPa.

The following comments can be made on the basis of an examination of Figures from 4.37 to 4.48:

- The unpiled raft R exhibits an almost linear stress–settlement curve and, as expected, it settles more than the piled raft foundations at the same applied stress (Figures 4.37 and 4.41).
- The piled raft stress–settlement curves are non linear and they are characterised by a progressive decay in the stiffness as the applied pressure increases (Figures 4.37 and 4.41); a sharp change in their slope occurs at the settlement at which the yielding load of the piles (Q_{py}) is mobilised (Figures 4.38 and 4.42). The yielding settlement increases for an increasing number of piles. At larger w/d_r than the yielding settlement, the load carried by the piled rafts further

increases, at an almost steady rate, which is greater than that of the unpiled raft R.

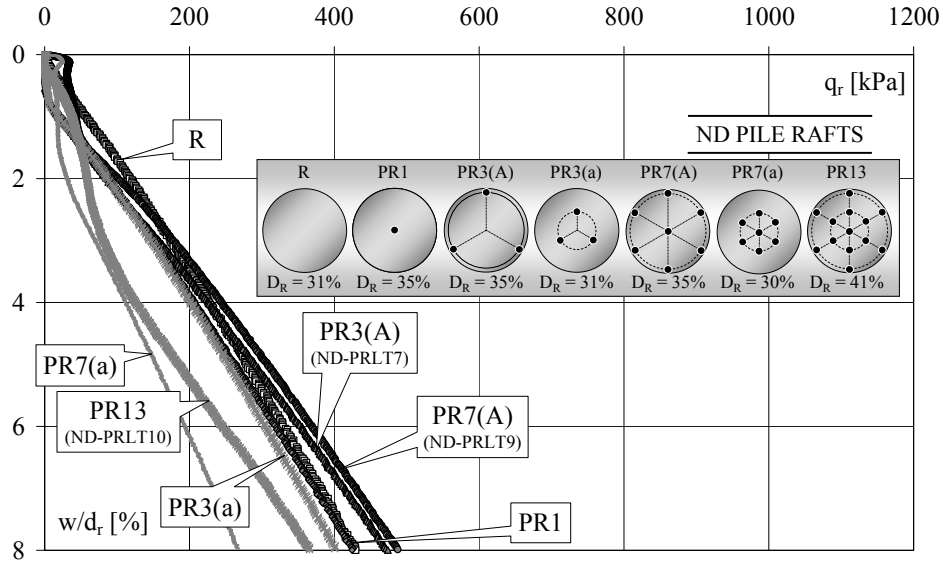

Figure 4.39. Pressure directly transmitted by the raft to the soil q_r vs. the raft relative settlement w/d_r for the ND pile rafts.

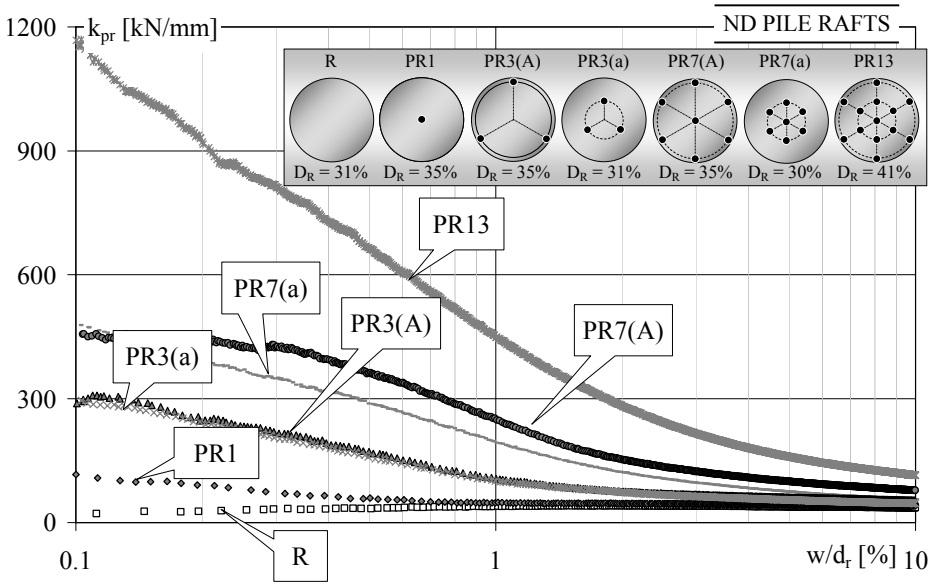

Figure 4.40. Piled raft stiffness k_{pr} vs. the raft relative settlement w/d_r for the ND piled rafts. Prototype scale.

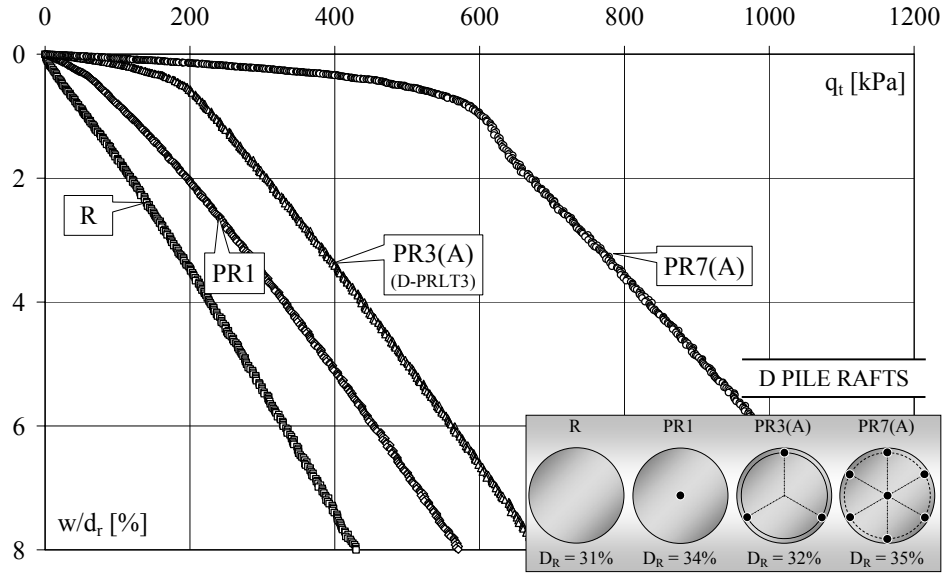

Figure 4.41. Total applied stress q_t vs. the raft relative settlement w/d_r for the D pile rafts.

- The piled raft foundations do not reach their ultimate loads in the explored settlement range.
- Comparing Figures 4.37 and 4.41, it can be seen that at a given value of q_t, the rafts on the ND piles exhibit a larger relative settlement than the analogous models on the D piles, the difference becoming more marked as the number of piles increases (see also Figures 4.47 and 4.48).
- At small w/d_r, the piles support most of the applied load (Figures 4.38 and 4.45, 4.42 and 4.46) and the piled raft stiffness mainly reflects that of the pile group. As a consequence, as the number of piles increases the foundation stiffness increases and, as the pile spacing decreases, the number of piles being the same (see PR7(A) and PR7(a) models in Figure 4.41 and 4.42), the piled raft stiffness decreases (as can be seen in Section 4.4, the interactions between the piles become stronger as the piles become closer).

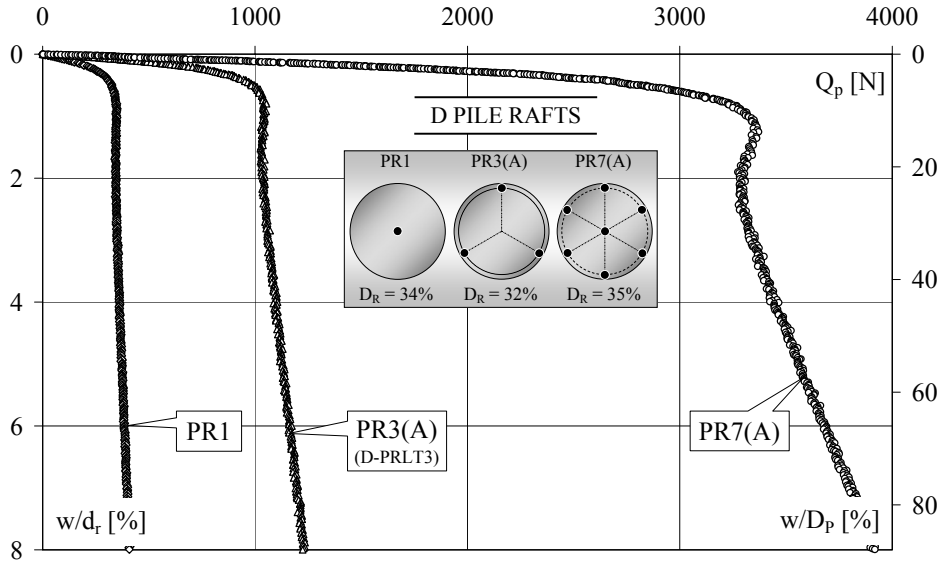

Figure 4.42. Load transmitted to the piles Q_p vs. the raft relative settlement w/d_r for the D pile rafts. Model scale.

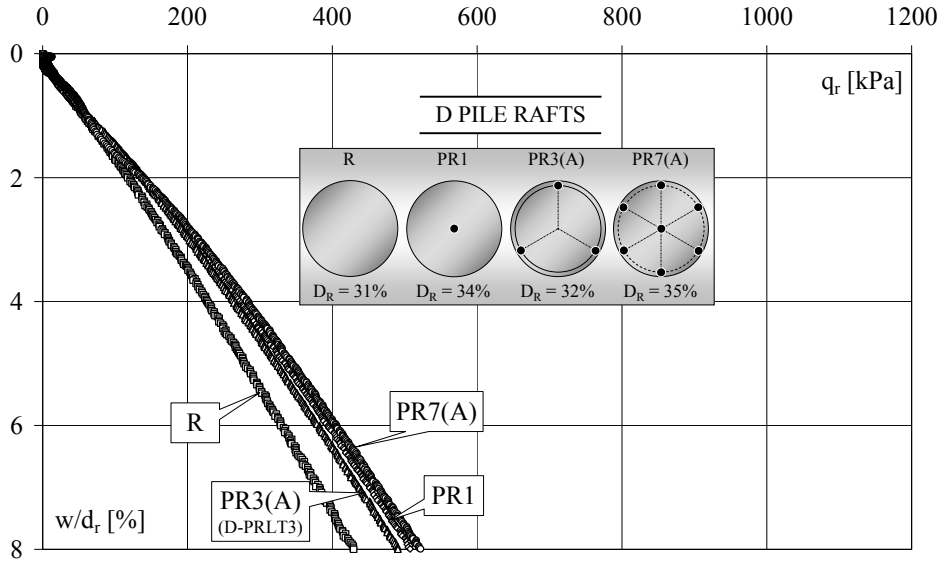

Figure 4.43. Pressure directly transmitted by the raft to the soil q_r vs. the raft relative settlement w/d_r for the D pile rafts.

- At larger settlements than the yielding value, the steady increase in the stress q_t carried by the piled rafts is mostly transmitted to the soil (Figures 4.39 and 4.45, 4.43 and 4.46) and the foundation stiffness begins to be controlled by that of the raft–soil contact. However, once the piles have reached their limit capacity, Q_p still increases slightly as the raft settlement increases, due to the increase in the vertical and radial stresses acting on the pile shaft produced by the pressure transmitted via the soil–raft contact, q_r ("$\Delta\sigma'_r$ effect" described in Sections 4.3 and 4.4). Accordingly, even at large settlements, the piled raft tangent stiffness values are larger than the values observed for the unpiled raft R.

- In the ND pile rafts, the pile group yielding load, Q_{py}, (see Figure 4.38) results to be approximately proportional to the number of piles in models PR3(A), PR3(a), PR7(A) and PR7(a) (i.e. $Q_{py,PR3(A)} \approx 3Q_{py,PR1}$, $Q_{py,PR3(a)} \approx 3Q_{py,PR1}$, $Q_{py,PR7(A)} \approx 7Q_{py,PR1}$ and $Q_{py,PR7(a)} \approx 7Q_{py,PR1}$), while in PR13 $Q_{py,PR13} > 13Q_{py,PR1}$. In the D pile rafts, the pile group limit load, Q_{py} (see Figure 4.42) is proportional to the number of piles in model PR3(A), while in PR7(A), $Q_{py,PR7(A)} > 7Q_{py,PR1}$. These results reflect the behaviour of the individual piles analysed in Sections 4.4.1 and 4.4.2: the bearing capacity of each pile in the group in the models ND PR13 and D PR7(A) results to be significantly higher than that of the single pile beneath the raft, due to the confinement effect exerted by the neighbouring piles and, but only for the D piles, also due to the soil densification and radial stress increase produced by the pile jacking.

- In the ND PR7(A), PR7(a) and PR13 models, the pile group tangent stiffness is affected by interactions of the pile in the group, at smaller settlement than the yielding value.

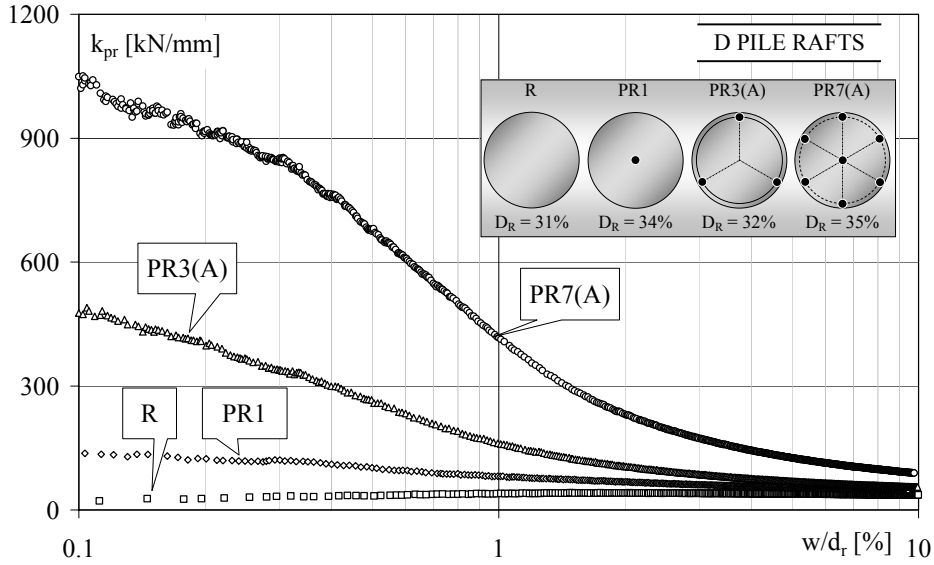

Figure 4.44. D pile raft stiffness k_{pr} vs. the raft relative settlement w/d_r. Prototype scale.

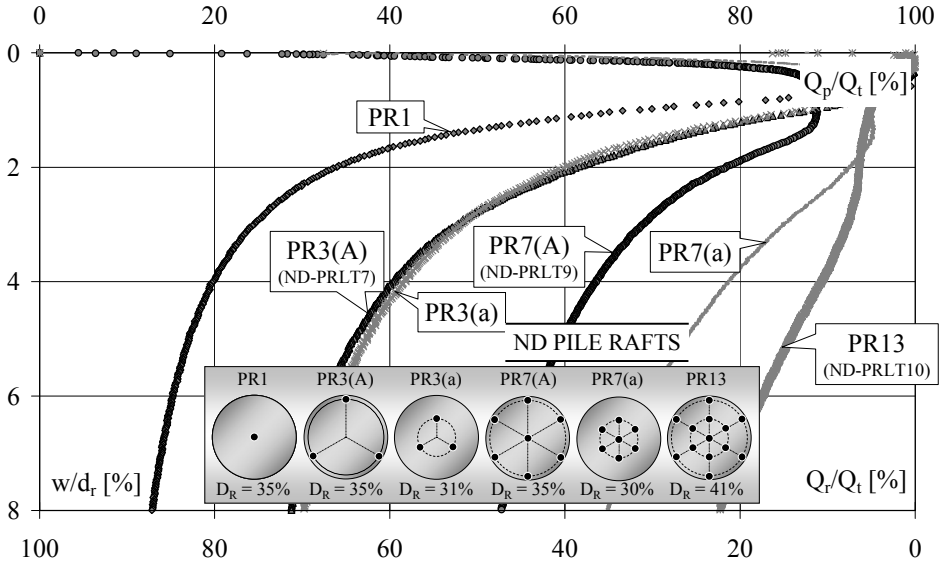

Figure 4.45. Load sharing mechanism for the ND pile rafts.

- Figure 4.43 shows that the q_r curves of the D pile rafts are almost linear; at settlement $w/d_r < 2\%$ they are approximately superimposed over the R curve, while at larger w/d_r, the load carried by the soil is slightly higher in the piled raft than in the unpiled raft. This would seem to suggest that the displacement field induced by the piles in the soil does not influence the stiffness of the raft to any great extent. As for the piled rafts with the ND piles (Figure 4.39), the q_r curves of models PR1, PR3(A) and PR7(A) are more scattered than the analogous D pile raft curves, and they are characterised by an initial non linearity, probably due to a modest misaligning of the pile heads with respect to the sand surface and to a non uniform contact between the raft and the soil, which cause a minor transfer of the applied load from the raft to the soil at the initial loading stage. However, at $w/d_r > 2\%$, the curves approach the R curve, confirming what was observed for the D pile raft models, i.e. the negligible effect of the raft–pile interaction on the raft transfer mechanism. In the PR7(a) and PR13 models, the q_r curves are remarkably non linear and a lower q_r value is transmitted to the soil: in these models, the displacement fields induced in the soil mass by the very close piles cause a significant decrease in the contact pressure beneath the raft next to the pile shaft.

- The load sharing mechanism between the raft and the piles in the ND pile raft models is illustrated in Figure 4.45, where the ratios, Q_p/Q_t and Q_r/Q_t are plotted versus w/d_r. The Figure illustrates that the share of the total applied load transmitted to the soil (Q_r/Q_t ratio) decreases as the number of piles increases. Taking the value $w/d_r = 1.5\%$ as reference settlement, the computed values of Q_r/Q_t are 55% for PR1, 30% for both PR3(A) and PR3(a) and 15% for PR7(A); modest or even negligible values have been obtained for PR7(a) and PR13. As

for the D pile rafts (Figure 4.46), in a similar ways to what has been observed for the ND piles, Q_r/Q_t decays as the number of piles increases. At the settlement value w/d_r = 1.5%, the magnitude of Q_r/Q_t is 64% for PR1, 37% for PR3(A) and 14% for PR7(A).

- The piled raft efficiency ζ depends on the number and type of piles and on their limit load. As shown in Figures 4.47 and 4.48, which report the ζ curves of the ND and the D pile rafts, ζ results to be almost constant before the pile group limit load is reached, then ζ decays as q_t increases; comparing the values of ζ for the same number of piles, the ND piles are less effective as settlement reducers than the D piles. In order to achieve $\zeta > 0.5$ over the whole q_t range considered, at least 3 D piles or 7 ND piles are necessary. The piled raft with 7 D piles and that with 13 ND piles have about the same efficiency for $q_t \leq$ 530 kPa, $\zeta \approx 0.95$, (the pile group yielding load has not been reached).

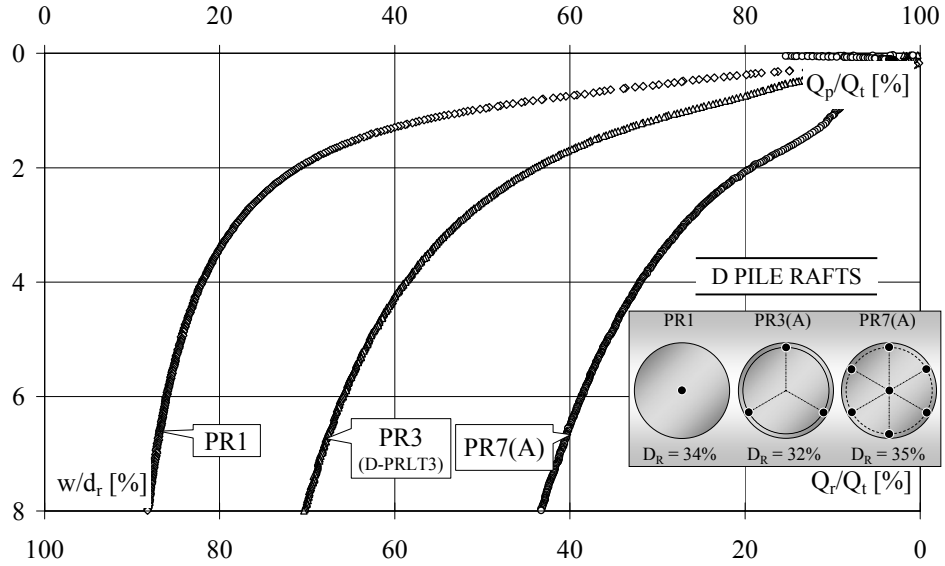

Figure 4.46. Load sharing mechanism for the D pile rafts.

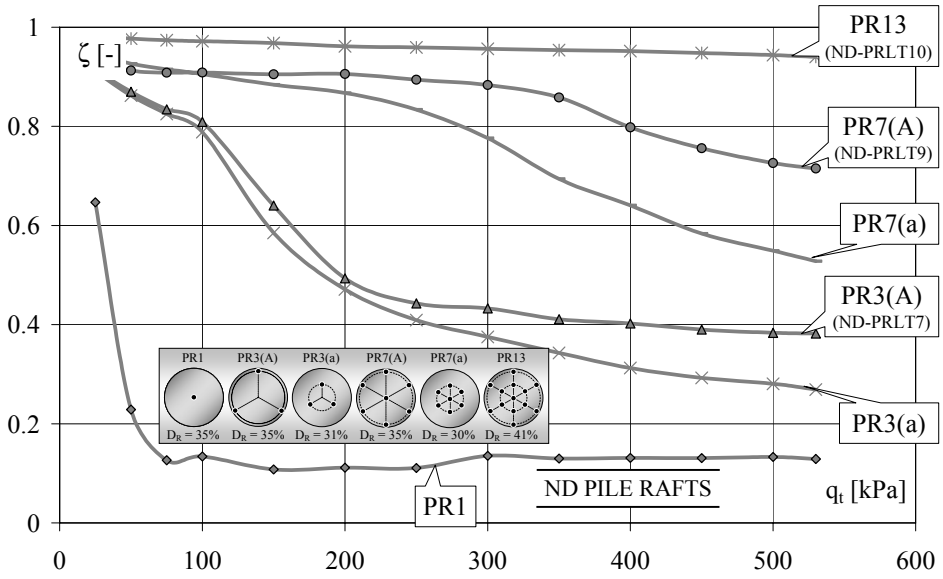

Figure 4.47. Settlement efficiency ζ for the ND pile rafts.

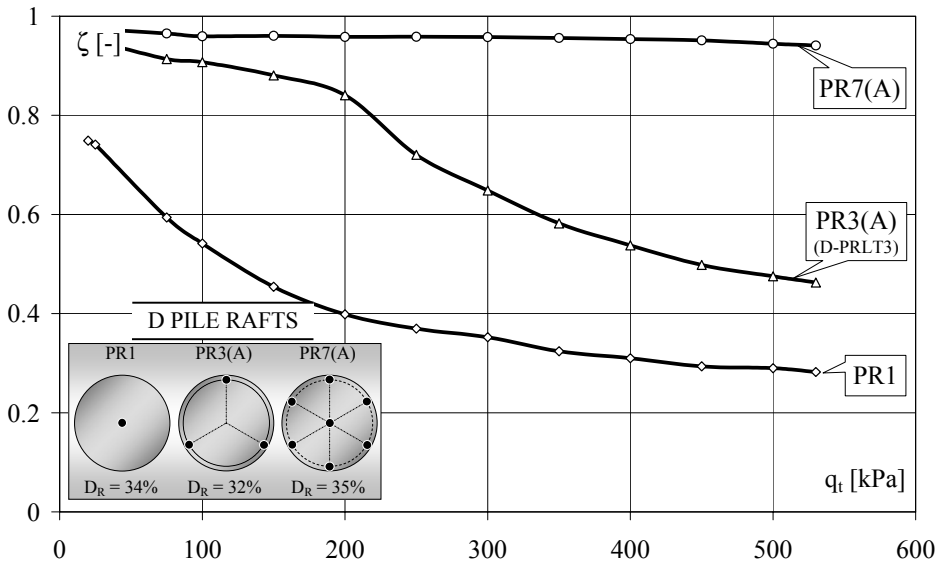

Figure 4.48. Settlement efficiency ζ for the D pile rafts.

Chapter 5

Piled raft bearing capacity and stiffness

5.1 Introduction

The results of centrifuge tests performed on piled raft models are analysed in this chapter in terms of bearing capacity and stiffness.

The piled raft *bearing capacity* has been examined according to the load efficiency method proposed by Phung (1993) and the following quantities have been compared, at the same settlement level:

i) the total, shaft and base resistances of the average pile of a piled raft with the analogous resistances of an isolated single pile;
ii) the total load per pile within a piled raft with the total capacity of an isolated single pile;
iii) the load carried by the raft within a piled footing with the load carried by an unpiled raft;
iv) the total load carried by a piled raft with the load carried by an unpiled raft.

The piled raft *stiffness* has been analysed by comparing the values obtained from centrifuge tests with those evaluated through the simplified method proposed by Randolph (1983, 1994), which allows the overall stiffness of a piled raft foundation to be calculated thorough the

estimation of the interaction effects between its component elements (raft and piles).

The results of the following tests have been analysed in this chapter (see Figures 3.15 and 3.16 and Table 3.7):

- unpiled raft: test URLT0 – R model;
- ND isolated pile: test ND-PLT6 – IP model;
- ND piled rafts: tests ND-PRLT 5, 7, 9, 10, 12, 13 – models PR1, PR3(A), PR3(a), PR7(A), PR7(a), PR13;
- D isolated pile: test D-PLT3 – IP model;
- D piled rafts: tests D-PRLT 1, 3, 4 – models PR1, PR3(A) and PR7(A).

5.2 Load efficiency and piled raft bearing capacity

The concept of *group efficiency* was originally used to compare the ultimate bearing capacity of a free–standing pile group with that of an isolated single pile, under equal soil conditions, in order to highlight the effect of the pile–pile interactions on the group ultimate capacity [Kishida and Meyerhof (1965), Vesic (1969)]. Many researchers have used the same concept for piled footings; Phung (1993) defined several *load efficiencies* for piled footings with respect to isolated piles and shallow foundations under equal soil conditions, in order to highlight the pile–pile and pile–raft interactions within a piled raft. Load efficiencies should be related to the displacement rather than to the ultimate loads, particularly when dealing with piled raft foundations, where the interaction mechanisms between the soil, piles and raft are progressively

mobilised and a gradual load redistribution take place with increasing displacements.

Efficiency function ξ_1 compares the behaviour of an individual pile belonging to a free–standing pile group with that of an isolated piled at the same settlement level; it therefore shows the effects of the pile–pile interactions:

$$\xi_1(w/d_r) = (Q_{p,FG}/n)/Q_{p,IP} \quad [-] \quad (5.1)$$

where:

n = number of piles [-];

$Q_{p,FG}$ = load on a free–standing pile group [F];

$Q_{p,IP}$ = load on a single isolated pile [F].

Efficiency ξ_2 compares the behaviour of an individual pile belonging to a piled raft with that of an isolated pile at the same settlement level, hence it shows the total effects of both the pile–pile and pile–raft interactions on the pile behaviour:

$$\xi_2(w/d_r) = (Q_{p,PR}/n)/Q_{p,IP} \quad [-] \quad (5.2)$$

where:

$Q_{p,PR}$ = load carried by the piles in a piled raft [F].

Efficiency function ξ_3 compares a single pile–raft unit with an isolated pile at the same settlement level, and therefore shows the effects of the pile–pile and pile–raft interactions on the piled raft capacity:

$$\xi_3(w/d_r) = (Q_{t,PR}/n)/Q_{p,IP} \quad [-] \quad (5.3)$$

where:

$Q_{t,PR}$ = total load on a piled raft [F].

Comparing the share of the total load carried by the raft in a piled footing with the load carried by the corresponding unpiled raft at the same settlement level, efficiency function ξ_4 shows the influence of the pile–raft interactions on the raft behaviour:

$$\xi_4(w/d_r) = Q_{r,PR}/Q_{r,UR} \quad [-] \quad (5.4)$$

where:

$Q_{r,PR}$ = load carried by the raft in a piled raft [F];

$Q_{r,UR}$ = load on an unpiled raft [F].

Finally, efficiency function ξ_5 compares the total load carried by the piled footing with the load carried by the unpiled raft, at the same settlement level, therefore it expresses the contribution of the raft to the piled raft capacity.

$$\xi_5(w/d_r) = Q_{t,PR}/Q_{r,UR} \quad [-] \quad (5.5)$$

The load efficiencies ξ_2, ξ_3, ξ_4 and ξ_5 obtained from the performed centrifuge tests are presented in this section; the loads acting on the piled rafts and on their bearing elements are compared with the loads carried by the isolated pile and by the unpiled raft, at the same settlement level. Efficiency ξ_2 has been subdivided into two components, the tip and shaft efficiencies, i.e.:

$$\xi_{2S}(w/d_r) = (Q_{S,PR}/n)/Q_{S,IP} \quad [-] \quad (5.6)$$

$$\xi_{2B}(w/d_r) = (Q_{B,PR}/n)/Q_{B,IP} \quad [-] \quad (5.7)$$

where:

$Q_{S,PR}$ = total shaft resistance of the piles in a piled raft [F];

$Q_{B,PR}$ = total base resistance of the piles in a piled raft [F];

$Q_{S,IP}$ = shaft resistance of the isolated pile [F];

$Q_{B,IP}$ = base resistance of the isolated pile [F].

5.2.1 ND pile rafts – load efficiency functions ξ_2 and ξ_3

The ξ_2 functions (Eq. 5.2) evaluated for the ND pile rafts with respect to the ND isolated pile, are plotted in Figure 5.1. In Figures 5.2 and 5.3, the ξ_2 curves have been subdivided into the two components, ξ_{2S} = shaft efficiency of the group (Eq. 5.6) and ξ_{2B} = base efficiency of the group (Eq. 5.7). Figure 5.4 reports the ξ_3 (Eq. 5.3) curves for the same tests.

Efficiency ξ_2 of the group of piles results to be larger than unity over almost the whole range of investigated settlements for all the ND pile raft models analysed, and it has a tendency to increase with increasing settlement. Only at very small settlements (i.e. $w/d_r < 0.5\%$), where the ND piles are influenced by the softening effect of the pile–pile interactions, are the ξ_2 values of all the models (except PR1) < 1 (see Figures 4.7, 4.12, 4.16, 4.20 and 4.24).

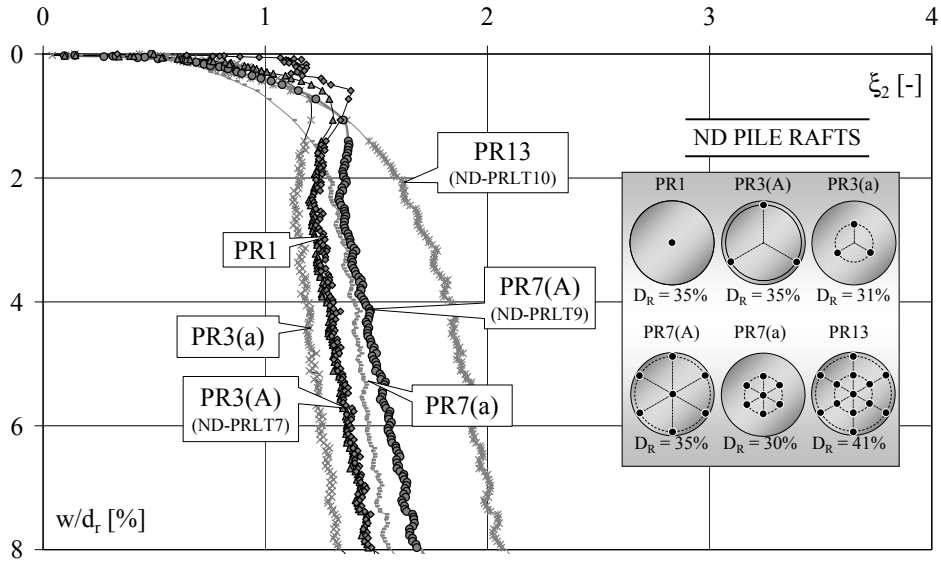

Figure 5.1. Load efficiency ξ_2 for the ND pile rafts.

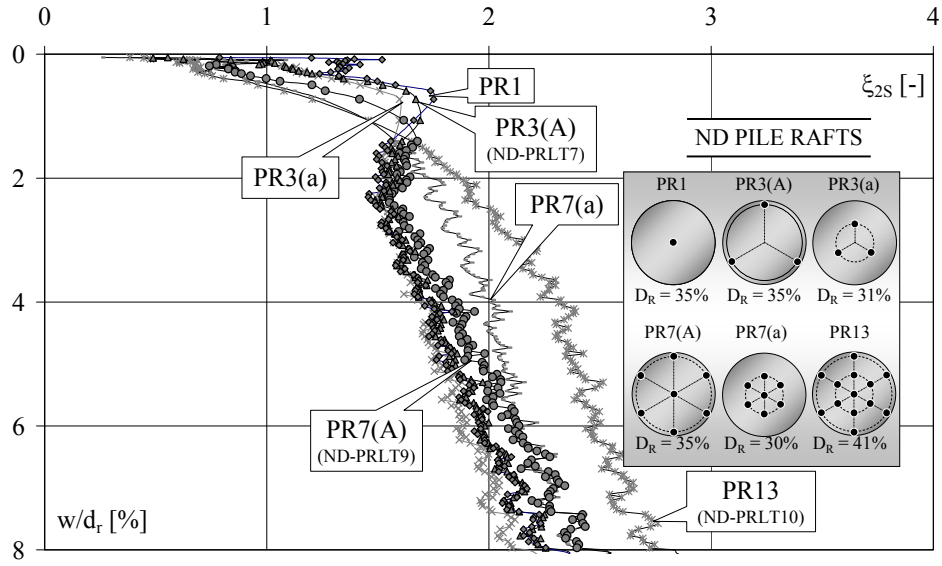

Figure 5.2. Load efficiency ξ_{2S} for the ND pile rafts.

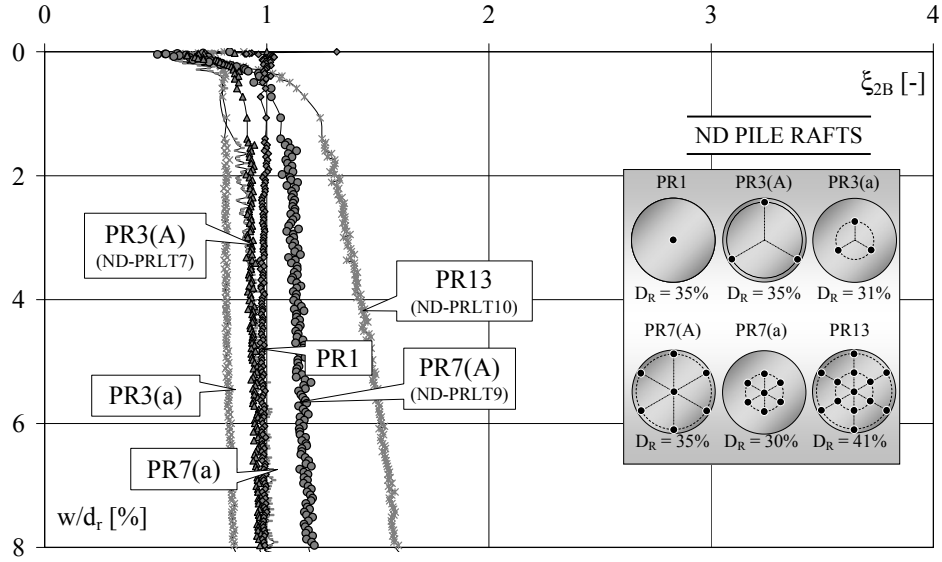

Figure 5.3. Load efficiency ξ_{2B} for the ND pile rafts.

Thus, the ξ_2 values of the ND PR1 model increase from ≈ 1, at the beginning of the test, to ≈ 1.5 at w/d_r = 8%. The ξ_2 values of the other ND

models increase from slightly lower values than unity, at $w/d_r < 0.5\%$, to values that are even higher than 1.5 (PR7(A) and PR13) at $w/d_r = 8\%$.

The ξ_{2S} curves assume higher values than unity at $w/d_r > 0.5$. The ξ_{2S} curves of the PR1, PR3(A) and PR3(a) groups experience a peak (when the piles mobilise the shear stress peak values), while the ξ_{2S} values of the PR7(A), PR7(a) and PR13 groups increase progressively. At settlement $w/d_r > 1.5\%$, the ξ_{2S} value of all the models increases almost linearly, from $\approx 1.5 \div 1.9$ at $w/d_r = 1.5\%$, to $\approx 2.2 \div 2.8$ at $w/d_r = 8\%$.

The higher shaft efficiency than unity of the ND piles can be attributed to the "$\Delta\sigma'_r$ effect", which enhances the pile shaft capacity; for the PR7(A), PR7(a) and PR13 groups, the ξ_{2S} values > 1 can also be attributed to the confinement effect exerted by the neighbouring piles, which improves the shaft capacity even more.

As far as the base efficiency is concerned, ξ_{2B} is approximately equal to unity in all the ND pile groups, except in PR13, for which ξ_{2B} ranges from 1, at the beginning of the test, to 1.6 at $w/d_r = 8\%$. As shown in Section 4.3, the raft pressure on the soil surface in the performed tests produced negligible effects on the ND pile end bearing capacity, (Figure 4.7); however, interactions between pile tips have been observed in a close spaced pile group, such as the PR13 group, and these interactions cause a higher base capacity than that of the isolated pile (see Figure 4.24).

As for load efficiency ξ_3, which compares the load on a single pile–raft unit with the load carried by an isolated pile, Figure 5.4 shows that ξ_3 increases almost linearly with increasing settlement for each ND pile raft model, from values ≈ 1 at the beginning of the tests to significantly higher values than unity at large w/d_r. On the other hand, ξ_3 decreases with an increasing number of piles, since, as shown in Section 4.5

(Figure 4.45), at a given raft settlement, the raft contribution to the piled raft capacity decreases as the number of piles increases. At a given pile number, ξ_3 is slightly lower for the smaller pile spacing.

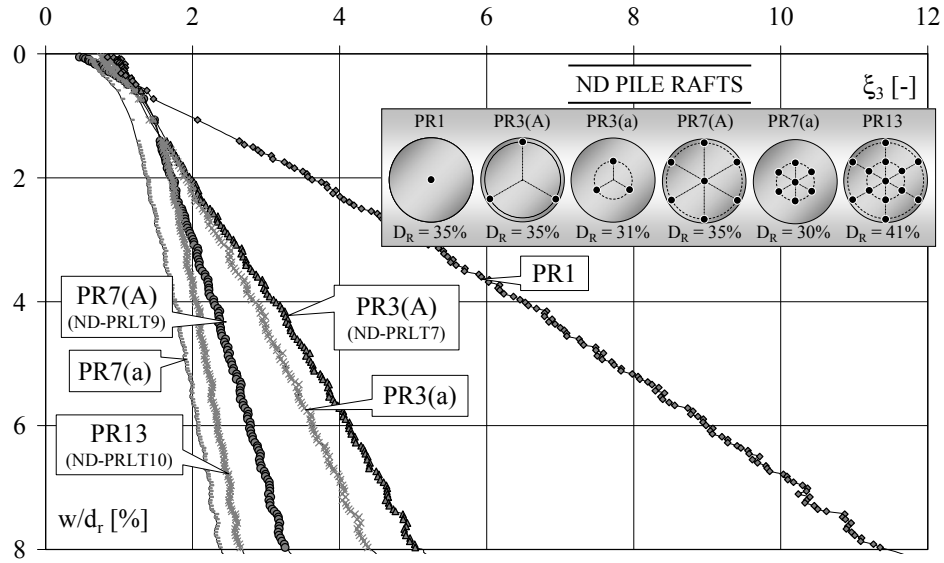

Figure 5.4. Load efficiency ξ_3 for the ND pile rafts.

5.2.2 ND pile rafts – load efficiency functions ξ_4 and ξ_5

Figures 5.5 and 5.6 report the ξ_4 and ξ_5 efficiency functions (Eqs. 5.4 and 5.5) evaluated for the ND pile rafts with respect to the unpiled raft.

The ξ_4 values of the PR1, PR3(A), PR3(a) and PR7(A) models increase, as the settlement increases, up to a relative settlement $w/d_r \approx 4\%$, then they approach unity, indicating that, at large settlements, the effects of the raft–pile interactions on the raft capacity are negligible. The lower efficiency than unity at $w/d_r < 4\%$ is due to the non uniform contact between the raft and the soil at the initial stage of the tests, which caused a lower raft contribution to the foundation capacity (see Figure 4.39).

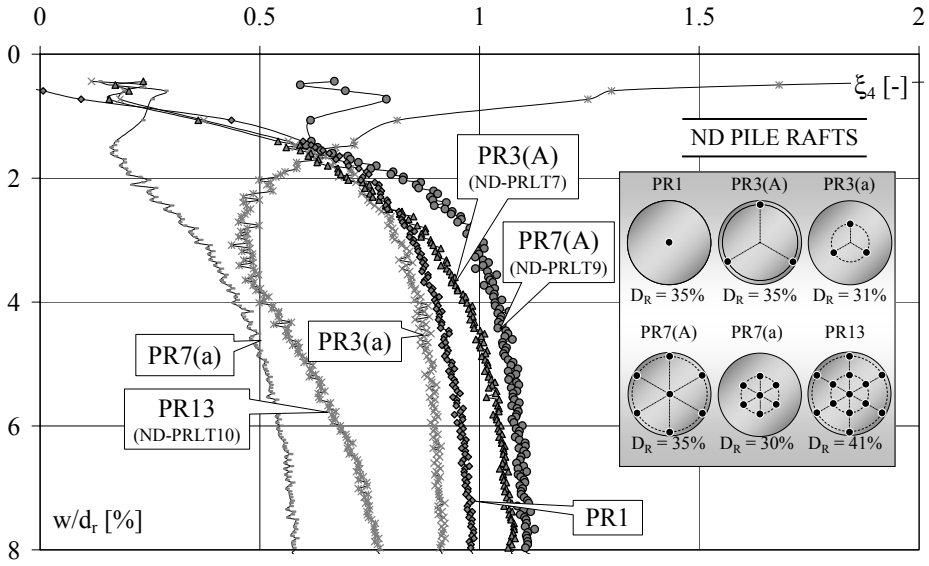

Figure 5.5. Load efficiency ξ_4 for the ND pile rafts.

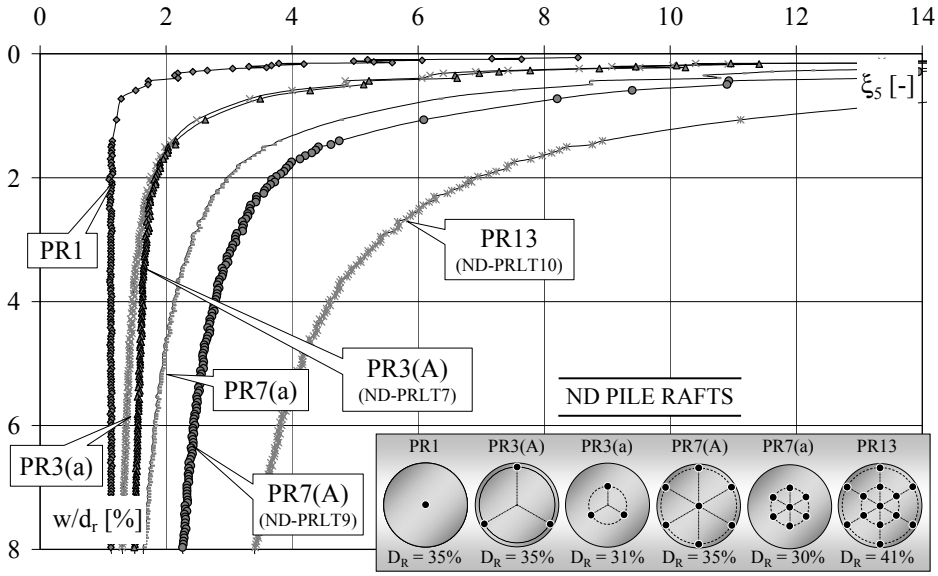

Figure 5.6. Load efficiency ξ_5 for the ND pile rafts.

The ξ_4 values of the PR7(a) and PR13 models are significantly lower than unity over the whole settlement range that has been analysed, indicating that, in close spaced pile groups, the pile–raft interaction

effects on the raft capacity cause a decrease in the contact pressure beneath the raft next to the pile shaft.

The ξ_5 curves reported in Figure 5.6 have the same shape for all the ND pile rafts: at settlement $w/d_r < 1\% \div 1.5$, i.e. before the piles reach their limit load and the applied load is carried above all by the piles, ξ_5 assumes very high values and then it drops rather quickly towards the steady values that are reached at large settlements. The steady ξ_5 values mainly depend on the amount of the raft contribution to the piled raft capacity: the higher the raft contribution (as in PR1 with respect to PR13, see Figure 4.45), the lower the ξ_5 steady values reached at large settlements.

5.2.3 D pile rafts – load efficiency functions ξ_2 and ξ_3

The ξ_2 load efficiency functions (Eq.5.2) evaluated for the D pile rafts, with respect to the D isolated pile, are plotted in Figure 5.7. In Figures 5.8 and 5.9, the ξ_2 curves have been subdivided into the two components, ξ_{2S} = shaft efficiency of the group (Eq.5.6) and ξ_{2B} = base efficiency of the group (Eq.5.7). The load efficiency ξ_3 (Eq. 5.3) obtained from the same tests is plotted in Figure 5.10.

For all the analysed D pile rafts, the total efficiency ξ_2 of the pile group is larger than unity over the whole range of investigated settlements, and it has a tendency to increase with increasing settlement. The ξ_2 values of the PR1 and PR3(A) groups increase almost linearly from 1.1, at the initial stage of the tests, to ≈ 1.5 at $w/d_r = 8\%$. In the PR7(A) group, ξ_2 ranges from 1.2, at small settlements, to 2 at $w/d_r = 8\%$. The ξ_2 values of the D PR7(A) group are similar to those of the ND PR13 group.

In all the D pile groups, the ξ_{2S} values are higher than unity. At settlement $w/d_r \approx 1\% \div 1.2\%$, the ξ_{2S} curves reach a peak, in

correspondence to the mobilisation of the pile shaft friction peak value, and then they increase almost linearly with increasing w/d_r.

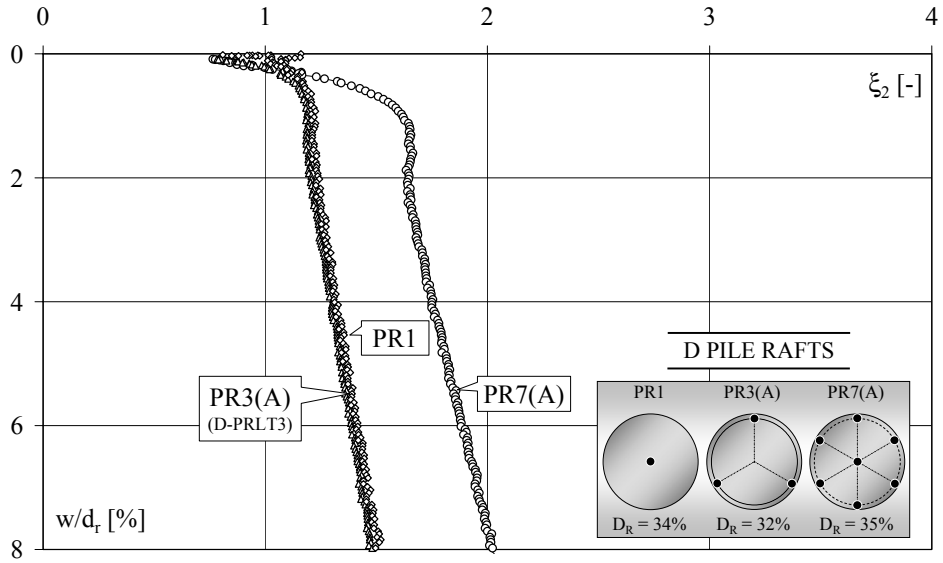

Figure 5.7. Load efficiency ξ_2 for the D pile rafts.

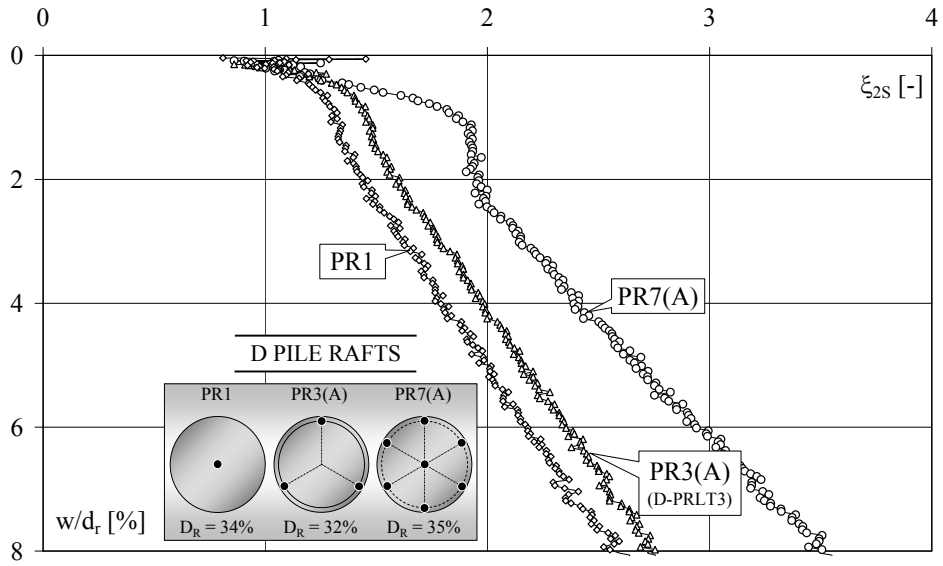

Figure 5.8. Load efficiency ξ_{2S} for the D pile rafts.

The higher shaft efficiency than unity of the D piles can be attributed to the "$\Delta\sigma'_r$ effect", which enhances the pile shaft capacity and, as far as the PR7(A) group is concerned, to the confinement effect exerted by the neighbouring piles, which further improves the shaft capacity. Moreover, the ξ_{2S} values of the D PR7 group are greater than those of the ND PR7 group, due to the effect of the sand compaction produced by jacking, which noticeably enhances the shaft capacity of all the piles in the group (see Figure 4.34).

The base efficiency, ξ_{2B} is roughly equal to unity in PR1 and PR3(A) and it is ≈ 1.35 in PR7(A). As seen for the ND pile rafts, the contact pressure of the raft on the soil surface in the performed tests has no significant influence on the D pile end bearing capacity (see Figure 4.9); the high base efficiency of the PR7(A) group is mainly due to the effect of the compacted sand zones under the tips produced by the pile jacking, which leads to an improved base capacity (see Figure 4.33).

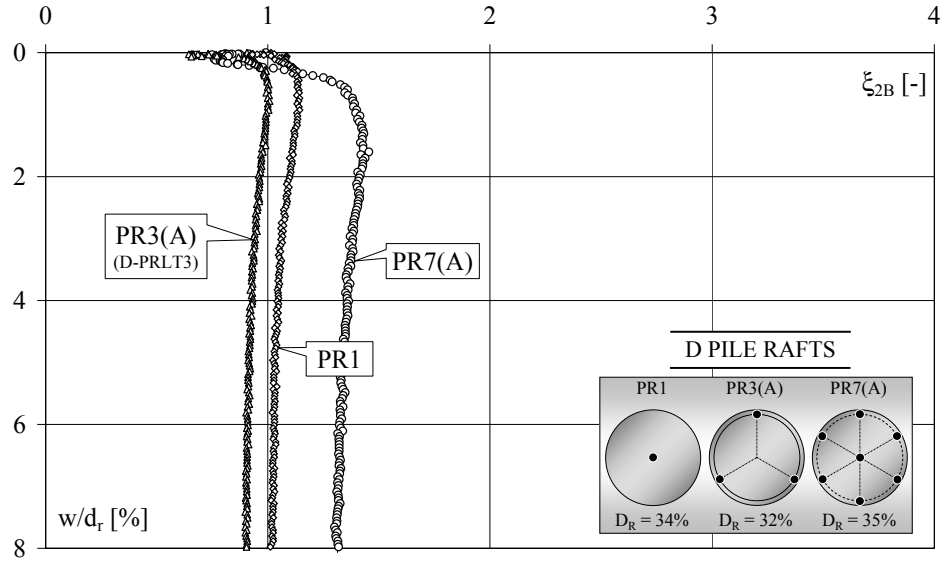

Figure 5.9. Load efficiency ξ_{2B} for the D pile rafts.

The ξ_3 load efficiency function of the D pile rafts, plotted in Figure 5.10 vs. the raft relative settlement, w/d_r, increase almost linearly with increasing settlements, from values ≈ 1 at the initial loading stage to significantly higher values than unity at large w/d_r. At a given raft settlement, ξ_3 decreases with an increasing number of piles, since the raft contribution to the piled raft capacity decreases as the number of piles increases (Figure 4.46).

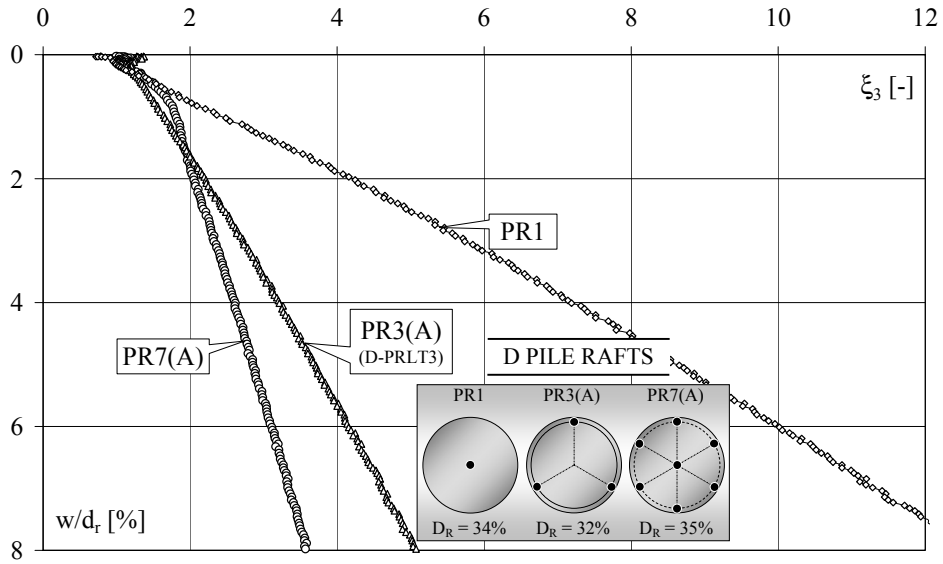

Figure 5.10. Load efficiency ξ_3 for the D pile rafts.

5.2.4 D pile rafts – load efficiency functions ξ_4 and ξ_5

Figures 5.11 and 5.12 report the ξ_4 and ξ_5 efficiency function (Eqs. 5.4 and 5.5) evaluated for the D pile rafts with respect to the unpiled raft.

The ξ_4 curves of all the D pile rafts tend to a constant value ($\xi_4 \approx 1.15$), which is reached at w/d_r = 1.5%÷2% (see also Figure 4.32), indicating negligible effects of the pile–raft interactions on the raft capacity.

The ξ_5 curves shown in Figure 5.12 have the same shape as those observed for the ND pile rafts: at settlement w/d_r < 1% ÷ 1.5%, ξ_5 assumes very high values and then drops rather quickly towards steady

values which are reached at large settlements. The steady ξ_5 values depend on the contribution amount of the raft to the piled raft capacity: the higher the raft contribution (as in PR1, see also Figure 4.46), the lower the ξ_5 steady values reached at large settlements.

The ξ_5 efficiency values of the D pile rafts are higher than those of the ND pile rafts for the same test layout.

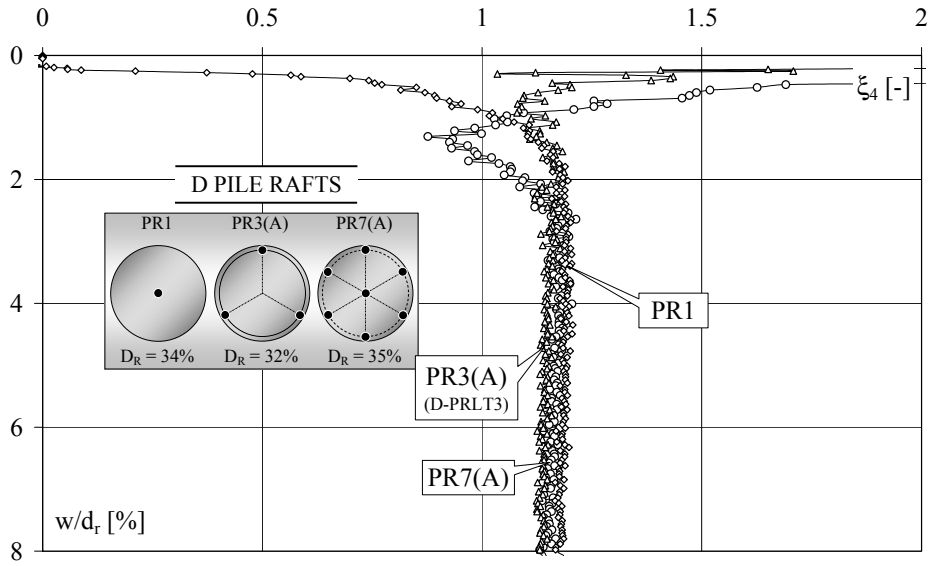

Figure 5.11. Load efficiency ξ_4 for the D pile rafts.

5.2.5 Piled raft bearing capacity

As proposed by Phung (1993), the total capacity of a piled raft may be calculated as follows:

$$Q_{t,PR} = n\,(\xi_{2S}\cdot Q_{S,IP} + \xi_{2B}\cdot Q_{B,IP}) + \xi_4 Q_r \qquad [F] \qquad (5.8)$$

where:

n = number of piles [-];

ξ_{2S}, ξ_{2SB} = shaft, base efficiency of an individual pile in a piled raft [-];

$Q_{S,IP}$, $Q_{B,IP}$ = shaft and base capacities of the isolated pile [F];

ξ_4 = efficiency of the raft in a piled footing [-];

Q_r = unpiled raft capacity [F].

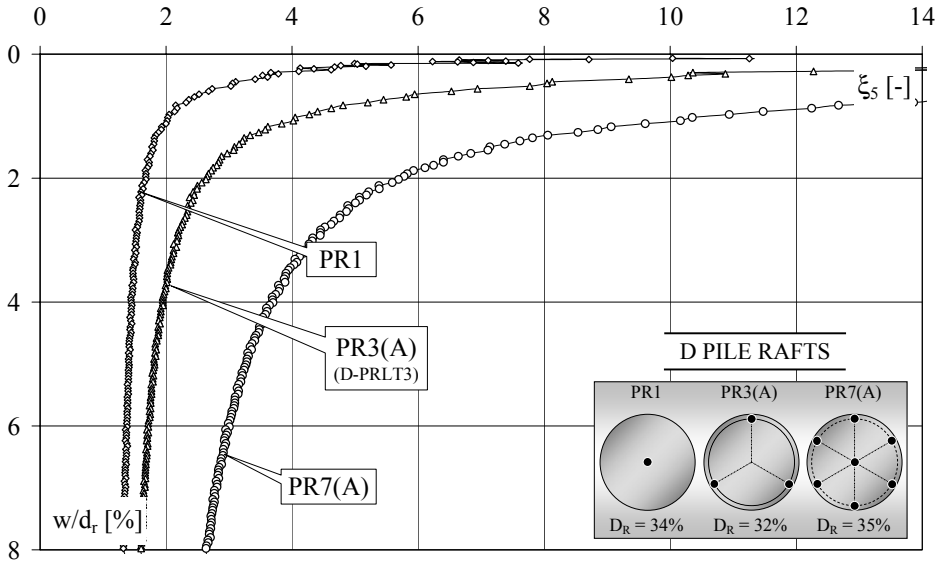

Figure 5.12. Load efficiency ξ_5 for the D pile rafts.

The efficiencies ξ_{2S} and ξ_{2B} consider the pile–pile and the pile–raft interaction effects on the pile shaft and base capacities.

In the performed tests, the influence of the raft on the base capacity was negligible, but the base efficiency ξ_{2B} can assume higher values than unity due to the interaction effect between the pile tips and, in the case of jacked piles, due to the effects of the soil densification produced by the pile installation (see PR13 in Figure 5.3 and PR7 in Figure 5.9).

The performed tests have shown that the values of efficiency ξ_{2S} depend on many factors.

In the case of ND piles, at very small settlement ($w/d_r < 0.5\%$), negative group effects, due to the superimposition of the individual pile displacement fields, can produces a decrease in the shaft friction mobilisation rate, which leads to lower values of ξ_{2S} than unity. At larger settlements, ξ_{2S} can result to be higher than unity due to the pile–raft interaction effects ("$\Delta\sigma'_r$ effect"), and shows a tendency to increase as

the number of piles increases, due to the confinement effects between the neighbouring piles.

In the case of D piles, the shaft efficiency can be significantly higher than unity, even at small settlements, due to the superimposition of several effects: the "$\Delta\sigma'_r$ effect", confinement effects between the neighbouring piles and the soil densification effect produced by the jacking of groups of piles.

As far as the load efficiency ξ_4, which represents the pile–raft interaction effect on the raft capacity, is concerned, the centrifuge test results as shown in Figures 5.5 and 5.11 suggest that ξ_4 can be assumed equal to unity in small groups of piles, while in large groups of piles or in close spaced groups, the raft contribution to the piled raft capacity can be lower than unity.

5.3 Piled raft stiffness

5.3.1 Introduction

Several approaches have been proposed in recent years to analyse piled raft foundations: from simplified analytical methods involving a simple constitutive soil model and a simplified soil profile [e.g. Poulos and Davis (1980), Randolph (1983), Randolph (1994), Franke et al. (1994)], to very complex procedures employing three–dimensional finite element or boundary element analyses and more realistic elastic–plastic constitutive soil models [e.g. Katzenbach et al. (1998), Franke et al. (2000), Katzenbach et al. (2000)].

The applicability of complete numerical analyses to real problems is limited, due to the magnitude of the computational resources required for foundations of practical proportions.

Simplified approaches, which rely on the extrapolation of results produced for single pile raft units, from necessity have to incorporate approximations, but they are more practical for the routine design of piled rafts.

Randolph's simplified approach employs a flexibility matrix to combine the individual stiffnesses of a pile group and a raft to derive the overall stiffness of a piled raft. The piles are assumed to be loaded below their failure load; the settlement of each foundation component is expressed as:

$$\begin{Bmatrix} w_p \\ w_r \end{Bmatrix} = \begin{bmatrix} 1/k_p & \alpha_{pr}/k_r \\ \alpha_{rp}/k_p & 1/k_r \end{bmatrix} \begin{Bmatrix} Q_p \\ Q_r \end{Bmatrix} \qquad [L] \qquad (5.9)$$

where:

k_p, k_r = overall stiffness (i.e. load/displacement) of a pile group and of a raft in isolation, respectively [FL^{-1}];

α_{rp}, α_{pr} = interaction factors, that quantify the influence of the pile group on the raft and the influence of the raft on a pile group, respectively [-];

Q_p, Q_r = loads on the piles and on the raft, respectively [F].

According to the reciprocal theorem, the terms on the trailing diagonal of the flexibility matrix must be equal, therefore the interaction factors are related by:

$$\alpha_{pr} = \alpha_{rp} \frac{k_r}{k_p} \qquad [-] \qquad (5.10)$$

Since the (average) settlements of the piles and raft are identical, Eqs. 5.9 and 5.10 allow the overall stiffness of a piled raft, k_{pr} to be calculated as:

$$k_{pr} = \frac{k_p + k_r\left(1 - 2\alpha_{rp}\right)}{1 - \alpha_{rp}^2\left(k_r / k_p\right)} \qquad [FL^{-1}] \qquad (5.11)$$

On the basis of superimposition of the displacement field induced by a single pile and by a circular cap, Randolph (1983) has shown that the interaction factor α_{rp} for a single capped pile (single pile–raft unit) may be approximated by:

$$\alpha_{rp} = 1 - \frac{\ln(b)}{\ln(2r_m / D_p)} \qquad [-] \qquad (5.12)$$

where:

b = ratio of the circular cap diameter to pile diameter D_p [-]

r_m = radius of influence of a pile [L], related to the embedded pile length L_p by [Randolph and Wroth (1978)]:

$$r_m = 2.5 \cdot \rho_s \cdot L_p \cdot (1 - \nu_s) \qquad [L] \qquad (5.13)$$

where:

ρ_s = soil inhomogeneity factor [-];

ν_s = Poisson's ratio of the soil [-].

The value of α_{rp} for pile groups can be calculated by considering a representative single pile–raft unit, where the representative unit has a raft area that is equal to the mean raft area per pile of the complete foundation.

The raft stiffness, k_r, can be estimated via the elastic theory, for example using the Fraser and Wardle (1976) or Mayne and Poulos (1999) solutions. The pile group stiffness, k_p, can also be estimated from the elastic theory, if the single pile stiffness is known and using approaches such as those described by Poulos and Davis (1980) or Fleming et al. (1992).

The approach proposed by Poulos and Davis (1980) and reviewed by Poulos (1989), expresses the increase in settlement Δw of a pile in a group due to interaction, in terms of an interaction factor α (which is the

ratio of Δw to the settlement for a single isolated pile under its own load) and it assumes that Δw may be obtained by superimposition of the values of α of the individual piles in the group. In a group of n piles with the same geometry, the settlement w_k of pile k of the group is given by:

$$w_k = \omega_1 \sum_{j=i}^{n} Q_j \cdot \alpha_{kj} \qquad [L] \qquad (5.14)$$

where:

ω_1 = displacement of a single isolated pile under unit load (i.e. pile flexibility), which can be computed from the elastic theory or derived from a pile load test [$F^{-1}L$];

Q_j = the load on pile j [F];

α_{kj} = interaction factor for pile k due to any other pile j within the group, corresponding to the spacing s_{kj} between piles k and j [-].

The interaction factors have been computed from boundary element analysis and presented by the Authors in graphical form.

Eq. 5.14 can be written for each pile in the group, thus leading to a total of n equations, which, together with the equilibrium equation, can be solved for the cases of: i) a flexible raft and known load on each pile, i.e. non–uniform settlement among the piles; ii) a rigid pile cap and uniform settlement of the piles, i.e. non–uniform distribution of the load in the piles.

5.3.2 Piled raft stiffness from Randolph's approach

In this section, the measured foundation stiffness is compared, for each centrifuge test on ND and D piled raft model, with that computed using Randolph's simplified approach, which is expressed by Eq. 5.11. The measured stiffness values are reported for relative settlements $w/d_r >$

0.1%; smaller measured displacement values have not been considered reliable enough.

The raft stiffness, k_r, introduced into Eq. 5.11, has been estimated on the basis of the results of the unpiled raft centrifuge test. The unpiled raft R exhibited an almost linear load–settlement curve, as shown in Figures 4.37 and 4.41. In Figure 5.13, the measured k_r is plotted at the prototype scale vs. w/d_r; limited scatter of the experimental data around the mean value can be observed. Hence, a constant k_r value has been assumed in the computation, k_r = 37.5 kN/mm.

The pile group stiffness, k_p, has been derived from the ND and D isolated pile load–settlement curves, using the interaction factor approach described by Poulos and Davis (1980). The reference stiffness values obtained from the isolated pile tests, $k_{p,IP}$, are plotted in Figure 5.14 at the prototype scale vs. the pile settlement normalised to the raft diameter, w/d_r.

As suggested by Randolph (1994) and by Mandolini and Viggiani (1997), the interaction factors have only been applied to the elastic component of the settlement of adjacent piles, since the plastic component of settlement is due to localised phenomenon and is not transmitted to the neighbouring piles. The group pile response has been constructed from the softened elastic response of the isolated pile, to which the original plastic displacement of the single isolated pile has been added.

The interaction factors have been computed using the low–strain (far field) elastic Young's modulus, to take into account the small strain level that occurs in the soil between the piles.

Randolph's approach for the computation of k_{pr} has been used up to the settlement required to mobilise the limit shaft capacity of the pile groups.

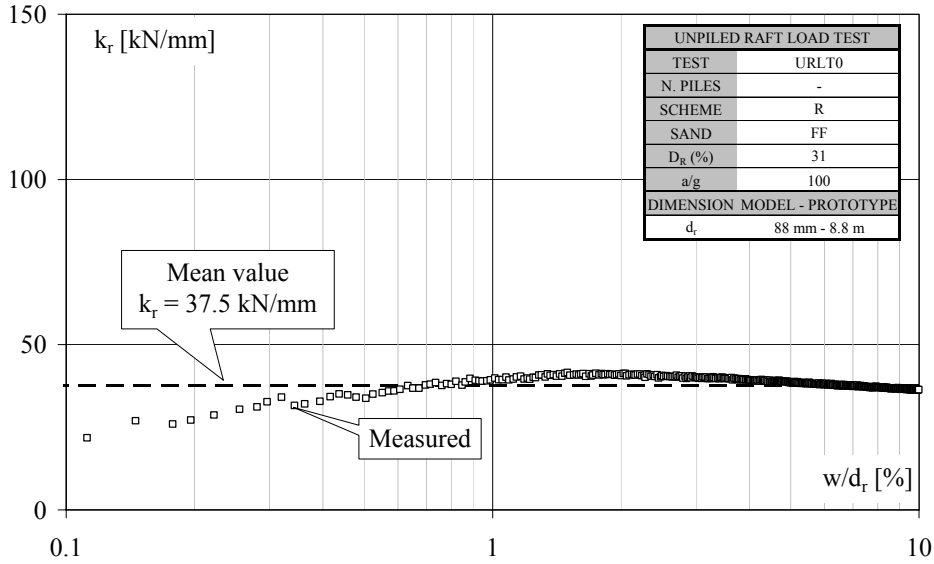

Figure 5.13. Measured unpiled raft (R) stiffness k_r vs. the raft relative settlement w/d_r. Prototype scale.

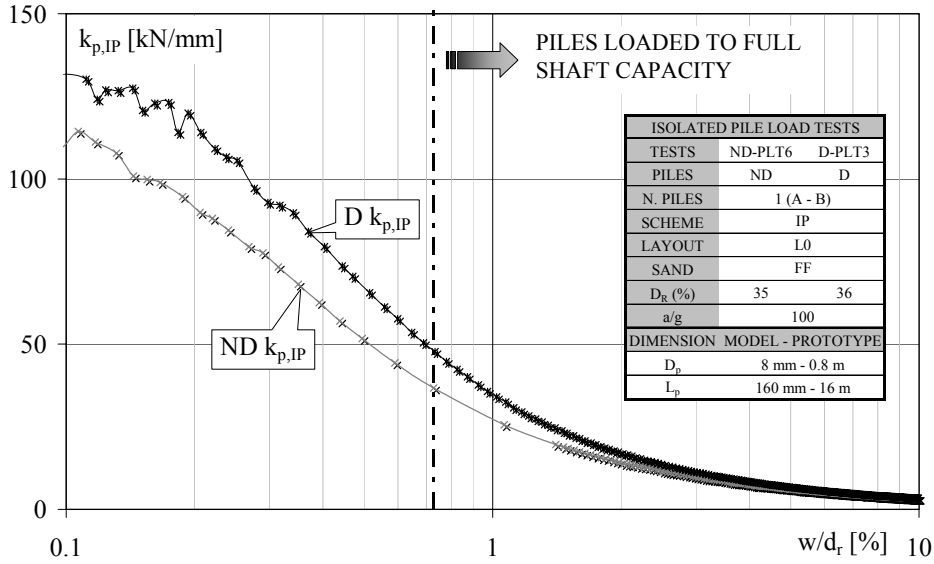

Figure 5.14. Isolated pile measured stiffness $k_{p,IP}$ vs. the pile settlement normalised to the raft diameter w/d_r for the ND and D IP piles. Prototype scale.

For larger applied loads, the piled raft settlement and stiffness have been evaluated following the procedure suggested by Randolph (1983) for piles loaded to full shaft capacity:

- the load carried by the raft has been evaluated as the total applied load less the load carried by the piles when the limit shaft capacity of the group is mobilised (group pile yielding load), i.e. $Q_r = Q_t - Q_{py}$;
- the settlement of the raft has been estimated as a function of the load transferred to the raft (i.e. $w_r = Q_r/k_r$);
- the additional pile contribution to the raft settlement has been obtained by multiplying the settlement at which the group piles mobilise their limit load, by the interaction factor given in Eq. 5.12.

A similar approach has been described by Thorburn et al. (1983).

5.3.1.1 Non displacement pile raft stiffness

Figures 5.15 to 5.20 compare the piled raft stiffness values measured from centrifuge tests on ND pile footings with those computed following the previously described procedure. The k_{pr} curves in the Figures are represented at the prototype scale vs. the raft relative settlement, w/d_r. The Figures also report the measured and computed pile group stiffness, k_p. The computed k_p has been evaluated, up to the settlement required to mobilise the limit shaft capacity of the pile groups, from the ND isolated pile stiffness, $k_{p,IP}$ (ND-PLT6 test, Figure 5.14).

The measured k_{pr} curves reported in Figures 5.15–5.20 are characterised by a progressive stiffness decay. The early values are likely to be slightly underestimated since, at the initial loading stage, the misaligning of the ND pile heads, with respect to the sand surface, caused a non uniform contact between the raft and the soil, i.e. incomplete contribution of the

raft to the foundation overall stiffness at small displacements. Thus the experimental k_{pr} values at small w/d_r are very close to the k_p values.

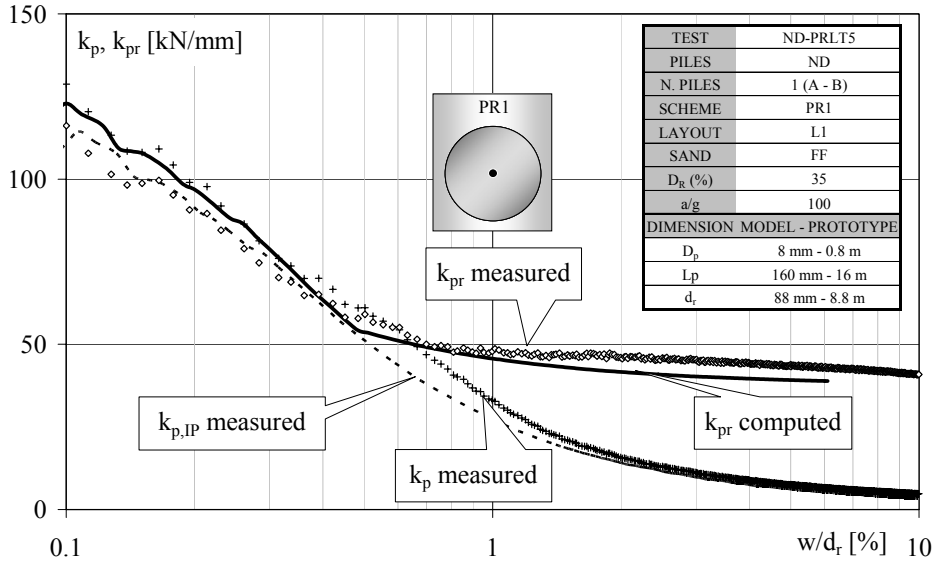

Figure 5.15. Measured and computed overall stiffness k_{pr} and pile group stiffness k_p vs. the raft relative settlement w/d_r for the ND PR1 model. Prototype scale.

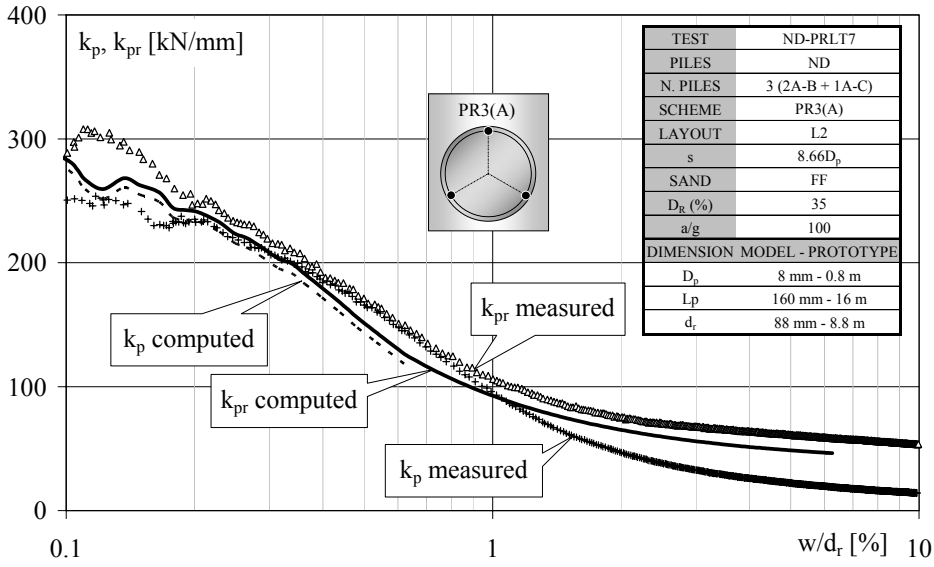

Figure 5.16. Measured and computed overall stiffness k_{pr} and pile group stiffness k_p vs. the raft relative settlement w/d_r for the ND PR3(A) model. Prototype scale.

However, at small settlements, the measured k_{pr} mainly reflect the pile stiffness, thus as the number of piles increases, the foundation stiffness increases; as the pile spacing decreases, the number of piles being the same, the piled raft stiffness decreases.

At larger relative settlement than 1%, the k_{pr} curves tend towards a steady value, which mainly reflects the unpiled raft R stiffness.

As for the computed stiffness, the k_{pr} curves are very close to the k_p computed curves at smaller w/d_r than the value required to mobilise the pile full shaft capacity, indicating a limited contribution of the raft stiffness to the computed stiffness k_{pr}.

For the PR1, PR3(A) and PR3(a) models, the computed curves are in good agreement with the measured ones (Figures 5.15, 5.16 and 5.17, respectively), over the whole settlement range that was analysed. For the PR7(A), PR7(a) and PR13 models (Figures 5.18, 5.19 and 5.20, respectively), the computed k_{pr} values result to be lower than the measured ones, especially at $w/d_r < 1\%$.

The underestimation of the computed k_{pr} for the foundations with 7 and 13 ND piles can mainly be attributed to the underestimation of the computed pile group stiffness, k_p, i.e. to the overestimation of pile interaction factors.

As seen in Sections 4.4.1 and 5.2.1, in the 7- and 13- ND pile rafts, the interactions between the neighbouring piles on one hand produce a decrease in the pile stiffness and on the other an enhanced pile capacity. The latter "positive" effects are likely to partially compensate the former "negative" effects. This compensating effect, which cannot be taken into account in the k_p computations, could explain the underestimation of the computed k_{pr} stiffness.

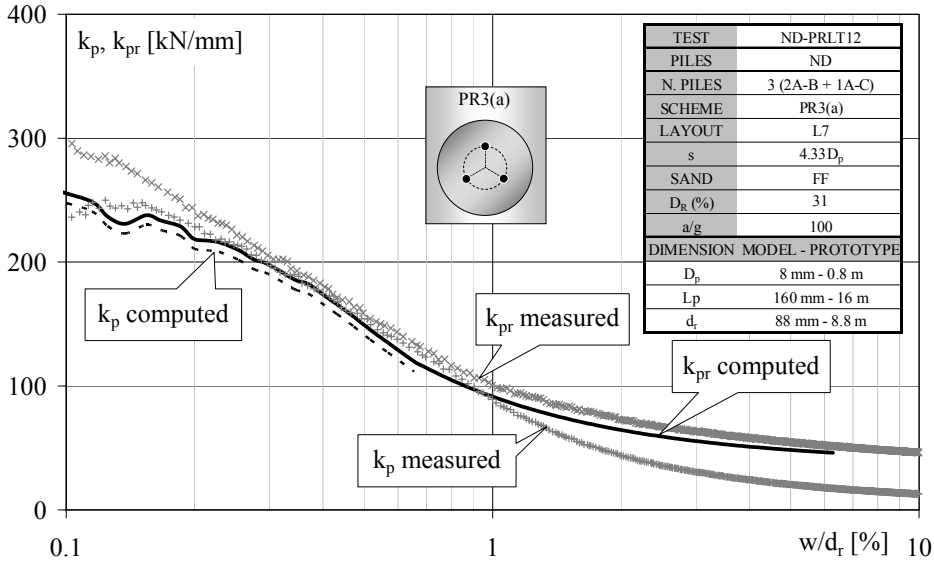

Figure 5.17. Measured and computed overall stiffness k_{pr} and pile group stiffness, k_p vs. the raft relative settlement w/d_r for the ND PR3(a) model. Prototype scale.

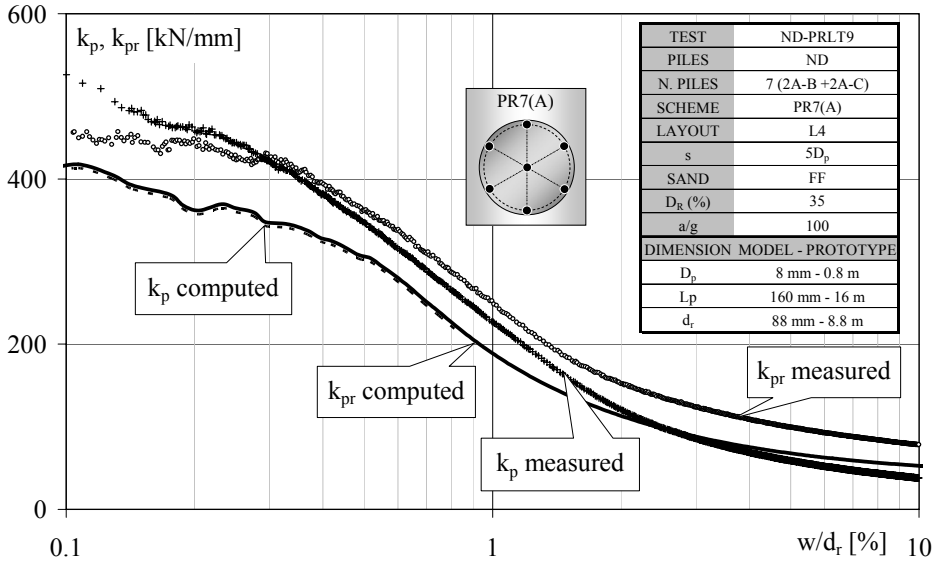

Figure 5.18. Measured and computed overall stiffness k_{pr} and pile group stiffness k_p vs. the raft relative settlement w/d_r for the ND PR7(A) model. Prototype scale.

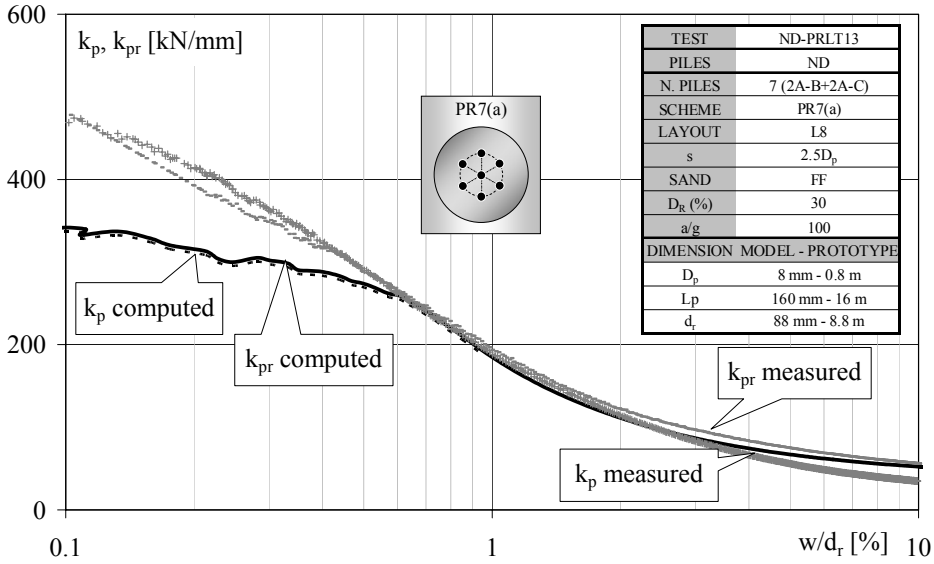

Figure 5.19. Measured and computed overall stiffness k_{pr} and pile group stiffness k_p vs. the raft relative settlement w/d_r for the ND PR7(a) model. Prototype scale.

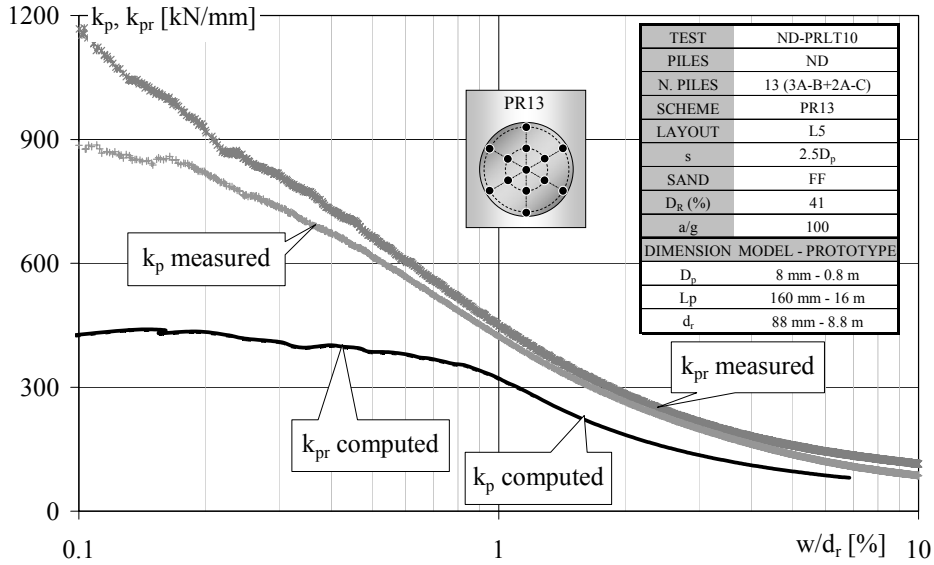

Figure 5.20. Measured and computed overall stiffness k_{pr} and pile group stiffness k_p vs. the raft relative settlement w/d_r for the ND PR13 model. Prototype scale.

5.3.1.2 Displacement pile raft stiffness

Figures 5.21 to 5.23 compare the piled raft stiffness values obtained from centrifuge tests on D pile footings with those computed according to Randolph's procedure. The k_{pr} curves in the Figures are represented at the prototype scale vs. the raft relative settlement, w/d_r. The Figures also report the measured and computed pile group stiffness, k_p. The computed k_p has been evaluated up to the settlement required to mobilise the limit shaft capacity of the pile groups, from the D isolated pile stiffness, $k_{p,IP}$ (D-PLT3 test, Figure 5.14).

As seen for the ND pile rafts, the D pile raft k_{pr} curves are characterised by a progressive stiffness decay. At small settlements, the piled raft stiffness mainly reflects that of the pile group, thus as the number of piles increases, the initial stiffness of the foundations also increases.

At larger settlement than 1%, the k_{pr} curves tend towards a steady value, which mainly reflects the unpiled raft R stiffness.

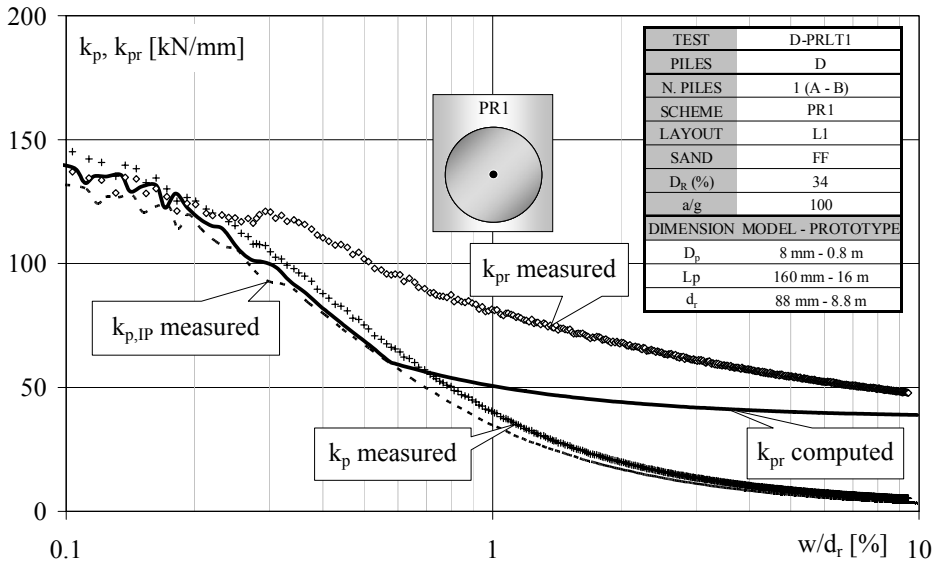

Figure 5.21. Measured and computed overall stiffness k_{pr} and pile group stiffness k_p vs. the raft relative settlement w/d_r for the D PR1 model. Prototype scale.

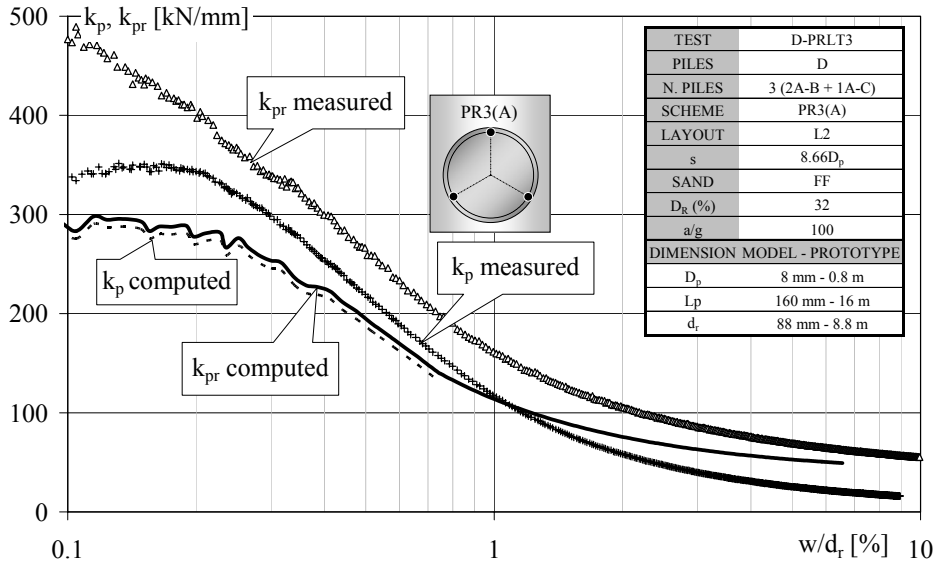

Figure 5.22. Measured and computed overall stiffness k_{pr} and pile group stiffness k_p vs. the raft relative settlement w/d_r for the D PR3(A) model. Prototype scale.

The D pile rafts have measured higher k_{pr} values than the values measured for the analogous models with non displacement piles, over the whole range of settlements analysed. This is partially due to the higher values of the stiffness of the D pile groups compared with the ND pile groups and partially to the more uniform contact between the raft and the sand surface at the initial loading stage (i.e. full contribution of the raft to the overall stiffness of the foundations at small displacements). The contribution of the raft to the foundation stiffness is significant over the entire range of settlements experienced.

The computed k_{pr} values are below the measured values, the trend becoming more marked as the number of piles increases.

At settlement $w/d_r < 1\%$ (smaller w/d_r than the value required to mobilise the pile full shaft capacity), the computed k_{pr} curves are very similar to the computed k_p curves, indicating a limited contribution of the raft stiffness to the computed k_{pr}. However, the underestimation of the

computed k_{pr}, can mainly be attributed to the underestimation of the computed pile group stiffness, k_p, in other words to overestimation of the pile interaction factors.

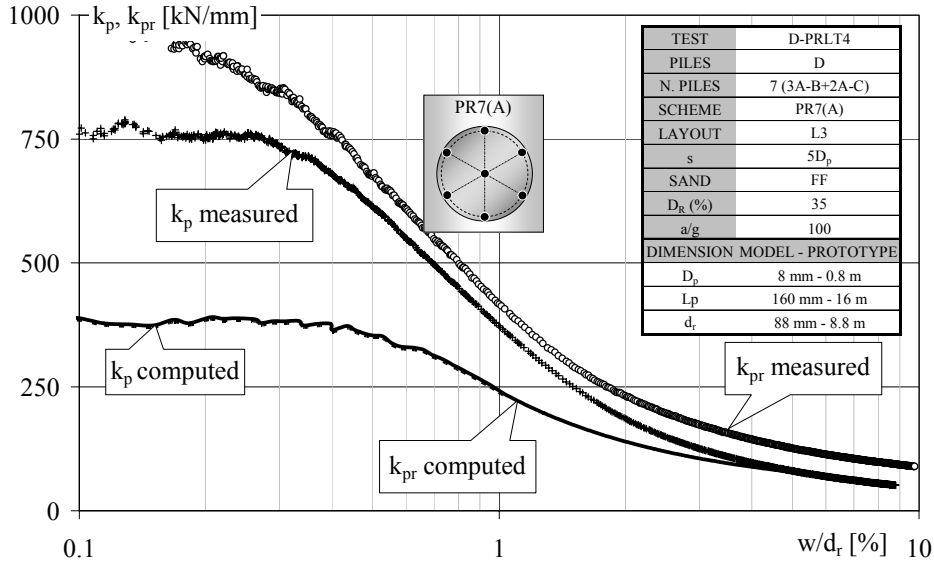

Figure 5.23. Measured and computed overall stiffness k_{pr} and pile group stiffness k_p vs. the raft relative settlement w/d_r for the D PR7(A) model. Prototype scale.

As seen in Sections 4.4.2, the effect of the soil densification produced by the jacking of a group of piles and, in PR7(A), the confinement effect exerted by neighbouring piles, compensate for and even exceed the pile–pile "negative" interactions and a softer pile response has not been observed. In order to take into account this experimental evidence, a second calculation of k_{pr} has been carried out for the PR3(A) and PR7(A) models, assuming interaction factors equal to zero and the pile group stiffness equal to $k_{p,PR3(A)} = 3 \cdot k_{p,IP}$ and $k_{p,PR7(A)} = 7 \cdot k_{p,IP}$, respectively. The second set of computation results are reported in Figures 5.24 and 5.25 and are labelled as "computed 2". The new computed k_{pr} values are closer to the measured values, but still lower than those, probably due to

(i) the underestimation of the raft contribution (ii) the underestimation of the confining effects, which have significantly enhanced the pile capacity in the PR7(A) model.

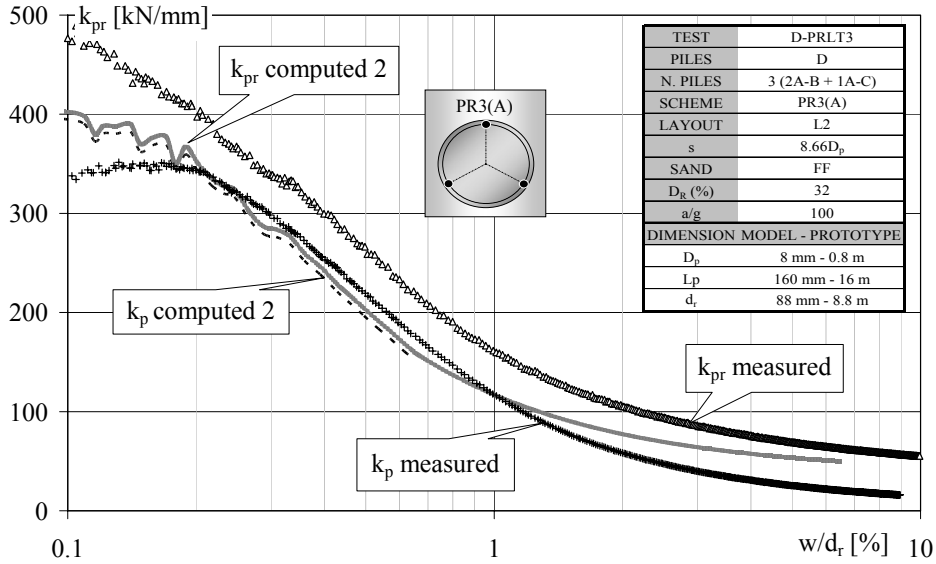

Figure 5.24. Measured and computed overall stiffness k_{pr} vs. the raft relative settlement w/d_r for the D PR3(A) model. Prototype scale.

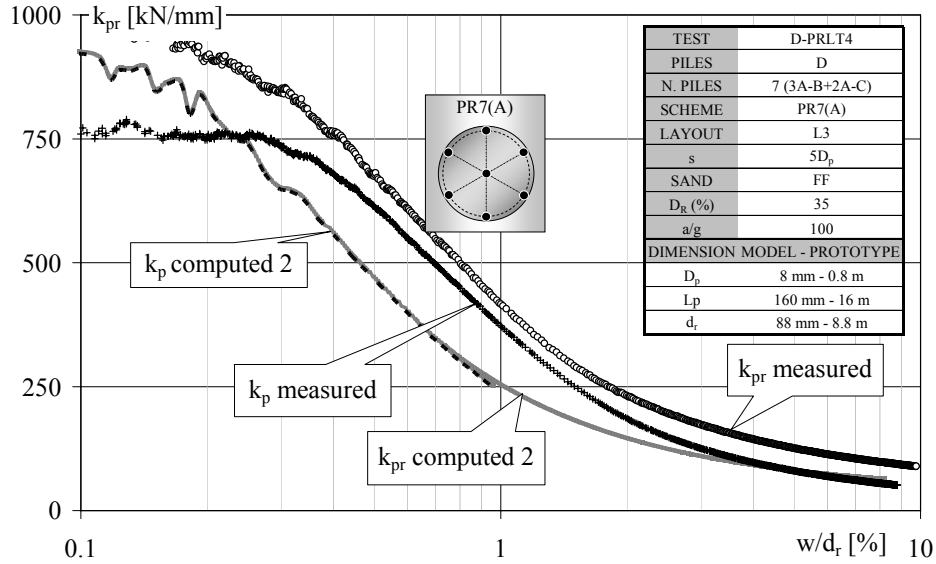

Figure 5.25. Measured and computed overall stiffness k_{pr} vs. the raft relative settlement w/d_r for the D PR7(A) model. Prototype scale.

Chapter 6

Numerical analyses

6.1 Introduction

A series of numerical simulations have been carried out on unpiled raft, non displacement isolated pile and non displacement 1-pile raft models. The numerical analyses were aimed at reproducing the centrifuge tests, thus the same geometry and dimensions as the physical models were adopted for the numerical simulations, which were carried out applying a gravitational field of 100*g* to the mesh (which should have reproduced the centrifuge acceleration field).

Two–dimensional axisymmetric analyses were performed, using the Tochnog (1989) code, a three-dimensional free explicit/implicit FE programme, developed by FEAT.

In this chapter, the results of the numerical analyses are compared with those of the centrifuge tests, with the main aim of highlighting the effect of the pressure transmitted by the raft to the soil on the behaviour of the single pile under the raft.

6.2 Constitutive model parameter calibration

The numerical analyses have been performed using the elasto–plastic strain hardening model proposed by Li and Dafalias (2000), which was implemented in the Tochnog code by Fontana (2004).

This constitutive model treats the dilatancy as a state–dependent quantity (i.e. dilatancy d dependent on the current state parameter ψ of the soil and on the stress ratio $\eta = q/p'$) within the framework of critical–state soil mechanics.

The state parameter ψ, which represents the difference between the current void ratio, e, and the critical state void ratio corresponding to the current confining pressure, e_{cv}, [i.e. $\psi = e - e_{cv}$, Been and Jefferies (1985)], is used to measure how far the material state is from the critical state. The position of the critical state line in the e-p' space is determined through the approach proposed by Li and Wang (1998), described in Eq. 3.1.

With the state parameter as the state variable, a particular form of a state–dependent dilatancy is proposed which represents a modification to the dilatancy function in the original Camclay model:

$$d = \frac{d_0}{M}(Me^{m\psi} - \eta) \qquad [-] \qquad (6.1)$$

where:

M = critical stress ratio [-];

d_0, m = positive modelling parameters [-].

The model assumes that plastic deformations occur when the stress ratio η exceeds its historic maximum and a constant η path induces no plastic deformation. On the basis of the state–dependent dilatancy relation that has been proposed and assuming a yield criterion of the form $f = q - \eta p'$

= 0, the following constitutive equations, which relate the volumetric and distortional stress increments, *dp'* and *dq*, to the volumetric and distortional strain increments, $d\varepsilon_v$ and $d\varepsilon_q$, are deduced:

$$\begin{Bmatrix} dq \\ dp' \end{Bmatrix} = \left[\begin{pmatrix} 3G & 0 \\ 0 & K \end{pmatrix} - \frac{h(L)}{K_p + 3G - k\eta d} \begin{pmatrix} 9G^2 & -3KG\eta \\ 3KGd & -K^2\eta d \end{pmatrix} \right] \begin{Bmatrix} d\varepsilon_q \\ d\varepsilon_v \end{Bmatrix}$$

$$[FL^{-2}] \qquad (6.2)$$

where:

G = elastic shear modulus [FL^{-2}];

K = elastic bulk modulus [FL^{-2}];

h(L) = Heaviside function, with h(L) = 1 for L > 0 and h(L) = 0 for L $\leq$0;

K_p = plastic hardening modulus [Dafalias (1986)] [FL^{-2}].

Li and Dafalias (2000) suggest expressing the elastic shear modulus *G* via the by Richart et al. (1970) empirical equation, as a function of the current mean stress state, *p'*, the current void ratio, *e*, and a material non dimensional constant, G_0^*. The elastic bulk modulus *K* can be derived from *G* via the elastic theory as a function of Poisson's ratio, *v*. In the model, *v* is considered as a material constant that is independent of the pressure and density. For the plastic modulus K_p, the following relation is proposed:

$$K_p = \frac{hGe^{n\psi}}{\eta}(Me^{-n\psi} - \eta) \qquad [FL^{-2}] \qquad (6.3)$$

where:

h, n = positive model parameter [-].

The Authors have found that a variable *h* with density fitted the experimental data better and propose a simple linear dependence: $h = h_1 - h_2 e$.

There are eleven material parameters in the model: the elastic parameters G_0^* and K; the critical state parameters M, e_Γ, λ and ξ; the dilatancy parameters d_0 and m and the hardening parameters h_1, h_2 and n.

The Li and Dafalias constitutive model is able to predict the critical state, to produce the correct soil stiffness at small and large strains and to simulate the behaviour of sand not only under triaxial compression/extension but also for other conditions, thus it has been considered adequate to simulate the shaft shearing process. In order to consider the plastic deformation at constant η, which can influence the load–settlement behaviour of the raft, a *p'* controlling cap was added to the original model, in the performed analyses [Fontana (2009)].

The model parameters of the FF sand introduced into the numerical analyses presented in this chapter, have been calibrated on the basis of the results of triaxial tests performed on the low density and low confining pressure FFS specimens previously shown in Chapter 3, following the calibration procedure suggested by the Authors. They were then adjusted to reproduce the unpiled raft centrifuge test results (see Section 6.4.1 and Figure 6.8). The model parameters for the FFS are reported in Table 6.1.

Table 6.1. Model parameters calibrated for the FFS.

Elastic parameters [-]	Critical state parameters [-]	Dilatancy parameters [-]	Hardening parameters [-]
$G_0^* = 25$ $\nu = 0.25$	$M = 1.35$ $e_\Gamma = 1.15$ $\lambda = 0.026$ $\xi = 0.901$	$d_0 = 0.8$ $m = 2$	$h_1 = 2.528$ $h_2 = 2.08$ $n = 1.5$

In order to check the accuracy of the calibrated parameters, the first step in the FE analyses regarded the triaxial tests simulation. Figures 6.1 to 6.6 compare the triaxial test results with the results of the numerical

simulations. The results have been considered acceptable even though better results could be achieved.

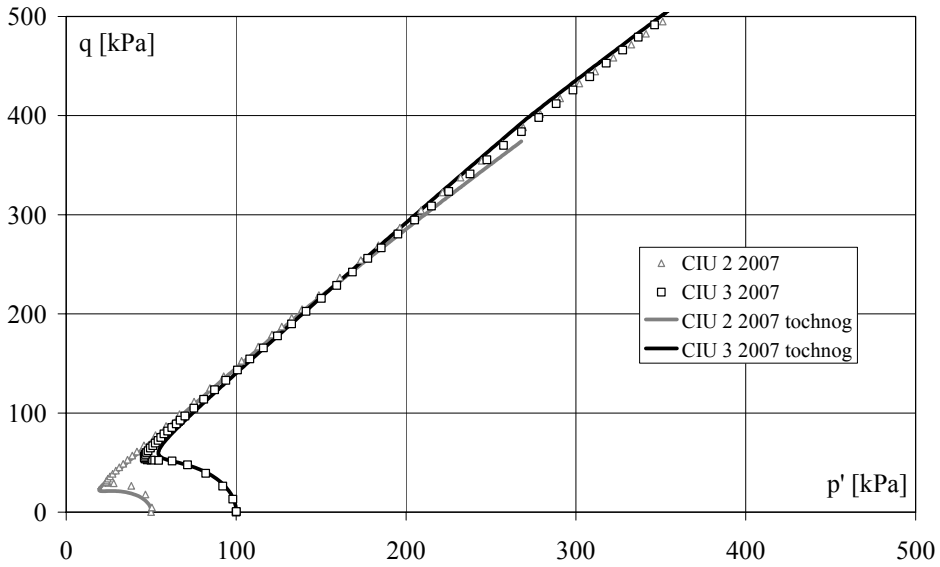

Figure 6.1. Experimental and numerical results of the undrained tests: effective stress paths.

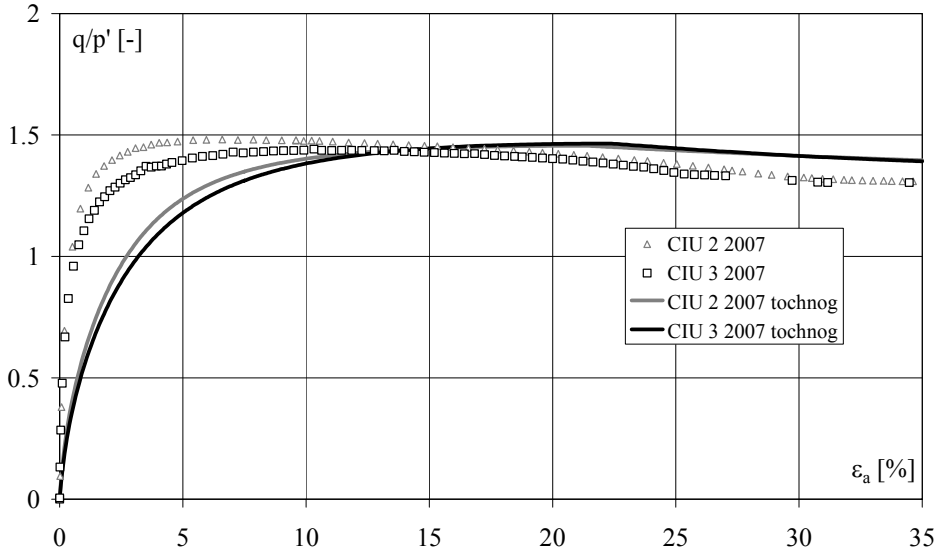

Figure 6.2. Experimental and numerical results of the undrained tests: stress–strain response.

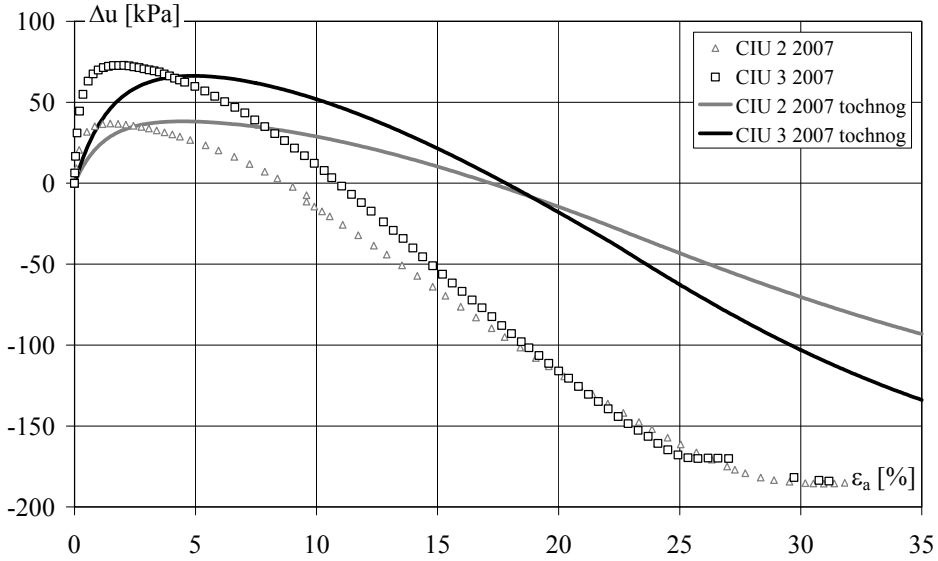

Figure 6.3. Experimental and numerical results of the undrained tests: pore water pressure Δu.

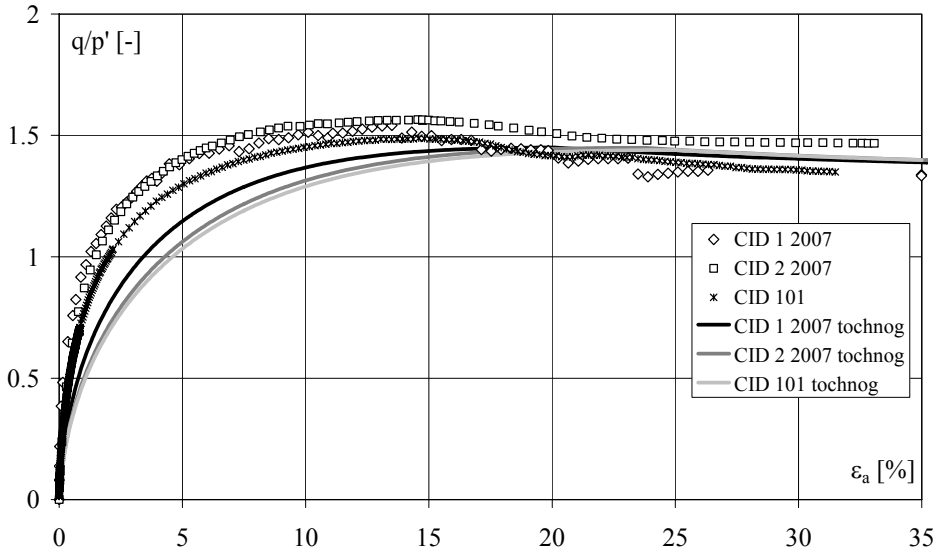

Figure 6.4. Experimental and numerical results of the drained tests: stress–strain response.

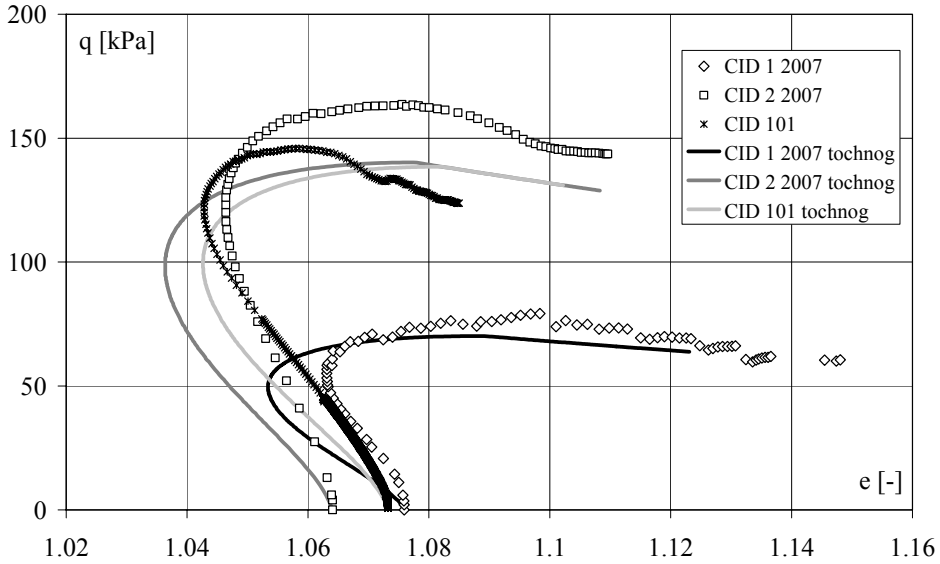

Figure 6.5. Experimental and numerical results of the drained tests: q-e paths.

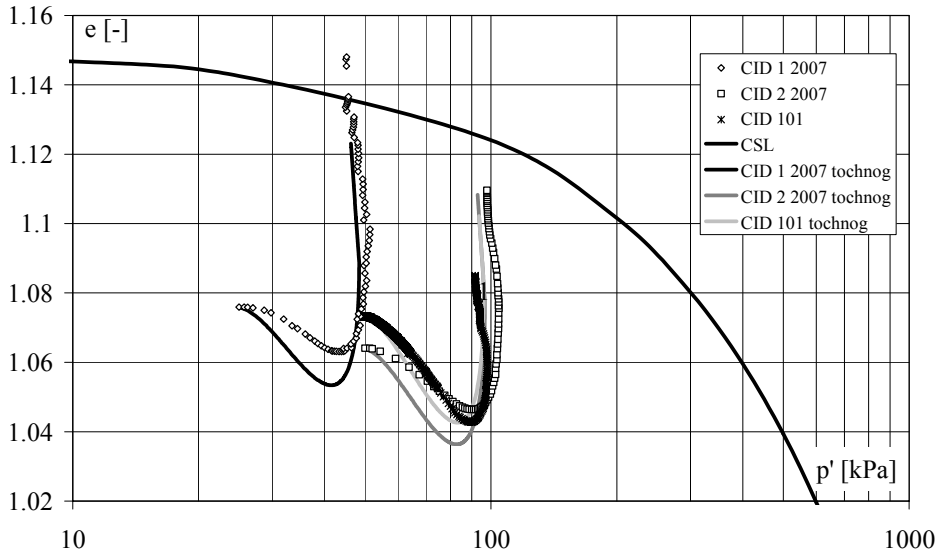

Figure 6.6. Experimental and numerical results of the drained tests: e-p' paths.

6.3 Finite element models and simulation procedures

Two–dimensional axisymmetric simulations have been carried out; the analyses domain was discretised by means of four–nodded quadrilateral elements.

Three models were simulated: an unpiled raft, a non displacement isolated pile and a non displacement 1-pile raft.

The numerical analyses were aimed at reproducing the centrifuge models, thus the geometry and the dimensions of the numerical models corresponded to those of the physical ones (models R, IP and PR1, see Figure 3.15 and Table 3.7) and the simulations were carried out applying a gravitational field of 100*g* to the mesh.

A 44 mm radius raft and a 4 mm radius and 160 mm long pile, embedded in a 200 mm radius and 440 mm deep soil model, have been considered. The analyses were performed assuming a homogeneous soil with an initial void ratio $e = 1.067$.

The mesh and the boundary conditions used for the two–dimensional axisymmetric simulations of the 1-pile raft model are shown in Figure 6.7. The mesh contains 14836 elements and 15102 nodes. The size of the first soil elements in contact with the lateral boundary that represents the pile shaft was set equal to 1 mm, a value which is very close to the mean grain size ($D_{50} \approx 0.093$ mm). The adopted contact element size did not produce any local numerical instability due to the high concentration of shear strains in the interface elements, which are generally observed in medium dense and dense sand, as quoted by Loukidis and Salgado (2008).

The rigid boundary, which represents the raft bottom, was removed in the isolated pile model. The rigid boundaries, which represent the pile shaft

and base, were removed in the unpiled raft model and the mesh was extended to the symmetry axis of the model.

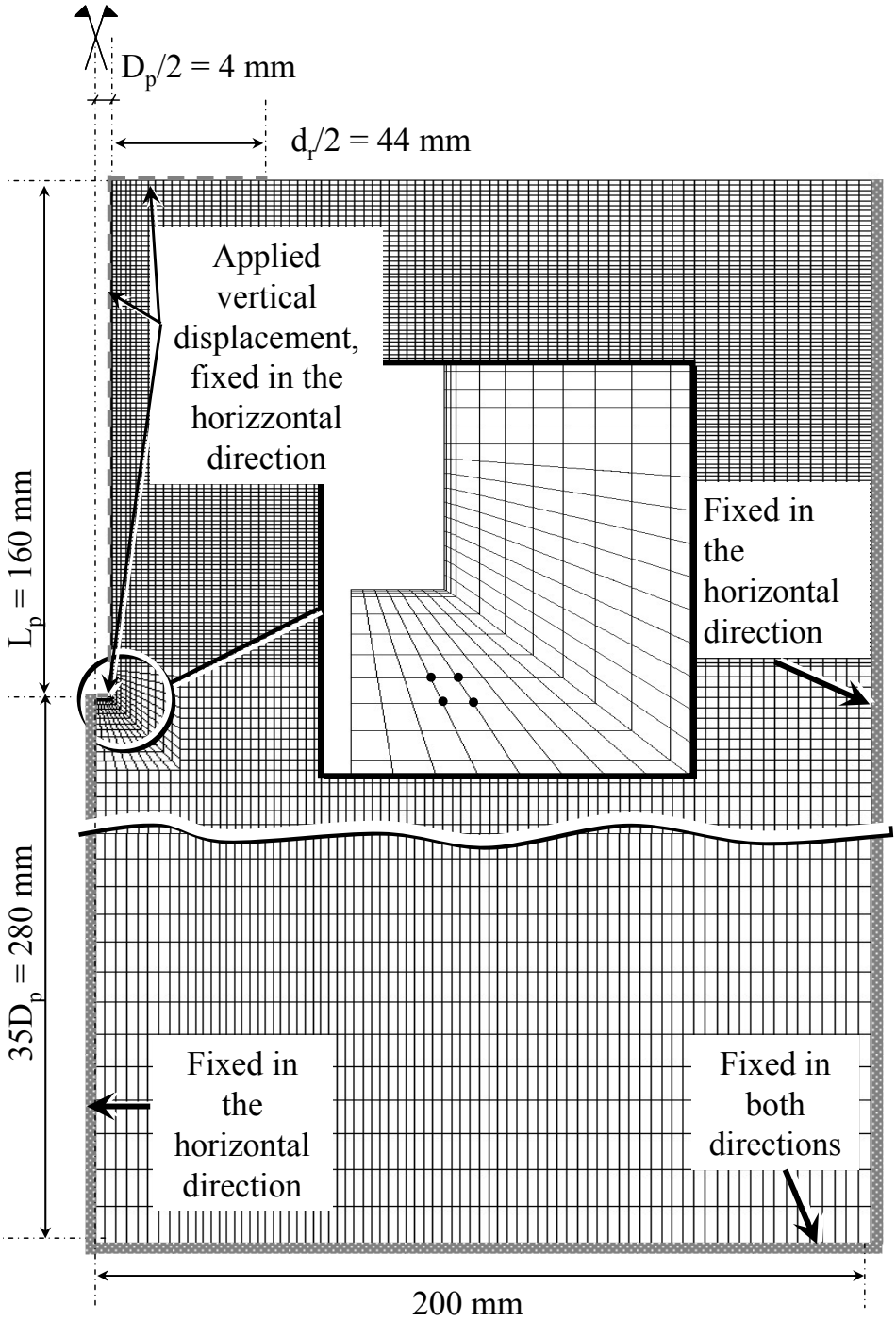

Figure 6.7. Finite element mesh and boundary conditions in the 1-pile raft simulation.

The following simulation procedures have been adopted.

Unpiled raft R

The simulations were carried out applying uniform displacement increments along the entire raft–soil interface, assuming a perfectly rigid raft; the maximum relative settlement achieved was w/d_r = 5%.

Non displacement isolated pile IP

Uniform displacement increments were applied along the entire pile–soil interface, including the pile tip, assuming a perfectly rigid pile.
In order to replicate the installation procedure of the non displacement pile carried out during centrifuge tests, i.e. to simulate the alignment of the pile head with the soil surface which took place in–flight at 75*g* and the subsequent loading test carried out at 100*g* (described in Chapter 3), the pile was preloaded up to a settlement of w/D_p = 15% and then unloaded. At the end of the installation simulation, residual forces, which were comparable to those measured during the centrifuge tests, acted on the pile. Subsequently, the pile was reloaded up to a pile relative settlement of w/D_p = 36%.

Non displacement 1-pile raft PR1

Uniform displacement increments were applied along the entire raft–soil interface and pile–soil interface, including the pile tip, assuming a perfectly rigid raft and pile. The pile preloading procedure was adopted. The maximum pile relative settlement achieved during the loading phase was w/D_p = 46% (w/d_r = 4.2%).

6.4 Results

In following sections, the length quantities are presented in non–dimensional form: the depth z is normalised to the pile length, z/L_p; the settlement w is normalised to the raft diameter or to the pile diameter, w/d_r or w/D_p; the distance from the model axis of symmetry R is normalised to the raft radius, R/r_r (where $r_r = d_r/2$).

6.4.1. Unpiled raft R

Figures 6.8 to 6.11 report some of the results of the numerical simulations of unpiled raft model R. Figure 6.8 compares the simulated stress–settlement curve (applied pressure q_t vs. the raft relative settlement w/d_r) to that measured in the centrifuge (test URLT0, see Figure 3.15 and Table 3.7). The numerical q_t curve is almost superimposed over the centrifuge one, at a lower settlement than 2%, then it diverges slightly as w/d_r increases and reaches 10% higher values at w/d_r = 5%.

Figures 6.9 and 6.10 show the profiles of the increment in the vertical and radial effective stresses, $\Delta\sigma'_v$ and $\Delta\sigma'_r$, respectively, as a function of z/L_p, at several R/r_r. Figure 6.11 reports the profiles of $\Delta\sigma'_r$ as a function of R/r_r, at several z/L_p. The values of $\Delta\sigma'_v$ and $\Delta\sigma'_r$, which have been evaluated as the current values of the vertical and radial effective stresses, σ'_v and σ'_r, minus the initial overburden values, σ'_{v0} and σ'_{r0} (i.e. $\Delta\sigma'_v = \sigma'_v - \sigma'_{v0}$; $\Delta\sigma'_r = \sigma'_r - \sigma'_{r0}$), are represented in Figures 6.9 to 6.11 for five values of w/d_r, ranging from 0.45% to 2.27%.

The $\Delta\sigma'_v$ and $\Delta\sigma'_r$ curves reported in Figures 6.9 to 6.11 show a significant stress concentration under the raft at $z/L_p < 0.5$. The stress increment due to the raft pressure becomes progressively lower at greater depth, and it is quite negligible at the depth z/L_p=1. As expected, the

stress concentration just beneath the raft is higher at the raft edge (R/r_r = 1) and lower at the raft centre (R/r_r = 0).

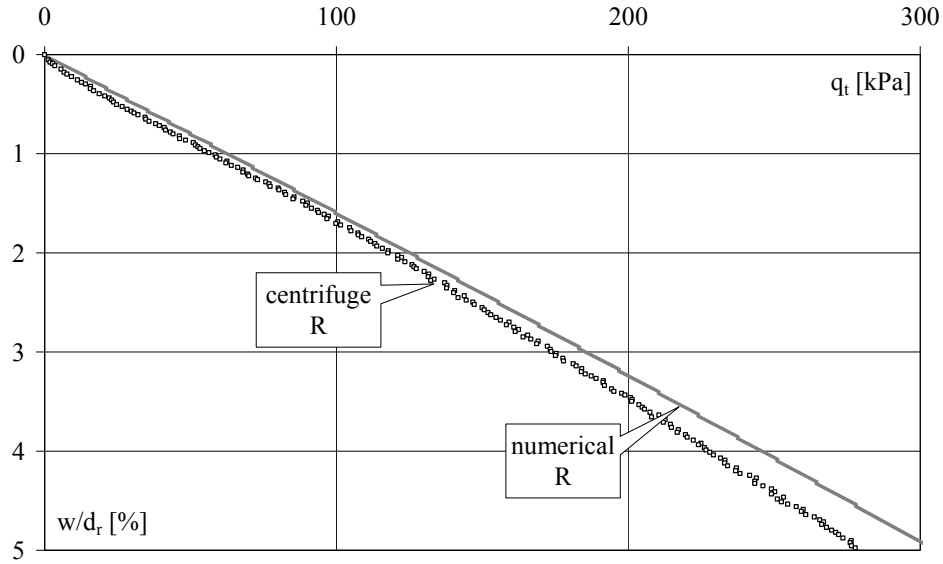

Figure 6.8. Unpiled raft: numerical simulation vs. centrifuge test results. Total applied pressure q_t vs. the relative settlement w/d_r.

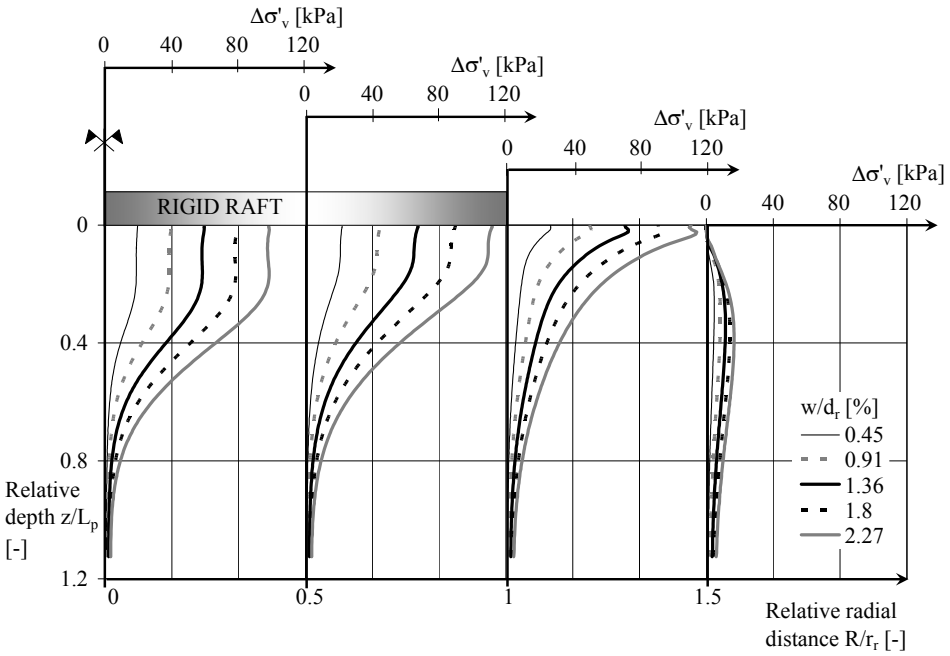

Figure 6.9. Numerical simulation of the unpiled raft. Profiles of the increment in the vertical effective stress $\Delta\sigma'_v$ with the relative depth z/L_p at several radial distances from the raft axis R/r_r and at several relative settlements w/d_r of the raft.

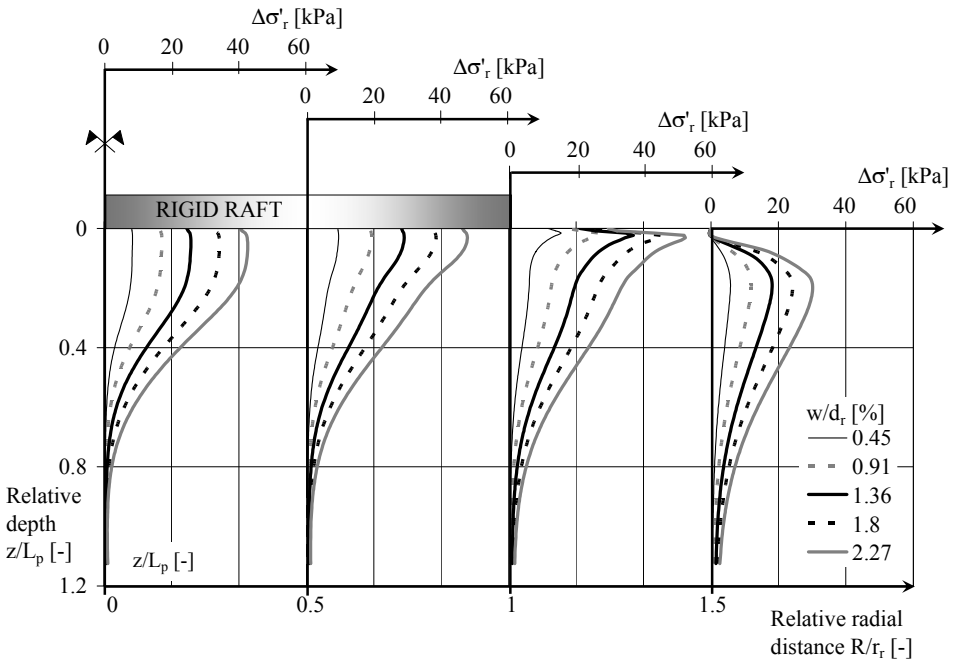

Figure 6.10. Numerical simulation of the unpiled raft. Profiles of the increment in the radial effective stress $\Delta\sigma'_r$ with the relative depth z/L_p at several radial distances from the raft axis R/r_r and at several relative settlements w/d_r of the raft.

6.4.2. Isolated non displacement pile IP

Figures 6.12 to 6.17 report the results of the numerical simulations of the IP isolated pile. The loads acting on the pile head and base, q_A and q_B, and the shaft friction τ_S are represented in Figures 6.12 and 6.13 vs. the pile relative settlement, w/D_p. The Figures also reports the q_A and q_B, and the shaft friction $\tau_{S,AB}$ values obtained from the centrifuge test on the non displacement IP pile (test ND-PLT6, see Figure 3.15 and Table 3.7). The numerical q_A, q_B and τ_S curves have a similar mobilisation pattern as the experimental curves, but the computed values of the base resistance and the shear stress are lower than the measured values, over almost the whole investigated settlement range.

Figure 6.14 reports the profiles of the shear stress acting along the pile shaft, τ_s, as a function of the depth relative to the pile length, z/L_p, for

w/D_p values ranging from 1% to 26%. Figure 6.15 reports the profiles of the vertical and radial effective stresses, σ'_v and σ'_r, acting at the pile interface at w/D_p = 10.1%. Figures 6.16 and 6.17 show the profiles of the increments in the vertical and radial effective stresses along the pile shaft, $\Delta\sigma'_v$ and $\Delta\sigma'_r$, as a function of z/L_p. The values of $\Delta\sigma'_v$ and $\Delta\sigma'_r$, which have been evaluated as the current values of the vertical and radial effective stresses, σ'_v and σ'_r, minus the initial overburden values, σ'_{v0} and σ'_{r0}, are represented in Figures 6.14 to 6.16 for values of w/D_p ranging from 1% to 26%.

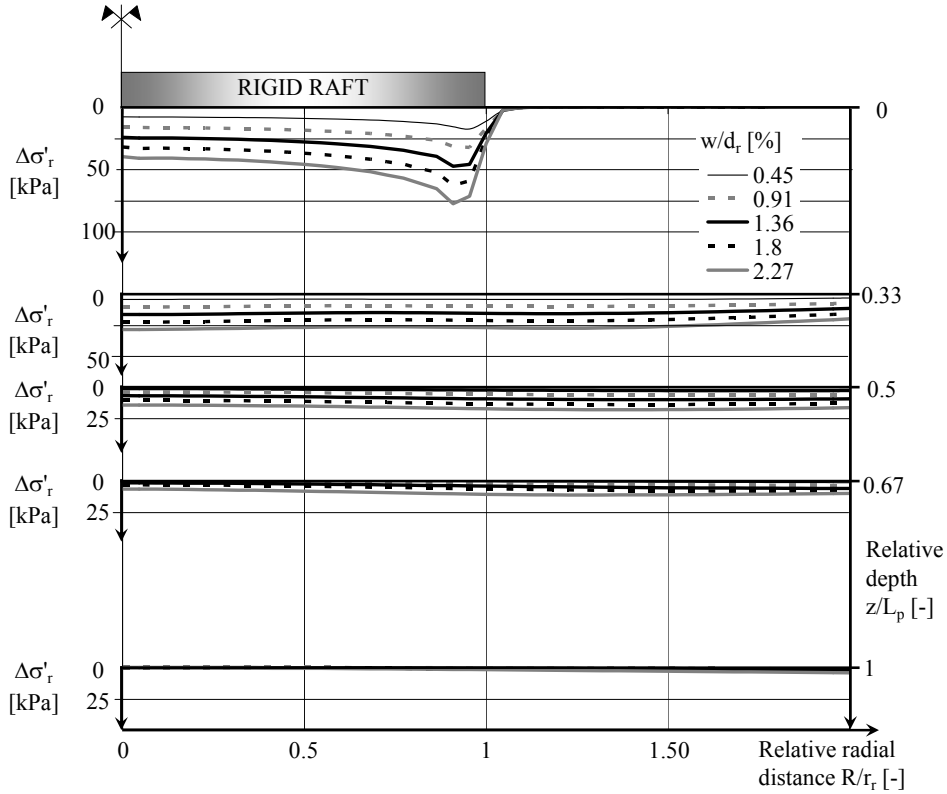

Figure 6.11. Numerical simulation of the unpiled raft. Profiles of the increment in the radial effective stress $\Delta\sigma'_r$ with the radial distance from the raft axis R/r_r at several relative depths from the raft bottom z/L_p and at several relative settlements w/d_r of the raft.

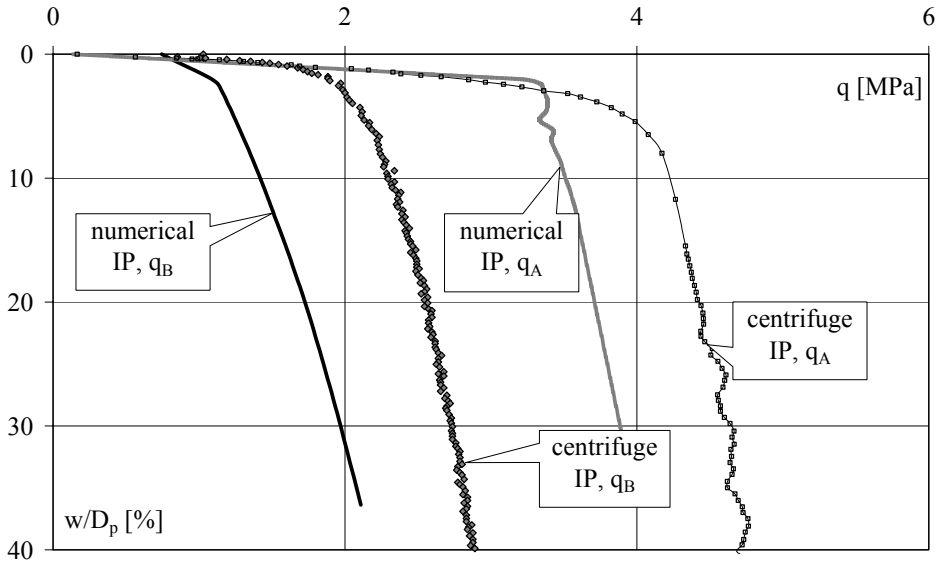

Figure 6.12. Isolated non displacement pile: numerical simulation vs. centrifuge test results. Loads on pile head q_A and base q_B vs. the pile relative settlement w/D_p.

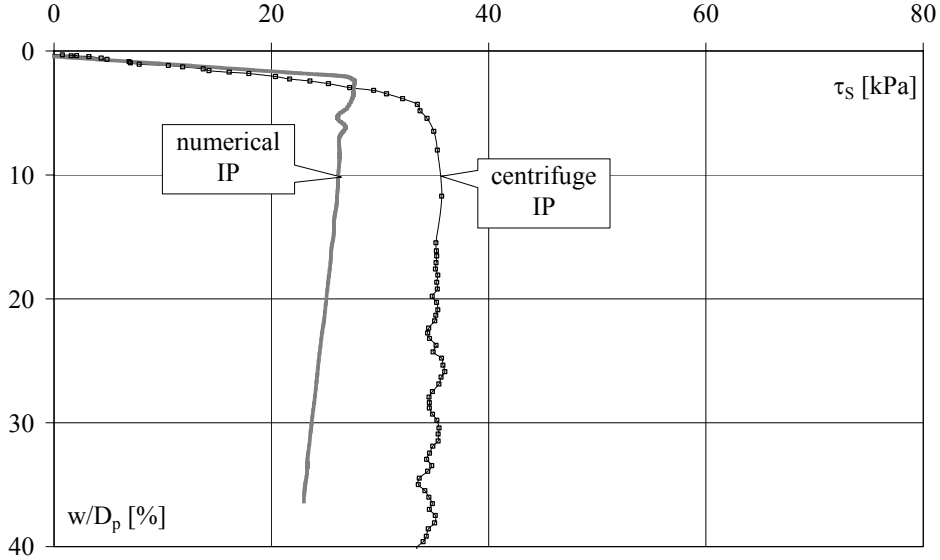

Figure 6.13. Isolated non displacement pile: numerical simulation vs. centrifuge test results. Shaft friction τ_S vs. the pile relative settlement w/D_p.

As described by Loukidis and Salgado (2008), as the pile is subjected to axial loading, it drags the surrounding soil down and the increasing pile load is diffused in the soil through increasing shear stresses (Figures 6.13

and 6.14). As shearing proceeds the interface soil elements are subjected to the rotation of the principal effective stress directions.

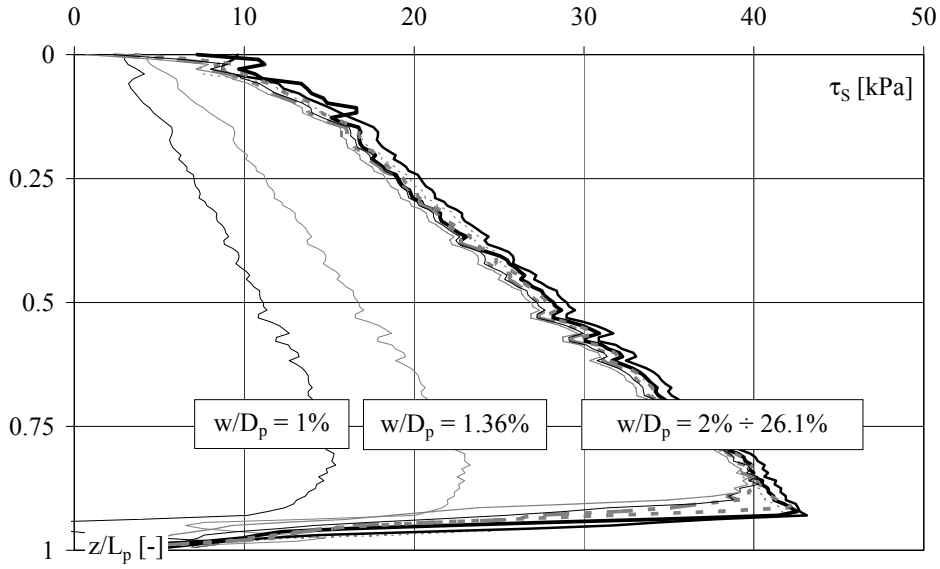

Figure 6.14. Isolated non displacement pile: numerical simulation. Profiles of the shaft friction τ_S at several pile relative settlements w/D_p.

The deformation mode is similar to that of simple shear, even though the change in soil volume leads to both radial and hoop strains. If the soil is generally dilative, the elements closer to the pile push against the neighbouring soil elements that lie in the same radial plane, a process that leads to a decrease in the vertical effective stress and an increase in the lateral effective stress. After a certain amount of vertical displacement of the pile (w/D_p = 2%), the soil close to the shaft reaches a critical state and stops dilating. This leads to an overall steady state of stress at which the shaft resistance reaches its limit value (Figures 6.13 and 6.14), the principal effective stress directions have an inclination of $\pm$45° with the vertical, and the radial and vertical effective stresses are almost equal, as can be seen in Figure 6.15, where the profiles of σ'_v and σ'_r, acting at the pile interface at w/D_p = 10.1%, are compared with the profiles of the

initial values σ'_{v0} and σ'_{r0}. A loss of σ'_v and σ'_r occurs in the region at approximately $1.5D_p$ above the pile base, as the soil elements are subject to extension due to the compressed soil underneath.

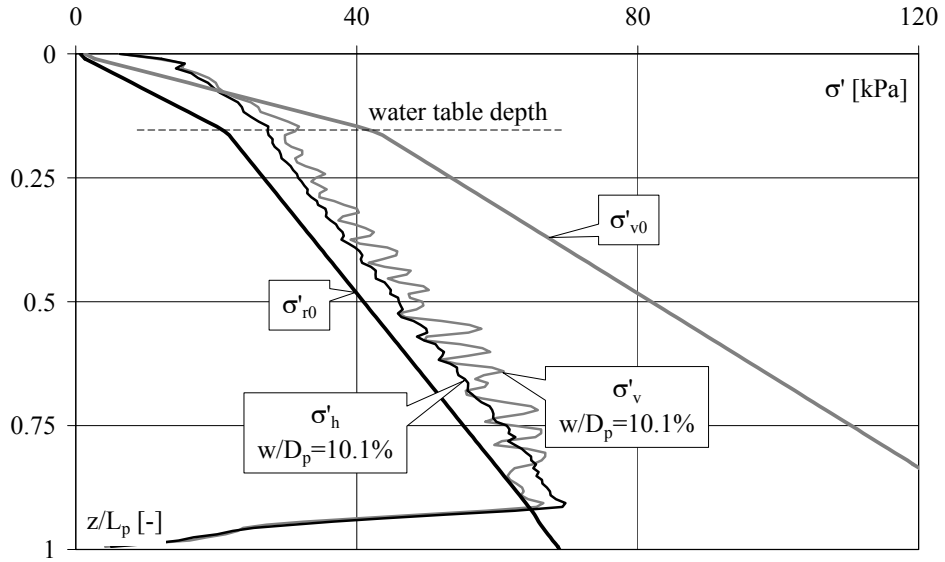

Figure 6.15. Numerical simulation of the isolated non displacement pile. Profiles of the vertical and radial effective stresses along the pile shaft at rest and at the relative pile settlements w/D_p=10.1%.

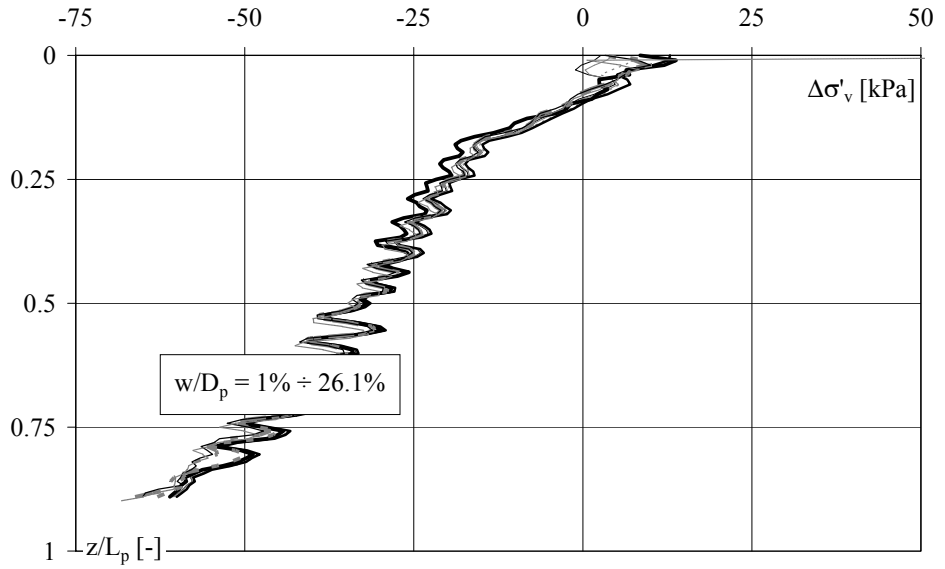

Figure 6.16. Numerical simulation of the isolated non displacement pile. Profiles of the increment in the vertical effective stress $\Delta\sigma'_v$ along the pile shaft at several pile relative settlements w/D_p.

The vertical effective stress decrease due to the shearing ($\Delta\sigma'_v < 0$ in Figure 6.16) is more significant at greater depths. The radial effective stress increase ($\Delta\sigma'_r > 0$ in Figure 6.17) is almost uniform along the pile shaft.

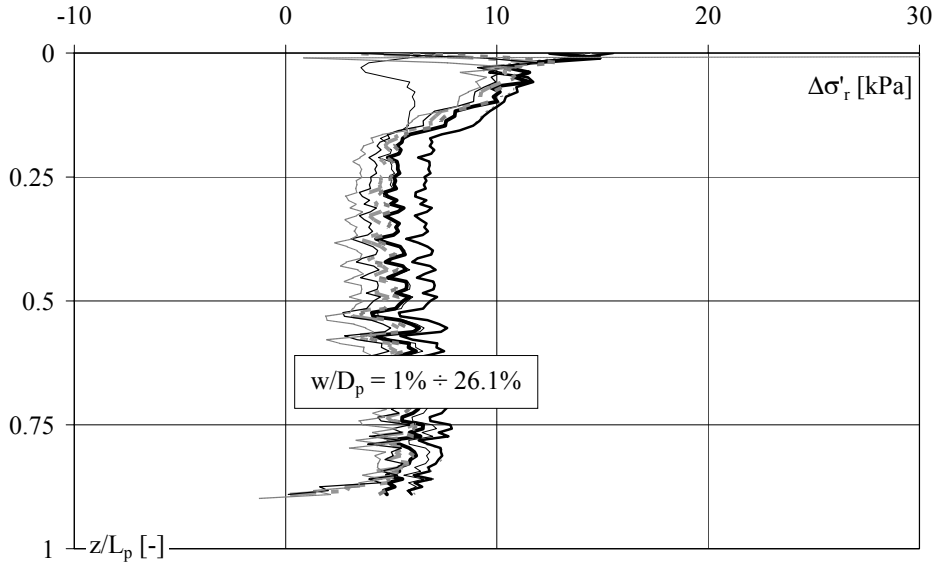

Figure 6.17. Numerical simulation of the isolated non displacement pile. Profiles of the increment in the radial effective stress $\Delta\sigma'_r$ along the pile shaft at several pile relative settlements w/D_p.

6.4.3. Non displacement 1-pile raft PR1

Figures 6.18 to 6.25 report the results of the numerical simulations of the non displacement 1-pile raft (PR1 scheme). The total applied load, q_t, and the load transmitted to the soil, q_r, are represented in Figure 6.18 vs. the settlement normalised to the raft diameter, w/d_r. The Figure also reports the q_t and q_r values obtained from the centrifuge test on the non displacement 1-pile raft (test ND-PRLT5, see Figure 3.15 and Table 3.7). The numerical and experimental load sharing mechanisms are reported in Figure 6.19.

The loads acting on the pile head and base, q_A and q_B, and the shaft friction τ_S are represented in Figures 6.20 and 6.21 vs. the settlement

normalised to the pile diameter, w/D_p (left hand side) and to the raft diameter, w/d_r (right hand side). The Figures also reports the q_A, q_B and $\tau_{S,AB}$ values obtained from the centrifuge test.

Figures 6.22 and 6.23 show the profiles of the increment in the vertical and radial effective stresses, $\Delta\sigma'_v$ and $\Delta\sigma'_r$, respectively, as a function of z/L_p, at several R/r_r for values of w/D_p ranging from 1% to 26% (w/d_r from 0.09% to 2.4%). Figure 6.24 reports the profiles of $\Delta\sigma'_r$ as a function of R/r_r, at several z/L_p, for the same settlement range. Figure 6.25 reports the profiles of the shear stress acting along the pile shaft, τ_s, as a function of the depth relative to the pile length, z/L_p, for w/D_p values ranging from 1% to 26%.

The load transfer mechanism from the raft to the soil and the pile is well reproduced by the numerical simulation, as can be seen in Figures 6.18 and 6.19.

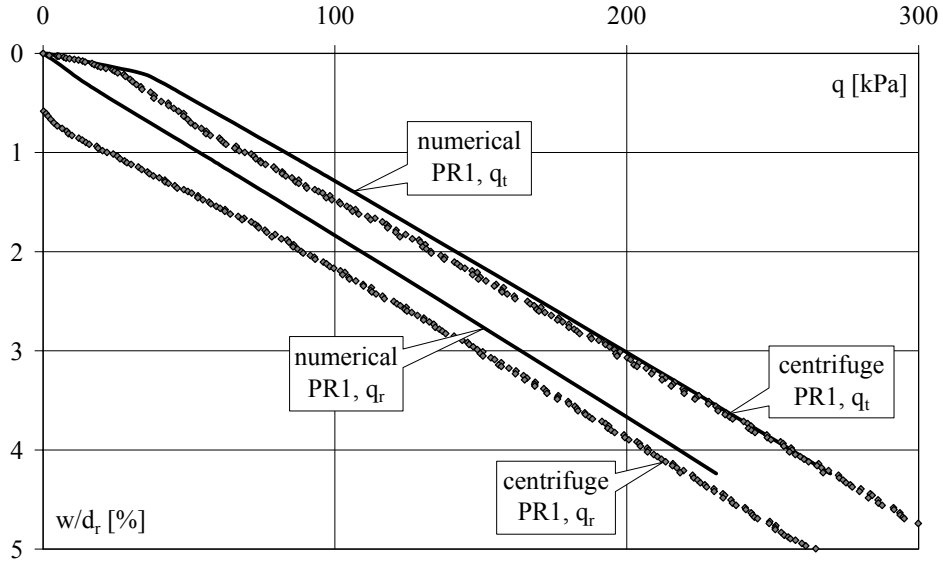

Figure 6.18. Non displacement 1-pile raft numerical simulation vs. centrifuge test results. Total applied pressure q_t and pressure transmitted to the soil q_r vs. the raft relative settlement w/d_r.

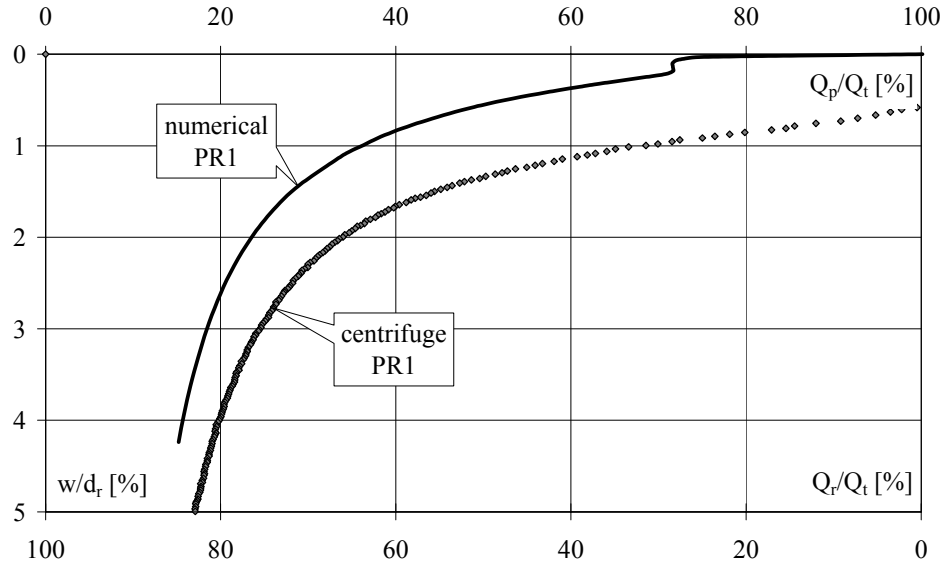

Figure 6.19. Non displacement 1-pile raft numerical simulation vs. centrifuge test results. Load sharing mechanism.

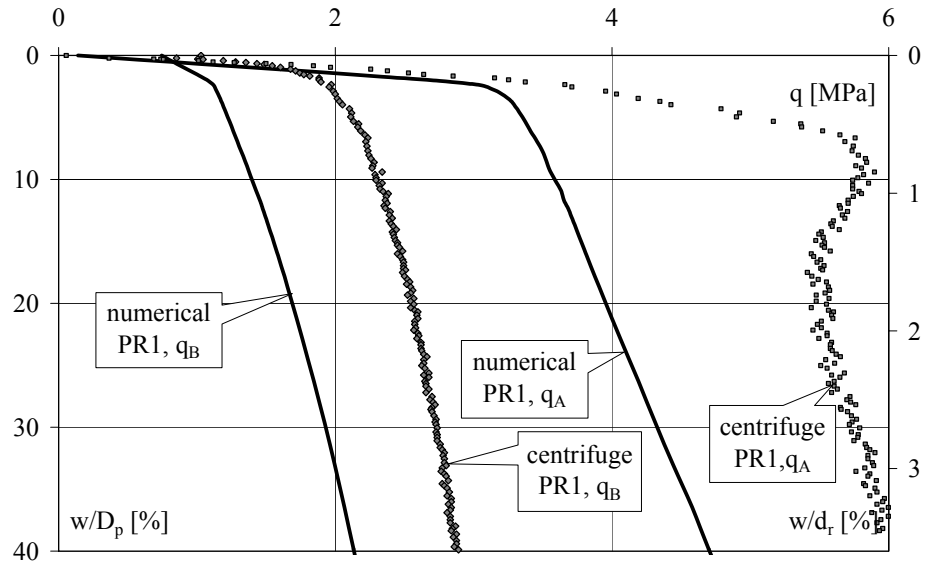

Figure 6.20. Non displacement 1-pile raft: numerical simulation vs. centrifuge test results. Loads on pile head q_A and base q_B vs. the pile and raft relative settlements w/D_p (left hand side) and w/d_r (right hand side).

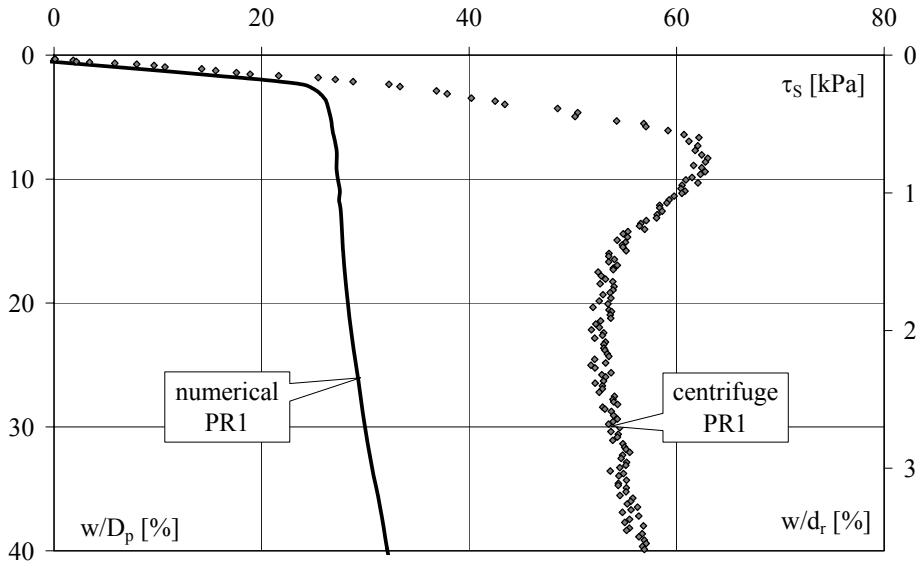

Figure 6.21. Non displacement 1-pile raft: numerical simulation vs. centrifuge test results. Shaft friction τ_S vs. the pile and raft relative settlements w/D_p (left hand side) and w/d_r (right hand side).

However, the pile shaft and base capacity are underestimated as in the isolated single pile simulation (Figure 6.20 and 6.21). As far as the shaft friction mobilisation is concerned, after a limit value has been reached, τ_S increases further at large settlements ("$\Delta\sigma'_r$ effect" described in Chapter 4).

The profiles of the increment in the vertical and radial effective stresses, $\Delta\sigma'_v$ and $\Delta\sigma'_r$, reported in Figures 6.22, 6.23 and 6.24, highlight a combination of two effects along the pile–soil interface. Shearing effects, which cause a vertical stress reduction, as seen for the isolated pile, prevails at small settlements. The predominant effect at large settlements is that of the raft pressure on the soil, which causes an increase in both the vertical and radial stresses.

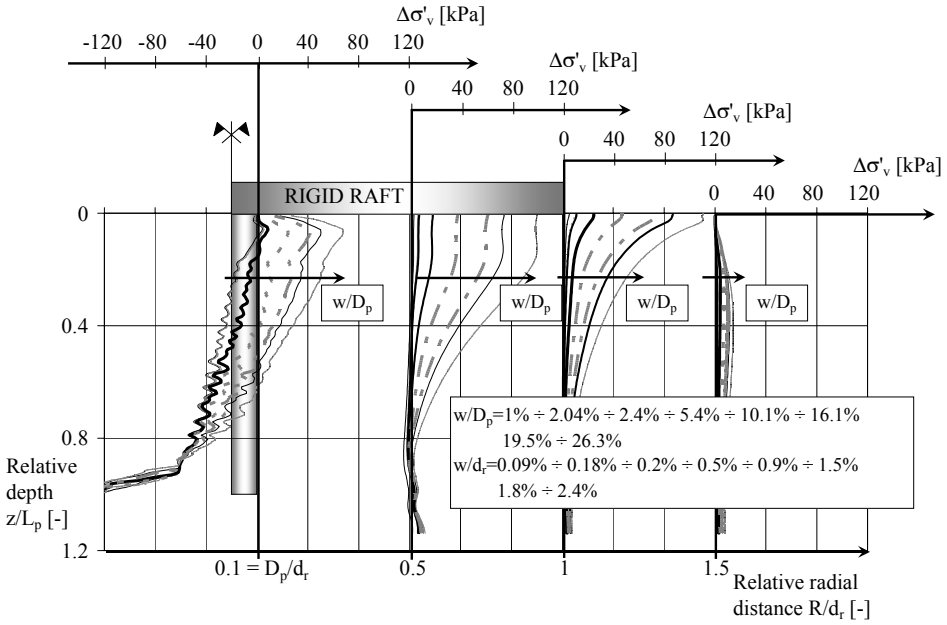

Figure 6.22. Numerical simulation of the 1-pile raft. Profiles of the increment in the vertical effective stress $\Delta\sigma'_v$ with the relative depth z/L_p at several radial distances from the raft axis R/r_r and at several raft and pile relative settlements w/d_r and w/D_p.

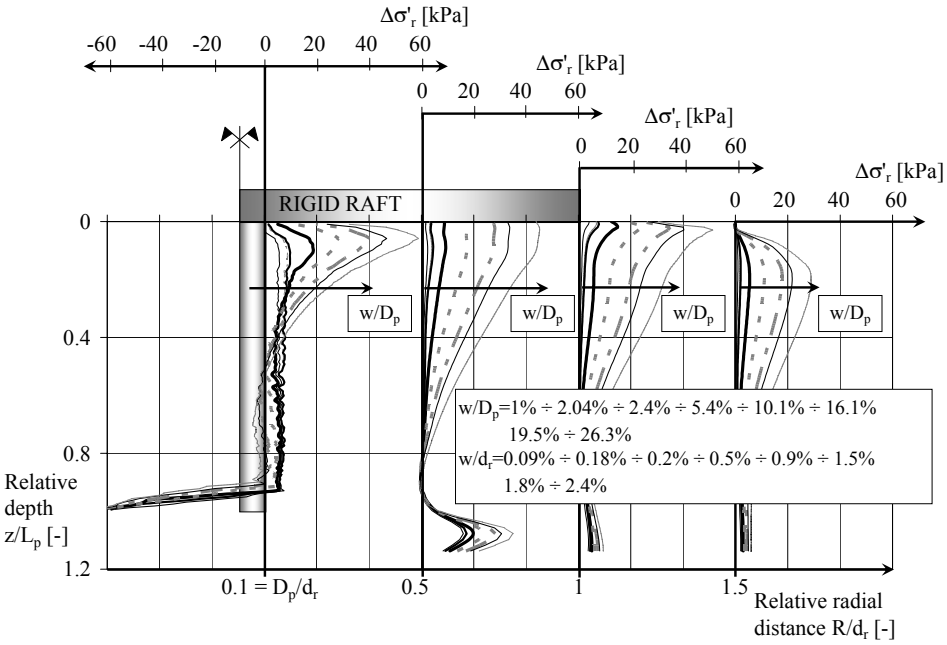

Figure 6.23. Numerical simulation of the 1-pile raft. Profiles of the increment in the radial effective stress $\Delta\sigma'_r$ with the relative depth z/L_p at several radial distances from the raft axis R/r_r and at several raft and pile relative settlements w/d_r and w/D_p.

As a consequence, the shear stress contours reported in Figure 6.25 are characterised by similar a pattern as the isolated pile at $w/D_p < 2\%$, then, at large settlements, a progressive increment in the shear stress is caused in the upper pile shaft by the progressive increase in the vertical stress. The effect of $\Delta\sigma'_r$ at the pile base depth (z/L_p=1) appears to be negligible. Figure 6.25 also highlights the shielding effect that the raft exerts on the pile: the soil under the raft is forced to settle by the same amount as the piles and no skin friction can develop at the pile heads. Thus, the degree of shaft friction mobilisation is maximum at the pile bases and reduces to zero at the pile tops.

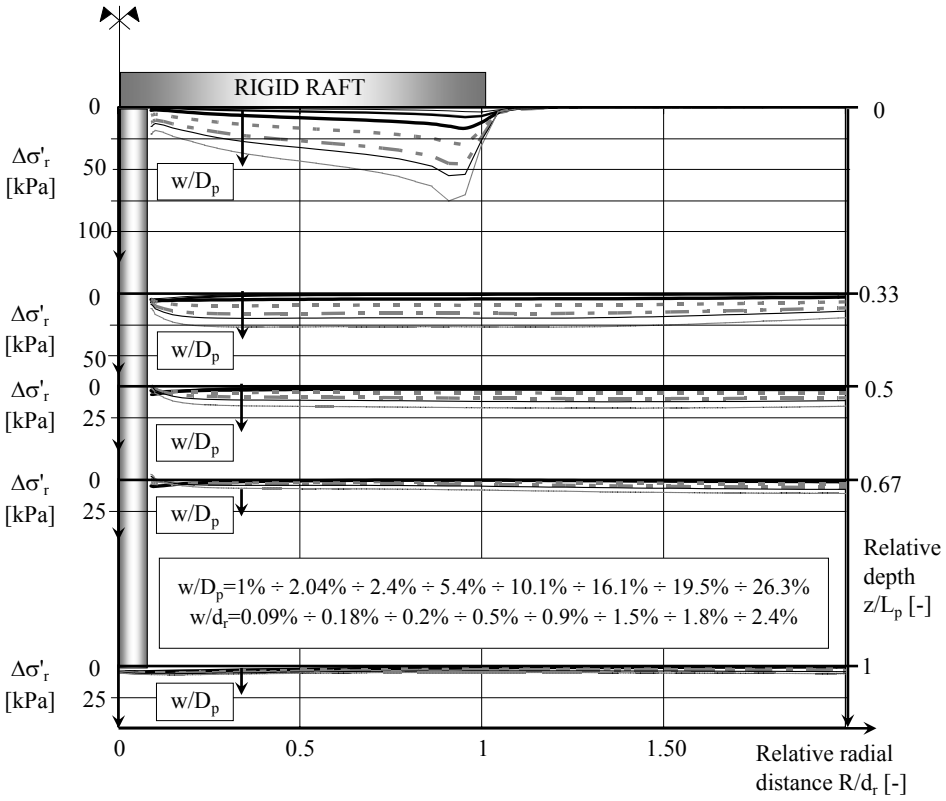

Figure 6.24. Numerical simulation of the non displacement 1-pile raft. Profiles of the increment in the radial effective stress $\Delta\sigma'_r$ with the radial distance from the raft axis R/r_r at several relative depths from the raft bottom z/L_p and at several raft and pile relative settlements w/d_r and w/D_p.

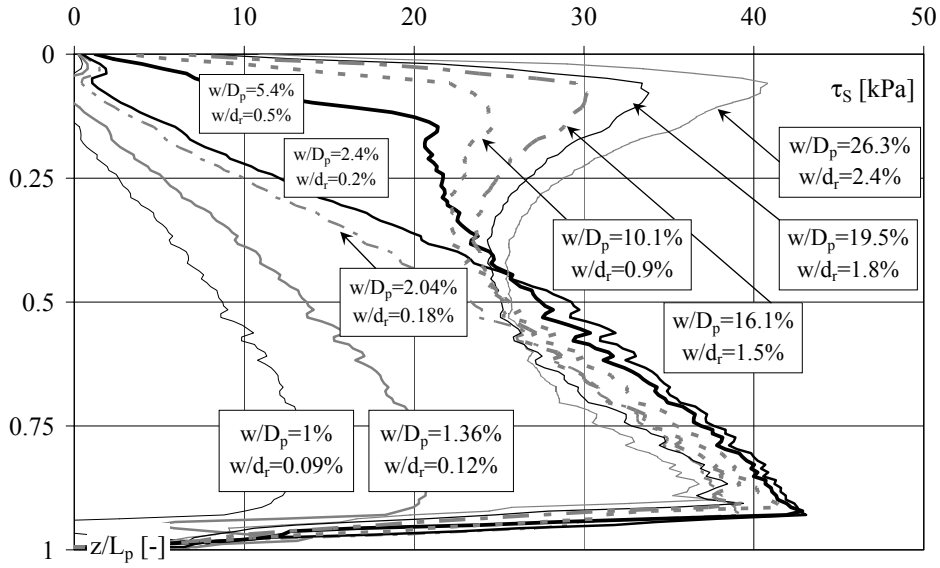

Figure 6.25. Non displacement 1-pile raft: numerical simulation. Profiles of the shaft friction τ_S at several raft and pile relative settlements w/d_r and w/D_p.

Chapter 7

Contact vs. non–contact piled raft foundations

7.1 Introduction

When piles are used as settlement reducers, the main design aims, when attempting to achieve an economic foundation, are to minimise the number of piles and to fully utilise their bearing capacity.

A relatively small number of piles could produce high bending moments and cracking in the raft and a concentration of axial stresses in the pile heads. In seismically active zones, if the piles are structurally connected to the slab, high horizontal shear forces and overturning moments may develop on the pile heads due to cyclic or dynamic lateral loads. In all these cases, the pile carrying capacity may be governed by their structural capacity rather than by their geotechnical capacity. Constraint reactions between the pile heads and the raft can be reduced by disconnecting the piles from the raft with an interposed fill layer; disconnected piles carry the loads from the superstructure in an indirect manner, and may be regarded as stiffeners of the subsoil.

Some recent innovative piled footing projects have employed piled rafts with an interposed layer. Among others, mention can be made to the foundation system of the Rion Antirion Bridge [Garnier and Pecker

(1999), Pecker (2004)] which consists of vertical inclusions to improve the shear resistance of the foundation soils and to minimise the hazards related to differential settlements, plus a gravel bed to limit the shear forces and moments transmitted between the superstructure and the foundation soils.

Several authors have recently presented results of numerical simulations [Wong et al. (2000), Liang et al. (2003), Liang et al. (2006), Huang et al. (2007)] or 1g model tests concerning rafts on "non–contact" settlement reducing piles [Cao et al. (2004)].

In this framework, multi–g centrifuge tests have been performed at ISMGEO on piled raft models axially loaded to explore the influence of a granular layer, interposed between a raft and piles, on the overall load–settlement behaviour. The foundation system of the MOSE project – the mobile barrier system which has the aim of safeguarding the Venice lagoon from flooding, Burghignoli et al. (2007), Jamiolkowski et al. (2009) – was taken as a reference application. The MOSE system consists of a series of caissons, installed at the lagoon bottom inlets, which house flap gates. The gates will ensure the closure of the inlets when a high tide of +1.1 m elevation, or higher, is forecasted. The caisson bottoms lie on 0.5 m diameter and 19 m long driven piles covered by a 1 m thick layer of compacted coarse grained granular material. The piles have the purpose of mitigating the differential settlement due to spatial soil variability and to any possible placement imperfection linked to the complexity of the underwater works. The layer interposed between the pile heads and the caisson bottom has been designed to reduce overstressing at the connection between the piles and the caissons during cyclic excitation and to realise a more uniform pressure distribution which prevents local failure of the contact piles.

The centrifuge tests were aimed at investigating the influence of the raft–granular fill–soil–pile interactions on the bearing capacity and stiffness of the piled raft foundation.

In "traditional" piled rafts, the pile heads and the soil surface are forced to settle by the same amount as the raft, thus the pile–soil relative displacement is zero at the pile head and maximum at the pile tip and the shaft friction is mobilised from the pile point upwards [Burland (1995)]. The load is partially transferred from the raft to the shallow soil and partially to the pile heads, and from the piles it is diffused through the shaft and the base to deeper soil: contact piles act as settlement reducers by reducing the amount of load transmitted to the shallow soil. The load transmitted to the ground surface produces an increase in the vertical and horizontal stresses in the soil surrounding the piles and gives rise to an increase in the pile shaft capacity [Katzenbach and Arslan (1998), Katzenbach et al. (2000), Poulos (2001)]. The interaction between piles produces a decrease in the stiffness of each pile [El–Mossallamy and Franke (1998), Fioravante et al. (2008b)].

The insertion of a deformable layer between a raft and the pile heads allows downward soil–pile relative displacement which produces negative skin friction on the upper part of the shaft. Such a mechanism is mainly governed by the thickness and the stiffness of the interposed layer and by the stiffness of the subsoil. Non–contact piles act as vertical reinforcements of the subsoil and improve its mechanical properties by forming a new composite and stiffer material on which the raft rests [Wong et al. (2000), Liang et al. (2003), Liang et al. (2006), Huang et al. (2007), Fioravante (2010)].

This chapter shows some of the basic load transfer mechanisms on the bases of the interpretation of centrifuge tests.

7.2 Experimental set–up, test programme and test procedure

The presented centrifuge loading tests were performed in the ISMGEO Geotechnical Centrifuge (IGC), previously described in Chapter 3.

The adopted geometrical scaling factor of the models was $N = 65$; all the models were tested under an acceleration field of $a = 65g$. The distortion of the acceleration field was accounted for in the computation of the stress distribution with depth.

A scaling factor of $N = 65$ was chosen in order to model groups of piles with adequate spacing loaded by a sufficiently small raft to minimise the boundary effects due to the proximity of the lateral container walls and the container bottom.

7.2.1 Test sands, model raft and model piles

Experiments were performed using dry silica Venice Lagoon Sand (VLS), herein also called "subsoil", with 15% finer grains than 0.075 mm, characterised by:

- $\gamma_{d,min} = 13.08$ kN/m^3 = minimum dry density;
- $\gamma_{d,max} = 16.50$ kN/m^3 = maximum dry density;
- $D_{50} = 0.18$ mm = mean particle size;
- $U_C = 3.33$ = uniformity coefficient;
- $\varphi'_{cv} = 35°$ = angle of shearing resistance at critical state.

In the non–contact piled raft tests, the interposed granular layer was modelled using single sized siliceous Ticino sand (TS), herein simply called "interposed layer", characterised by:

- $\gamma_{d,min} = 13.65$ kN/m^3;
- $\gamma_{d,max} = 16.67$ kN/m^3;

– D_{50}=0.58 mm;

– U_C = 1.79;

– φ'_{cv} = 35°.

Figure 7.1 reports the grain size distribution of the test sands.

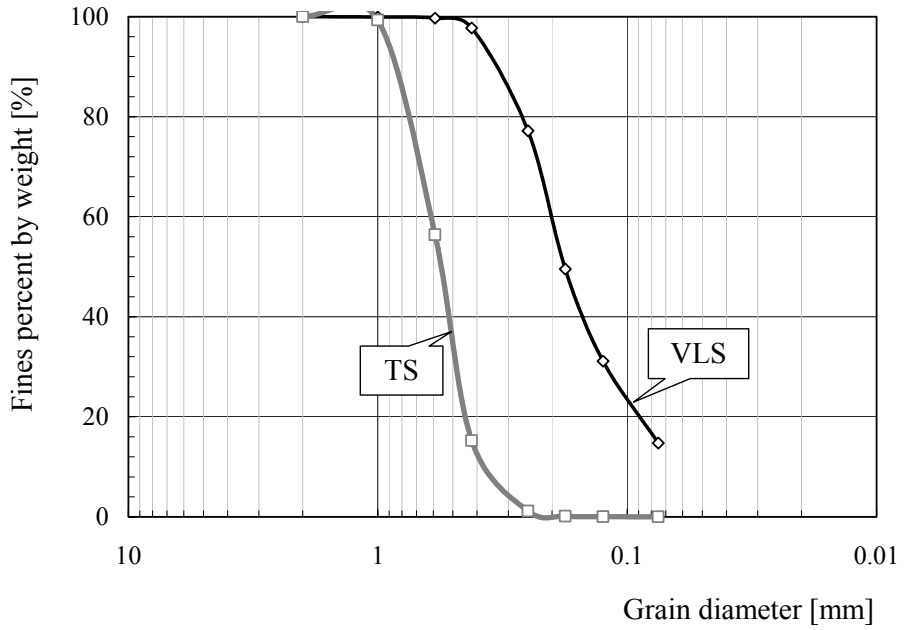

Figure 7.1. Grain size distribution of the test sands.

The model raft was a square 115 mm wide (B) and 25 mm thick (t_r) steel plate characterised by a modulus of elasticity of E_r=2.1*105 MPa. The raft–soil stiffness ratio k_{rs}, defined below, was sufficiently high (i.e. k_{rs} = 110) to consider the raft as rigid [Horikoshi and Randolph (1997)]. As a consequence, the settlement of the raft was considered uniform in the test interpretation.

$$k_{rs} = 5.57 \frac{E_r}{E_{s0}} \frac{1-\nu_s^2}{1-\nu_r^2} \left(\frac{t_r}{B}\right)^3 \qquad [-] \qquad (7.1)$$

where:

E_{s0} = 115 MPa = small strain subsoil modulus [FL^{-2}], evaluated at depth z= B/2, according to Mayne and Poulos (1999);

ν_s = 0.2 = Poisson modulus of the subsoil [-];

ν_r = 0.3 =Poisson modulus of the raft [-].

The E_{s0} value introduced in the calculation was computed via the elastic theory as a function of the small strain shear modulus, G_0, which was derived from the state parameter of the sand using the empirical correlation proposed by Saccenti (2006). The adopted correlation was calibrated on the basis of the shear wave velocity measurements performed through bender elements during triaxial tests on dry VLS specimens:

$$G_0 = C_G \cdot \left(\frac{p'}{p'_a} \right)^{0.52} \cdot e^{-0.68} \qquad [FL^{-2}] \qquad (7.2)$$

where:

C_G = 65 MPa = material constant [FL^{-2}];

p' = mean effective stress [FL^{-2}];

p'_a = 101 kPa = atmospheric pressure adopted for stress normalisation [FL^{-2}];

e = void ratio [-].

The free–headed and close–ended model piles had an external diameter D_p of 8 mm and a length L_p of 292 mm; their axial stiffness was estimated through a direct calibration in a Shenk–Trebble loading frame and it resulted comparable to that of tubular steel piles or cast in situ concrete piles. In the test interpretation, the piles were considered rigid and their settlements were assumed constant with depth.

The piles were made from an aluminium alloy hollow pipe and they had an external skin roughness $R_t \approx 120 \div 300$ μm, which was obtained through mechanical turning and measured peak to peak by a micrometrical profilometer; the minimum value of the relative roughness resulted to be $R_n = R_t/D_{50} = 0.67$. A relative roughness $R_n > 0.1$ ensures that shear failure occurs in the soil surrounding the pile and produces an interface friction angle, δ', equal to the shearing resistance angle at the critical state, φ'_{cv}, therefore the ultimate shear resistance does not depend on the pile roughness [Yoshimi and Kishida (1981), Kishida and Uesugi (1987), Jardine et al. (1993), Foray et al. (1995), Garnier and Konig (1998), Fioravante et al. (1999), Sarri (2001)].

The diameter of the model piles, normalised with respect to the particle size dimension, was $D_p/D_{50} = 45$; this ratio is below the lower limit given by Garnier and Konig (1998) ($D_p/D_{50} > 100$) and close to the limit suggested by Fioravante (2002) ($D_p/D_{50} > 50$). In the performed test, a larger value of D_p/D_{50}, which would minimise scale effects that can overestimate the value of the ultimate shear stress, was not feasible since the value of D_p was chosen as large as possible to allow a group of 9 model piles, with adequate spacing, to be loaded by a sufficiently small raft to minimise the geometrical constraints of the container, as shown in Figure 7.2, where the main geometrical characteristics of the model and the boundary conditions are reported. However, the possible increment in ultimate shear stress from the centrifuge tests does not affect the load transmission mechanisms, which are the main topic of the chapter. In the tests, the ratio between the diameter of the container and the raft side was > 3 and the distance of the pile tips from the container bottom was always greater than $20D_p$. Some of the model piles were instrumented in each test. The fairly small diameter allowed a maximum of two load cells

per pile to be incorporated, and these measured the loads at two positions along the shaft. The miniaturised load cells, made from stainless steel, had a 4x4 mm square cross–section; two active strain gauges were attached onto each of the four flat surfaces, one to measure the pile–longitudinal strains, the other the pile–transversal strains. The strain gauges were connected in a complex Wheatstone bridge which gave a very accurate measurement of the axial load.

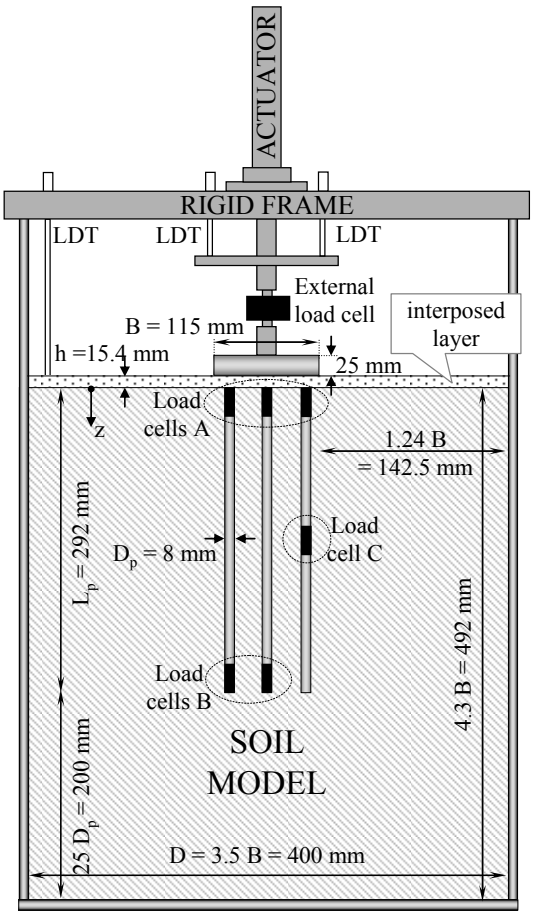

Figure 7.2. Boundary conditions and test model set–up for the loading tests on the piled raft with the interposed layer.

The instrumented cross–section was covered by a coaxial protective stainless steel jacket with an 8 mm external diameter, which prevented the strain gauges from being compressed by radial stresses, and it was

sealed with O–rings. The instrumented model piles were assembled in two configurations: the upper load cell was placed at the pile head (hereafter referred to as position A), while the lower load cell was placed at the pile base (position B) or alternatively at mid–pile (position C). The average sections of load cells A, C and B were at depths of $0.1L_p$, $0.5L_p$ and $0.95L_p$ from the pile top, respectively. The adopted instrumentation allowed the axial loads transmitted to each instrumented pile to be measured and the load transmitted through the shaft to be estimated. Figure 7.3 reports a draft of the instrumented model piles.

7.2 2 Test programme

The test programme consisted of twenty–one loading tests conducted on the nine model schemes shown in Figure 7.4 and listed below, of which P, R and NC0 have been used as reference tests. Al the foundations were subject to vertical axial loading. Table 7.1 summarises the main characteristics of the tests presented in this chapter, while the dimensions of the foundations are reported in the model and prototype scale in Table 7.2. Figure 7.5 shows the configurations of the load cells in each test.

P: isolated pile test (test T1);

R: unpiled raft test (T2);

PR1: 1–contact piled raft test (T3 and T4);

PR4: 4–contact piled raft test (T8);

PR9: 9–contact piled raft test (T9);

NC0: unpiled raft test with the interposed layer (T5);

NC1: 1–non–contact piled raft test (with the interposed layer between the raft and the pile head, tests T6 and T7);

NC4: 4–non–contact piled raft test (T10);

NC9: 9–non–contact piled raft test (T11).

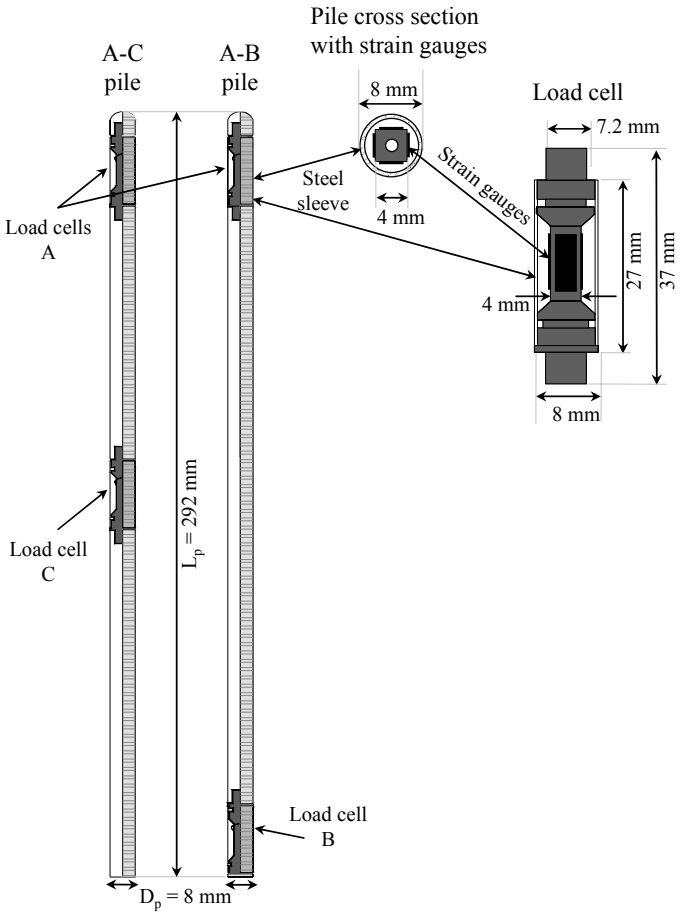

Figure 7.3. Instrumented model piles.

Table 7.1. Test programme.

Scheme	Test	Pile number n	Instrumentation	Spacing s	D_R (%)
P	T1	1	A–B	-	74
R	T2	0	–	-	72
PR1	T3	1	A–B	-	68
	T4	1	A–C	-	72
PR4	T8	4	2 A–B + 2 A–C	$9.625D_p$	77
PR9	T9	9	3 A–B + 2 A–C	$4.812D_p$	69
NC0	T5	0	–	-	72
NC1	T6	1	A–B	-	69
	T7	1	A - C	-	72
NC4	T10	4	2 A–B + 2 A–C	$9.625D_p$	72
NC9	T11	9	3 A–B + 2 A–C	$4.812D_p$	70

Table 7.2 Foundation dimensions (model and prototype scale).

Dimension		Model (mm)	Prototype (m)
Raft side (B)		115	7.5
Pile length (L_p)		292	19
Pile diameter (D_p)		8	0.5
Pile spacing s	4 piles	77	5
	9 piles	38.5	2.5
Interposed layer thickness (h)		15.4	1

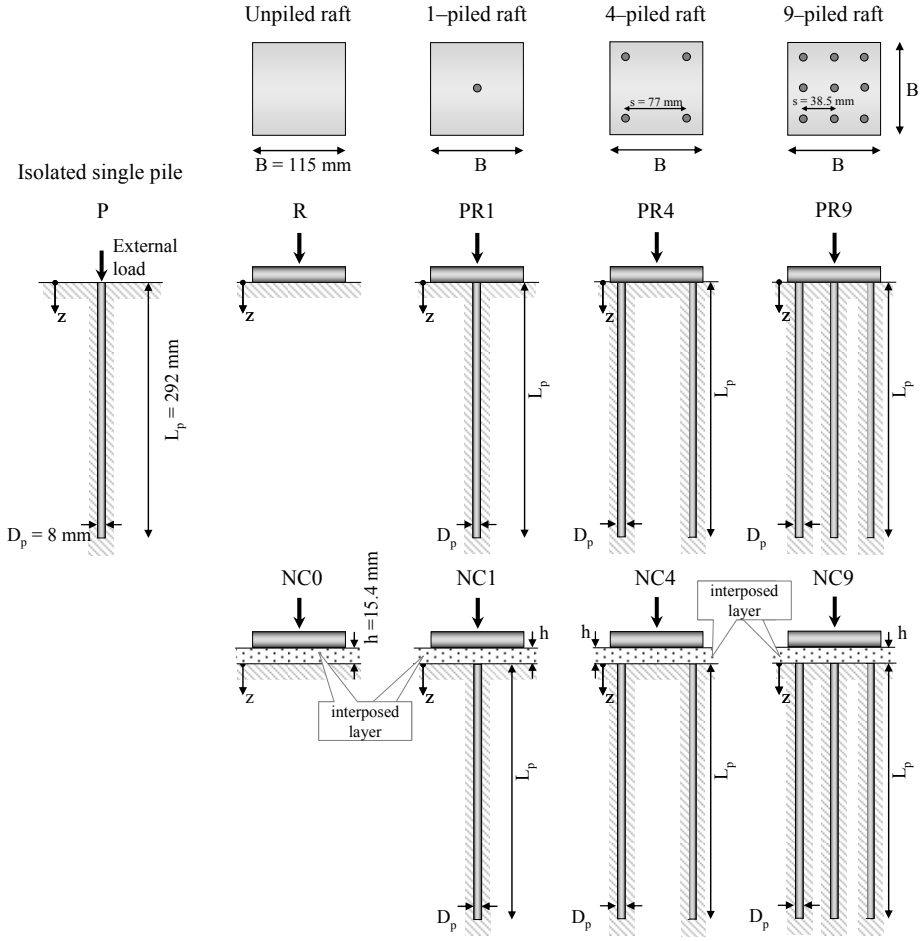

Figure 7.4. Model schemes.

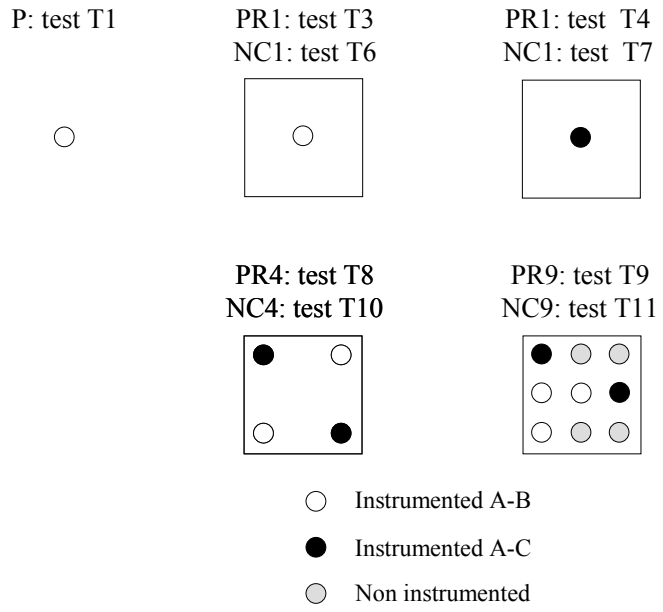

Figure 7.5. Configuration of the load cells.

7.2.3 Test procedure

The following test procedure was adopted:

(a) *At 1g*: each soil model was reconstituted to a relative density $D_R \approx$ 60%, by means of pluvial deposition of the dry sand, in a rigid steel cylindrical container with an internal diameter of 400 mm and a height of 755 mm, the surface of the soil model being located at a level of 492 mm above the container bottom, as shown in Figure 7.2, which reports the set–up of an NC piled raft loading test and the boundary conditions. After soil deposition, the model piles were partially jacked into the soil until 15 mm (1 m in the prototype scale) of the piles remained above the soil surface. A very rigid frame, which held a hydraulic actuator, two linear displacement transducers (LDTs) to monitor the raft displacement, an external load cell to measure the applied load and the raft plate (all these elements were rigidly connected to each other), was mounted onto the container top and then the model was embarked in centrifuge and

accelerated to *65g*. In the isolated pile test, the raft plate was replaced by a 8 mm diameter piston.

(b) *At 65g*: as the model was subjected to the acceleration field in the centrifuge, the soil surface settled due to consolidation (the settlement of the sand surface was measured with an LDT fixed to the container walls, see Figure 7.2); the presented data refer to the average soil density attained at the end of the in–flight consolidation, which was always about $D_R \approx 70\%$ (only in test PR4 was the final soil density higher, i.e. $D_R \approx 77\%$) and it was assumed constant with depth. At the end of the in–flight consolidation, the model piles were jacked completely into the soil model at 65*g* by means of the raft plate (or by the piston), then the raft was lifted up and the jacking load removed.

Contact piled rafts:

(c) *At 65g*: without stopping the centrifuge, the raft plate (or the piston) was slowly lowered until contact with the pile heads and the soil surface was achieved and the loading test was performed.

Non–contact (NC) piled rafts:

(c) The centrifuge was stopped and a 15.4 mm thick granular bed (1 m in the prototype scale) was applied through pluvial deposition *at 1g* to a very high relative density, then the soil model was again accelerated to *65g*.

(d) *At 65g*: the soil model was again allowed to consolidate. At the end of the second in–flight consolidation, the raft plate was lowered until contact with the interposed layer surface was achieved and the loading test was performed.

The jacking and the loading phases were executed at a constant loading rate, which was applied by the servo–controlled hydraulic actuator and measured by the external load cell. The raft settlement was obtained by averaging the measurements of the two LDTs placed in diametrically opposite positions from the actuator, as shown in Figure 7.2.

The "quasi–displacement" procedure adopted to install the model piles produced less densification of the soil around the piles than a 65*g* full pile length penetration would, but it was necessary to simultaneously jack a group of free headed piles. However, this procedure was assumed adequate to allow the full mobilisation of the shearing and bearing capacity to be attained.

The residual stresses produced by the in–flight consolidation of the soil, by the jacking phase and by the additional overburden of the interposed layer, in the case of the NC piles, have been taken into account in the test result interpretation.

The soil model uniformity was checked by means of in–flight static cone penetration tests, performed on dummy models ($D_R \approx 48\%$ and 66%, respectively), by means of a miniaturized electrical piezocone (diameter of 11.3 mm and apex angle of 60°), penetrating at a rate of 2 mm/s. The measured cone point resistance, q_c is plotted in Figure 7.6 versus the vertical effective stress, σ'_v. In the Figure, the measured resistance profiles are compared with those computed using the empirical correlation proposed by Jamiolkowski et al. (2003). The correlation has been adapted to centrifuge results, modifying the first coefficient of the original expression. The trend of the measured q_c indicates the achievement of an acceptable level of uniformity.

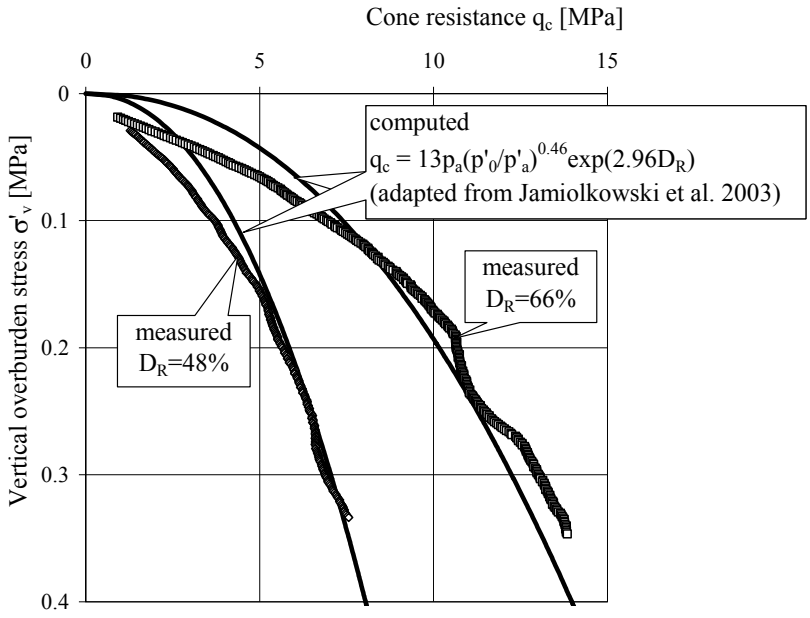

Figure 7.6. In–flight Cone Penetration Test at $D_R \approx 48$ and 66%.

The very limited scatter of the loads measured by the instrumented piles during the jacking phase of tests T1, T3, T4, T6 and T7 proved the repeatability of the soil model preparation method [Fioravante (2010)] and therefore the results of different loading tests on the same model scheme can be compared. The validity of this hypothesis allowed the results of analogous 1–piled raft tests, in which the pile was alternatively instrumented A–B and A–C (T3 and T4 for the contact piles, T6 and T7 for the NC piles), to be merged to compose an "equivalent A–B–C pile" and the axial load distribution with depth to be evaluated.

Due to the axial–symmetry of the load and geometry, it has also been assumed that the piles placed at the same distance from the raft centre have experienced the same load distribution with depth; therefore, the measurements obtained from model piles alternatively instrumented A–B and A–C have been merged to compose an equivalent A–C–B pile, at that distance.

7.2.4 Constraint conditions

In the contact piled rafts, the rigid raft imposed compatibility of the displacements and the pile heads and the subsoil surface were forced to settle by the same amount as the raft:

at $z = 0$ $\quad w_r = w_s = w_p$ [L] (7.3)

where:

z = depth from the initial subsoil model surface [L] (see Figures 7.2 and 7.4);

w_r = measured raft settlement [L];

w_p = pile settlement [L];

w_s = subsoil surface settlement [L].

In NC piled rafts, the interposed layer compressibility allows the piles to settle less than the surrounding soil, i.e. downward subsoil surface–pile relative displacement takes place (Fioravante 2010):

at $z = 0$ $\quad w_r > w_s > w_p$ [L] (7.4)

The load transfer mechanisms in the contact and non–contact piled rafts can be summarised as schematically represented in Figure 7.7; a trace of the possible soil settlement distribution with depth is also shown.

The settlements w_s and w_p were not measured in the NC piled raft tests presented here.

7.3 Stress–settlement behaviour of the piled rafts

Figure 7.8 reports the results of the load tests on the contact piled rafts (left–hand side) and those of the NC piled rafts (right–hand side) with respect to the raft relative settlement, w_r/B.

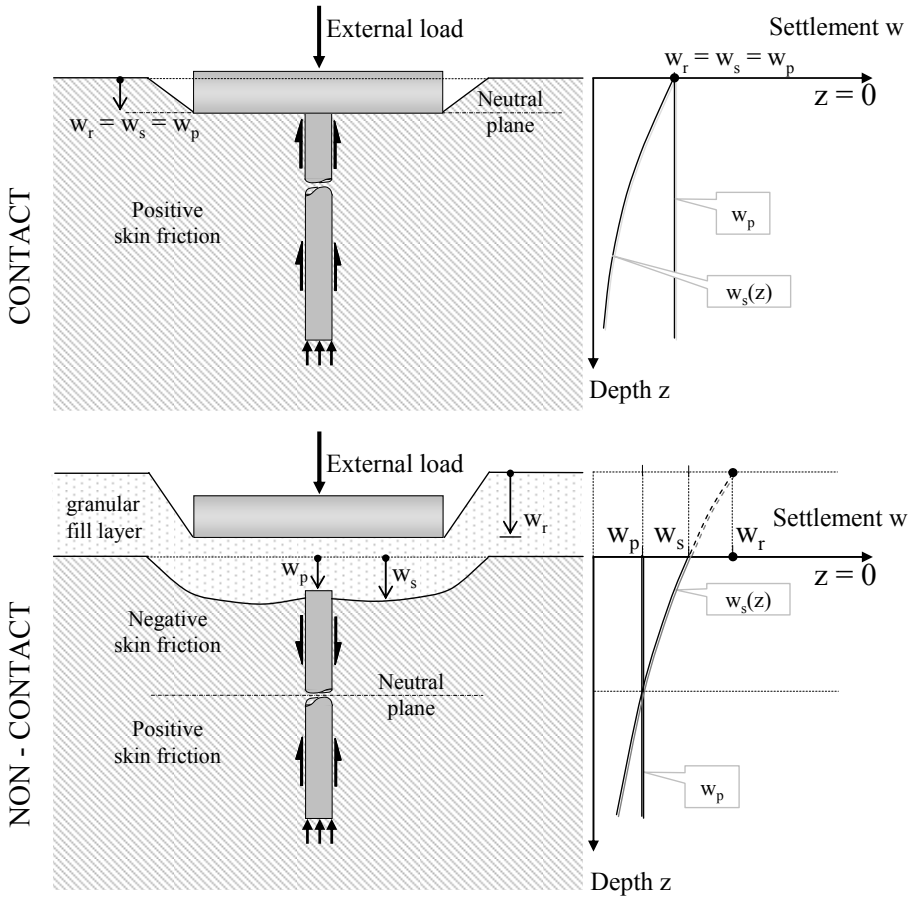

Figure 7.7. Schematic of the load transfer mechanisms in contact and NC piled rafts, with probable profiles of soil displacement with depth $w_s(z)$.

The total unit load applied to raft, q_t (shown in Figure 7.8a), the pressure transmitted by the raft to the subsoil, q_r (Figure 7.8b) and the total axial load transmitted by the raft to pile heads, Q_p (Figure 7.8c, where the load is represented in model scale) have been computed as:

$$q_t = Q_t/B^2 \qquad [FL^{-2}] \qquad (7.5)$$

$$q_r = \frac{Q_r}{B_e^2 - n \cdot \frac{\pi D_p^2}{4}} \qquad [FL^{-2}] \qquad (7.6)$$

$$Q_p = \sum_{i=1}^{n} Q_{Ai} \qquad n = 1, 4, 9 \qquad [F] \qquad (7.7)$$

where:

Q_t = measured load applied to the raft [F];

$Q_r = Q_t - Q_p$ = load transmitted to the subsoil [F];

B_e = loading area side [L], equal to B in the contact piled rafts, while, in the presence of the interposed layer, a loading spread of 45° was assumed, i.e.: $B_e = B + 2h$, with h = interposed layer thickness [L];

n = number of piles [-];

Q_{Ai} = axial load measured at the head of the i^{th} pile [F].

Figures 7.8a and b also report the results of the unpiled raft load tests (R on the left–hand side and NC0 on the right–hand side) for which $q_t = q_r$.

In tests PR9 and NC9, the axis symmetry of the geometry and of the loading conditions allowed us to account for the non instrumented piles, which were considered to be loaded to the same extent as the instrumented piles placed at the same distance from the raft centre.

The load sharing between the soil and the piles was evaluated from the results reported in Figure 7.8 and the Q_r/Q_t and Q_p/Q_t, ratios are plotted in Figure 7.9 vs. w_r/B (left–hand side contact piled rafts, right–hand side NC piled rafts). The piled raft settlement efficiency function, ζ was derived from the same results; the ζ curves, evaluated, at a certain applied q_t, as the settlement of the unpiled raft minus the settlement of the piled rafts normalised to the settlement of the unpiled raft, are reported in Figure 7.10 as a function of the number of piles, for values of q_t ranging from 25 to 700 kPa.

Observing Figures 7.8, 7.9 and 7.10, the following comments can be made:

- The unpiled raft R shows an almost linear stress–settlement curve while the curves of piled rafts PR1, PR4 and PR9 are non–linear (Figure 7.8a, left–hand side). The piled raft stiffness values at small settlements depend on the pile number. Yielding occurs at $w_r/B \approx$ 0.3% for PR1 and PR4, at $w_r/B \approx 1.2\%$ for PR9 and it causes a sharp decrease in the tangent stiffness which, at larger relative settlements, becomes almost steady and similar to R (unfortunately test PR4 was interrupted at $w_r/B = 0.7\%$). In the explored range of loads, the piled raft foundations did not reach their ultimate load capacity and the load–settlement curves can be reproduced, as a first approximation, as bi–linear functions, according to the first and the second segments of the tri–linear curve defined by Poulos (2001) and sketched in Figure 7.11.
- The foundation yielding is caused by the yielding of the piles (Figure 7.8c); after yielding, the observed steady increase in the total unit load q_t, carried by PR1, PR4 and PR9, is mainly due to the almost linear increase in the stress transmitted to subsoil, q_r (Figure 7.8b).
- In PR4, the pile group yielding load results to be $Q_{py,PR4} \approx 4Q_{py,PR1}$, and $Q_{py,PR4}$ is reached at about the same settlement as $Q_{py,PR1}$; in PR9, the pile group yielding load is $Q_{py,PR9} >> 9Q_{py,PR1}$ and it is reached at a higher settlement than PR1. In PR9, the increased pile yielding load can mainly be attributed to the effect of the compaction of the sand produced by the jacking of the 9 piles; the pile group is probably influenced by interactions between the piles which cause a softer response.

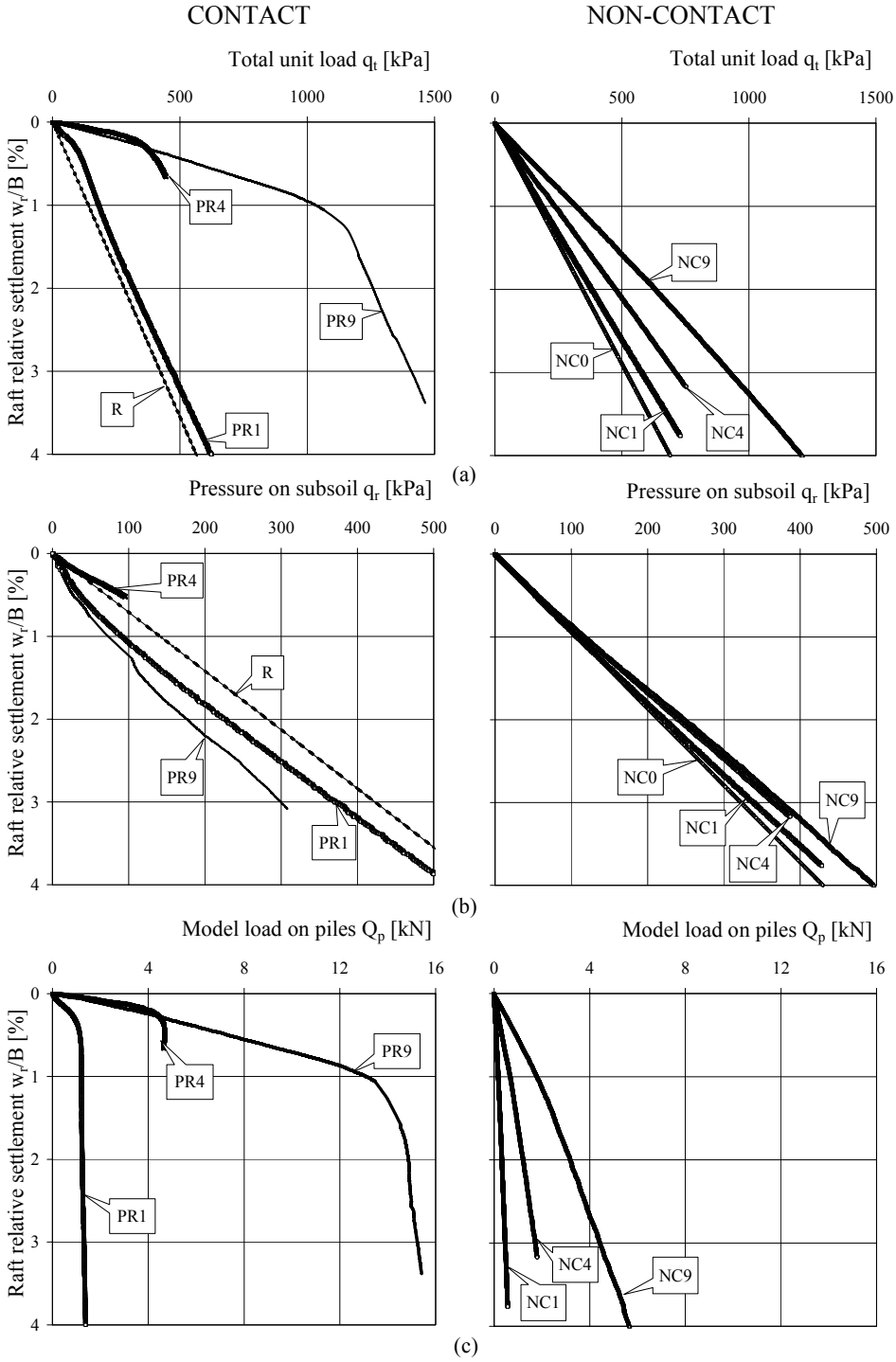

Figure 7.8. Load–settlement relationships of the piled rafts: (a) total unit load q_t, (b) unit load transmitted to subsoil q_r and (c) total load on piles Q_p (model scale), for the contact (left–hand side) and non–contact (right–hand side) piled rafts.

- The q_r curves of PR1, PR4 and PR9 reported in Figure 7.8b, after an initial non–linearity, which is probably due to a non–uniform contact between the raft and the soil surface, are almost linear. PR1 and PR9 show similar tangent stiffness to R, while PR4 seems to be stiffer, probably because of the higher soil density ($D_{R,PR4} \approx 77\%$ while the average value of the other tests is $D_R \approx 70\%$).
- As far as load sharing is concerned, the contact piles carry most of the applied load at small settlements while the subsoil is loaded progressively as the raft settles (Figure 7.9 left–hand side). After the piles yield, the further increment of the applied load is carried by the subsoil, which still has linear behaviour.
- The piled raft efficiency function ζ depends on the number of piles and on their yielding load. As shown in Figure 7.10, the efficiency of the 1–piled raft is $\zeta_{PR1} = 0.5$ before yielding ($q_t \leq 100$ kPa); after yielding, ζ_{PR1} decreases with increasing q_t and reaches a steady value of 0.1 for $q_t \geq 250$ kPa. The efficiency of PR4 is almost constant for $q_t \leq 300$ kPa, $\zeta_{PR4} = 0.85$; it decreases for $q_t \geq 300$ kPa and reaches a value of 0.5 at $q_t = 700$ kPa. As for PR9, $\zeta_{PR9} \approx 0.88$ for $q_t \leq 700$ kPa and the yielding load has not been reached.

Non–contact piled rafts

- The NC0 curve is almost linear and it is slightly stiffer than R due to the higher overburden stresses in the shallow soil and to the high density interposed layer (Figure 7.8a right–hand side). The stress–settlement relationships of the NC1, NC4 and NC9 tests are quite linear – the first segment of the tri–linear curve defined by Poulos (2001), Figure 7.11 – and the piled foundation systems have not mobilised the yielding load of the pile group (Figure 7.8c). The

foundation tangent stiffness increases with an increase in the number of piles. At a serviceability raft settlement, which can be estimated as approximately $w_r/B < 0.1\% \div 0.5\%$ [O'Neill et al. (2001), Reul (2003], the NC pile foundations carry lower loads than the analogous contact pile rafts.

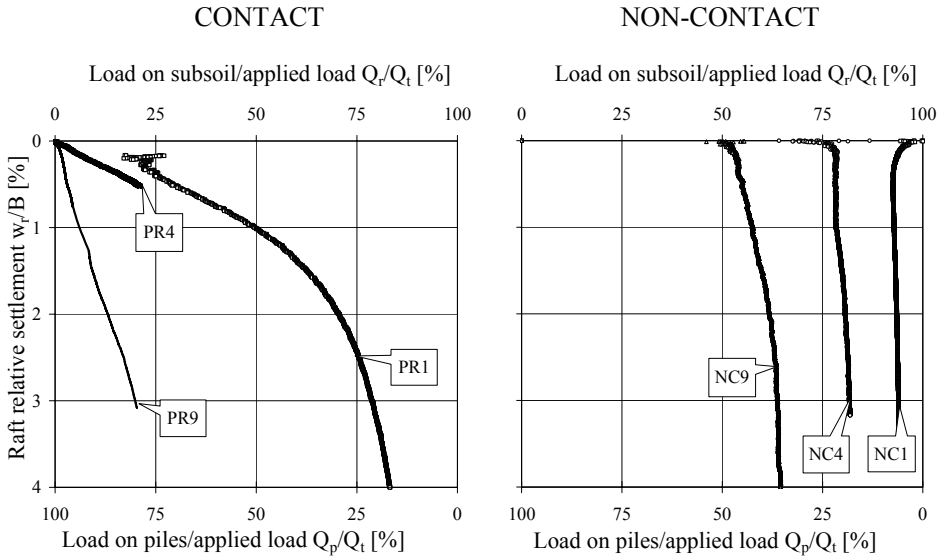

Figure 7.9. Load sharing for the contact (left–hand side) and non–contact (right–hand side) piled rafts.

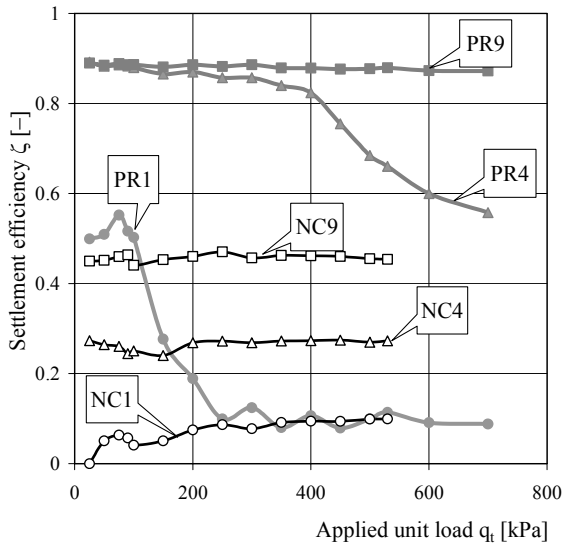

Figure 7.10. Piled raft settlement efficiency.

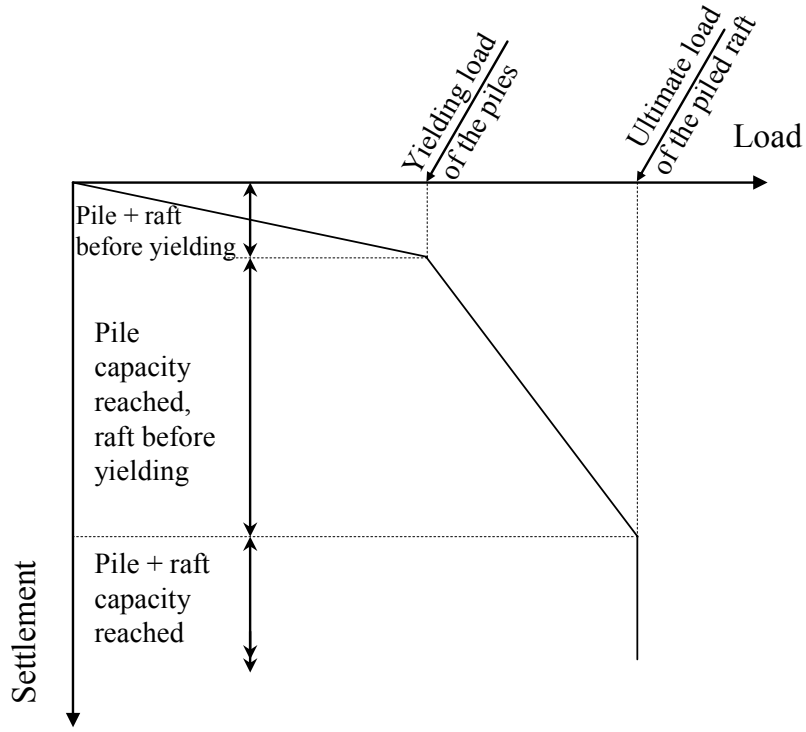

Figure 7.11. Simplified contact piled raft load–settlement curve, adapted from Poulos (2001).

- The Q_p curves reported in Figure 7.8c seem to be softer than those of the contact piles since they are plotted vs. the raft settlement w_r, which is higher than w_p (see Figure 7.7); in this scale, the pile contribution to the foundation resistance, as the raft settles, can be directly evaluated.
- The load progressively transmitted to the pile heads, as the total applied load increases, results to be approximately proportional to the number of piles, up to the maximum settlement reached, i.e. $Q_{p,NC4} \approx 4Q_{p,NC1}$ and $Q_{p,NC9} \approx 9Q_{p,NC1}$ (Figure 7.8c).
- The q_r curves of NC1, NC4 and NC9 reported in Figure 7.8b are approximately linear, slightly stiffer than NC0 and almost superimposed.
- The total applied load is mainly carried by the subsoil and only a small quantity is transmitted to the pile heads, as shown in Figures

7.8b and c. The load sharing plotted on the right–hand side of Figure 7.9 does not show a redistribution of the load as the raft settles and the Q_p/Q_t ratios remain almost constant in the experienced range of w_r.

- Since the piled raft yielding has not been reached, the settlement efficiency is approximately constant in the experienced displacement range and it depends on the number of piles: ζ = 0.08, 0.25 and 0.46 for NC1, NC4 and NC9, respectively (Figure 7.10).

7.4 Pile behaviour

The dissimilar stiffness mobilisation shown by the contact and non–contact piled rafts, as can be observed in Figure 7.8a, can be explained by the different constraint conditions at the raft–soil interface represented in Figure 7.7.

In contact piled rafts, the piles are directly loaded by the raft through their heads and the pile capacity mobilisation depends on the relative stiffness of the pile–subsoil. At the initial loading stage, the piles are much stiffer than the surrounding soil and they carry most of the applied load, until their capacity is fully mobilised; the initial foundation stiffness mainly depends on the pile stiffness.

In NC piled rafts, the load sharing and the pile capacity mobilisation are governed by the compressibility of the interposed layer, whose deformations modify the load transfer mechanism from the raft to the piles, allowing downward raft–subsoil–pile relative displacement. As a consequence, the initial foundation stiffness also depends on the interposed layer stiffness.

The base and the shaft contribution of the piles have been analysed to focus on the aforementioned mechanisms. As extensively described by Fioravante (2010), the base resistance and the shaft friction mobilisation

curves of NC piles plotted vs. w_r significantly differ from those of contact piles, since $w_r > w_p$. To allow a comparison between contact and non–contact piles, the base and shaft resistance curves have to be expressed as a function of the pile settlement. Since the w_p of the NC piles was not directly measured in the tests, it was deducted indirectly. On the basis of the results reported below, the pile tips were considered not to be influenced by the load induced by the plate on the shallow soil at the settlements reached in the tests, hence the base mobilisation functions of the NC piles were assumed identical to those of the homologous contact piles:

$$[\sum_{i=1}^{n} Q_{Bi}(w_p)]_{NC} = [\sum_{i=1}^{n} Q_{Bi}(w_p)]_{PR} \qquad n = 1, 4, 9 \qquad [F] \qquad (7.8)$$

where:

Q_{Bi} = axial load measured at the base of i^{th} pile [F].

Thus, each value of ΣQ_{Bi} measured in the NC tests was associated to the value of w_p measured in the corresponding contact pile tests. The thus calculated w_p ranged from 5% of w_r for NC1 and NC4 to 15% of w_r for NC9, in the range of raft settlement experienced in the performed tests.

Figure 7.12 reports the measured unit loads acting on the pile head q_A (Figure 7.12a) and base q_B (Figure 7.12b) and the mean shear stress $\tau_{S,AB}$ (Figure 7.12c) for the contact (left–hand side) and the NC piles (right–hand side); q_A, q_B and $\tau_{S,AB}$ are plotted with respect to the measured pile relative settlement w_p/B for the contact piles and vs. the computed w_p/B for the NC piles. The results of the loading tests on the isolated pile P are also reported on the left–hand side of Figure 7.12.

The values of q_A, q_B and q_C (where q_C is the unit load acting at mid–pile) gathered from the PR1, PR4 and PR9 tests are plotted vs. the depth

relative to the pile length, z/L_p, at values of w_r/B = 0, 0.25, 0.5, 1, 2%, on the left–hand side of Figure 7.13; the analogous values obtained from the NC1, NC4 and NC9 tests are reported on the right–hand side of Figure 7.13.

The unit loads q_A, q_B and q_C and $\tau_{S,AB}$ were computed as:

$$q_X = \frac{\sum_{i=1}^{n} Q_{Xi}}{n \cdot \frac{\pi D_p^2}{4}} \qquad X = A, B, C \quad n = 1, 4, 9 \qquad [FL^{-2}] \tag{7.9}$$

$$\tau_{S,AB} = \frac{\sum_{i=1}^{n} Q_{Si,AB}}{n \cdot L_{AB} \cdot \pi D_p} \qquad n = 1, 4, 9 \qquad [FL^{-2}] \tag{7.10}$$

where:

n = number of piles [-];

$\sum_{i=1}^{n} Q_{Ai}$ = the total axial load measured at the pile heads [F];

$\sum_{i=1}^{n} Q_{Bi}$ = the total axial load measured at the pile tips [F];

$\sum_{i=1}^{n} Q_{Ci}$ = the total axial load measured at the mid–piles [F];

$\sum_{i=1}^{n} Q_{Si,AB} = \sum_{i=1}^{n} \left(Q_{Ai} - Q_{Bi} + W_{AB}\right)$ = the total shaft resistance acting between load cells A and B [F];

L_{AB} = the distance between the measurement sections of cells A and B [L];

W_{AB} = the dead weight of the pile between load cells A and B [F].

Some considerations can be derived from the data presented in Figures 7.12 and 7.13.

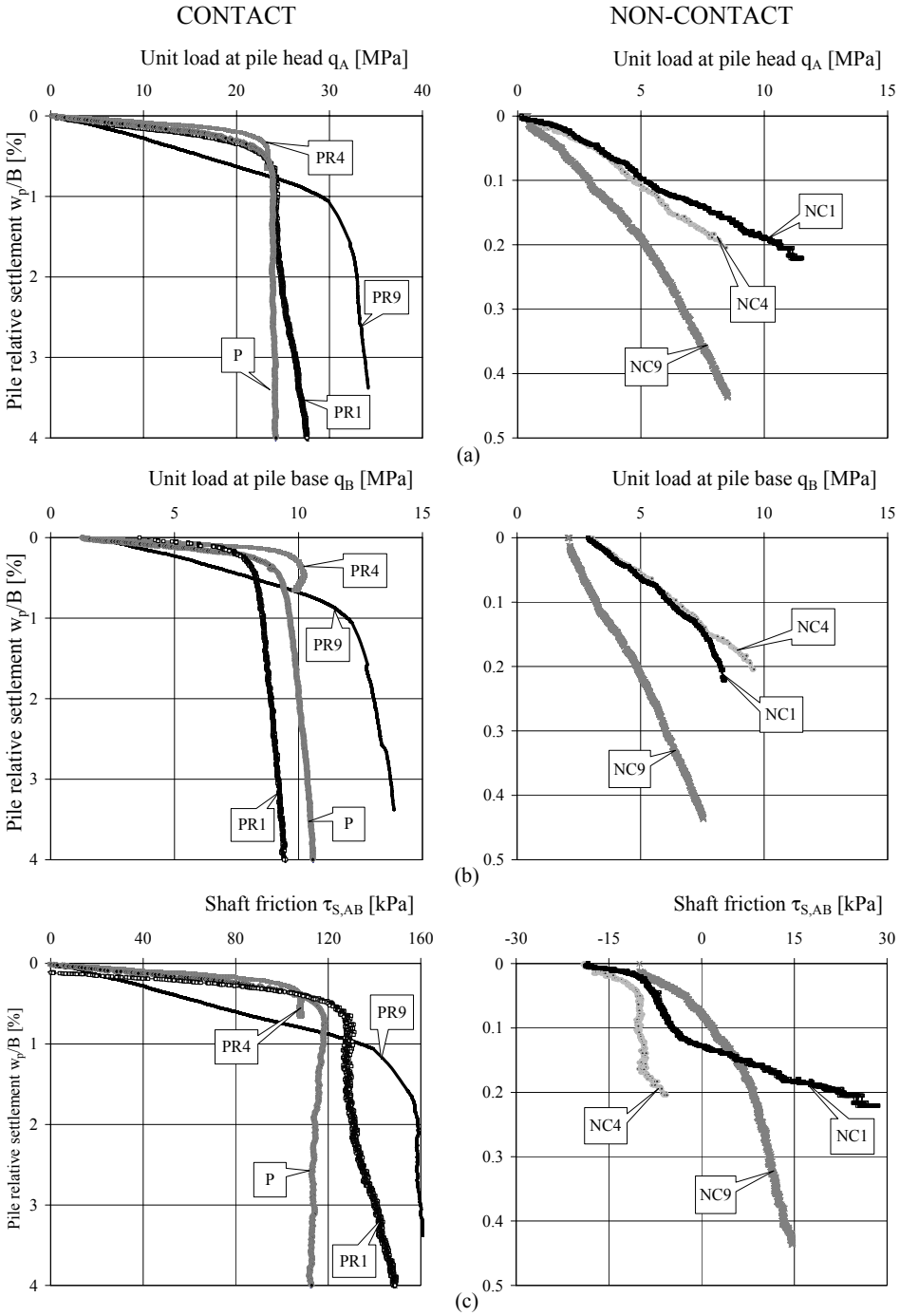

Figure 7.12. Load – settlement relationships of the contact (left–hand side) and non–contact (right–hand side) piles: (a) unit load acting on the pile heads q_A, (b) unit base load q_B and (c) mean A–B shear stress $\tau_{S,AB}$.

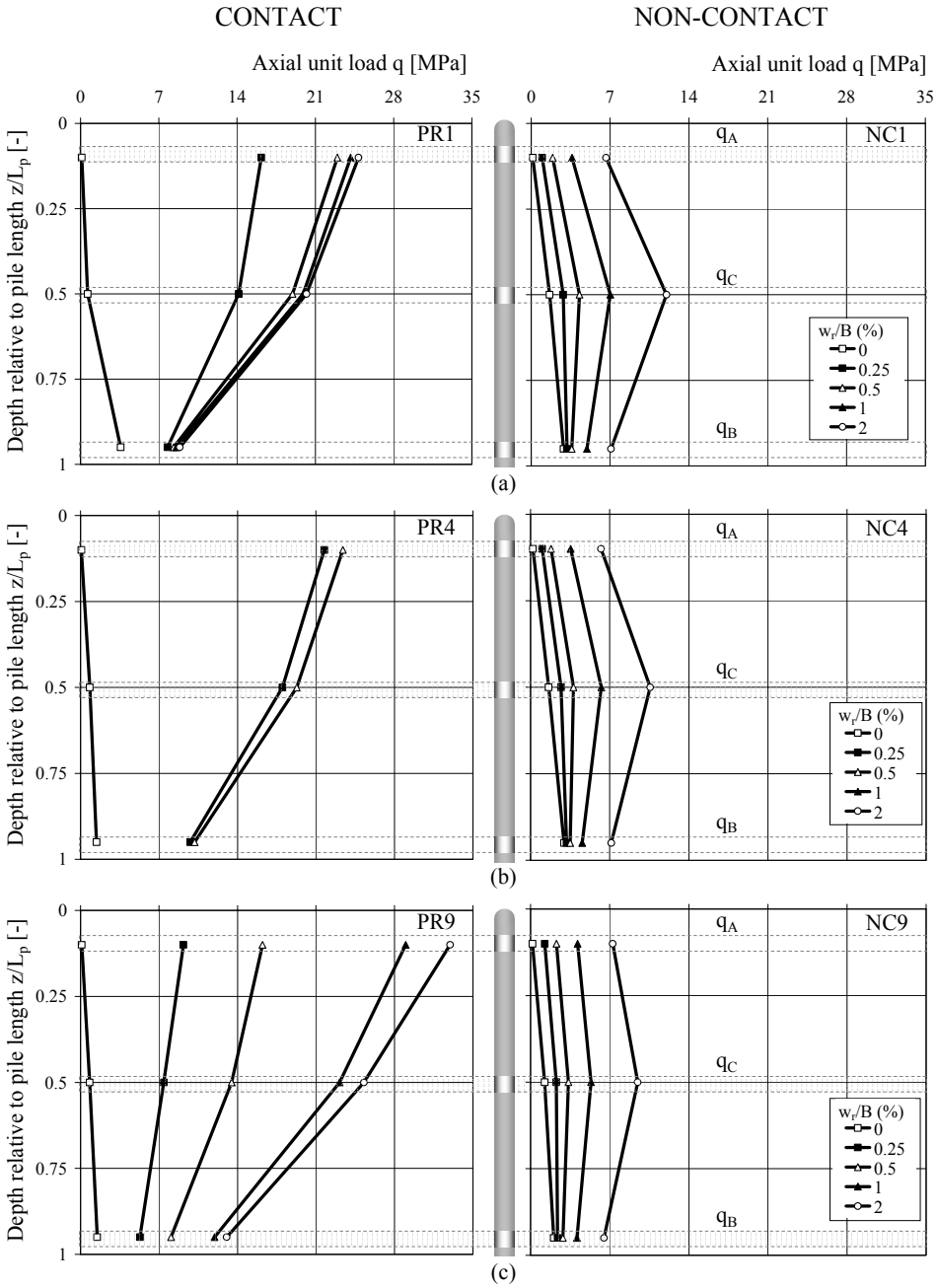

Figure 7.13. Axial unit load distribution along the pile shaft: (a) 1–piled rafts, (b) 4–piled rafts and (c) 9–piled rafts, for the contact (left–hand side) and NC (right–hand side) piled rafts.

Contact piles

- The limit load of the P, PR1, PR4 and PR9 piles is mobilised at small settlements; after yielding, q_A remains constant or increases slightly with settlement (Figure 7.12a). The axial unit load is transmitted from the piles to the subsoil by positive shaft friction and tip resistance, as shown on the left–hand side in Figures 7.12b, c and 7.13.
- *Isolated pile*: the ductile behaviour of P is due to the combination of the shaft friction and the base resistance, which are both mobilised at $w_p/B \approx 0.5 \div 0.6\%$, then $\tau_{S,AB}$ decreases slightly towards a steady value which is reached at large w_p/B (Figure 7.12c), while q_B increases slightly (Figure 7.12b).
- *Single pile beneath the raft*: the q_A curve of PR1 reaches a yielding value at $w_p/B \approx 0.5 \div 0.6\%$ with almost the same tangent stiffness as the isolated pile P, and then, from $w_p/B > 1.6\%$, it exhibits a steady tendency to increase as the pile settles (Figure 7.12a). The $\tau_{S,AB}$ curve achieves a higher limit value than that of P with the same gradient, and then it steadily increases from $w_p/B > 1.6\%$, reaching 15% higher values than the yielding value (Figure 7.12c). The difference between the $\tau_{S,AB}$ of PR1 and P suggests an enhanced pile response due to the increment in the vertical and horizontal stresses produced by the raft pressure at the soil surface, q_r; such an effect becomes more significant when the pile is approaching its yielding load. The q_B curve has a similar trend to that of P, even though it reaches 12% lower values, which suggests negligible effects of q_r on the pile base resistance in this series of tests (Figure 7.12b).
- *PR4 piles*: the q_A vs. w_p/B curve of the PR4 test is similar to that of PR1 with slightly larger q_B and slightly smaller $\tau_{S,AB}$ than those of PR1; unfortunately, the test was interrupted at $w_p/B = 0.7\%$.

- *PR9 piles*: compared to PR1, the PR9 piles reach higher yielding values of both q_B and $\tau_{S,AB}$, which would seem to suggest an improved pile capacity caused by the compaction of the sand produced by the jacking of 9 piles with spacing $s = 4.8D_p$; the softer pile response at small w_p/B can be attributed to the overlapping of the individual displacement field of the neighbouring piles (Figures 17.12b and c).

Non–contact piles

- The q_A and q_B curves from the NC1, NC4 and NC9 tests are almost linear and do not yield at the experienced settlement. The NC4 group exhibits a similar initial stiffness to NC1, while the group of 9 piles shows softer behaviour, probably due to group effects.
- The piles are loaded partially through their heads and partially by means of negative skin friction, which acts on their upper shaft (Figures 7.12c and 7.13, right–hand side). The pile–soil relative displacement is maximum at the pile heads and tips and is zero at a certain depth from the pile head (neutral plane). As a result, the shaft friction is mobilised from the pile heads downwards (upper shaft negative skin friction) and from the pile base upwards (lower shaft positive skin friction), while it is zero at the neutral plane.
- The maximum axial stress of the piles shifts downwards from the pile heads, as shown on the right–hand side of Figure 7.13. This Figure shows that the maximum unit load is measured by mid–pile load cells C, as the mid–pile regions are compressed between the upper shaft negative shear stress and the pile head load on one hand, and the lower shaft positive shear stress and base resistance on the other. The neutral plane is probably at a lower depth than the mid–pile at the beginning of the load tests (negative average $\tau_{S,AB}$ at small raft settlement shown

on the right–hand side of Figure 7.12c) and then moves upwards as the applied load is increased (positive average $\tau_{S,AB}$ at large displacements).

7.5 Non–contact piled raft stiffness

Several contact piled raft design approaches have been proposed in recent years and have been summarised by Poulos et al. (1997) and Poulos (2001): from simplified analytical methods for preliminary design purposes, involving simple constitutive soil models and simplified soil profiles, to very complex methods employing three–dimensional finite element analyses and realistic elasto–plastic constitutive soil models.

The NC piled raft stiffness was reproduced from the loading mechanisms observed in the performed physical model tests on piled rafts with the interposed layer according to the following rough procedure and the computed values have been compared with the measured ones.

The interaction effects between the raft and piles reduce the stiffness of the pile group. At the same time, the increment in vertical and horizontal stresses due to the pressure of the raft on the subsoil causes an enhanced pile response. The opposite effects of raft–pile interaction on the pile response seem to compensate each other in the performed tests (see PR1 in Figure 7.12). The interaction effects between the raft and piles could also reduce the stiffness of the raft, but the test results show that the raft stiffness does not seem to be dependent on the number of piles (Figure 7.8b). These observations justify the assumption that the piles and the raft can be considered as independent non linear springs, i.e.:

$$w_r = Q_r/k_r \quad \text{and} \quad w_p = Q_p/k_p \quad [L] \qquad (7.11)$$

where:

k_r = unpiled raft stiffness, deduced from the NC0 test [FL^{-1}];
k_p = pile group stiffness [FL^{-1}], evaluated as a function of the isolated pile P stiffness at small settlements, $k_{p,P}$ as: $k_p = n\,\mu\,k_{p,P}$, where $\mu = n^{-e}$ is the pile group efficiency, according to Fleming et al. (1992) and e = coefficient ranging from 0.3 to 0.6.

A value of μ =1 was assumed in NC4, since group effects were not observed in PR4, which would seem to suggest that in this series of tests the group effects between the piles were negligible at the spacing s = $9.6D_p$. A value of $\mu = 0.33$ ($e = 0.5$) was assumed in NC9.
Since the total applied load is shared between the piles and the subsoil, i.e:

$$Q_t = Q_p + Q_r \qquad [F] \qquad (7.12)$$

the piled raft settlement can be deduced from Eqs. 7.11 and 7.12 as:

$$w_{pr} = Q_t/k_{pr} = (k_r\,w_r + k_p\,w_p)/k_{pr} \qquad [L] \qquad (7.13)$$

where:
k_{pr} = piled raft stiffness [FL^{-1}], which results to be:

$$k_{pr} = k_r\,w_r/w_{pr} + k_p\,w_p/w_{pr} \qquad [FL^{-1}] \qquad (7.14)$$

For non–contact piles, $w_p < w_r$ and $w_r = w_{pr}$, thus the NC piled raft stiffness can be computed as:

$$k_{pr} = k_r + k_p\,w_p/w_{pr} = k_r + \beta\,n\,k_{p,P} \qquad [FL^{-1}] \qquad (7.15)$$

where:
$\beta = \mu\,w_p/w_{pr}$ = pile group stiffness coefficient [-], which is equal to 0.05 in the performed tests.

The w_p/w_{pr} ratio is likely to depend on the interposed layer thickness and stiffness and on the pile group stiffness.

This very simplified procedure has been employed to reproduce the applied unit load–settlement curves of the non–contact piled raft foundations; the results are shown in Figure 7.14, where the measured (solid lines) and computed (dots) q_t values are plotted vs. w_r/B.

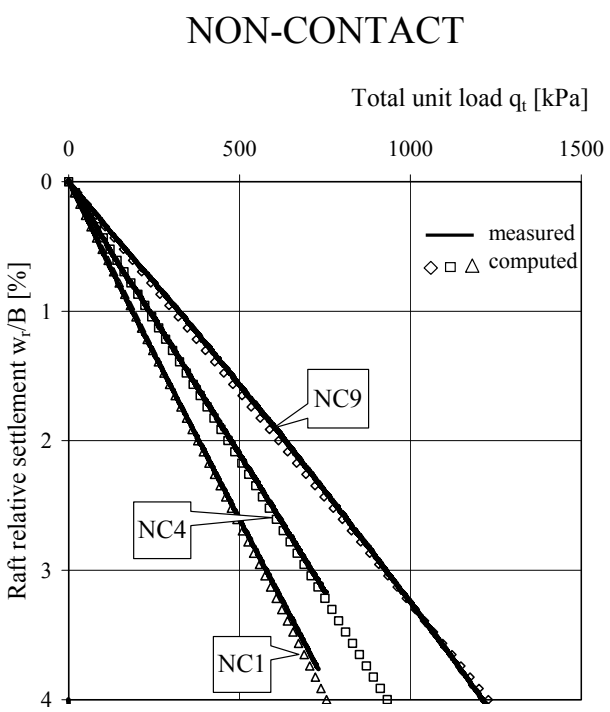

Figure 7.14. Measured (solid lines) and computed (dots) q_t values vs. w_r/B.

7.6 Closing remarks

The physical model test results have highlighted some major differences in the load–settlement behaviour of the contact and non–contact piled rafts, due to the different constraint conditions at the raft–soil interface.

In the contact piled rafts, the raft and piles settle by the same amount and the piles are directly loaded by the raft through their heads. The load sharing mechanism depends on the pile–subsoil relative stiffness.

At the initial loading stage, the piles are much stiffer than the surrounding soil and they carry most of the applied load until their

capacity is fully mobilised, while the subsoil is loaded progressively as the raft settles. At this stage, the contact piles reduce the foundation settlements by transferring a large amount of the total applied load to deeper and stiffer soil and the initial foundation stiffness mainly depends on the pile stiffness.

When the piles reach their limit load and yield, further increments in the applied load are mainly carried by the subsoil, which still has linear behaviour, and the piled raft tangent stiffness becomes similar to that of the unpiled raft.

The loading tests on contact piled rafts have also shown that the pressure transmitted by the raft to the subsoil increases the vertical and horizontal effective stresses and thus enhances the pile shaft capacity compared to the isolated pile, both before and after yielding. This effect could be further improved by the compaction of the sand which is caused by the jacking of close spaced piles. On the other hand, the test results have shown that, in a close spaced pile group, the overlapping of the individual displacement fields of neighbouring piles produces a decrease in the tangent stiffness of each pile.

In the NC piled rafts, the insertion of a deformable layer between the raft and the pile heads allowed downward subsoil–pile relative displacement, which took place in a range of depth from the pile heads. The piles are loaded through their heads and through the negative skin friction acting on their upper shaft; the head load and the negative skin friction cause the pile to settle, with the consequent mobilisation of the positive skin friction on the lower shaft and the base resistance. This mechanism is likely to be governed by the interposed layer stiffness and thickness. If the granular fill is not stiff enough, the pile bearing capacity is not fully

mobilised and the efficiency of the NC piled rafts could result to be below that of the analogous contact piled raft.

In this chapter, a rough procedure has been followed to reproduce the NC piled raft stiffness, which has been expressed as a function of the isolated pile stiffness, of the number of piles and of the unpiled raft stiffness. The influence of the compressibility of the interposed layer and the interaction effects between neighbouring piles has been expressed by a coefficient β which, from test interpretation, resulted equal to 0.05.

Chapter 8

Summary and conclusions

The behaviour of *rigid rafts on settlement reducing piles in sand*, subject to vertical axial loading, has been examined in this research.

A large numbers of *centrifuge tests* have been performed on piled raft models with the aim of:

- highlighting the raft–soil–piles interaction effects on the pile behaviour and on piled raft resistance and stiffness;
- analysing the load transfer mechanisms that take place within a piled raft and investigating the factors which govern the load sharing between the raft and the piles;
- comparing two pile installation methods (displacement and non displacement piles) in terms of efficiency as settlement reducers;
- highlighting the effect of a granular layer inserted between the raft bottom and the pile heads (piles not in contact with the raft) on the load transfer mechanism and on the piled raft stiffness.

A series of *numerical analyses* has also been carried out to understand more clearly the effect of the pressure transmitted directly by the raft to the soil on the behaviour of a single pile in contact with the raft.

8.1 Centrifuge test results

Two extensive centrifuge test series were performed.

First series of centrifuge tests

The tests were carried out on ***rigid circular raft models*** lying on a bed of ***very fine loose saturated silica sand*** (FF sand). The testing programme included the unpiled raft and the rafts on 1, 3, 7 and 13 ***contact piles***. Two types of model piles were installed beneath the rafts: ***displacement*** (D) and ***non displacement*** (ND) piles. Load tests on models of isolated single pile were also performed, in order to establish the shaft and the base capacity as well as the load–settlement curves of the two kinds of piles. Altogether twenty load tests were carried out.

- *Pile–raft interaction effects: single pile under the raft vs. isolated pile*
  The comparison between the load–settlement behaviour of the isolated pile and the single pile beneath the raft, for both the D and the ND piles, highlighted different shaft friction mobilisation mechanisms which can be ascribed to the effect of the pressure transmitted directly by the raft to the underlying soil. This load induced an increase in the vertical stress in the soil which, in turn, caused an increase in the radial stress acting on the pile shaft, which generated a significant *increase in the shaft friction limit value* mobilised at small settlements, especially in the upper pile portion ("$\Delta\sigma'_r$ *effect*"). The "$\Delta\sigma'_r$ effect" became more relevant when the pile approached its ultimate shear stress and it resulted to be slightly more pronounced in the ND pile than in the D pile. It had a negligible influence on the base resistance mobilisation, at least in the settlement range that has been investigated and for the pile length adopted.

At lower settlements than the limit values, neither a softer pile response, caused by the overlapping of the individual displacement fields of the cap and the pile, nor a minor shear stress mobilisation due to the shielding effect of the raft, were observed, as they were probably compensated for by the "$\Delta\sigma'_r$ effect". Instead, the single piles beneath the raft resulted to be slightly *stiffer* than the isolated piles.

The presence of the pile did not modify the load transfer mechanism from the raft to the soil, with respect to the unpiled raft.

- *Pile–pile interaction effects and installation method effect*

  Raft on non displacement pile groups

  The tests on piled raft models on ND pile groups showed that the interactions between the piles caused a *slower mobilisation of the shaft friction* than the single pile beneath the raft, the trend becoming more marked as the number of piles increased, and, for the same number of piles, as the pile spacing decreased. Instead, in large pile groups, the confining effect exerted by the neighbouring piles enhanced the "$\Delta\sigma'_r$ effect" that was observed for the single pile under the raft, and gave *higher values of the shaft limit resistance.* Interaction between the pile tips was also observed in large pile groups, and this caused an *improved end bearing capacity*, especially for the more confined piles.

  Raft on displacement pile groups

  The tests on the piled raft models on the D pile groups showed that the interactions between the piles which produced a softer pile response were compensated for, or even exceeded, by the *effect of the soil densification and increase in radial stresses* induced in the soil by the

jacking of the groups. Moreover, the superimposition of the compaction zone under the tips, produced by the pile jacking, caused a significant *enhancement of the end bearing capacity* in the close spaced pile group.

- *Load sharing and efficiency of the piled rafts*

  The tests showed that the load sharing mechanism between the piles and the raft depended on the pile–subsoil relative stiffness. The raft and piles settled by the same amount and the piles were directly loaded by the raft through their heads. At the initial loading stage, the piles were stiffer than the surrounding soil and they carried most of the applied load until their capacity was fully mobilised, while the subsoil was loaded progressively as the raft settled. At this stage, the share of the total applied load transmitted to the soil decreased as the number of piles increased. The piles reduced the foundation settlements by transferring a great amount of the total applied load to deeper and stiffer soil and the foundation stiffness mainly depended on the pile group stiffness. As a consequence, as the number of piles increased the foundation stiffness increased and, as the pile spacing decreased, the number of piles being the same, the piled raft stiffness decreased (due to increasing interaction effects between the piles).

  When the piles reached their limit load and yield, the further increments of the applied load were mainly carried by the subsoil, which still showed linear behaviour, and the piled raft tangent stiffness began to be controlled by that of the raft–soil contact.

  The efficiency of the piles as settlement reducers depended on the number and type of piles and on their limit load. The efficiency functions resulted to be almost constant before the pile group limit

load was reached, then it decayed as the applied load increased; the ND piles were less effective as settlement reducers than the D piles.

- *Piled raft bearing capacity*

  The *piled raft bearing capacity* was examined according to a *load efficiency method*, in order to understand the influence of the pile–pile and pile–raft interactions on the piled raft resistance.

  The piled raft total capacity was expressed as a function of the shaft and base resistance of the isolated pile and of the unpiled raft capacity, at a given settlement level, by means of shaft, base and raft efficiency functions, which accounted for the pile–pile and pile–raft interactions.

  The *base efficiency functions* assumed higher values than unity over the whole investigated settlement range due to the interaction effect between the pile tips and, only in the case of jacked piles, due to the effects of the soil densification under the bases produced by the pile installation.

  The *shaft efficiency functions* resulted to depend on many factors. In the case of *ND piles*, it was influenced by the interaction effects between the piles, at small settlements (lower shaft efficiency functions than unity), by the pile–raft interaction effects ("$\Delta\sigma'_r$ effect") and by the confining effects between the piles, at large settlements (higher shaft efficiency functions than unity).

  In the case of *D piles*, the "$\Delta\sigma'_r$ effect", the confining effects between the neighbouring piles and the soil densification effect produced by the jacking of groups of piles caused higher shaft efficiency functions than unity over the whole investigated settlement range.

  The *raft efficiency function* resulted to be equal to unity in small groups of piles and lower than unity in large groups of piles or in close spaced groups.

- *Piled raft stiffness*

  The *measured foundation stiffness* was compared with that computed using *Randolph's simplified approach*. A general underestimation of the computed piled raft stiffness values was observed with respect to those measured, due to the underestimation of the contribution of the raft to the overall stiffness and to the overestimation of the interaction factors between the piles. The "$\Delta\sigma'_r$ effect", the confinement effect exerted by the neighbouring piles and, only in the case of displacement piles, the effect of the densification produced by the jacking, compensated for or even exceeded the effects of the interactions between the piles which caused a softer pile response.

Second series of centrifuge tests

The second series of centrifuge tests was performed on ***rigid square piled rafts models*** in ***dry dense Venice Lagoon Sand*** (VLS). The testing programme included the unpiled raft, the displacement isolated pile and the piled rafts with 1, 4 and 9 displacement piles. The piled raft tests were carried out with the ***piles*** both ***in direct contact with the raft*** and ***separated from the raft by an interposed granular layer*** (non contact piles). Eleven load tests were performed.

- *Contact pile raft*

  The tests confirmed what has been observed during the first series of tests, i.e. the "$\Delta\sigma'_r$ effect", the interaction effects between the pile shafts and the bases, the effect of the soil densification and the increase in radial stresses due to the jacking.

- *Non contact piled raft: effect of the granular layer*

  The tests showed that the insertion of a deformable layer between the raft and the pile heads allowed downward shallow soil–pile relative

displacement, which took place over a range of depth from the pile heads. The piles, which settled less than the surrounding soil and the raft, were loaded through their heads and through the negative skin friction acting on their upper shaft; the head load and the negative skin friction caused the pile to settle, with the consequent mobilisation of the positive skin friction on the lower shaft and the base resistance. The pile bearing capacity was only partially mobilised. The interposed layer stiffness and thickness governed this mechanism.

A rough procedure was followed to reproduce the observed foundation stiffness, which was expressed as a function of the isolated pile stiffness, of the number of piles and of the unpiled raft stiffness. The influence of the compressibility of the interposed layer and the interaction effects between neighbouring piles was expressed by a coefficient β which, from test interpretation, resulted equal to 0.05.

8.2 Numerical analyses results

Finite element numerical analyses, using the ***state dependent dilatancy constitutive model*** proposed by Li and Dafalias (2000), were performed in order to ***reproduce some of the centrifuge tests carried out on the circular piled raft models***: the unpiled raft, the ND isolated pile and the raft on 1 ND pile models.

The parameters of the constitutive model adopted were calibrated on the basis of the results of the triaxial tests performed on the FFS specimens, and they were then adjusted to reproduce the unpiled raft centrifuge test results.

The geometry and the dimensions of the numerical models corresponded to those of the physical ones and the simulations were carried out applying an accelerated gravitational field to the mesh.

Reasonable agreement was obtained between the simulated and the measured load–settlement curves.

- *Non displacement isolated pile simulation*

  The simulation showed that, as the pile was subjected to axial loading and the shearing proceeded, the interface soil elements were subjected to the rotation of the principal effective stress directions. The elements close to the shaft pushed against the neighbouring soil elements that were lying on the same radial plane, a process that led to a decrease in the vertical effective stress and an increase in the lateral effective stress. After a certain amount of vertical displacement of the pile, the soil close to the shaft reached a critical state and stopped dilating. This led to an overall steady state of stress at which the shaft resistance reached its limit value, the principal effective stress directions had an inclination of $\pm 45°$ with the vertical, and the radial and vertical effective stresses were almost equal.

- *Raft on 1 non displacement pile simulation*

  The numerical simulation highlighted that the behaviour of the capped pile was a result of two effects which took place along the pile–soil interface. At small settlements the shearing effects prevailed, and they caused a rotation of the principal direction, a vertical stress reduction and a radial stress increase, as seen for the isolated pile. At large settlements the predominant effect was that of the raft pressure on the soil, which caused an increase in both the vertical and radial stresses and a consequent increase in the shaft resistance with respect to the isolated pile.

References

Akinmusuru, J.O. (1980). Interaction of Piles and Cap in Piled Footings. Journal of the Geotechnical Engineering Division, Vol. 106, No. 11, November 1980, pp. 1263-1268.

Baldi, G., Belloni, G., Maggioni, W. (1988). The ISMES Geotechnical Centrifuge. In Centrifuge 88, Paris, Corté J. F. Ed., Balkema, Rotterdam, pp. 45-48.

Been, K. and Jefferies, M.G. (1985). A State Parameter for Sands. Geotechnique, Vol. 35, No. 2, pp. 99-112.

Bolton, M.D., Gui, M. W., Garnier, J., Corte, J. F., Bagge, G., Laue, J. & Renzi, R. (1999). Centrifuge Cone Penetration Tests in Sand. Geotechnique, Vol. 49, No. 4, pp. 543-552.

Boulon, M., Foray, P. (1986). Physical and Numerical Simulation of Lateral Shaft Friction along Offshore Piles in sand. In Proceedings of the 3rd International Conference on Numerical Methods in Offshore Piling, Nantes, Editions Technip, Paris, pp. 127-147.

Boulon, M. (1988). Numerical and Physical Modeling of Piles Behaviour under Monotonous and Cyclic Loading. In Proceedings of the International Symposium on Modeling Soil–Water–Structure Interactions SOWAS '88, Delft, Kolkman,P.A. et al. Eds, Balkema, Rotterdam, pp. 285-293.

Boulon, M. (1989). Basic Features of Soil-Structure Interface Behaviour. Computers and Geotechnics, Vol. 7, No. 1-2, pp. 115-131.

Bowles, J.E. (1988). Foundation Analysis and Design. McGraw-Hill, Inc.

Burghignoli, A. Jamiolkowski, M.B. and Viggiani C. (2007). Geotechnics for the Preservation of Historic Cities and Monuments: Components of a Multidisciplinary Approach. In Proceedings of the 14th European Conference on Soil Mechanics and Geotechnical Engineering, Madrid, Spain. pp. 3-38.

Burland, J. B., Broms, B.B., De Mello, V.F.B (1977). Behaviour of foundations and structures. In Proceedings of the 9th International Conference on Soil Mechanics and Foundation Engineering, Tokio, Japan, Vol. 2, pp.495-546.

Burland, J. B. (1995). Piles as Settlement Reducers. In Proceedings of the 19th Italian National Geotechnical Congress, Pavia, Italy, Vol. 2. pp. 21-34.

Butterfield, R. and Banerjee, P.K. (1971). The Elastic Analysis of Compressible Piles and Pile Groups. Geotechnique, Vol. 21, No. 1, pp. 43-60.

Cao, X.D., Wong, I.H., Chang, M-F. (2004). Behavior of Model Rafts Resting on Pile–Reinforced Sand. Journal of Geotechnical and Geoenviromental Engineering 130: 129-138.

Clancy, P. and Randolph, M.F. (1993). An Approximate Analysis procedure for Piled Raft Foundations. International Journal for Numerical and Analytical Methods in Geomechanics, Vol. 17, pp. 849-869.

Conte, G., Mandolini, A., Randolph, M.F. (2003). Centrifuge Modelling to Investigate the Performance of Piled Rafts. In Proceedings of the 4th International Geotechnical Seminar on Deep Foundations on Bored and Auger Piles, Van Impe, W.F. Ed., Millpress, Rotterdam, pp. 359-366.

Cooke, R. W., Price, G. & Tarr, K. W. (1980). Jacked Piles in London clAy: Interaction and Group Behaviour under Working Conditions. Geotechnique, Vol. 30, No. 2, pp. 449-471.

Cooke, R. W. (1986). Piled Raft Foundations on Stiff Clays. A Contribution to Design Philosophy. Geotechnique, Vol. 35, No. 2, pp. 169-203.

Dafalias, Y. F. (1986). An Anisotropic Critical State Soil Plasticity Model. Mech. Res. Commun. Vol. 13, No. 6, pp. 341-347.

El-Mossallamy, Y. & Franke, E. (1997). Pfahl-Platten-Gründungen. Theorie und Anwendung. Bautechnik, Vol. 74, No.11, pp 755-764.

Fioravante, V. (2000). Anisotropy of Small Strain Stiffness of Ticino and Kenya Sands from Seismic Wave Propagation Measured in Triaxial Testing. Soils and Foundations, Vol. 40, No. 4, pp.129-142.

Fioravante, V. (2002). On the Shaft Friction Modelling of Non-Displacement Piles in Sand. Soils and Foundations, Vol. 42, No. 2, pp. 23-33.

Fioravante, V. (2010). Load Transfer Mechanism Between a Pile and a Raft with an Interposed Granular Layer. In press on Geotechnique.

Fioravante, V., Ghionna, V. N., Jamiolkowski, M.B. and Sarri, H. (1999). Shaft Friction Modelling of Non-Displacement Piles in Sand. In Proceedings of the International Conference On Analysys, Design Construction and Testing of Deep Foundation (Supplement), Offshore Technology Research Center, Austin.

Fioravante, V and Jamiolkowski, M.B. (2005). Physical Modelling of Piled Raft. In Proceedings of the International Geotechnical Conference on Soil-Structure Interaction, Saint Petersburg. Ulitsky,V.M. Ed. ASV Publishers Saint Petersburg-Moscow, pp 89-95.

Fioravante, V., Colombi, A., Jamiolkowski, M.B. (2006). On the Effects of Residual Tangent Stresses in Centrifuge Pile Tests. In Physical Modelling in Geotechnics, 8th ICPMG, Ng, Zhang and Wang Eds., Taylor and Francis group, London, pp. 827-833.

Fioravante V., Guerra L. & Jamiolkowski M. B. (2008a). Tensile shaft capacity of bored piles in sand from centrifuge modelling. Proc. Research Symposium on the Characterization and Behaviour of Interfaces, Atlanta, Georgia, D. Frost Ed.

Fioravante V., Giretti D. and Jamiolkowski, M.B. (2008b). Physical Modelling of Raft on Settlement Reducing Piles. From Research to Practice in Geotechnical

Engineering, Geotechnical Special Publication No. 180, Laier, J.E., Crapps, D.K., Hussein, M.H. Eds., pp.206-229.

Fleming, K., Elson, K., Weltman, A., Randolph, M.F. (1992). Piling Engineering, 3rd Ed. Surrey University Press Ed.

Fontana, M. (2004). Personal Communication.

Fontana, M. (2009). Personal Communication.

Foray, P., Balachowski, L., Labanieh, S. (1995). Modélisation physique des ouvrages géotechniques en chambre d'étalonnage. Colloque, Les modèles réduits en génie civil, Nantes.

Foray, P., Balachowski, L., Raoult, G. (1998). Scale Effect in Shaft Friction due to the Localisation of Deformations. Centrifuge '98, Tokyo, Kimura, Kusakabe & Takemura Eds, Balkema, Rotterdam, pp. 211-216.

Fox, E.N. (1948). The Mean Elastic Settlement of a Uniformly Loaded Area at a Depth below the Ground Surface. In Proceeding of the 2nd international Conference on Soil Mechanics and Foundation Engineering, Rotterdam, Vol. 1, pp. 129-132.

Franke, E., Lutz, B. and El-Mossallamy, Y. (1994). Measurements and Numerical Modelling of High-Rise Building Foundations on Frankfurt Clay'. Geot. Spec. Pub. 40, ASCE, 2: 1325-1336.

Franke, E., El-Mossallamy, Y. and Wittmann, P. (2000). Calculation Methods for Raft Foundations in Germany. Design Application of Raft Foundations. Edited by J.A. Hemsley, Telford. pp. 282-322.

Fraser, R. A. & Wardle, L. J. (1976). Numerical Analysis of Rectangular Rafts on Layered Foundations. Geotechnique, Vol. 26, No. 4, pp. 613-630.

Garnier, J. and Konig, D. (1998). Scale Effects in Piles and Nails Loading Tests in Sand. In Centrifuge '98, Kimura, Kusakabe and Takemura (ed.), Balkema, Rotterdam. pp. 205-210.

Garnier, J and Pecker, A. (1999). Use of Centrifuge Tests for the Validation of Innovative Concepts in Foundation Engineering. Earthquake Geotechnical Engineering, Sêco e Pinto (ed). Balkema, Rotterdam, pp. 431-439.

Garnier, J. (2002). Size Effects in Shear Interfaces. Workshop on Constitutive and centrifuge modelling: two extremes, Monte Verità, Springman Ed., Swets & Zeitlinger Lisse, pp. 5-19.

Hansbo, S. (1984). Foundation on Friction Creep Piles in Soft Clays. International Conference on Case Histories in Geotechnical Engineering, St. Louis, Prakash, S. Ed. Vol.2, pp.913-922.

Hansbo, S. and Jendeby, L. (1983). Case Study of Two Alternative Foundation Principle; Conventional Friction piling and Creep Piling. Vag-och Vattenbyggaren, No.7-8, pp.29-31.

Horikoshi,K. (1995). Optimum design of Piled Raft Foundations. Ph.D. Thesis. The University of Western Australia.

Horikoshi,K. and Randolph, M.F. (1996). Centrifuge Modelling of Piled Raft Foundations on Clay. Geotechnique Vol. 46, No. 4, pp. 741-752.

Horikoshi, K. and Randolph, M.F. (1997). On the Definition of Raft–Soil Stiffness Ratio for Rectangular Rafts. Geotechnique Vol. 47, No. 5, pp. 1055-61.

Horikoshi,K. and Randolph, M.F. (1998). A Contribution to Optimal Design of Piled Rafts. Geotechnique Vol. 48, No. 3, pp. 301-317.

Huang, M, Liang, F.Y. and Li, Z. (2007). Recent advances of pile foundation in China. Advances in deep Foundations, Edited by Kikuchi, Otani, Kimura and Morikawa. pp.115-124.

Ishihara, K., Tatsuoka, F. and Yasuda, S. (1975). Undrained Deformation and Liquefaction of Sand Under Cyclic Stresses. Soils Foundations Vol. 15, No. 1, pp. 29-44.

Katzenbach, R. and Reul, O. (1997). Design and Performance of Piled Rafts. In Proceedings of the 14th International Conference on Soil Mechanics and Foundation Engineering, Vol. 4, pp. 2256-2256.

Katzenbach, R., Arslan, U., Moormann, C. and Reul, O. (1998). Piled Raft Foundation – Interaction Between Piles and Raft. Darmstadt Geotechnics, Darmstadt Univ. of Technology, No. 4, pp. 279-296.

Katzenbach, R., Arslan, U. and Moormann, C. (2000). Piled Raft Foundation Projects in Germany. Design Application of Raft Foundations. J.A. Hemsley Ed., Telford. pp. 323-390.

Kishida, H. and Uesugi, M. (1987). Tests of the interface between sand and steel in the simple shear apparatus, Géotechnique Vol. 37, No. 1, pp. 37: 45-52.

Kishida, H. and Meyerhof, (1965). Bearing Capacity of Pile Groups under Eccentric loads in sand. In the Proceedings of the 6th International Conference on Soil Mechanics and Foundation Engineering, Vol. 2, pp. 270-274.

Jamiolkowski, M.B., Lo Presti, D.C.F., Manassero, M. (2003). Evaluation of Relative Density and Shear Strength from CPT and DMT. Soil Behavior and Soft Ground Construction, Ladd Symposium, MIT, Cambridge Mass. Geotechnical Special Publication No. 119, Germaine J.T., Sheahan, T.C., Whitman, R.V. Eds., pp. 201-238.

Jamiolkowski, M.B., Ricceri, G., Simonini, P. (2009). Safeguarding Venice from high tides: site characterization & geotechnical problems. In Proceedings of the 17th International Conference on Soil Mechanics and Geotechnical Engineering, Alexandria, Vol. 4, pp. 3209-3230.

Jardine, R.J., Lehane, B.M., Everton, S.J. (1993). Friction coefficients for piles in sands and silts. Offshore Site Investigation and Foundation Behaviour, Society for Underwater Technology, Vol. 28. pp. 661-677.

Lee, S.H. and Chung, C.K. (2005) An Experimental Study of the Interaction of Vertically Loaded Pile Groups in Sand. Canadian Geotechnical Journal, Vo. 42, No. 5, pp. 1485-1493

Li, X. S. & Dafalias, Y. F. (2000). Dilatancy for cohesionless soils. Geotechnique, Vol. 50, No. 4, pp. 449-460

Li, X. S. & Wang, Y. (1998). Linear representation of steady-state line for sand. Journal of Geotechnical and Geoenvironmental Engineering, Vol. 124, No. 12, pp. 1215-1217.

Liang, F.Y, Chen, L.Z., Shi, X.G. (2003). Numerical Analysis of Composite Piled Raft with Cushion subjected to Vertical Load. Computers and Geotechnics, Vol. 30, No. 6, pp 443-453.

Liang, F.Y., Li, J. and Chen, L.Z. (2006). Optimization of Composite Piled Raft Foundation with varied Rigidity of Cushion. Foundation Analysis and Design: Innovative Methods, Geotechnical Special Publication No. 153., pp. 29-34.

Loukidis, L. and Salgado, R. (2008). Analysis of the Shaft Resistance of Non-Displacement Piles in Sand. Geotechnique, Vol. 58, No. 4, pp.283-296.

Mandolini, A. and Viggiani, C. (1997). Settlement of Piled Foundations. Geotechnique, Vol. 47, No.4, pp. 791-816.

Mandolini, A. (2003). Design of Piled Raft Foundations: Practice and Development. In Proceedings of the 4th International Geotechnical Seminar on Deep Foundations on Bored and Auger Piles, Ghent, Van Impe, W.F. Ed. Millpress, Rotterdam, pp. 59-80.

Mayne, P.W. and Poulos, H.G. (1999). Approximate Displacement Influence Factors for Elastic Shallow Foundations. Journal of Geotechnical and Geoenvironmental Engineering, Vol. 125, No. 6, pp. 453-460.

Mylonakis, G. and Gazetas, G. (1998). Settlement and Additional Internal Forces of Grouped Piles in Layered Soil. Geotechnique, Vol. 48, No.1, pp. 55-72.

O'Neil, M. W. (1983). Group Action In Off-Shore Piles. Geotechnical Practice in Offshore Engineering. Stephen W. Wright Ed. Geotechnical Engineering Division, ASCE, University of Texas, pp. 25-64

O'Neill, M.W (2005). Advances in Designing and Testing Deep Foundations. Vipulanandan, C. and Townsend, F.C.Eds. Geotechnical Special Publication No. 129, pp. 70-81.

Padfield, C.J. and Sharrock, M.J. (1983). Settlement of Structures on Clay Soil. Construction Industry Research and Information Institute, Special Publication 27, CIRIA Ed., London.

Pecker, A. (2004). Design and Construction of the Rion Antirion Brigde. Geotechnical Engineering for transportation projects, Geotechnical Special Publication 126, Yegian M.K. and Kavazanjian E. Eds., pp.216-240.

Phung, D.L. (1993). Footings with Settlement-Reducing Piles in Non-Cohesive Soil. Ph.D Thesis. Unversity of Technology, Göteborg, Sweden.

Poulos, H.G. (1968). Analysis of the Settlement of Pile Group. Geotechnique. Vol 18, No 4, pp. 449-471.

Poulos, H.G. (1991). Analysis of Piled Strip Foundations. Computer Methods & Advances in Geomechanics, Beer et al Ed., Balkema, Rotterdam, Vol. 1, pp. 183-191.

Poulos, H.G. (1993). Settlement Prediction for Bored Pile Groups. In In Proceedings of the 2th International Geotechnical Seminar on Deep Foundations on Bored and Auger Piles, Ghent, Van Impe, W.F. Ed. Millpress, Rotterdam, pp. 103-117.

Poulos, H.G. (1994). An Approximate Numerical Analysis of Pile-Raft Interaction. International Journal for Numerical and Analytical Methods in Geomechanics, Vol. 1, No.18, pp. 73-92.

Poulos, H.G. (2001a). Piled Raft Foundations: Design and Applications. Geotechnique Vol. 51, No. 2, pp. 95-113.

Poulos, H.G. (2001b). Methods of Analysis of Piled Raft Foundations. A Report Prepared on Behalf of Technical Committee TC18 on Piled Foundations. International Society of Soil Mechanics and Geotechnical Engineering.

Poulos, H.G. and Davis, E.H. (1980). Pile Foundation Analysis and Design. Wiley, New York.

Poulos, H.G., Small, J.C., Ta, L.D., Sinha, J. and Chen, L. (1997). Comparison of some Methods for Analysis of Piled Rafts. In Proceedings of the 14th International Conference on Soil Mechanics and Foundation Engineering, Hamburg, Vol. 2, pp. 1119-1124.

Randolph, M.F. (1983). Design of Piled Raft Foundations. Recent Developments in Laboratory and Field Tests and Analysis of Geotechnical Problems, Bangkok, pp. 525-537.

Randolph, M.F. (1994). Design Methods for Pile Groups and Piled Rafts. In the Proceedings of the 13th International Conference on Soil Mechanics and Foundation Engineering, New Delhi, Vol. 5, pp. 61-82.

Randolph, M.F. (2003). Science and Empiricism in Pile Foundation Design. Geotechnique, Rankine Lecture.

Randolph, M.F. and Wroth, C.P. (1978). Analysis of Deformation of Vertically Loaded Piles. Journal of the Geotechnical Engineering Division, Vol. 104, No. 12, pp. 1465-1488.

Randolph, M.F. and Wroth, C.P. (1979). An Analysis of the Vertical Deformation of Pile Groups. Geotechnique, Vol. 29, No. 4, pp. 423-439.

Randolph, M.F. and Clancy, P. (1994). Design and Performance of a Piled Raft Foundation. Geotechnical Special Publication No. 40, Yeung, A.T. and Felio, G.Y. Eds., pp.314-324.

Randolph M.F., Jamiolkowski M.B. and Zdravkovic,L. (2004). Load Carrying Capacity of Foundations. Advances in Geotechnical Engineering, The Skempton Conference, Institution of Civil Engineers London, Jardine, R. J., Potts, D.M. Higgins, K.G. Eds Thomas Telford London, Vol. 1, pp. 207-240.

Reul, O. (2003). Influences on the performance of piles observed by means of field measurements on combined pile raft foundations. Field Measurements in Geomechanics, Myrvoll. Ed., pp. 293-298.

Richart, F. E. Jr., Hall, J. R. & Woods, R. D. (1970). Vibrations of Soils

and Foundations. Englewood Cliffs, NJ: Prentice-Hall.

Russo, G. (1998). Numerical Analysis of Piled Rafts International Journal for Numerical and Analytical Methods in Geomechanics, Vol. 22, No. 6, pp. 477-493.

Russo, G. and Viggiani, C. (1998). Factors Controlling Soil-Structure Interaction for Piled Rafts. Darmstadt Geotechnics, Darmstadt Univ. of Technology, No. 4, pp. 297-322.

Saccenti, A. 2006. Sul comportamento meccanico dei terreni della Laguna di Venezia. PhD Thesis (in Italian). The University of Ferrara, Ferrara.

Sarri, H. (2001). Bored piles in sand subject to axial loading: physical and numerical modelling. PhD Thesis (in Italian), Technical University of Torino, Torino, Italy.

Schofield, A.N. (1980). Cambridge Geotechnical Centrifuge Operations. Geotechnique, Vol. 24, No. 4, pp. 227-268.

Thorburn, S., Laird, C.L. and Randolph, M.F. (1983). Storage tanks founded on soft soils reinforced with driven piles. Piling and Ground Treatment. Telford, London, pp. 157-164.

Tochnog (1989). A free explicit/implicit GFE program, developed by FEAT, Finite Element Application Technology (http:/tochnog.sourceforge.net).

Tomlinson, M.J. (2001). Foundation design and construction practice, 7th Ed. Pearson Education Ltd.

Vesic, A.S. (1969). Experiments with Instrumented Pile Groups in Sand. Performance of Deep Foundations, ASTM STO 444, pp. 177-222.

Viggiani, C. (2001). Analysis and Design of Piled Foundations. 1st Arrigo Croce Lecture, Rivista Italiana di Geotecnica, No.1/2001, pp. 47-75.

Wernick, E. (1978). Skin Friction of Cylindrical Anchors in Non-Cohesive Soils. Symposium on Soil Reinforcing and Stabilising Techniques, New South Wales Institute of Technology Sydney, pp. 201-219.

Wong, I.H., Chang, M.F. and Cao, X.D. (2000). Raft Foundations with Disconnected Settlement–Reducing Piles. Design Application of Raft Foundations, J.A. Hemsley Ed., Telford, pp. 469-486.

Yoshimi, Y. and Kishida, T. (1981). Friction between sand and metal surface. In Proceedings of the 10th International Conference on Soil Mechanics and Foundations Engineering, Stockholm, pp. 831-834.